Projected Forecast of Hydrodynamic Conditions in the North Sea for the 21st Century

Dissertation

Zur Erlangung des Doktorgrades der Naturwissenschaften
im Fachbereich Geowissenschaften der Universität Hamburg

vorgelegt von

Moritz Mathis

Hamburg, 2013

Als Dissertation angenommen
vom Fachbereich Geowissenschaften der Universität Hamburg

Auf Grund der Gutachten von **Dr. PD Thomas Pohlmann**
und **Prof. Dr. Jan Backhaus**

Hamburg, den 30. April 2013

(Datum der vorläufigen Bescheinigung)

Prof. Dr. Jürgen Oßenbrügge
Leiter des Fachbereichs Geowissenschaften

Declaration

I, Moritz Mathis, declare that this thesis entitled ¨Projected Forecast of Hydrodynamic Conditions in the North Sea for the 21st Century´ and the work presented in it are my own.

I confirm that

- This work was done wholly or mainly while in candidature for a research degree at this University.
- Where any part of this thesis has previously been submitted for a degree or any other qualification at this University or any other institution, this has been clearly stated.
- Where I have consulted the published work of others, this is always clearly attributed.
- Where I have quoted from the work of others, the source is always given. With the exception of such quotations, this thesis is entirely my own work.
- I have acknowledged all main sources of help.
- Where the thesis is based on work done by myself jointly with others, I have made clear exactly what was done by others and what I have contributed myself.

Signed: _____

Date: _____

Abstract

A projected forecast of hydrodynamic conditions in the North Sea is carried out for the 21st century by means of a dynamical downscaling with the shelf ocean model HAMSOM (University of Hamburg). The investigation is based on the IPCC (International Panel of Climate Change) SRES A1B scenario. In order to force the HAMSOM model, results from the global ocean model MPIOM (Max Planck Institute for Meteorology, Hamburg) are used at the open lateral boundaries of the HAMSOM model domain and results from the regional atmosphere model REMO (Max Planck Institute for Meteorology, Hamburg) are used for the meteorological forcing at the air-sea interface. A bias correction method relative to ERA40 reanalysis data (European Centre for Medium-Range Weather Forecasts) and WOA-2001 climatology (National Oceanographic Data Center) is applied to the forcing variables, respectively, in order to reproduce reasonable hydrodynamic present-day conditions in the North Sea. The entire simulation period is subdivided into the control period 1951-2000, to be used as reference, and the scenario period 2001-2099.

In the analysis of the HAMSOM model results particular attention is drawn on regional issues in order to provide a better understanding of potential climate change impacts on the North Sea. The analysis generally focuses on changes of the atmospheric forcing variables, the general circulation in the North Sea, heat fluxes and water temperature, thermocline parameters, fresh water fluxes and salinity, and changes of the sea surface elevation. Thereby, it comprehends trend analysis of time series of the various variables to address change signals as well as EOF analysis to address regional anomalies in the spatial distribution of the variables.

According to the model results, in the 21st century more frequent westerly winds over the North Sea enhance its general circulation in spring with an increase of northerly inflow by about +21%. Slightly decreasing wind speeds in the other seasons, however, entail a slight weakening of the general circulation in summer, autumn, and winter. The increase of annual mean air temperature by about +2.11 °C, with a distinctly stronger warming trend in winter than in summer, is reflected by the water temperature of the North Sea with an increase of annual mean SST by about +1.78 °C. The decomposition of the total surface heat flux reveals increasing cloud cover in spring and summer to cause significant decrease of ingoing short wave radiation in the warm seasons, while converging air-sea temperature differences in autumn and winter to cause significant decrease of sensible heat flux in the cold seasons. The strong warming in the cold seasons finally turns out to be the main driver for the total warming of the North Sea in the 21st century. In accordance to the changing wind speeds and the strong winter warming, the mean depth of the thermocline is slightly decreasing, i.e. the thermocline is raising, and the intensity of the mean vertical temperature gradient is weakened, respectively. Decreasing salinities of the inflowing Atlantic waters, increasing Baltic discharge, and higher positive surface fresh water fluxes give rise to a drop of the North Sea salinity by about -0.59 psu. The estimated global mean sea level rise for the 21st century amounts to about +0.46 m, while the maximum sea level change in the North Sea of about +0.6 m is observed in the eastern part because of steric effects and more frequent westerly winds.

Contents

Chapter 1

Introduction

1.1 Motivation, Objectives and General Approach

Hydrodynamic conditions in the ocean describe the distribution of hydrographic physical parameters like sea water temperature, salinity, and density as well as the direction and magnitude of ocean currents. The currents are able to transport a vast amount of heat over thousands of kilometers across the oceans and with this, significantly influence the constitution of the world´s climate. Moreover, hydrographic conditions are one of the most essential aspects governing the prevailing regime that biota are encountered in the ocean. Whereas the physical state variables have a direct impact on the regime, the hydrodynamic conditions rather control the nutrients and particle transport and decomposition and the dispersion of various plankton species and fish larvae. Therefore, hydrodynamic conditions are also a decisive factor in investigating marine ecosystems.

In the context of the present study a future projection of hydrodynamic conditions in the North Sea is examined for the 21st century by means of a Computerized Fluid Dynamics (CFD) simulation with the Hamburg Shelf Ocean Model (HAMSOM). The branch of applied CFD in ocean sciences was established in the 1950s, initiated by limitations in space and time as well as large costs of traditional oceanographic ship sampling. Since that time, various numerical models have been developed in order to investigate physical, chemical, and biological processes in the ocean, encouraged by the rapid advances in computing capacity. Compared to field measurements, numerical ocean models provide closed spatiotemporal coverage of all involved parameters, albeit the density of the parameter values depends on the respective grid resolution and time step size of the model. By analyzing model results, regions of scientific interest can thus be detected easier and more precise and hence, the efficiency of observational surveys can be increased. In turn, field measurements are used to evaluate model results and to improve the model parameterizations themselves. Besides, numerical ocean models also permit projective forecasting because of the prognostic and deterministic representation of respective parameters. Field measurements and model results therefore well complement each other so that nowadays, numerical modelling represents an indispensable tool in ocean sciences.

In particular in the North Sea there is a long history of ocean modelling ranging in complexity from barotropic tidal and storm surge models to three-dimensional baroclinic models with ecosystem components. Reviews of hydrodynamic modelling in the North Sea are given by e.g. Jones (2002), Lenhart and Pohlmann (2004) and Delhez et al. (2004). Regional circulation models (RCMs) have thereby proven to be useful tools for the study of regional dynamics in the ocean and atmosphere such as ocean currents (e.g. Pohlmann, 2006; Ådlandsvik and Bentsen, 2007; Melsom et al., 2009) or energy and fresh water cycles (e.g. Jacob, 2001; Schrum et al., 2003, 2005), as well as for the prediction of climate changes on a regional scale (e.g. Schrum, 2001; Déqué et al., 2005; Meier, 2006; Ådlandsvik, 2008). There is a consensus that dynamical downscaling using RCMs is the most appropriate option for regional impact studies and vulnerability analyses related to climate change (Feser et al., 2011). Adaptation measures to climate change, as opposed to mitigation policies, are an inherent local- and regional-scale issue.

In contrast to general circulation models (GCMs), the model domain of a RCM does not cover the entire globe but is typically restricted to some hundred or thousand kilometers in meridional and zonal directions. This feature allows for long-term simulation of physical processes with a high horizontal resolution at comparatively low computational costs. In general, a fine resolution is important to resolve small-scale features of the circulation, for instance near-shore processes affected by bottom topography and coastline morphology, or small-scale fronts and associated baroclinic eddies and frontal jets. Beside the value-added spatial details of a RCM simulation, the models are also expected to simulate a more reasonable temporal variability, which is often a weakness of GCMs.

The restriction to a certain geographical region and the aim to simulate physical processes on climatological time scales (i.e. 30 years or more) implies that information on the large-scale state of the ocean or atmosphere outside the regional model domain has to be provided by another source. These lateral boundary conditions can be extracted from GCM simulations or from global-scale observations and re-analysis products, where the RCM is said to be nested into the respective large-scale forcing. This technique is referred to by dynamical downscaling and, as in the present study, is usually carried out in a one-way mode, that is, without feedback to the large-scale system. Hence, the RCM inherit any large-scale error from the parent global model via the lateral boundary conditions (Pielke and Wilby, 2012). Beyond the mentioned advantages, the uncertainties of a given global climate projection are therefore not reduced by the method of one-way nesting. In recent years, however, also two-way nesting methods have been developed (e.g. Lorenz and Jacob, 2005) which are able to affect the large-scale circulation, at least if the dynamics of the downscaling region significantly contributes to it.

In this context the coupled global atmosphere-ocean circulation model ECHAM5/MPIOM of the Max Planck Institute for Meteorology (MPI-M) poses as the origin of the presented regional climate projection for the North Sea (Fig. 1.1). Short descriptions and references for all involved models are given in section 2.1. The respective IPCC (see section 1.3) future scenario run of ECHAM5/MPIOM was regionalized for the greater European atmosphere by means of dynamical downscaling with the regional atmosphere circulation model REMO. Thereby, the results of the atmosphere model ECHAM5 have been used for prescribing the conditions at the open lateral boundaries of the regional domain, whereas the results of the ocean model MPIOM have been used for prescribing sea surface conditions. The atmosphere-land interactions are fully implemented in REMO and therefore not required to be prescribed. Thus far, the model simulations have been carried out by the MPI-M community. In the present study, finally, the results of REMO and MPIOM are used analogously to drive the shelf ocean model HAMSOM in order to provide the respective North Sea regionalization. However, a linear bias correction is applied to both model results, based on ERA40 reanalysis data and WOA-2001 climatologies, respectively (see section 2.2.3 and 2.2.3). Riverine discharge along the North Sea coasts is treated as monthly climatological means, gathered by Damm (1997) and O'Driscoll et al. (2012) (see section 2.3), since for the North Sea region no other fresh water supply than the one descending from the Baltic catchment area is incorporated in the ECHAM5/MPIOM simulation. Moreover, to account

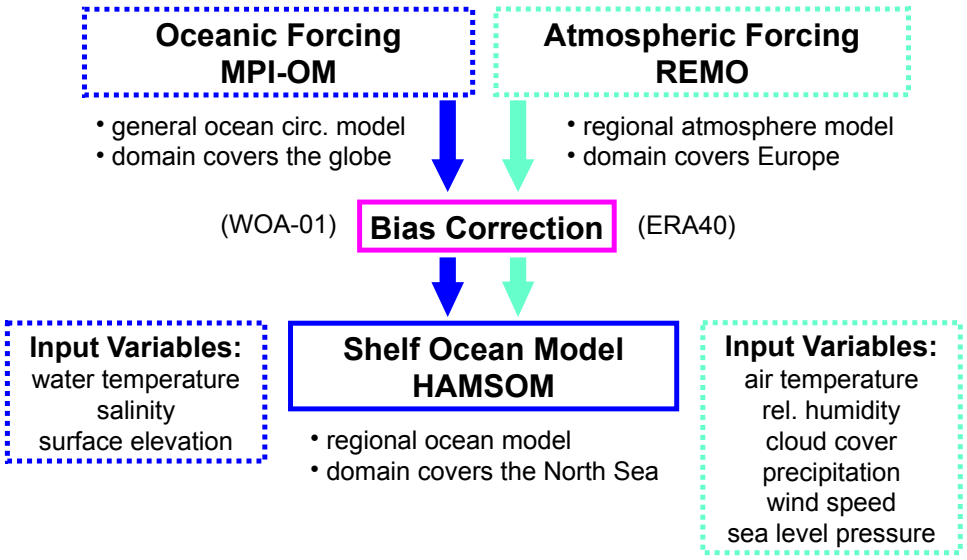

Figure 1.1: Schematic model setup of the uncoupled dynamical downscaling for the North Sea.

for tidal mixing and tidal residual flow, semi-diurnal lunar tidal oscillations as provided by the Oregon State Tidal Inversion Software (OTIS) are added onto the sea surface elevation prescribed at the open boundaries (see section 2.4). Further model- and method-specific details are described in chapter 2.

The involved model simulations always cover the total time period of investigation 1951-2099, as being composed of the control run 1951-2000 and the A1B scenario run 2001-2099. The respective forcing data for the control run originate from the historic ECHAM5/MPIOM model run 20C3M, initialized in the year 2240 of a preindustrial spin up run which was defined as representing the year 1860. This run was then continued until the year 2000 but, unlike the subsequent scenario run, with observed anthropogenic greenhouse gas concentrations.

In the present study the control run was used, firstly, to evaluate and improve the boundary conditions extracted from REMO and MPIOM as well as the HAMSOM model configuration itself by comparing model results with observations and accordingly, reanalysis data. However, in simulating a potential future climate, the scenario period was necessarily run in so-called free mode, that is, without any data assimilation incorporated. In order to be consistent with the scenario simulation, the control period was run in free mode, too. In such a free run the actual weather events certainly cannot be reproduced, expecting any modeled time series to deviate from observations or reanalysis data. Nevertheless, the climate statistics should be simulated adequately in order to assign any degree of reliability and confidence to specific future scenario runs. The evaluation procedure is thus based on the comparison of monthly climatological means derived both from the 50-year control period, regarded as statistically representative long-term model characteristics, and from observations or reanalysis data. Secondly, to address any climate change signal, the two 30-year periods 1971-2000 from the end of the control run and 2070-2099 from the end of the scenario run are used to encompass the 100-year period subject to detailed anal-

ysis. A period of at least 30 years is suggested by the World Meteorological Organization (WMO, 2009) to illustrate climate change in excluding interannual variabilities from climate trends, albeit also 20-year periods are commonly used, e.g. in the IPCC 4th assessment report.

The operational objective of this study is to elaborate a reliable model system to be used as dynamical downscaling for the North Sea of potential global climate scenario runs, while its scientific objective is to provide a comprehensive examination and quantification of changes of hydrodynamic conditions in the North Sea for the 21st century by accounting for regional issues in the analysis of the model results and by that, to provide a better understanding of potential climate change impacts on hydrodynamic conditions in the North Sea. In this respect the study contributed to the EU/BMBF-funded MarinERA project *ECODRIVE - Ecosystem Change in the North Sea: Processes, Drivers, Future Scenarios*. Being an interdisciplinary project, ECODRIVE is conceived as an intimate cooperation of climatologists, modellers, planktologists, fisheries experts, and ecophysiologists with the aim to assess and model historical and projected future changes in the trophodynamic structure and function of the North Sea ecosystem. The project advances predictive understanding of the impacts of various drivers of ecosystem change, including those acting via climate change and variability as well as those acting more regionally via anthropogenic forcing such as fisheries exploitation and eutrophication.

1.2 The North Sea - Physical

For a better understanding of the present study, a short description of the physical present-day condition of the North Sea and its overlying atmosphere is given in the following paragraphs. If not cited otherwise in the text, the information is summarized from Otto et al. (1990), Rodhe (1998), OSPAR (2000), Steele et al. (2009), and Schlünzen and Krell (2004).

1.2.1 Topography, Bathymetry and Morphology

The North Sea model domain investigated in this study spans from 50.9°N to 60.3°N and from 4.1°W to 13.1°E (Fig. 2.2). The meridional extension spreads from the English Channel in the south up to the Shetland Islands in the north, where the zonal extension spreads from Scotland in the west up to the connection into the Baltic Sea in the east. Situated on the Continental shelf of north-west Europe, the North Sea is a shallow marginal sea. The colors in Fig. 2.2 refer to the topography/bathymetry of the domain. Its characteristics subdivide the North Sea into the shallow southern North Sea with water depths less than 50 m, the central North Sea with water depths up to 100 m, the northern North Sea with water depths up to 200 m at the shelf edge, the comparatively deep Norwegian Trench, penetrating from the Norwegian Sea south-eastward along the coast of Norway, with a maximum water depth of 700 m in the Skagerak and a sill depth of about 230 m off western Norway, and the Kattegat as the transition zone between the Baltic Sea and the North Sea. In general, the water depth of the North Sea increases continuously towards

north-west. This topographic incline is broken by the shallow area of the Dogger Bank with a mean water depth of just 15 m, which separates the southern and central North Sea.

Besides frequent regional changes by human intervention, also the natural morphology of the North Sea coastlines varies considerably. Vertical uplift of the northern sea bed due to deglaciation since the last ice age emerged the rocky coasts of Scotland and Norway with their characteristic fjords and offshore archipelagos. The east coast of England is characterized by estuaries and flats of sandy mud, whereas cliffs and river valleys dominate the southern coast along the English Channel. From the English Channel to the Danish west coast, sandy beaches and dunes prevail at the European mainland coast, where numerous rivers discharge into the tidally governed Wadden Sea. Similarly, the Danish coastline is formed by sandy beaches, shoals, and large lagoon-like areas.

For this study focuses on hydrodynamic conditions in the North Sea, the model merely accounts for the geometrical shape of coastlines and bottom topography, which is regarded as temporally invariant on the considered time scale, rather than for the specific composition of coastlines, the bottom geology, and sediments. In Fig. 2.2 the HAMSOM model domain is depicted in its meso-scale horizontal resolution of about 3 km (see HAMSOM model description in section 2.1.3). Since the model solely deals with wet grid cells, any region with a water depth less than 5 m is excluded from the domain in order to assure a permanent flooding of all cells over the entire tidal cycle. In the remaining domain maximum sea surface depressions due to semi-diurnal tidal amplitudes in combination with wind effects empirically do not exceed 5 m in the simulations and the incorporated global sea level rise just enhances the flooding with progression of simulated time.

1.2.2 Meteorology

Situated in the european midlatitudes, the North Sea experiences pronounced seasonal changes in meteorological conditions. According to ERA40 reanalysis data, the annual cycle of monthly mean near-surface air temperature (1958 to 2000) varies from about 3 °C in Febuary to about 15 °C in August with a standard deviation of about ±1 °C, whereas a minimum in summer months and a maximum in winter months is recorded for total cloud cover, precipitation, wind speed, and relative humidity.

These atmospheric parameters describe the temperate climate present in northwestern Europe, which in general results from the meridionally directed change of solar radiation and the zonally directed influence of the North Atlantic Current carrying relatively warm subtropical water northward towards the Arctic Ocean. Unlike the North Atlantic Current, the North Sea, as being a shallow marginal sea, does generally not supply enough heat energy required to influence climate substantially but rather reacts quite sensitively on regional climate conditions and even weather conditions. Nonetheless, because of the higher heat capacity of sea water (about 4000 J/(kg·K)) than of atmospheric air (about 1000 J/(kg·K)), the near-surface air temperature averaged over the entire North Sea is

higher than the sea surface temperature in summer and lower in winter to the amount of about 0.5 to 1 °C.

In the eastern North Atlantic and the North Sea off-shore wind speeds face a shift in the scale of driving processes in the transition from open ocean to coastal areas. In open-ocean areas surface wind speed is strongly determined by large synoptic-scale cyclones and pressure systems (Harold et al., 1999), while in coastal areas, local medium- to small-scale wind regimes contribute more strongly to its characteristics. The predominant westerly atmospheric circulation in the North Sea region frequently contains low pressure systems causing one-hour averaged gale wind speeds of about 36 m/s to blow on average at 30 days per year. In particular from September to April the North Sea is exposed to a series of storms usually tracking eastward. The strength and persistence of westerly winds in winter is governed by the pressure gradient between Iceland and the Azores, reflected by the North Atlantic Oscillation (NAO) Index. Though westerlies determine the dominant wind direction, strong winds can blow from any direction, where the typical size of storms is in the order of the North Sea itself and larger. As a result, the North Sea climate is charcterized by large variations in wind speed and direction, a high level of cloud cover, and relatively high precipitation rates.

1.2.3 Tides

Tides in the North Sea result from gravitational and inertial forces between the celestial bodies of our solar system acting on the Atlantic Ocean (Banner et al., 1979). The responding oscillations in the ocean propagate across the shelf edge and enter the North Sea both north of Scotland and through the English Channel. The predominant tidal constituents in the North Sea are the semi-diurnal signals M_2 and S_2, governed by the moon and the sun, respectively. Spring and neap tides thus occur in a monthly and 6-monthly cycle with large spring tides near the spring and autumn equinoxes. In general, tidal oscillations are regular and repetitive, and in virtue of Newton's mechanics, the phases are accurately predictable. The amplitudes, on the contrary, are affected by local weather conditions as well as resonances with the configuration of coasts and depth of the seabed (Vincent and Provost, 1988), where the degree of resonance is sensitive to global sea level change, since the speed of tidal waves depends on the water depth. Fig. 2.34 shows the mean M_2 spring tidal range and co-tidal lines for the northwest European shelf region, where three amphidromic points with almost zero tidal range can be identified in the North Sea.

As progressive Kelvin waves, tidal oscillations are mainly adhered to the coast passing the North Sea in cyclonic sense, while they gradually lose energy because of dissipation by bottom friction. Associated tidal currents are the most energetic fluid motion in the North Sea with amplitudes usually less than 1 m/s and local spring tidal maxima up to 2-5 m/s. However, bottom friction causes the amplitude of tidal currents to be reduced in the bentic boundary layer. Tidal currents near the sea bed are therefore in advance by up to half an hour of those in the overlying water column, where the amplitude of tidal currents does not vary significantly with depth. Nonetheless, explained by the phenomenon referred to as

Stokes Drift, the orbital trajectories of any gravity waves are not strictly closed. In addition to the predominating cyclic tidal currents, thus, a net residual flow between 1-3 cm/s in the North Sea remains in the propagation direction of the tidal waves.

In stratified waters tides can generate internal waves propagating along the density interface, where the breaking of such waves causes regions of enhanced vertical mixing. In the shallow southern North Sea, however, strong tidal currents alongside the coast and the resulting bottom friction supply enough turbulent energy to prevent stratification (see section 1.2.7). The induced vertical mixing entails the formation of a tidal front (see section 1.2.8), which inhibits horizontal exchange between coastal and offshore waters, forcing riverine fresh water discharge to remain close to the Continental coast.

1.2.4 General circulation

As in any Continental shelf sea, currents in the North Sea are primarily induced by tides, winds, baroclinic density gradients, and barotropic pressure gradients due to local wind-driven differences in sea surface height (SSH), discontinuities in the atmospheric pressure field, and SSH gradients across open boundaries. Circulations in the North Sea thus occur over a wide range of frequencies, from subtidal to monthly scales. Since short-term circulations and respective variations of advective fluxes largely cancel out on the long time scale, they are not relevant for addressing climate change issues. The introduction to the North Sea circulation in this chapter but also various analyses in the subsequent chapters are therefore restricted to the general circulation represented by monthly mean velocity vectors.

In most places of the North Sea the strength of the general circulation is less than 0.1 m/s and hence, much smaller than tidal or short-term wind-driven currents, being difficult to quantify its characteristics from measurements only. Currents frequently acquire small spatial extensions, change in magnitude significantly, and change horizontal flow direction vertically from the sea surface to the sea bed. Vertical flows in the water column are even hardly measurable in field studies at all. In theoretical model studies, however, these difficulties can be accounted for, again underlining the importance of applying model studies in ocean sciences. Nonetheless, there is an overall long-term mean pattern as shown in Fig. 1.2, drawn up clearly by the distribution of released tracers and drifters. The mean currents in the North Sea form a cyclonic circulation, where the bulk of the transport is concentrated to the northern part of the North Sea because of major water exchange with the Norwegian Sea. The main inflow of water of Atlantic origin occurs across the northern boundary (annual mean 0.67-1.71 Sv) with a maximum along the western slope of the Norwegian Trench. Considerable inflow of mixed Atlantic and shelf water also occurs east of the Shetland Islands and between the Shetland and Orkney Islands. The largest portion of this inflow, about 76%, immediately turns eastward to form the Dooley Current along the 100 m isobath. The remaining 24% proceed flowing southward along the British east coast and enter the central North Sea, where further topographic obstructions like the Dogger Bank allow just 5% finally to pass through the southern North Sea (Damm et al.,

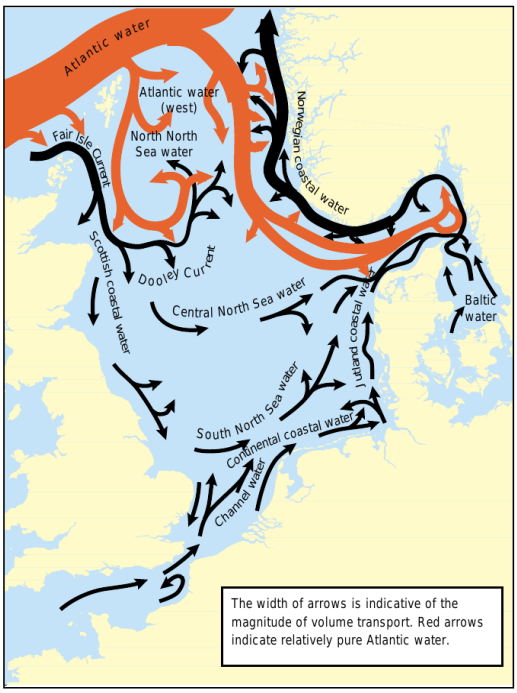

Figure 1.2: Schematic diagram of the general circulation in the North Sea after Turrell (1992) as published in OSPAR (2000).

1994). In the Southern Bight another inflow of saline Atlantic water into the North Sea occurs via the Dover Strait (annual mean 0.06-0.17 Sv). Stong fresh water discharge along the Continental coast from rivers like the Rhine and Elbe lower the salinity of the coastal flow, which is directed northwards in the German Bight to form the Jutland Current off Danmark. Northwest of Danmark, the Jutland Current joins the aforementioned northern inflow along the western side of the Norwegian Trench, which follows the Norwegian Trench southeastwards and recirculates cyclonically in the Skagerrak (annual mean 0.50-1.50 Sv). Low-salinity waters from the Baltic Sea intrude into the Skagerrak via the Kattegat (annual mean 0.014-0.016 Sv), where they considerably lower the surface salinity in the Skagerrak region down to about 30 psu. The only major outflow in the North Sea occurs along the eastern side of the Norwegian Trench, where all of the inflows are compensated by the Norwegian Coastal Current (annual mean 1.00-2.33 Sv) leaving the North Sea northward into the Norwegian Sea and Arctic Ocean.

The cyclonic circulation pattern of the North Sea is generally enhanced by westerly winds, whereas easterly winds weaken the circulation and are even able occasionally to reverse the pattern into anti-cyclonic sense (Dooley and Furnes, 1981). Observations have shown that the wind-driven short-term variations of the horizontal transport in the Norwegian Trench are of the same order of magnitude as its mean value (Furnes and Saelen, 1977). However, in all other North Sea regions, these variations are one order of magnitude larger than its mean, affirming the remarkably high variability of North Sea transports. In tidally well-mixed waters, i.e. in the western and southern regions of the North Sea, movements of water masses are vertically rather homogeneous and hence, independent of depth.

1.2.5 Storm Surges

Beside tides, wind forcing is responsible for the second strongest currents in the North Sea. Since the North Sea is a semi-enclosed sea, respective wind conditions can set up considerable sea level gradients against a coast, counterbalancing the wind stress. The resulting near-coastal storm surges potentially lead to a threat of coastal flooding, in particular when they coincide with spring tides. During the setting up and relaxing of the sea level gradients, sizeable current speeds can be generated. Storm surges frequently occur at the Belgian, Dutch, German, and Danish coasts because of predominant westerly winds in the North Sea region (see section 1.2.2).

1.2.6 Fresh Water Input

Fresh water input into the North Sea occurs via riverine discharge, intrusion of low-saline Baltic waters, and direct precipitation from the atmosphere. The river system of the North Sea covers a total catchment area of about 850000 km², where fresh water from rivers enters the North Sea in the order of 300 km³ per year. However, the annual cycle of riverine discharge shows a strong seasonality, since the North Sea is situated in the European mid-latitudes. Governed by melt water runoff, the maximum monthly mean river runoff in spring amounts up to twice the monthly mean river runoff in autumn and winter. Additionally, a high daily and interannual variability is superimposed on the runoff seasonality. Nonetheless, the dominating source of fresh water in the North Sea are the rivers discharging into the Baltic Sea. The baltic catchment area of about 1650000 km² supplies a river runoff in the order of 470 km³ per year, obeying the same seasonality and variability as the North Sea river runoff. Because of the high ratio between river discharge into the Baltic and the geographical extension of this semi-enclosed sea, the Baltic discharge enters the North Sea with a comparatively low salinity between 8 and 10 psu. Continuous decrease of salinity in the Baltic Sea is prevented by instantaneous near-bottom inflow of saline North Sea waters into the Baltic Basin. According to measurements between 1930 and 1990 (summarized in Damm, 1997), the ratio of the annual volume transport of intruding Baltic Sea waters and of fresh water discharging from North Sea rivers equals:

$$\text{Baltic Sea} : \text{Norw. coast} : \text{Cont. coast} : \text{Engl. coast} = 100 : 31 : 25 : 4$$

Considering the entire North Sea area on at least monthly scales, fresh water input via precipitation from the atmosphere is approximately balanced by evaporation to the atmosphere (Otto, 1976) but indeed accounts for a lesser source of fresh water (Becker, 1981). Highest precipitation rates prevalently occur along the Norwegian coast, caused by wind-forced uplift of moist air against high and steep mountain ranges. Salinity time series from 1870 to 1993 measured at Helgoland (inner German Bight) and analyzed by Becker et al. (1997) indicate a rather stable ratio between advection of saline North Atlantic waters into the North Sea and fresh water input mainly originating from the Elbe and Weser drainage area.

1.2.7 Stratification

In winter months most areas of the North Sea are vertically well mixed. Water parcels that are cooled at the surface balance the heat loss with a compression of volume. Their increased density forces them to sink, while this process continues until the entire water column has acquired uniform conditions. In turn, as the solar heat input into the North Sea increases in the course of the prevalent seasonality, the warming of the surface layer in spring causes thermal expansion of the upper water parcels and hence, a decrease of their density. However, unlike the winter situation, the induced buoyoncy forces the light and warm waters to stay at the surface where they are exposed to further solar heating. Consequently, this process yields a stratified water column in which warm surface waters are seperated from cold bottom waters by the thermocline, a strong vertical temperature gradient. In the central and northern North Sea the thermocline is well pronounced from about May to September, whereas in the northwestern region and in the shallow southern North Sea strong tidal currents and bottom friction prevent thermal stratification. The mean depth of the thermocline ranges from about 10 to 40 m. The highst intensities tend to occur early in the thermocline period where the strong increase of solar heat input and relatively calm weather conditions favor maximum vertical gradients of up to 5 °C/m. However, the greatest depths of the thermocline tend to occur at the very end of the period where increased wind speeds transfer more and more turbulent energy into the water column, causing a deepening of the thermocline and a weakening of its intensity. The increased wind speeds in combination with the seasonally induced decreased solar heat input finally destroy the thermocline in autumn and lead over to the well-mixed water column to be present in winter.

Contrary to the thermocline, the halocline is indicated by a strong vertical salinity gradient in the water column. Light, fresh water discharging from rivers tend to form a thin surface layer in estuaries, locally establishing a halocline in the region of fresh water influence (Simpson, 1997) close to the coast. According to the high variability of North Sea river runoff, haline stratification caused by river discharge can occur at any time of the year. In the eastern boundary region, in the Kattegat as well as in the Skagerrak and off the Norwegian coast the low salinity waters originating from the Baltic Sea also stay at the surface causing a stable halocline throughout the year. Hence, deep waters are generally not mixed with surface waters in these regions. Moreover, the thermal stratification in spring and summer is occationally encouraged and enhanced by the presence of the vertical salinity gradients which also tend to inhibit the final breakdown of thermal stratification in autumn. Hydrodynamically considered, there is hardly a difference between thermal and haline stratification, since the decisive property of a stratified water column is the induced vertical density gradient which keeps the surface and interior layers decoupled and provides internal waves to propagate along the density interface.

1.2.8 Fronts

Well-mixed and stratified regions are usually seperated by sharp fronts or frontal zones which identify the vertical boundaries between water masses. They inhibit horizontal dis-

persion of physical and chemical properties and may mark areas where surface water is subducted to form bottom water masses. Three types of fronts are present in the North Sea: tidal fronts, upwelling fronts, and salinity fronts. They can also co-exist as hybrid features of different types of fronts.

Tidal fronts form the boundary between thermally stratified waters and vertically mixed waters where tidally generated turbulence is sufficiently strong to prevent thermal stratification. The location of such seasonal fronts is generally determined by the water depth and the amplitude of the tidal current (Simpson and Hunter, 1974). In spring and summer a pronounced tidal front strikes southward in the western North Sea, bifurcates around the Dogger Bank, and passes the southern North Sea up to Denmark. The transition from stratified to mixed water is characterized by a spreading of the thermocline in which isopleths diverge from the thermocline and outcrop at the sea surface and the sea floor. The resulting discontinuity in sea surface temperature is occationally indicated by horizontal gradients up to 1 °C/km but can vanish at all in interaction with other frontal systems. The pressure gradient force induced by the local density distribution is largely balanced geostrophically, where considerable along-frontal flow velocities of 0.05 - 0.15 m/s are observed in the frontal zone (Simpson and Pingree, 1978). In addition, a cross-frontal circulation with extremely small velocities and an upwelling flow on the mixed side of the front are mainly caused by frictional processes. Nonetheless, the abundance of vortex-like horizontal flow structures and the formation of frontal eddies provide evidence for tidal fronts being dynamically unstable (Pingree, 1978; Griffiths and Linden, 1981; van Heijst, 1986), though along-frontal currents, meanders, and eddies are phenomena associated with all three types of fronts. Hydrographic surveys in the North Sea (van Aken et al., 1987) revealed occurrencies of both small-scale and large-scale horizontal baroclinic waves on fronts with wavelengths of the latter between 5 and 10 Rossby deformation radii.

Upwelling fronts form along coasts in stratified areas as a result of upwelling (Krause et al., 1986). Wind induced Ekman transport of surface water away from the coast forces bottom water to raise from the depth. Thus, upwelling fronts are associated with a density gradient at the surface between denser deep waters and lighter off-shore surface waters. The formation of such fronts are common in the Kattegat, Skagerak, and along the Norwegian coast, depending on local wind conditions.

Salinity fronts constitute the boundary of low salinity waters formed in the North Sea by riverine discharge or intrusion of Baltic sea water. While the formation of tidal fronts is essentially controled by spatial variation in the level of vertical mixing, there does not appear to be a single mechanism that controls the formation of salinity fronts in a variety of circumstances. In the vicinity of estuaries the frontal interface can extend continuously from the sea surface to the sea bed. Because of strong tidal currents along the southern North Sea coast, Continental river runoff is spread over the near-shore regions, forming a salinity front throughout the year. Off the German and Danish coasts, it matches and interacts with the tidal front present in spring and summer. Further prominent salinity fronts in the

North Sea separate surface waters in the Kattegat and Skagerak, where another salinity front can be identified at the offshore side of the Norwegian costal current.

1.3 IPCC AR4

As mentioned in section 1.1, the potential future scenario covering the period 2001-2100, which all the model runs involved in the present study rely on, are devised by the Intergovernmental Panel on Climate Change (IPCC). In this section a short description of the background of this influencial institution and of the storylines of four distinct future scenario groups is given.

The IPCC has been established by the World Meteorological Organization (WMO) and the United Nations Environment Programme (UNEP) to assess scientific, technical, and socio-economic information relevant for the understanding of climate change, its potential impacts, and options for adaptation and mitigation. A detailed description about the work of the IPCC can be found at the IPCC homepage (http://www.ipcc.ch). In general, the IPCC Assessment Reports reinforce the understanding that the radiative forcing of the Earth´s climate system is dominated by long-lived greenhouse gases and that the main driving forces of future greenhouse gas trajectories will continue to be demographic change, social and economic development, and the rate and direction of technological change. More specifically, changes in the atmospheric concentrations of greenhouse gases and aerosols, land cover, and solar radiation alter the energy balance of the climate system and with this, are primary drivers of climate change. They affect absorption, scattering, and emission of radiation within the atmosphere and at the Earth´s surface. The comparison of observations and hindcast model results indicates that it is likely that there has been significant anthropogenic global warming over the past 50 years. The observed patterns of warming were simulated only by models that include anthropogenic forcing. No coupled global climate model that used natural forcing only could reproduce the mean warming trends over the second half of the 20th century.

As a major achievement, the Special Report on Emission Scenarios (SRES; Nakicenovic and Swart, 2000) has been constructed to describe potential future developments in the global environment with special reference to the production of greenhouse gases and to aerosol precursor emissions. Thereby, a set of four scenario families for the 21st century (A1, A2, B1, B2) were developed, which cover a wide range of driving forces and thus, encompass a wide range of future greenhouse gas emissions. Nevertheless, since the latter are the product of complex dynamic systems, the possibility that any single emission path will indeed occur as described in the scenarios is highly uncertain. The presented compilation merely exclude outlying surprise or disaster scenarios devised from comprehensive literature search by the IPCC community.

The storylines of the different scenario families are summarized as follows:

A1: A future world of very rapid economic growth, global population that peaks in mid-

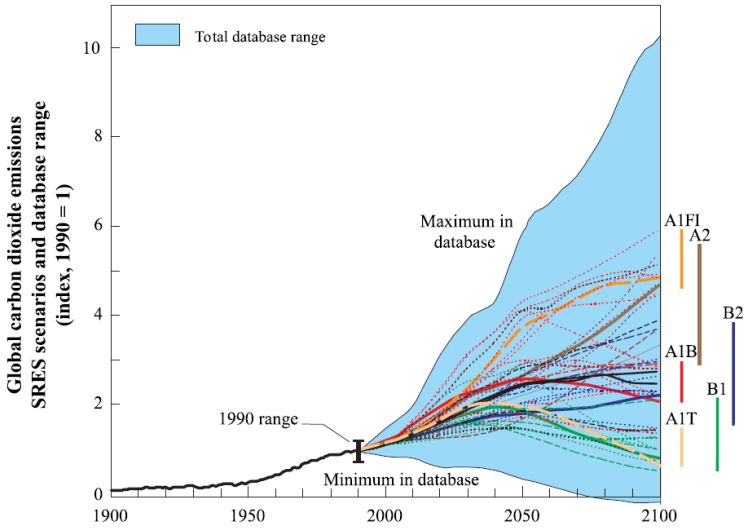

Figure 1.3: Global carbon dioxide emissions related to changes in the energy and industry system from 1900 to 1990 and for the 40 scenarios from 1990 to 2100, shown relative to 1990. Dashed lines: Individual scenarios. Blue shaded area: Total range of scenarios as documented in the SRES database. Highlighted lines: Illustrative marker scenarios. Coloured bars on the right: Ranges of emission in 2100 for the six scenario groups. (IPCC SRES, SPM, Fig. 2a)

century and declines thereafter, and rapid introduction of new and more efficient technologies.

A2: A very heterogeneous world with continuously increasing global population and regionally oriented economic growth that is more fragmented and slower than in other scenarios.

B1: A convergent world with the same global population as in the A1 scenario but with rapid changes in economic structures toward a service and information economy, with reductions in material intensity, and the introduction of clean and resource-efficient technologies.

B2: A world in which the emphasis is on local solutions to economic, social, and environmental sustainability, with continuously increasing population (lower than A2) and intermediate economic development.

Accounting for alternative developments of energy technologies, the A1 family was further subdevided into the scenario groups A1FI, referring to an intense use of fossil energy sources, A1T, referring to a predominantly non-fossil use, and A1B, referring to a balanced use across all kinds of energy sources. For each of the resulting six storylines, several different scenarios were developed (40 in total) using different modeling approaches to examine the range of outcomes arising from a range of models that use similar assumptions about driving forces. Finally, for each storyline, one illustrative scenario is provided, commonly referred to as the marker or key scenario, e.g. the A1B marker scenario, but also just *the* A1B scenario.

Suggested future time series of the driver quantities of climate change mentioned above were provided for every scenario by the SRES and finally entered the coupled athmosphere-

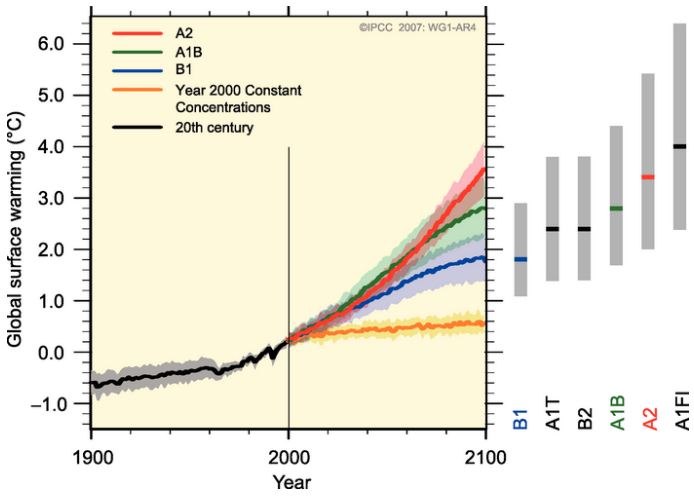

Figure 1.4: Solid lines: Multi-model global averages of surface warming (relative to 1980-1999) for the illustrative scenarios A2, A1B and B1, shown as continuations of the 20th century simulations. Shading: Standard deviation range of individual model annual averages. Orange line: Experiment where greenhouse gas concentrations were held constant at year 2000 values. Gray bars on the right: Best estimate (solid line within each bar) and the likely range assessed for all six illustrative scenarios. The assessment of the best estimate and likely ranges includes the AOGCMs in the left part of the figure as well as results from a hierarchy of independent models and observational constraints. (IPCC AR4, WG I, SPM, Fig. 5)

ocean gerneral circulation models that contributed to the 4th Assessment Report (AR4; Solomon et al., 2007). Fig. 1.3 and 1.4 summarize the progression of global carbon dioxide emissions according to the 40 scenarios and of projected global surface warming. Since the median of global carbon dioxide emission in 2100 as well as the median of global surface warming in 2100, as being a main quantifyer of climate change, are covered by the range of the A1B scenario group, the A1B marker scenario was chosen as a moderate emission scenario to be used for the projection of hydrodynamic conditions in the North Sea presented in this study. However, the A1B scenario must not be regarded as an estimate of a central tendency for all driving forces and emissions. The IPCC emphasizes that none of the SRES scenarios are more likely to occur than others, entailing neither one of them to represent a ¨best guess´ of future emissions. In addition to the storyline given above the A1B scenario is characterised by a low population trajectory with an increase to 8.7 billion by 2050 and a decline toward 7 billion by 2100, corresponding to socio-economic developments in the storyline, which combine low fertility with low mortality. A higher level of economic activity with a 26-fold gross world product in 2100 than today gives rise to a more affluent society and an assumed narrowing of regional differences in per capita income.

Chapter 2

Theory and Methods

2.1 Model Descriptions

2.1.1 ECHAM5/MPIOM

As one of the coupled atmosphere-ocean general circulation models relevant for the 4th IPCC Assessment Report, the ECHAM5/MPIOM model of the Max Planck Institute for Meteorology (MPI-M) in Hamburg provided respective model results of the A1B scenario run. In this model the general ocean circulation model MPIOM is coupled to the general atmosphere circulation model ECHAM5, using the OASIS3 coupler of the European PRISM model coupling framework. For the dynamical downscaling of the North Sea region presented in this study the results of ECHAM5/MPIOM were used by the shelf ocean model HAMSOM as lateral boundary conditions. In Journal of Climate (2006) various aspects of both ECHAM5 and ECHAM5/MPIOM are documented.

ECHAM5 is the 5th generation of the comprehensive general circulation model of the atmosphere evolving from the European Center for Medium-Range Weather Forecasts (ECMWF) model (Roeckner et al., 1992). The model dynamics are based on approximated hydrostatic primitive equations, which are solved in a hybrid sigma-pressure coordinate system for the prognostic variables vorticity, divergence, surface pressure, and temperature, expressed in terms of spherical harmonics with a triangular truncation. Water vapor, cloud liquid water, cloud ice, and tracer components are transported with a flux form semi-Lagrangian transport scheme (Lin and Rood, 1996). Cloud cover is predicted with a prognostic-statistical scheme solving equations for the distribution moments of total water (Tompkins, 2002). Convective clouds and convective transport are based on the mass-flux scheme of Tiedtke (1989) with modifications by Nordeng (1994). The solar radiation scheme (Fouquart and Bonnel, 1980) has 4 spectral bands, whereas the longwave radiation scheme (Mlawer et al., 1997; Morcrette et al., 1998) has 16 spectral bands. For time integration, a semi-implicit leapfrog scheme with Asselin time filter (Asselin, 1972) is employed. A more detailed model description can be found in Roeckner et al. (2003). For the IPCC AR4 experiments the configuration of the model resolves the atmosphere up to 10 hPa (~30 km) with 19 vertical layers. A Gaussian grid (the T63 configuration) with a spectral resolution was used which corresponds to a horizontal grid spacing of approximately 140 x 210 km at mid-latitudes.

The Max Planck Institute Ocean Model MPIOM is the ocean-sea ice component of the Max Planck Institute Climate Model (Marsland et al., 2003; Roeckner et al., 2006; Jungclaus et al., 2006a). MPIOM is a primitive equation model with implemented hydrostatic and Boussinesq assumption, applicable to Arakawa C-grids with z-coordinates and free surfaces. It includes an embedded dynamic/thermodynamic sea ice model with a viscous-plastic rheology following Hibler (1979) and a bottom boundary layer scheme for the flow across steep topography. The prognostic variables and tracers are horizontal and vertical velocity components, temperature, salinity, and surface elevation. For the barotropic part of the model a semi-implicit iterative solver is implemented. A detailed model description can be found in Marsland et al. (2003). For IPCC AR4 experiments, the MPIOM model was run on a bipolar orthogonal spherical coordinate system (the GR15 configuration) with

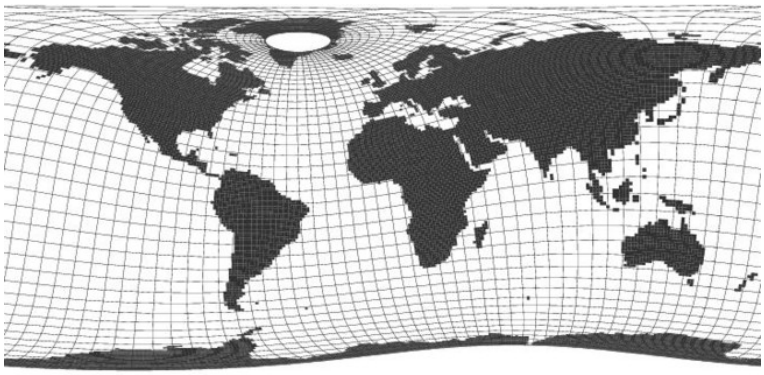

Figure 2.1: MPIOM grid configuration GR15 with non-diametrical poles located over Greenland and Antarctica as used in IPCC AR4 experiments. Every 5th grid line is shown. (http://www.mpimet.mpg.de)

non-diametrical poles located over Greenland and the Antarctic (Fig. 2.1). The mathematical singularities associated with convergence of meridians when approaching geographical poles were avoided by assigning a finite radius of uncovered land surrounding the poles. This measure also effectively reduces the number of land cells in the computational matrix. By choosing different locations of the grid poles, the higher horizontal resolution concentrated near the poles can be utilized for regional studies. The arrangement shown in Fig. 2.1, however, yields a fairly homogeneously distributed horizontal resolution around the globe, just in favor of the demands of global climate research. The horizontal resolution gradually varies between a minimum of 12 km close to Greenland and a maximum of 150 km in the tropical Pacific, giving rise to a resolution of about 1 x 1° in the North Sea region. The vertical resolution consists of 40 layers, with 20 layers confined in the upper 600 m.

2.1.2 REMO

The regional atmosphere model REMO (Jacob and Podzun, 1997; Jacob et al., 2001) of the Max Planck Institute for Meteorology evolved from the Europa-Modell of the Deutscher Wetterdienst (Majewski, 1991). The physical parameterization scheme in the model is adopted from the global atmosphere circulation model ECHAM4 (Roeckner et al., 1996). REMO solves the discretized primitive equations of atmospheric motion, where the hydrostatic assumption is implemented. As REMO was run in a one-way nesting mode as well as uncoupled to the ocean, boundary conditions were needed to be prescribed at the open lateral boundaries of the domain and at the atmosphere-ocean interface, whereas at the atmosphere-land interface, a simple bucket scheme is applied for the treatment of soil hydrology. At the lateral boundaries, the prescribed variables are air temperature, wind velocity components, surface pressure, specific humidity, and cloud liquid water, being the prognostic variables of REMO. At the atmosphere-ocean interface, the only prescribed variable is sea surface temperature. For horizontal discretization, the model uses a rotated spherical Arakawa C-grid with a resolution of 0.22 x 0.22° for the respective project. The origin of coordinates is thereby located in the geographical center of the model domain in order to minimize cell distortion at higher latitudes. In the vertical the atmosphere is resolved into 31 layers by a hybrid coordinate system (Simmons and Burridge, 1981). The temporal integration is accomplished by a leapfrog scheme with semi-implicit correction

and time filtering after Asselin (1972), adopted from the general circulation model ECHAM.

2.1.3 HAMSOM

The Hamburg Shelf Ocean Model HAMSOM (Backhaus, 1985, 1990; Pohlmann, 1991, 1996a,c) is a three-dimensional baroclinic hydrodynamic model based on the finite difference method. The underlying primitive equations of motion are defined in z-coordinates on an Arakawa C-grid, where the hydrostatic and Boussinesq assumption are implemented. Major stability constraints for surface gravity waves and the heat conduction equation are avoided by the implementation of implicit schemes. The employed turbulence closure scheme is related to a Mellor-Yamada level-2 type formulation (Mellor and Yamada, 1974), while a higher order scheme is incorporated for the Coriolis rotation in time. At the open lateral boundaries, a modified Sommerfeld radiation condition according to Orlanski (1976) is specified on outflow conditions. As the prognostic variables of HAMSOM, water temperature, salinity, and sea surface elevation are need to be prescribed at the open lateral boundaries, where air temperature, horizontal wind stress components, relative humidity, cloud cover, precipitation, and sea level pressure are need to be prescribed as atmospheric forcing at the atmosphere-ocean interface. For the discretization of the North Sea domain shown in Fig. 2.2 a quasi-orthogonal spherical grid is used which provides a meso-scale horizontal resolution of about 3 x 3 km. The maximum depth of 700 m is divided into 30 layers with successively increasing layer thickness from 5 to 50 m. The horizontal meso-scale resolution corresponds to the baroclinic Rossby radius of deformation in the North Sea, as being in the order of 3 km, too. The model thus permits to account for small-scale fronts and associated baroclinic eddies and frontal jets. Since a maximum water depth of about 150 m is not exceeded in the North Sea despite the Norwegian Trench, the horizontal resolution of just 3 km still yields an aspect ratio of 1/20, which justifies the application of the shallow water equations in the model.

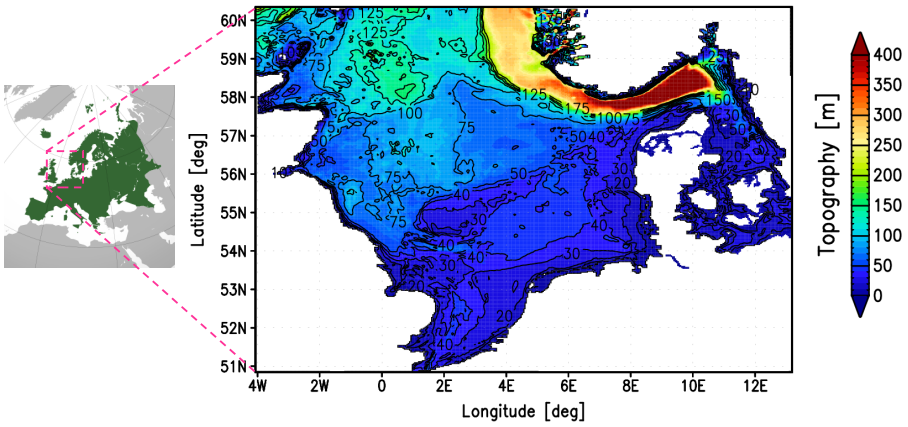

Figure 2.2: HAMSOM model domain of the North Sea region. Horizontal grid resolution about 3 x 3 km. Vertical grid resolution between 5 and 50 m.

2.2 Forcing Data

2.2.1 Lateral Open Boundaries

The open lateral boundaries for the North Sea model domain are made up of the connection to the North Atlantic and Norwegian Sea as the northern and western boundaries, the English Channel as the southern boundary, and the Arkona Sea (connection to the Baltic Sea) as the eastern boundary. However, because of the geographic peculiarity of the Baltic Sea being a semi-enclosed marginal sea itself with no other connection to the open ocean than the North Sea, in the present study the eastern boundary is represented by conditions normally applied to river input cells (see section 2.6). Nevertheless, at all these boundary sections, the three prognostic variables water temperature, salinity, and sea surface elevation are prescribed as driving variables to force the HAMSOM model. They are extracted from the MPIOM results of the global ECHAM5/MPIOM climate simulation, where the same simulation has also provided the boundary data for the atmosphere regionalization with REMO. Water temperature is supplied by MPIOM as potential temperature with respect to the geoid sea level, that is, the theoretical sea surface of an ocean resting under gravitational equilibrium. Likewise, sea surface elevation is defined as deviation from the geoid sea level. The MPIOM data was stored by the MPI-M community as monthly means solely, not preserving anomalies of sea water properties on shorter time scales. Moreover, tidal oscillations cancel out on a monthly scale and have therefore been neglected in the global simulations in favor of computational costs. Since the data was created by a coupled atmosphere-ocean model, the sea surface elevation is finally composed of the geostrophic dynamic height corrected by the inverse barometric effect of sea level pressure.

Since the MPIOM model is a general circulation model, its domain covers the entire world ocean. The horizontal grid resolution of the model is thus comparatively coarse, amounting to about 1 x 1° in the North Sea region. The HAMSOM grid, however, is designed to dissolve meso-scale hydrodynamic effects and therefore, possesses a much finer resolution of 1.5 x 2.5' in latitudinal and longitudinal direction, respectively. Also the vertical grid resolution is generally finer in the HAMSOM model. In order to provide boundary values at every cell of the HAMSOM grid with a continuous and smooth overall distribution, a refinement of the MPIOM data is necessary, which is realized in this study by a linear interpolation procedure consisting of the partial stages: vertical interpolation, horizontal interpolation, smoothing, and conversion of potential temperature into in-situ temperature. Just for simplicity reasons, in all figures showing MPIOM raw data, the non-diametrically bipolar MPIOM grid is remapped to a usual curvilinear grid with ordinary geographic north and south pole and a horizontal resolution of 1 x 1°. The described interpolation procedure, however, is still applied to the original grid.

Vertical Interpolation: In the globally expanded MPIOM grid the maximum depth of almost 6000 m is subdivided into 40 layers with successively increasing layer thickness of 6 to 550 m, whereas in the regional HAMSOM grid of the North Sea, the maximum depth of just 700 m is subdivided into 30 layers with thickness of 5 to 50 m. The refinement

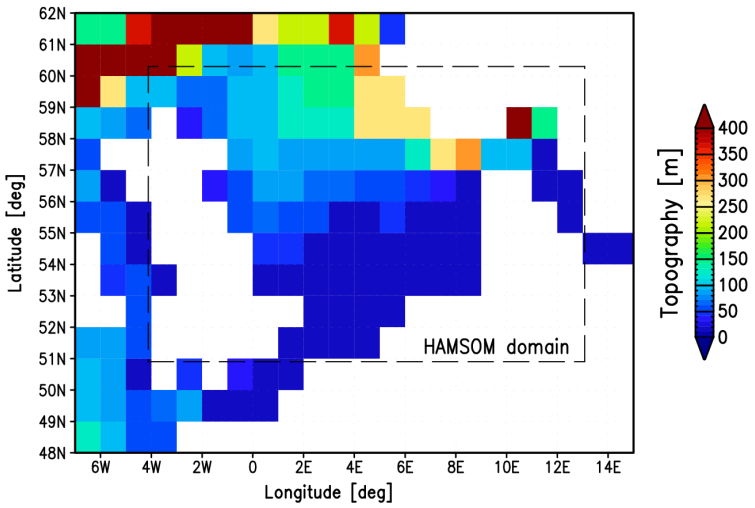

Figure 2.3: MPIOM topography of the greater North Sea region. Dashed box: Boundaries of the HAMSOM model domain.

of the vertical MPIOM grid resolution thus corresponds to a factor between 1.2 and 4, depending on the respective layer depth. Within a region horizontally at least two MPIOM cells larger than the HAMSOM domain (Fig. 2.3), the vertical distribution of the relevant variables water temperature and salinity is refined by means of linear interpolation. Sea surface height, however, is a two-dimensional variable, making vertical refinement redundant for this quantity. Being arranged on an Arakawa C-grid, the MPIOM variables water temperature and salinity are attached to cell centers. As such, the respective values represent spatial averages over the cells occupied volumes. For the interpolation scheme they are therefore considered to be representative at the cell centers. As long as any wet HAMSOM cell center within a given MPIOM cell column is vertically enclosed by two adjacent wet MPIOM cell centers, linear interpolation is applied to calculate the missing interstitial value. The differing horizontal grid resolution of the two models, however, also yields local discrepancies in topography and bathymetry, as can be seen in the vertical sections shown in Fig. 2.4. Hence, the centers of some HAMSOM bottom cells are located at a greater depth than the center of the deepest available MPIOM cell where only one value is available for interpolation. In such cases the MPIOM value is adopted unchanged by the respective HAMSOM bottom cells if the HAMSOM cell centers are located not deeper than the bottom of the corresponding deepest MPIOM cell. Otherwise, the HAMSOM cells are temporarily defined to be idle in order not to introduce unreasonable horizontal gradients of the variables. Values for such cells are allocated in the course of the horizontal interpolation described below. Similarly, the variable values of the MPIOM surface layer are adopted unchanged by the slightly thinner HAMSOM surface layer.

Horizontal Interpolation: Subsequent to the vertical grid adaptation, the horizontal refinement of the MPIOM data is realized by linear interpolation, too. However, unlike the vertical interpolation, values of the surrounding four direct neighbor cells are intuitively intended to be incorporated into the horizontal interpolation scheme. Thereby, the interpolated value is composed of respective fractions of each neighboring MPIOM value according to the distances between the destined HAMSOM cell center and the involved MPIOM cell

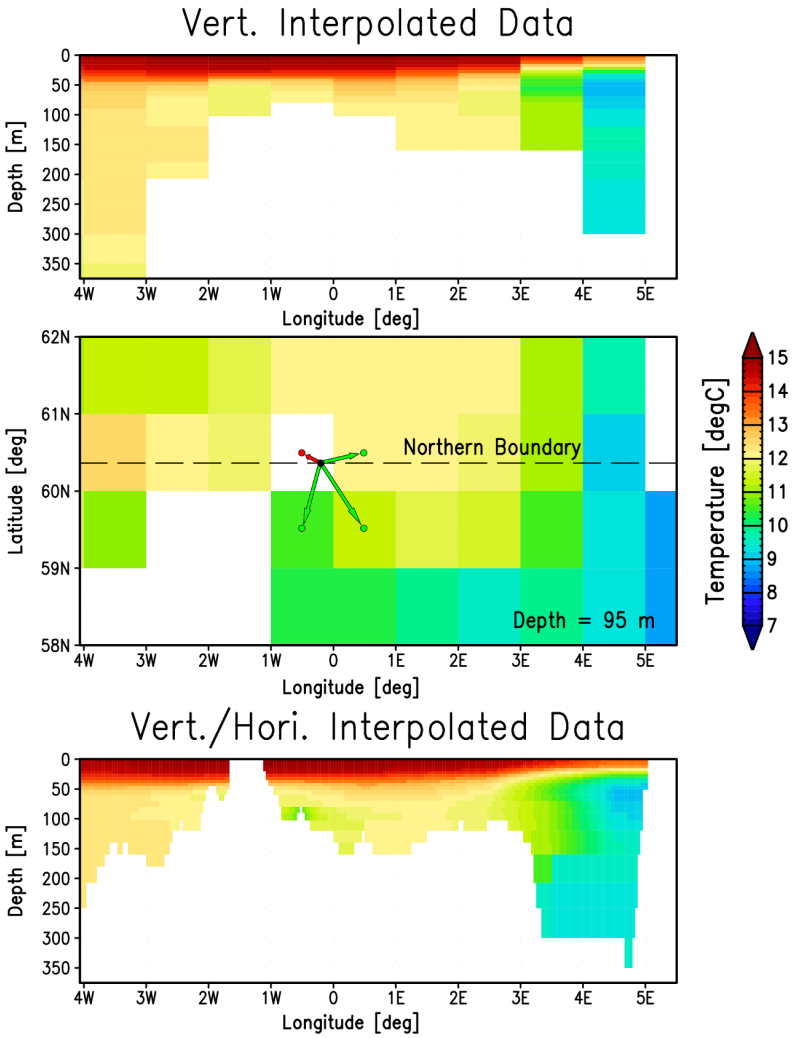

Figure 2.4: Upper part: Vertically interpolated temperature distribution at the northern boundary of the arbitrarily chosen month July 2051. Middle part: Horizontal section of the boundary region at 95 m depth. Lower part: Horizontally interpolated temperature distribution at the northern boundary as obtained by incorporating values from the interior of the HAMSOM domain. With this method, missing values to the east of the Shetland Islands in the deep are inappropriately extrapolated from the coarse grid.

centers. To account for the coarseness of the MPIOM grid, the values of the neighbor cells are additionally weighted according to their specific land-sea fraction. In case of a missing MPIOM value the same procedure is applied as linear extrapolation. The middle part of Fig. 2.4 highlights the four neighbor cells to be incorporated in the calculation of an instructive HAMSOM boundary value marked by the black dot. Since the nearest MPIOM cell pointed at by the red arrow is a dry cell, only the remaining three wet cells pointed at by the green arrows are incorporated and consequently, the procedure formally turns from interpolation to extrapolation.

This method yields reasonable results at the southern, western, and eastern boundary. At the northern boundary, however, it occasionally gives rise to unreasonable values and gradients at certain locations. Although this boundary is a hydrodynamically transparent boundary over a large area, i.e. it allows for both inflow and outflow, the predominant condition is the inflow of North Atlantic waters into the North Sea at any time of the year. The

incorporation of cells that are located inside the HAMSOM domain downstream the North Atlantic inflow can exert local spurious influence on the interpolated boundary conditions. In particular, because of the topography and its rough approximation by the MPIOM grid, bottom water masses to the south of the Shetland Islands are inadequately exchanged and hence, inevitably acquire physical properties that deviate from those of the surrounding waters (Fig. 2.4 middle part). The incorporation of such regions into the interpolation scheme thus alters the resulting boundary conditions artificially (Fig. 2.4 lower part). To avoid this negative effect, the MPIOM grid cells incorporated into the interpolation scheme at the northern boundary are restricted to cells intersected by the boundary plane itself. With this, the inappropriate region to the south of the Shetland Islands is excluded from the interpolation scheme. For consistency reasons, the same procedure is finally applied at the inflow-dominated western boundary, too, which is connected to the northern boundary via the north-western corner of the model domain. The result of the restricted interpolation scheme is shown in the upper part of Fig. 2.5.

However, the potential northern outflow region off the Norwegian coast is not discriminated on account of the restricted method, since outflow boundary conditions affect upstream hydrodynamics merely to a negligible extent (Orlanski, 1976). This holds particularly for variables that primarily disperse by advection rather than diffusion, just like water temperature and salinity in the North Sea. Nevertheless, for small current speeds, changes of sea surface elevation are indeed able to propagate upstream into the interior of the domain. Therefore, the unrestricted interpolation scheme based on four horizontally adjacent MPIOM cells was applied to the variable sea surface elevation. As reflecting surface processes, this variable does not suffer from the mentioned negative influence of the unrestricted interpolation scheme, anyway. On the Arakawa C-grid, sea surface elevation is attached to the midpoints of the cells´ top faces at the upper most layer, bringing about its values to represent spatial averages over the respective cells´ top face areas.

Smoothing of Interpolated Data: Even though disturbing influences on the water temperature and salinity distribution at the northern boundary originating from the interior of the domain are overcome by modification of the interpolation scheme, the topographic differences between the MPIOM and the HAMSOM grid yet bring up another difficulty. In the upper part of Fig. 2.4 a vertically interpolated temperature distribution at the northern boundary is exemplified. In the course of the horizontal interpolation all HAMSOM cells located between 3°E and 5°E at a depth greater than about 160 m, in particular the idle cells between 3°E and 4°E, are filled up with the respective MPIOM values from location 4.5°E (Fig. 2.5). No other neighbors exist in the vicinity of these cells to be used in the restricted horizontal interpolation scheme. However, immediately above the abyss, the interpolation algorithm encounters two adjacent MPIOM values in order to calculate a smooth horizontal transition. The resultant spatial arrangement thus induces a local vertical discontinuity at the edge of the Norwegian Trench to be remedied by the application of a smoothing scheme subsequent to the interpolation schemes.

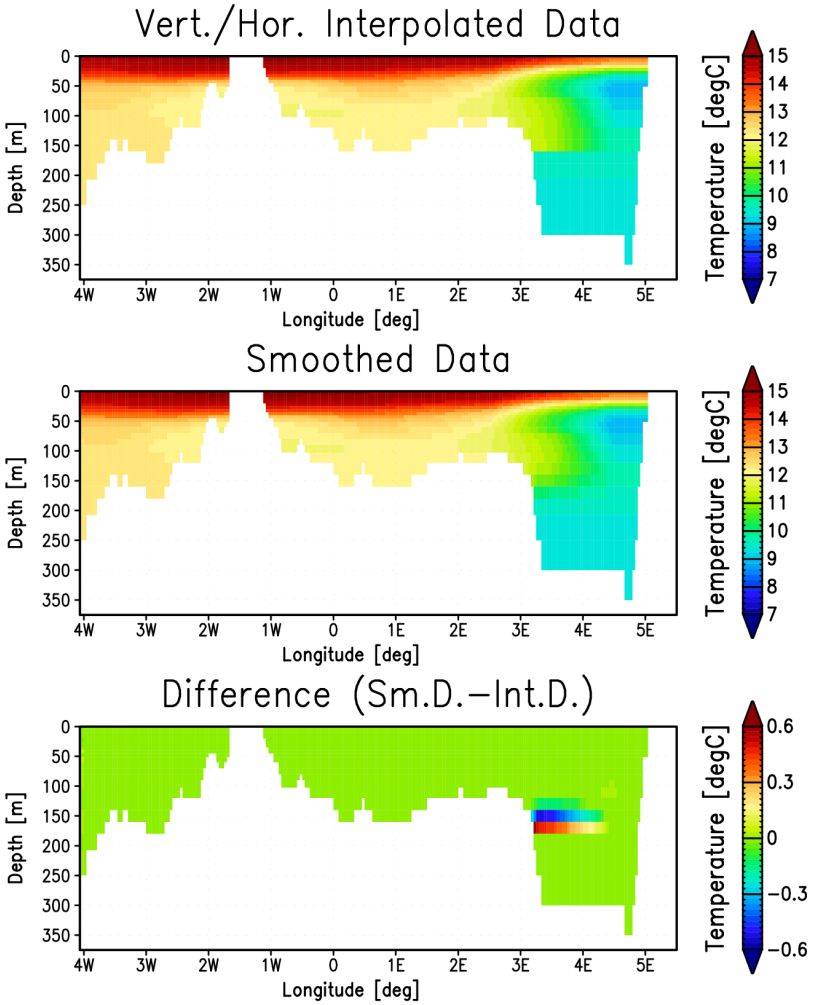

Figure 2.5: Upper part: Vertically and horizontally interpolated temperature distribution at the northern boundary for July 2051. Middle part: Smoothed temperature distribution. Lower part: Difference between the smoothed and the interpolated data.

Thereby, a maximal allowed gradient as an upper threshold is needed to be predefined in the smoothing algorithm for the respective high vertical gradients to be detected. However, if the predefined maximum gradient is too large, the smoothing will not affect the intended discontinuity at the edge of the Norwegian Trench. On the other hand, if the predefined maximum gradient is too small, the smoothing will not only reduce the intended discontinuity but also weaken the vertical temperature gradient of the thermocline developed in the warm seasons. Independent of this dilemma, wet cells that are connected to dry cells need to be treated in a different way by the algorithm than regular cells entirely surrounded by wet cells, because missing values of adjacent dry cells distort the determined local gradients. In order to deal with these difficulties, the smoothing scheme is applied at a limited region around the Norwegian Trench only and at selected regions at the western boundary with similar topographic conditions. For every cell within these regions, an average variable value is calculated according to the eight surrounding cells located in the boundary plane, with respect to their occupied volumes. Ten percent of the difference between this average value and the actual value is then added on the actual value. In doing so, the actual value approaches the average value and a given spatial discontinuity is successively attenuated (Fig. 2.5). To amplify the smoothing effect, this procedure is empirically repeated twenty

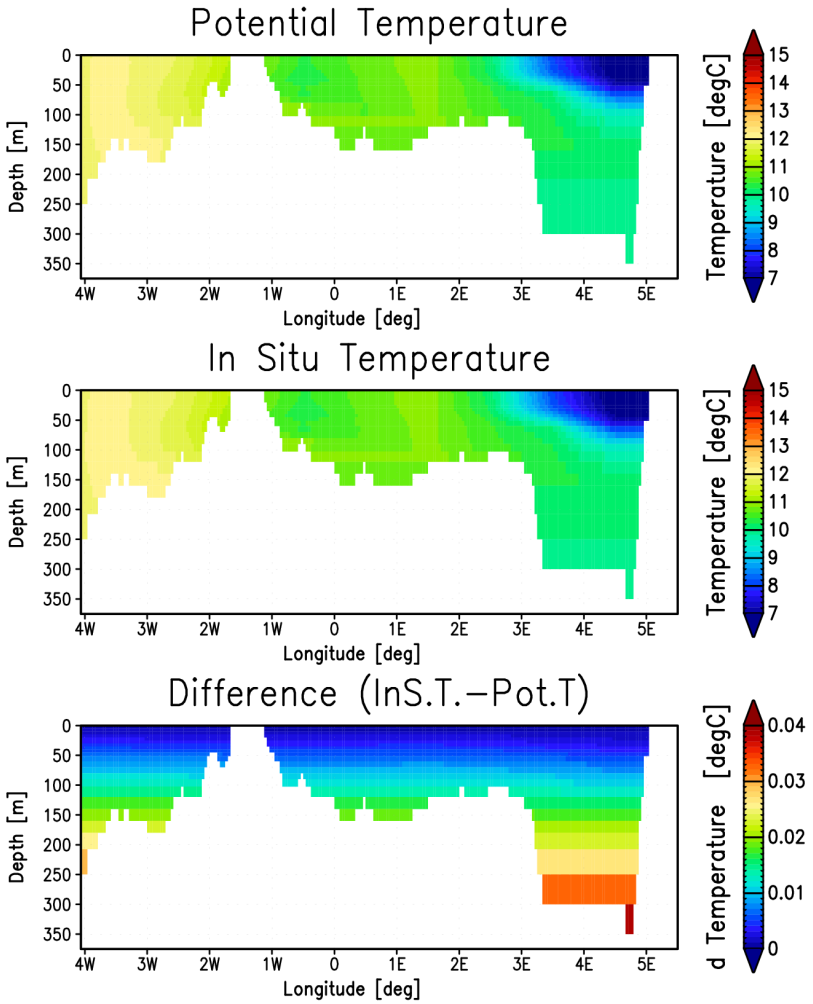

Figure 2.6: Upper part: Potential temperature distribution at the northern boundary for April 2051. Middle part: In-situ temperature distribution. Lower part: Difference between in-situ and potential temperature data.

times. Analogously, the same technique is applied in a two-dimensional manner to the variable sea surface elevation.

Determination of In-Situ Temperature: As mentioned above, the water temperature calculated by the MPIOM model is provided as potential temperature. In the HAMSOM model, however, this forcing variable is implemented as in-situ temperature. The alteration of a water parcel´s temperature due to compression by vertical displacement of 350 m at the most, which is the maximum depth at the lateral boundaries approximately, amounts to not more than about +0.04 °C (Pickard and Emery, 1990). This temperature change seems to be negligible, but for the sake of completeness the determination of in-situ temperature is still incorporated in the adaptation process of the forcing data. Thereby, an iterative approximation scheme after Gill (1982), Fofonoff (1977), and Bryden (1973) is applied in order to determine in-situ temperature values layer by layer. Fig. 2.6 illustrates the resulting temperature change at the northern boundary for the arbitrarily chosen example April 2051. The cold surface waters of the Norwegian Coastal Current in the east of the section provide for a local decrease of compressibility. The temperature increase due to compression at a given depth is thus slightly lower in this area than farther westwards,

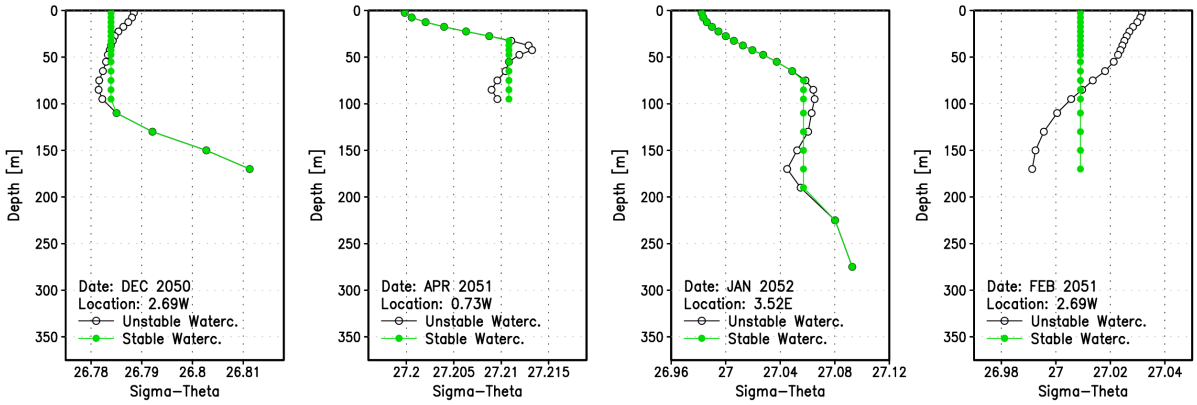

Figure 2.7: White dots: Potential density of the adapted boundary data at four different locations along the northern boundary and different months. Green dots: Potential equilibrium density obtained from theoretical adiabatic mixing of the unstable section in the water column.

indicated by a respective drop of the temperature difference shown in the lower part of Fig. 2.6. Likewise, the warmer waters in the west of the section give rise to a local increase of compressibility and hence, to a slightly higher temperature difference at given depth.

Since a lot of calculations and transformations are involved in the boundary data adaptation, the vertical hydrostatic stability of the resulting water column is analyzed in order to assure that no unreasonable physical conditions are introduced in the course of the adaptation procedure. Hydrostatic stability or instability is reflected by the vertical distribution of potential density. Heavier water of higher potential density overlaid by lighter water of lower potential density constitutes a vertically stable water column. As being the typical summer condition in the North Sea, the warming of surface waters by solar radiation and turbulent heat flux causes thermal expansion and a respective decrease of the waters density. In turn, the light and warm waters keep staying at the surface and give rise to the formation of a thermocline. However, lighter water overlaid by heavier water induces positive buoyancy of the light water and forces the two waters to mix. As being the typical winter condition in the North Sea, the cooling of surface waters by the atmosphere causes thermal compression and a respective increase of the water´s density. The heavy and cold waters now sink and mix with deeper waters to balance the unstable density condition, giving rise to a vertically homogeneous water column with respect to temperature and salinity.

Fig. 2.7 exemplifies potential density distributions for winter and early spring at four different locations along the northern boundary. The white dots represent the potential density of the adapted boundary data, whereas the green dots represent the corresponding equilibrium density distribution obtained from theoretical adiabatic mixing of the unstable section. The four examples demonstrate the occurrence of vertical instabilities at the surface, at the bottom, somewhere in between, as well as over the entire water column, respectively. The unstable surface layers exhibited in the first diagram are induced by the onset of surface cooling in early winter (December), where the entire water column exhibited in the last diagram is finally affected in late winter (February). However, exhibited in the second diagram, the onset of surface warming in early spring (April) again stabilizes the

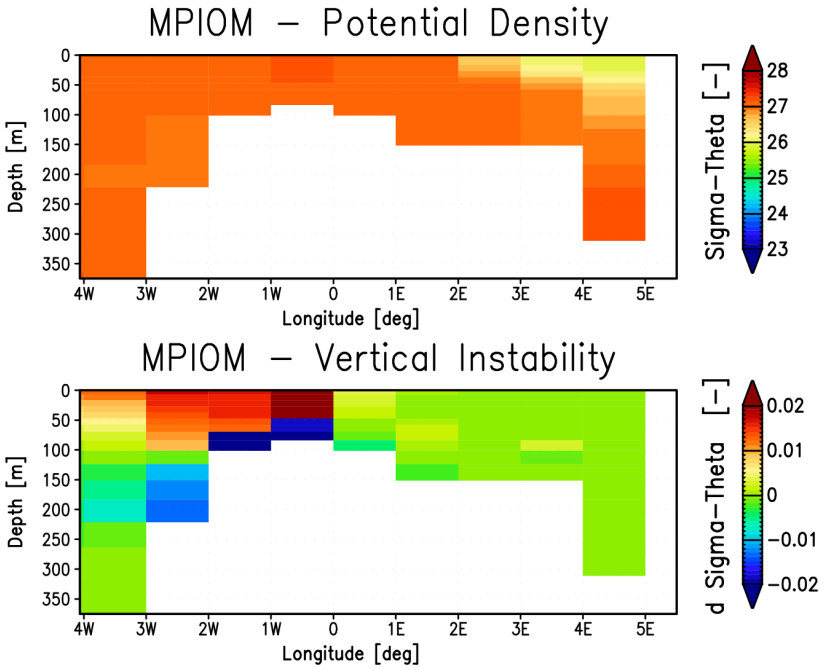

Figure 2.8: Upper part: Potential density distribution of MPIOM raw data at the northern boundary for February 2051. Lower part: Difference between the potential density and the vertically stable equilibrium condition. Heavy and light waters are indicated by red and blue colors, respectively.

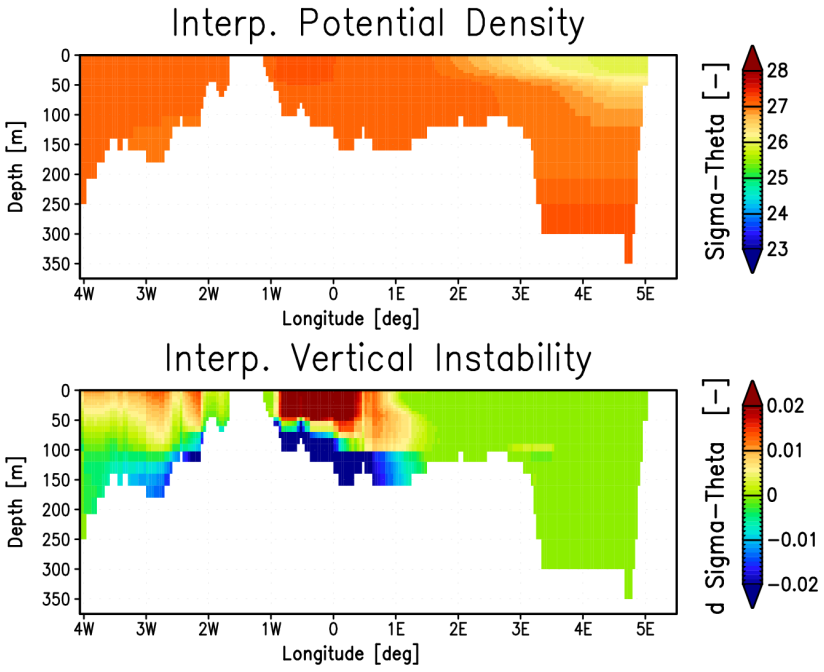

Figure 2.9: Upper part: Potential density distribution of the adapted data at the northern boundary for February 2051. Lower part: Difference between the potential density and the vertically stable equilibrium condition. Heavy and light waters are indicated by red and blue colors, respectively.

surface layers. The instability at intermediate depths, as exhibited in the third diagram, is induced by surface cooling similar to the first diagram, yet constantly overlaid by stable low salinity waters of the Norwegian Coastal Current.

Unfortunately, vertical instabilities cannot be readily visualized in potential density distributions. Both the level and the range of the vertical density variations along the north-

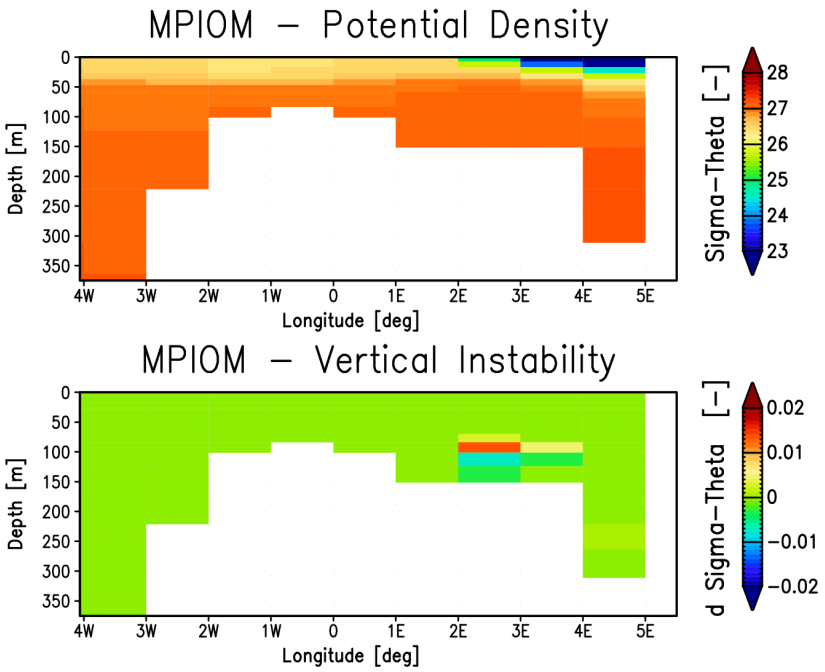

Figure 2.10: Analogous to Fig. 2.8 for August 2051.

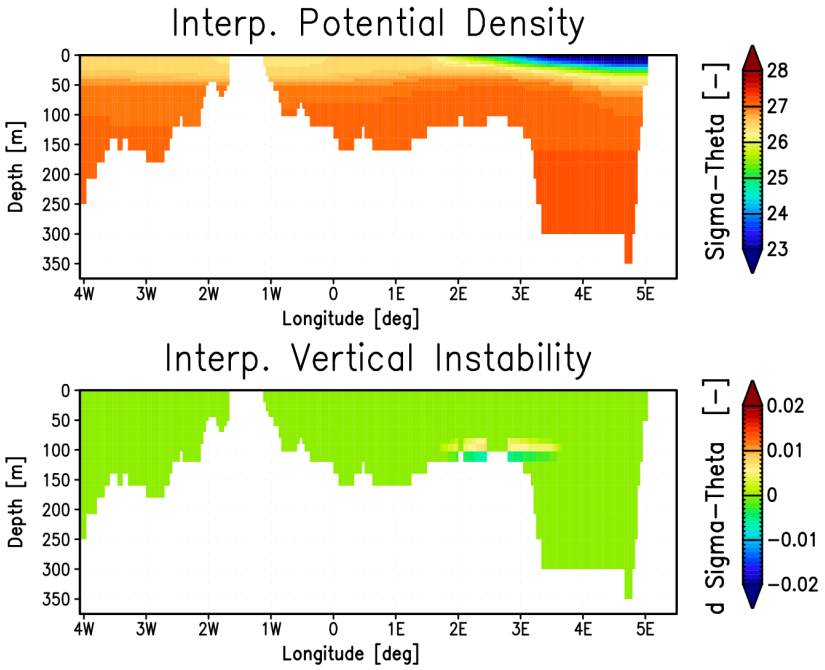

Figure 2.11: Analogous to Fig. 2.9 for August 2051.

ern boundary vary that much that any color bar needed to be carefully adjusted in order to highlight just one specific unstable region. Fig. 2.8 and 2.9 show the distributions of the potential density at the northern boundary for February 2051 and of the difference between the potential density and the vertically stable equilibrium condition, for the MPIOM raw data and for the adapted data, respectively. The unstable western part of the northern boundary as well as the stable eastern part are retained by the adaptation procedure. The stability of the eastern part arises from the low-salinity surface waters of the Norwegian Coastal Current stretching as far as 1°E in the given month. Fig. 2.10 and 2.11 show the

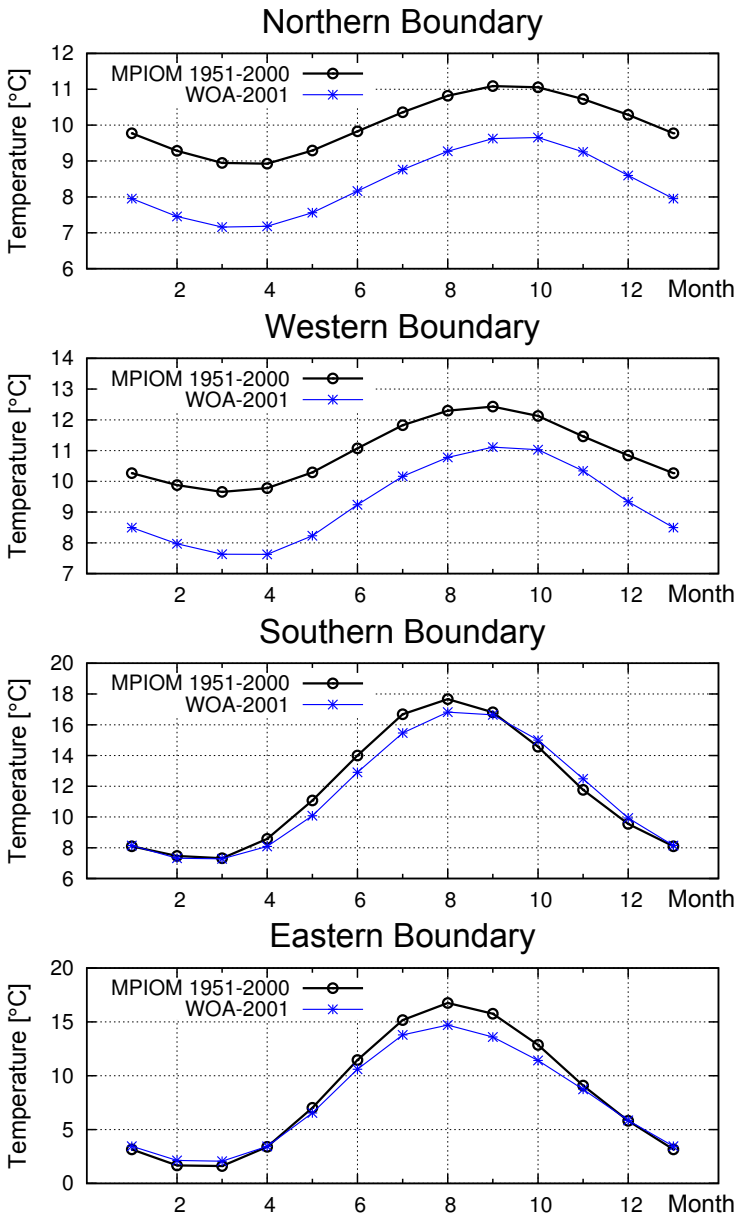

Figure 2.12: Comparison of MPIOM and WOA-01 mean sea water temperature at the four open lateral boundaries for 1951-2000.

same distributions for August 2051, where no instabilities occur despite a local discontinuity at the edge of the Norwegian Trench.

Be aware that the magnitude of the deviation from the equilibrium condition also depends on the local bathymetry. As an alternative of visualizing vertical instability, the buoyancy force can be analyzed, as being proportional to the vertical potential density gradient. However, as mentioned above, the potential density gradient covers a high magnitude range rendering this quantity inconvenient for visualization. Moreover, any stable gradients off the equilibrium condition, like at the upper and lower ends of the unstable section exhibited in diagram 2 and 3 of Fig. 2.7, and also unstable but low gradients off the stable equilibrium, as exhibited in diagram 4, are insufficiently comprised by depicting buoyancy.

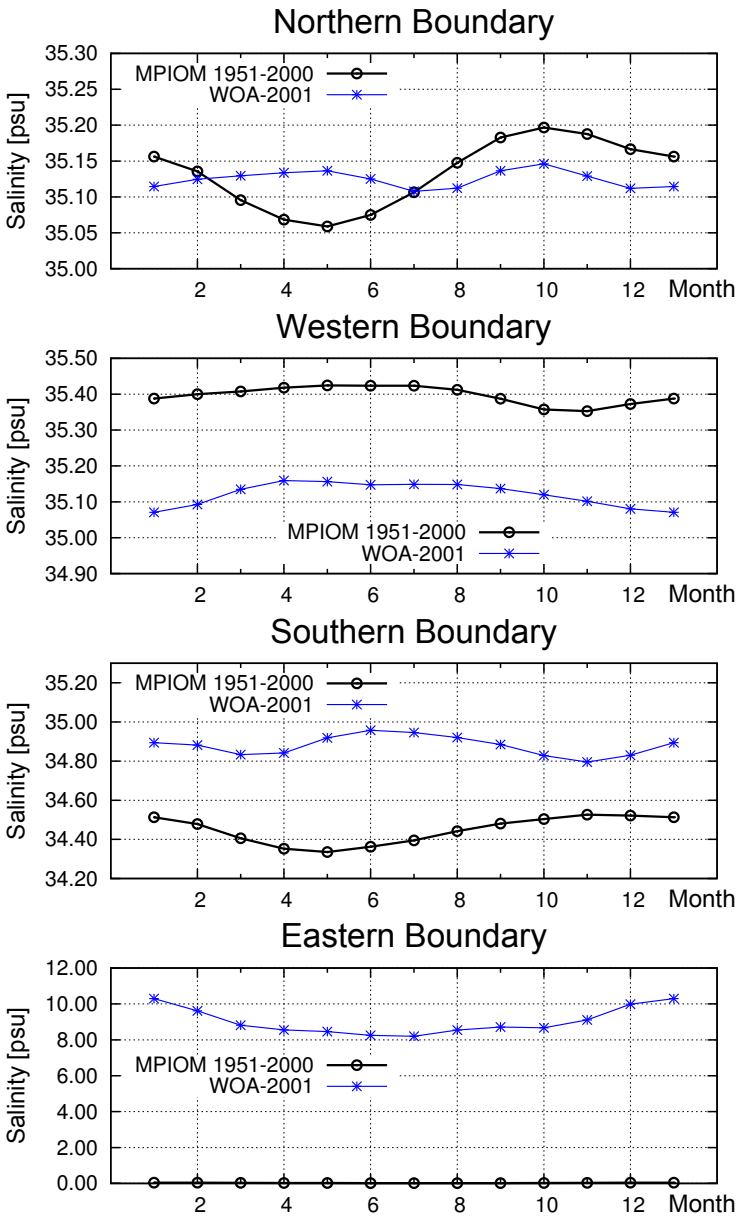

Figure 2.13: Comparison of MPIOM and WOA-01 mean salinity at the four open lateral boundaries for 1951-2000.

In order to evaluate the obtained lateral boundary conditions in a quantitative manner, water temperature and salinity are compared with the climatological ocean data set World Ocean Atlas 2001 (WOA-01) by Boyer et al. (2005). As mentioned in the introduction (section 1.1), the control period 1951-2000 was performed by MPIOM in free mode just like the scenario period 2001-2099. However, without any data assimilation incorporated, time series of the control run necessarily deviate from observations or reanalysis data. The evaluation is thus based on the comparison of monthly climatological means extracted both from the 50-year control run, regarded as statistically representative long-term model characteristics, and from the observation data set WOA-01. The mean values of temperature and salinity at the four lateral boundaries are exhibited in Fig. 2.12 and 2.13, respectively. Thereby, the MPIOM data show a warm temperature bias up to +2 °C relative to WOA-01. In particular at the northern boundaries (i.e. the northern and the western boundary), at which hydrographic conditions of the North Atlantic inflow are reflected, the deviation is

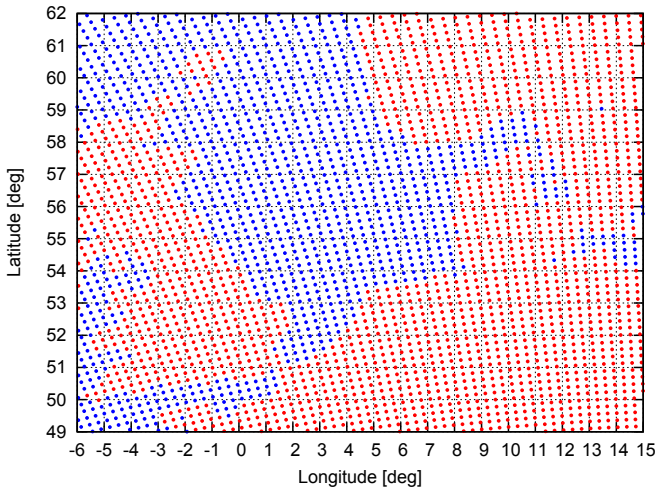

Figure 2.14: Land-sea mask of the REMO model for the North Sea region. Red: Cell centers of land cells. Blue: Cell centers of ocean cells. Coastal cells with a fractional land-sea composition are marked as land cells.

fairly constant, yielding a similar seasonal variability of MPIOM to WOA-01. However, at the southern and eastern boundaries, at which the water temperature is largely determined by atmospheric forcing, the warm bias only occurs in summer, though to a similar amount of up to +2 °C. Respective salinity deviations are pretty different at the individual boundaries but most stiking at the eastern boundary. The coarse horizontal representation of the Skagerrak, Kattegat, and the connection to the Baltic Sea by just one grid cell (see Fig. 2.3) does not allow MPIOM for an adequate simulation of the exchange dynamics between the North Sea and the Baltic, yielding a substantial underestimation of salinity in these regions with values close to 0 psu throughout the year.

2.2.2 Atmospheric Forcing

Similar to the open lateral boundaries, several variables are needed to be prescribed at the atmosphere-ocean interface to drive the HAMSOM model with wind-induced shear stress, surface heat and fresh water fluxes, and atmosphere pressure-induced barotropic pressure gradients in the water column. The atmospheric forcing variables are 2m air temperature, total cloud cover, precipitation (large-scale and convective), near-surface relative humidity, 10m wind speed, and sea level pressure. Taken from the model results of the regional climate model REMO, the variables are provided as 1-hourly data on a rotated curvilinear grid with a horizontal resolution of 0.22 x 0.22° and a displaced origin of coordinates. The REMO land-sea mask for the North Sea region is shown in Fig. 2.14. Since relative humidity is not provided by REMO as direct model output, this variable is calculated from air temperature and dewpoint temperature via the Magnus formula (e.g. Etling, 2008). To remap the REMO data onto the meso-scale HAMSOM grid with a horizontal resolution about 8 times finer than the REMO grid, the same horizontal interpolation scheme is applied as for the ocean variable sea surface elevation. However, coastal REMO cells with a fractional land-sea composition are excluded from the interpolation in order to avoid atmospheric conditions over sea to become influenced by conditions over land.

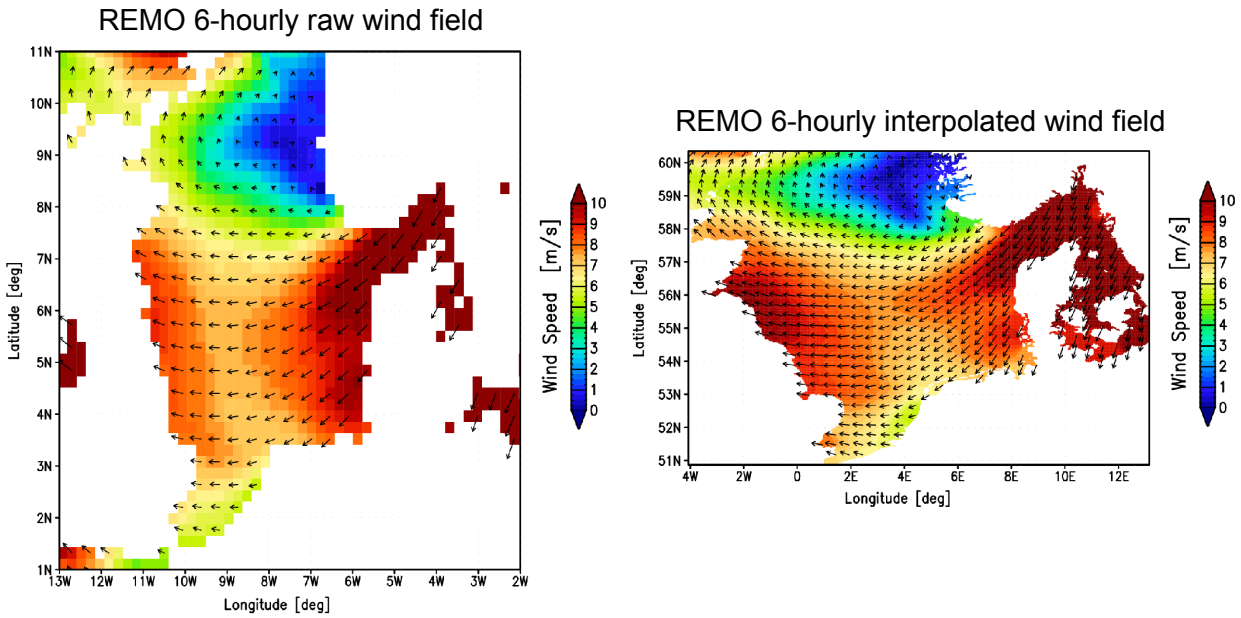

Figure 2.15: Left: Exemplified 6-hourly mean wind field of REMO raw data. Longitude and latitude refer to the displaced and rotated coordinate system used by REMO. Wind vectors are exhibited at every second grid cell. Right: Associated wind field, spatially interpolated onto the meso-scale HAMSOM grid. Vectors are exhibited at every 12th grid cell.

Furthermore, since the whole time period examined in this study covers nearly 150 years, the 1-hourly REMO data are averaged into 6-hourly means to reduce computer memory requirements. For a longer than 6-hourly averaging interval, it is not possible to retain semi-diurnal variations in the atmospheric forcing, which represent the highest of the dominant frequencies in the respective power spectra (see Fig. 2.16) along with diurnal and annual signals. However, the extrema in the diurnal cycle of the used atmospheric parameters do not prefer a common temporal position. Rather, they also vary spatially in the North Sea domain. Moreover, for various reasons like weather and seasonal changes, the variations of almost all atmospheric parameters are not truly periodic from day to day, referred to as non-cyclic variations (Chapman and Lindzen, 1970). Hence, in order not to favor a certain time of the day, non-weighted averaging is applied in calculating the 6-hourly means and the most practical partitioning of 0-6, 6-12, 12-18 and 18-24 o'clock is used. Fig. 2.15 shows an instructive wind field as 6-hourly mean of the REMO raw data and the respective spatially interpolated data.

In order to evaluate the obtained atmospheric forcing fields, power spectra of atmospheric parameters from the reanalysis data set ERA40 (Uppala et al., 2005) and REMO are compared in Fig. 2.16. Thereby, the 6-hourly time series of spatial averages over the whole North Sea are decomposed in their harmonic frequencies by Fast-Fourier-Transform. To provide for stationarity, means and linear trends are removed from the time series, for frequency analysis to become meaningful. Moreover, the shown spectra are smoothed by a running mean of 10 successive periods in order to reduce the increasing spread at short periods.

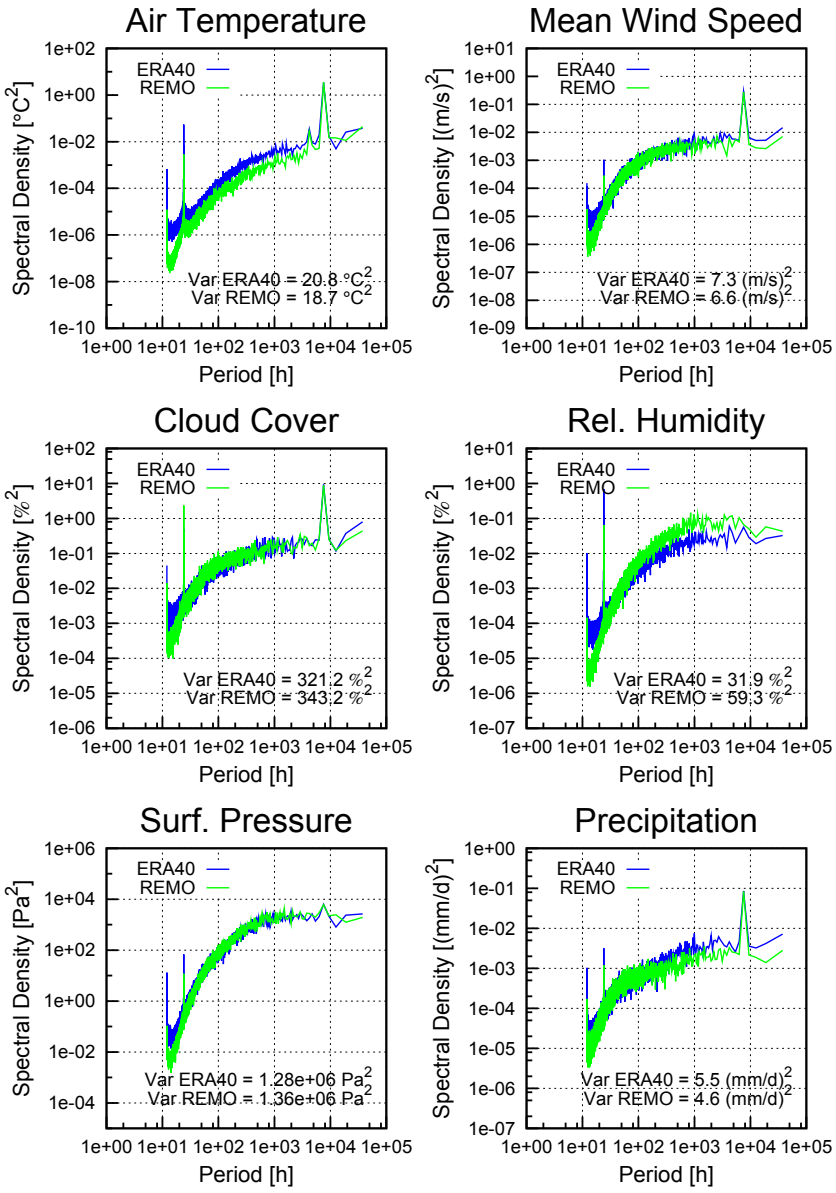

Figure 2.16: Power spectra of 6-hourly mean atmospheric parameters. Comparison between REMO (green) and ERA40 (blue) over the period 1958-2000. Spectra are smoothed by a running mean of 10 consecutive periods.

The characteristic annual cycle of atmospheric parameters at mid-latitudes results from the incline of the earth's rotation axis with respect to the ecliptic plane. The highest peak in the power spectra occurs at a period of one year, indicating the strongest signal in the time series to describe the annual cycle. The daily cycle is determined by the succession of day and night and the related periodic increase and decrease of air, ground, and sea temperature, which in turn affects many other atmospheric parameters. This diurnal cycle is represented in the spectra by the second pronounced peak at a period of one day, while the third peak at the Nyquist period of 12 hours refers to semi-diurnal variations known as atmospheric tides.

Whereas ocean tides are strongly affected by the disposition of the continents and hence, among others, boundary effects are very important, the dynamics of atmospheric tides are quite different (Gill, 1982). The designation atmospheric tides embraces the two distinct

phenomena known as thermal tides and gravitational tides in the atmosphere (Chapman and Lindzen, 1970). In general, thermal tides are caused by solar heating, whereas gravitational tides are caused by gravitation effects of our solar system just as ocean tides. The major contributions to atmospheric tides in descending order of magnitude are the solar semi-diurnal thermal tide, the solar diurnal thermal tide, and the lunar semi-diurnal gravitational tide.

Most of the solar radiation incident on the earth and its atmosphere is absorbed by the ground and sea. The daily variations thus produced in the ground temperature are conveyed to the adjacent atmosphere by turbulence and long-wave radiative transfer. This heating can excite upward transmitted oscillations in the atmosphere which already induce variations in the temperature, pressure, and wind fields. Nonetheless, a significant amount of solar radiation is absorbed in the atmosphere by water vapor and ozone. The daily variation in heating due to this absorption is distributed throughout the bulk of the atmosphere and constitutes the strongest thermo-tidal excitation. The atmospheric solar heating combined with upward eddy conduction of heat from the ground generates internal gravity waves in the atmosphere primarily at diurnal and semi-diurnal periods (Dai and Wang, 1999). This process is referred to as thermal tides. Gravitational excitation, on the contrary, is in general much weaker than thermal excitation. There is virtually no way of isolating solar gravitational tides from solar thermal tides in the data, but lunar tides are indeed distinguishable by virtue of their different period of about 12.42 hours (Chapman and Lindzen, 1970).

The atmospheric parameters used in the present study are physically not independent of each other and hence, they are subject to diurnal and semi-diurnal oscillations. Where the thermo-tidal oscillations can be easily identified in the power spectra of both the ERA40 data and the REMO data, the tidal oscillations due to the moon´s gravity amount to only a very small fraction of a millibar in the pressure field (Scorer, 1997) and are therefore not visible in the spectra without further, more sensitive analysis.

In general, the power spectra of the two data sets ERA40 and REMO (Fig. 2.16) show wide agreement. In expressing the energy that contributes from distinct harmonics to the total variability of the underlying time series, seasonal, diurnal, and semi-diurnal large-scale dynamics of the North Sea atmosphere are thus adequately represented by REMO. Nevertheless, at short periods, a systematic amplitude underestimation in the REMO spectra relative to ERA40 shows up. Despite the cumulative quantity precipitation, as representing the precipitation *rate* which requires the consideration of a time period, the ERA40 data consists of 6-hourly instantaneous parameter values, whereas the REMO data was averaged in the course of the forcing data adaptation from 1- into 6-hourly means, necessarily lowering the short-term variability. However, a comparison of 1- and 6-hourly REMO spectra (not shown here) quantifies the reduction at periods between 12 and 24 hours to merely amount to about 10% of the given ERA40-REMO high-frequency deviations. In any case, because of the comparatively low amount of energy contained in the high frequency bands, the deviations between ERA40 and REMO account just for a negligible fraction of

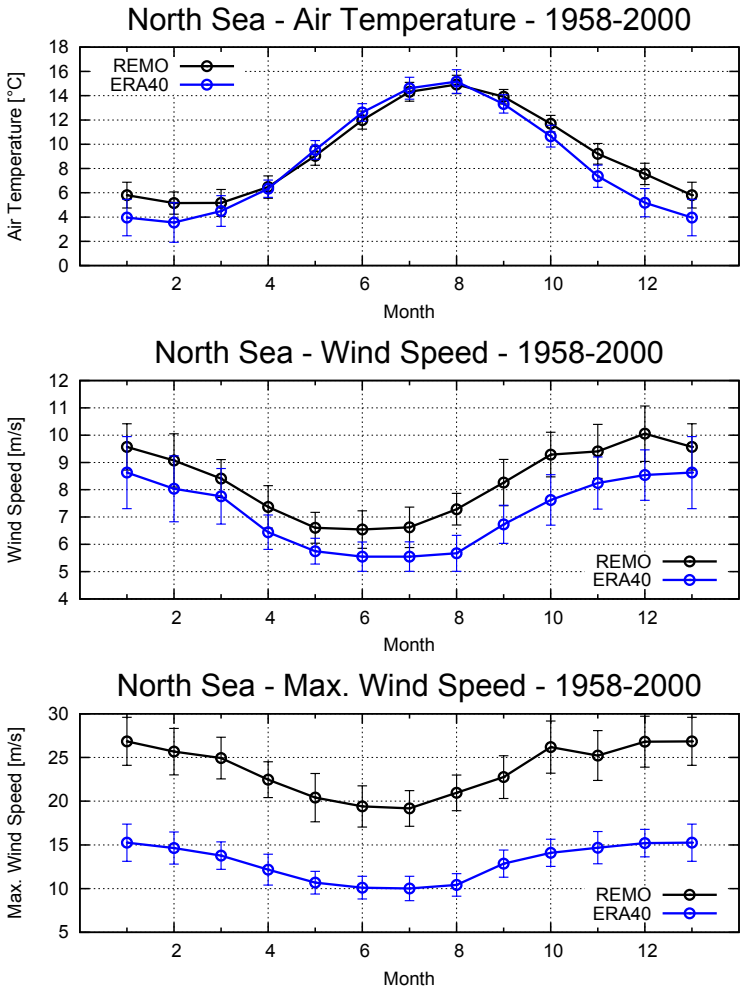

Figure 2.17: Monthly means of spatially averaged atmospheric parameters. Comparison between REMO (black) and ERA40 (blue) over the period 1958-2000. Standard deviation is represented by vertical error bars.

the total variability, entailing the corresponding variances of the two time series (quoted in the diagrams) to still fairly coincide. As being characteristic of atmospheric parameters, the spectra are strongly reddened (von Storch and Zwiers, 1999), that is, higher spectral densities at long periods and lower spectral densities at short periods.

Similar to the lateral boundary conditions, for further evaluation of the atmospheric forcing, monthly climatological means of REMO and ERA40 are compared in Fig. 2.17 to 2.19. Again, without any data assimilation incorporated, time series of the free REMO control run necessarily deviate from observations and reanalysis data, whereas on a climatological time scale, long-term model characteristics should be represented. The considered spatially averaged climatological means refer to the time period 1958-2000, which is covered by both the REMO control run and the ERA40 data set. Only atmosphere grid cells over sea are incorporated in the spatial averaging, whereas grid cells over land are excluded. To account for the differing spatial grid resolution of the two models, both data sets are interpolated onto the 3 km HAMSOM resolution. The temporal variability of each underlying time series of monthly means is indicated by the vertical error bars, representing the standard deviation.

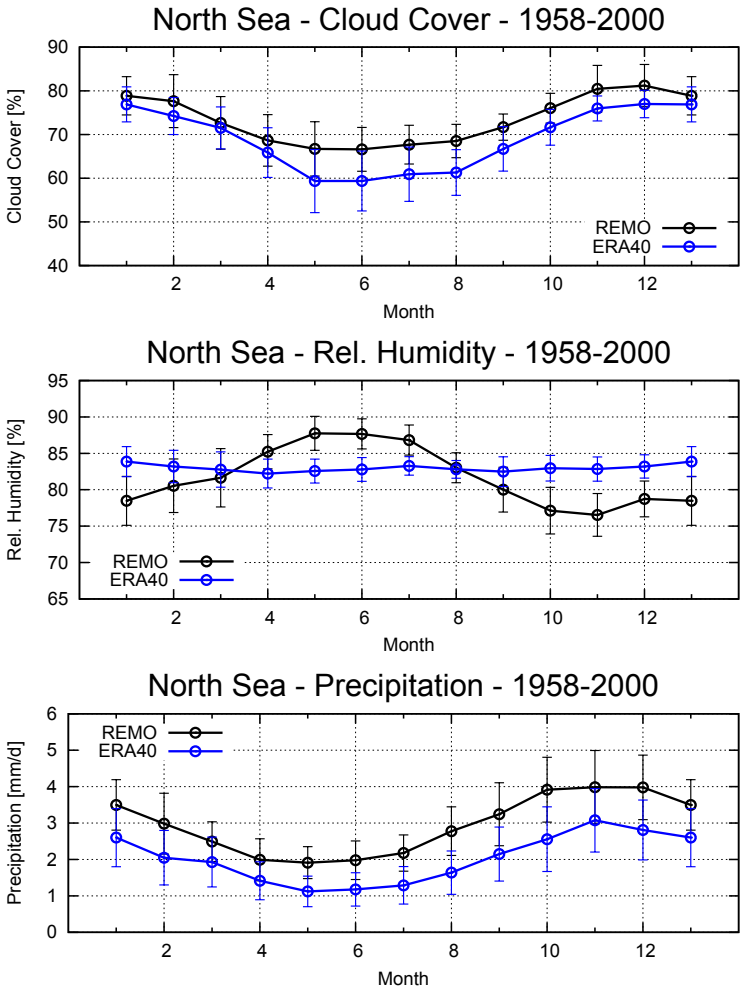

Figure 2.18: Analogous to Fig. 2.17.

Relative to ERA40, the annual cycle of REMO air temperature shows good agreement in the warm seasons spring and summer but a warm bias up to +2 °C in the cold seasons autumn and winter. The mean and maximum wind speeds are higher throughout the year by about +1.5 and +10 m/s, respectively. However, in comparing REMO and reanalysis data with wind observations from off-shore and near-shore platforms, Winterfeldt and Weisse (2009) and Larsén and Mann (2009) found a significant underestimation of coastal wind speeds in the NCEP/NCAR data (Kalnay et al., 1996), which is very similar in the North Sea region to ERA40. Additional comparison with the Hamburg Ocean-Atmosphere Parameters and Fluxes from Satellite (HOAPS) dataset (Andersson et al., 2010) in Fig. 2.20, a multisatellite product based on Special Sensor Micro-wave Imager (SSM/I) measurements starting in 1988, confirms their results for the open North Sea, too. The shown monthly mean and maximum wind speeds of REMO are calculated from the 6-hourly forcing time series obtained from time averaging the lateral and meridional vector components of the original 1-hourly wind fields separately. The 6-hourly wind speed as the magnitude of a 6-hourly wind vector thus differs from the 6-hourly wind speed as the average of the magnitudes of six 1-hourly wind vectors. However, monthly mean wind speeds in the North Sea calculated from 1-hourly and 6-hourly vector fields, respectively, do not differ by more than ±0.8%. Monthly maximum wind speeds are understood as the highest wind speed of a one month time series consisting of domain-wide spatially averaged 6-hourly wind

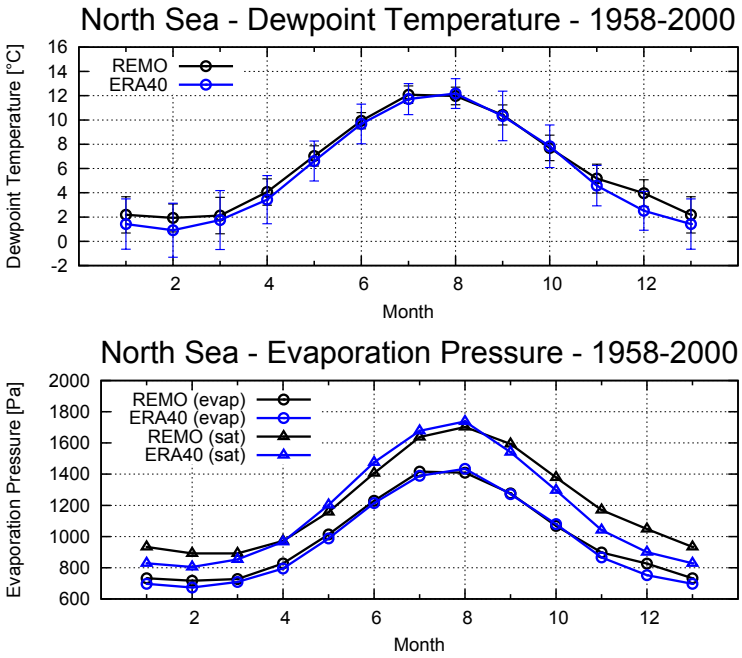

Figure 2.19: Analogous to Fig. 2.17.

speeds. Further analysis of the wind fields are presented in section 2.2.3. Total cloud cover of REMO is slightly higher than of ERA40, with larger difference in summer than in winter. As already mentioned, the relative humidity is calculated as the ratio of evaporation pressure and saturation evaporation pressure, which are approximated by entering air temperature and dewpoint temperature into the empirical Magnus formula, respectively. Unlike the other atmospheric parameters, the annual cycles of relative humidity of REMO and ERA40 show a qualitatively contraring progression. The ERA40 curve has a weak minimum in spring, where the North Sea surface water is cooler than the overlying air, and the latent heat flux and hence, evaporation is low. In turn, a weak maximum shows up in winter, where much of the water is warmer than the cold air and the latent heat flux is high. Moreover, the cold winter air is not able to carry the same amount of moisture as the warm summer air, necessarily increasing the relative humidity. The REMO curve, however, has pronounced extrema with a counter-intuitive maximum in spring and summer but a minimum in autumn and winter. Apparently uncritical deviations of air and dewpoint temperature between REMO and ERA40 indeed yield a higher ratio of evaporation and saturation evaporation pressure for the REMO data in summer and a lower ratio in winter (Fig. 2.19) and by that, give rise to the spurious relative humidity cycle. Precipitation is constantly higher in the REMO data, with deviations to ERA40 ranging from 0.5 to 1 mm/d. Even though over land, the coarse horizontal grid resolution of ERA40 often causes an inadequate hydrology owing to the rough representation of the bottom topography and associated river catchment areas, the comparison of REMO, ERA40, and HOAPS shown in Fig. 2.20 identifies precipitation as a reliable ERA40 parameter over sea. The standard deviations of all atmospheric parameters referred to fairly agree between REMO and ERA40.

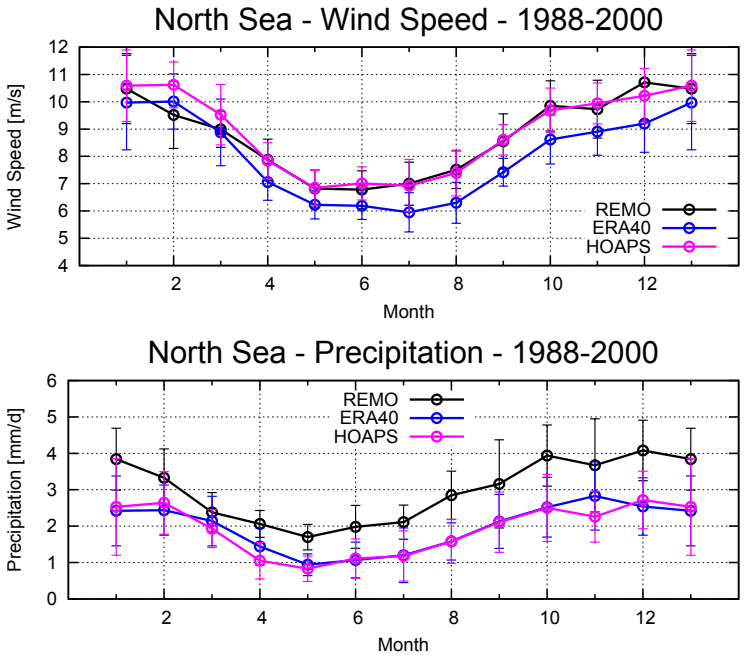

Figure 2.20: Monthly means of spatially averaged atmospheric parameters. Comparison between REMO (black), ERA40 (blue) and HOAPS (magenta) over the period 1988-2000. Coastal regions, Skagerrak and Kattegat are excluded from the analysis since they are not covered by the HOAPS data set. Standard deviation is represented by vertical error bars.

2.2.3 Bias Correction

Numerical simulations in general are affected by a number of errors, since the computed numerical solutions are always approximate solutions of a discretized physical problem. Numerous assumptions and qualitative simplifications necessarily have to be made both in deriving the transport equations for the variables involved in the simulation and in discretizing these equations as well as the geometry of the model domain. Moreover, iteration errors arise by solving the final algebraic equation system iteratively. The sum of these tradeoffs lead to differences between an actual physical state of the considered system and the associated solution of the mathematical model. The systematic deviation of simulated results with respect to the actual physical state described by observations fluctuates around zero for purely stochastic applications but adds up continuously to a non-zero deviation in realistic climate simulations. In the latter case the systematic deviation is called model bias (von Storch and Zwiers, 1999) and it can be addressed as the correspondence between a mean forecast and mean observation averaged over a certain domain and time (WMO, 2009).

Atmospheric Forcing - ERA40

The comparison of REMO and reanalysis data in section 2.2.2 reveals an inherent model bias of REMO relative to ERA40, which is composed of a contribution from the REMO model itself but also of an additional contribution from the inner dynamics caused by the free simulation mode. The former contribution is regarded as the difference between pure reanalysis data and a REMO run driven with that reanalysis data, where the latter contribution is regarded as the difference between a REMO run driven with reanalysis data and a

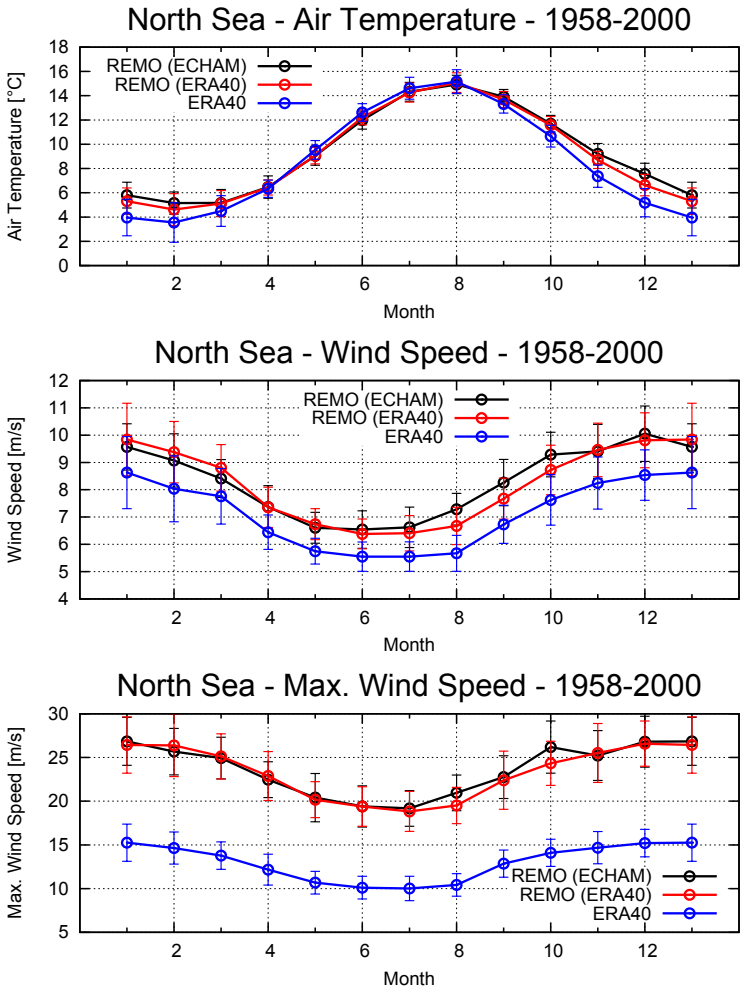

Figure 2.21: Monthly means of spatially averaged atmospheric parameters for the period 1958-2000. Black: REMO driven with results from the free model run ECHAM5/MPIOM. Red: REMO driven with ERA40 data. Blue: ERA40 data. Standard deviation is represented by vertical error bars.

REMO run driven with data coming from a free global model run (Fig. 2.21 and 2.22). The proportion of the respective contributions to the total bias vary for different atmospheric variables but are partially strong enough to yield unphysical behavior of certain variables and in turn, unreasonable behavior of the North Sea dynamics simulated with HAMSOM.

A linear bias correction scheme (Katzfey et al., 2009; Mudelsee et al., 2010; Nilson et al., 2010) is applied for five atmospheric variables used to drive the HAMSOM model, namely air temperature, total cloud cover, wind speed, relative humidity (indirectly via the correction of dewpoint temperature), and precipitation. The base of the correction scheme are spatial monthly δ-fields which reflect the difference between the climatological means of REMO and ERA40 for each variable. These δ-fields are imposed onto the 6-hourly REMO data either additively or multiplicatively in order to remove the bias by shifting the climatological means of REMO towards those of ERA40. Hence, the δ-field correction accounts for regional deviations between the two data sets on a monthly scale without altering short-term variabilities and long-term trends of the REMO time series, so that any climate change signals are largely retained. Even though the δ-fields are derived from the REMO control

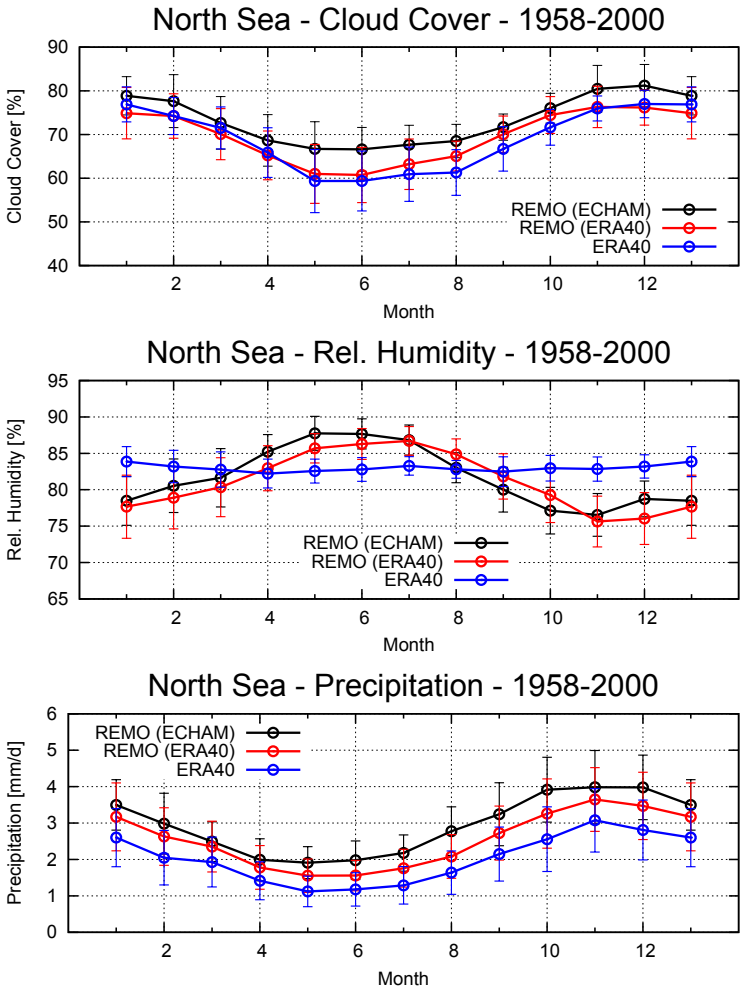

Figure 2.22: Analogous to Fig. 2.21.

run, the respective biases are anticipated to be present in the scenario period, too. In this anticipation the assumption is included that the dominating physical processes governing the condition of the atmosphere do not undergo significant change in the course of a possible regime shift. However, as explicated in the defending arguments later in this section, a regime shift in the atmosphere is not indicated by the time series of the atmospheric parameters. The control run δ-fields are thus consequently applied to the entire simulation period 1951-2099. However, wind directions are excluded from the correction scheme, since highly transient vector fields cannot be adequately modified without severely disturbing the spatial large-scale pattern and the conservation of mass in the atmosphere. The variable sea level pressure is also kept unchanged since it enters the HAMSOM code only in terms of the inverse barometric effect. A linear correction scheme was chosen, because in imposing a constant offset onto the entire time series, the method widely appreciates the model dynamics expressed by the uncorrected data, whereas more complex methods would additionally project further parameter characteristics (e.g. the frequency distribution) of the reference period into the future. The term correction thereby alludes to the application of a kind of postprocessing, analogously referred to in the literature as bias correction.

Fig. 2.23 and 2.24 instructively illustrates the proceeding of the correction scheme by means of the monthly climatological mean air temperature for February and August, re-

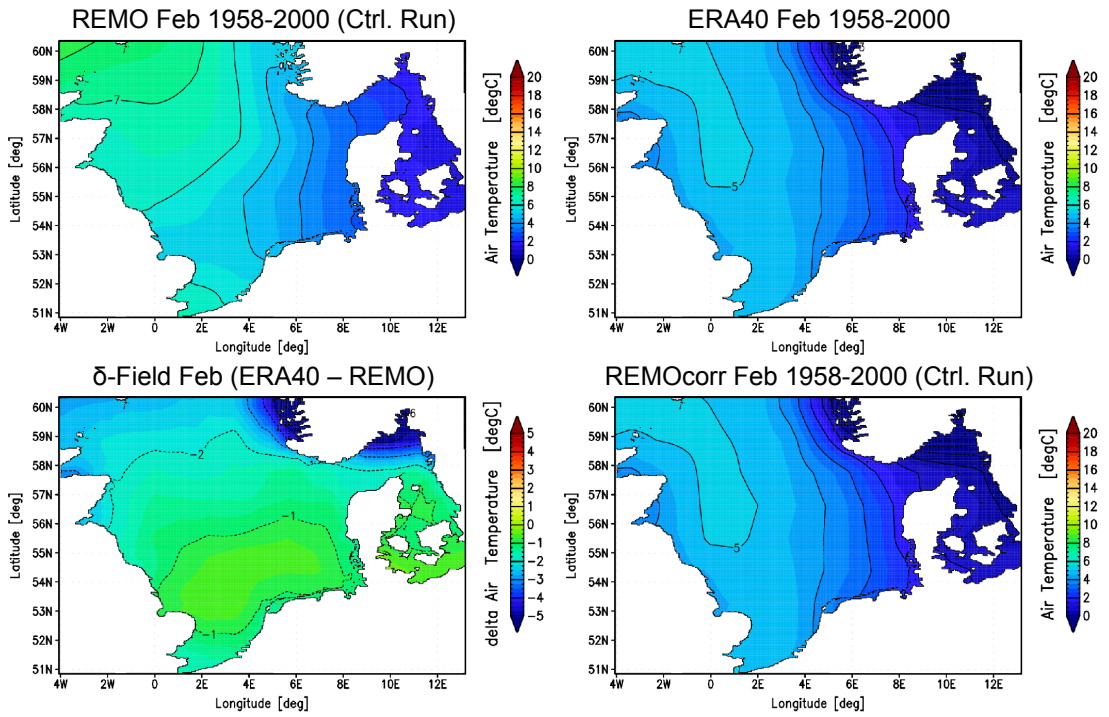

Figure 2.23: Proceeding of the additive bias correction scheme for February air temperature. Upper left: Uncorrected, though spatially interpolated REMO data. Upper right: Spatially interpolated ERA40 data. Lower left: Corresponding δ-field as the difference between ERA40 and REMO. Lower right: Corrected REMO data obtained from imposing the respective δ-fields onto the 6-hourly REMO time series.

spectively. The difference between the two spatial maps of REMO and ERA40 constitutes the corresponding δ-field (lower left parts). The resulting 12 monthly climatological δ-fields are regarded to be representative for the middle of the respective months. δ-fields for intermediate 6-hourly time steps are created via temporal interpolation of the two adjacent climatological δ-fields. In order to correct the REMO data, the associated δ-field is finally added to the REMO data at every 6-hourly time step. The corrected air temperature time series is depicted in Fig. 2.25 as annual means, spatially averaged over the entire North Sea. As intended, the mean of the period 1958-2000 of the corrected REMO data (green line) coincides with the ERA40 mean (blue line). The climatological mean air temperature fields as recalculated from the corrected 6-hourly REMO time series are shown in the lower right parts of Fig. 2.23 and 2.24. The great similarity to the ERA40 fields affirms the chosen monthly time scale to be appropriate for the correction scheme. A larger time scale, e.g. annual δ-fields, could not account for seasonal deviations, whereas a smaller time scale, e.g. weekly or daily δ-fields, would be problematic, since the reference means were no longer representative. Climatological annual cycles of the corrected REMO time series in comparison to the uncorrected REMO and ERA40 ones are shown in Fig. 2.27 and 2.28, time series of spatially averaged annual means are shown in Fig. 2.25 and 2.26.

Alternatively, multiplicative δ-fields can be derived as representing the factorial ratio between corresponding REMO and ERA40 fields. For variables that are restricted to positive values, an additive correction can be crucial if the offset between REMO and ERA40 is large relative to the uncorrected data. By contrast, multiplicative correction automatically

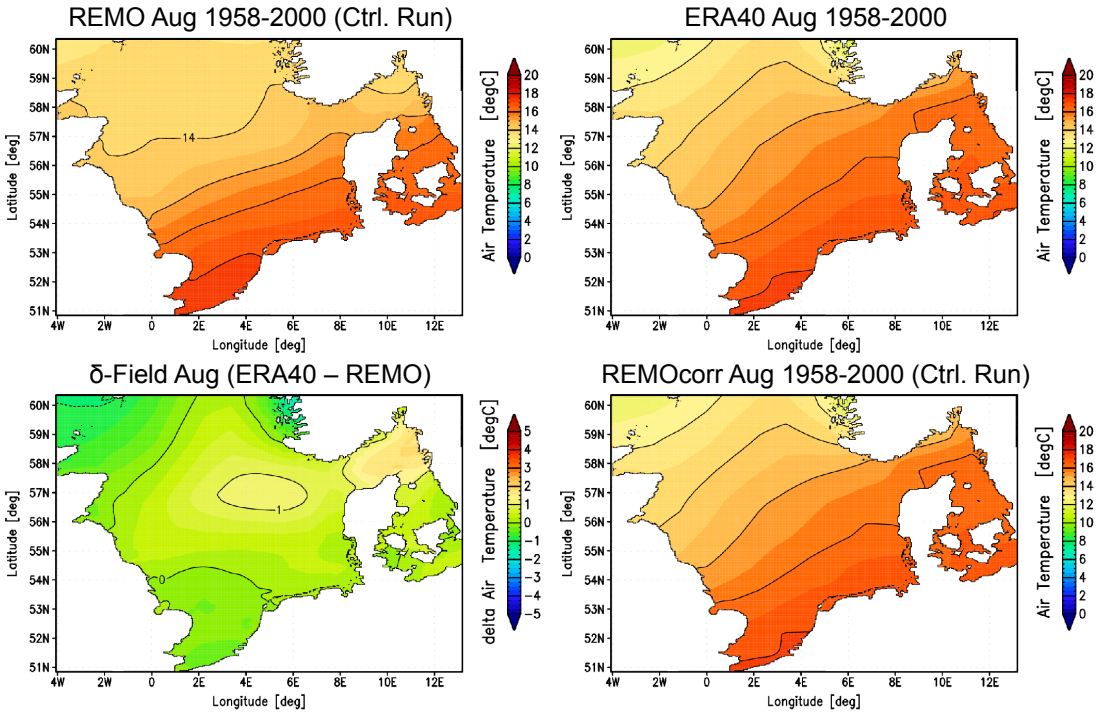

Figure 2.24: Proceeding of the additive bias correction scheme for August air temperature. Description analogous to Fig. 2.23.

accounts for the variable´s sign, qualitatively always retaining the spatial structure of the variable distribution. Nevertheless, higher values are generally stronger effected than lower values and any climate change signal is effected by multiplicative correction to the same factors.

Beside the variable air temperature, additive correction is analogously applied to the variables dewpoint temperature and cloud cover. The correction of both air temperature and dewpoint temperature finally yield a consistent annual cycle of relative humidity (Fig. 2.28). The reduction of cloud cover has to be bounded at 0% to rule out negative values. Multiplicative correction therefore appears to be preferential. However, since the largest correction of cloud cover amounts to just about 10% of the mean, additive correction indeed supplies good results (Fig. 2.26 and 2.28). Nevertheless, multiplicative correction is applied to the variables precipitation and wind speed. The reduction of precipitation amounts up to about 45% of the climatological mean, implying additive correction together with a lower limit at 0 mm/d to yield REMO climatologies still deviating from ERA40. While high values were indeed corrected properly, small values were just set to 0. Mean precipitation and also mean wind speed data of ERA40 are thus approximated more accurately from the REMO data by the application of multiplicative correction. The temporal progression of the 6-hourly wind fields states the wind speeds as well as the wind directions in the North Sea as highly variable throughout the year with hardly any regional preferences. For the correction of wind speed each of the 12 δ-fields is therefore spatially averaged to a single scalar, aside by which a direct violation of the conservation of mass in the atmosphere is avoided. Nevertheless, as mentioned above, the climate change signal of wind speed is effected by the multiplicative correction, too. However, the linear trend of the uncorrected wind speeds

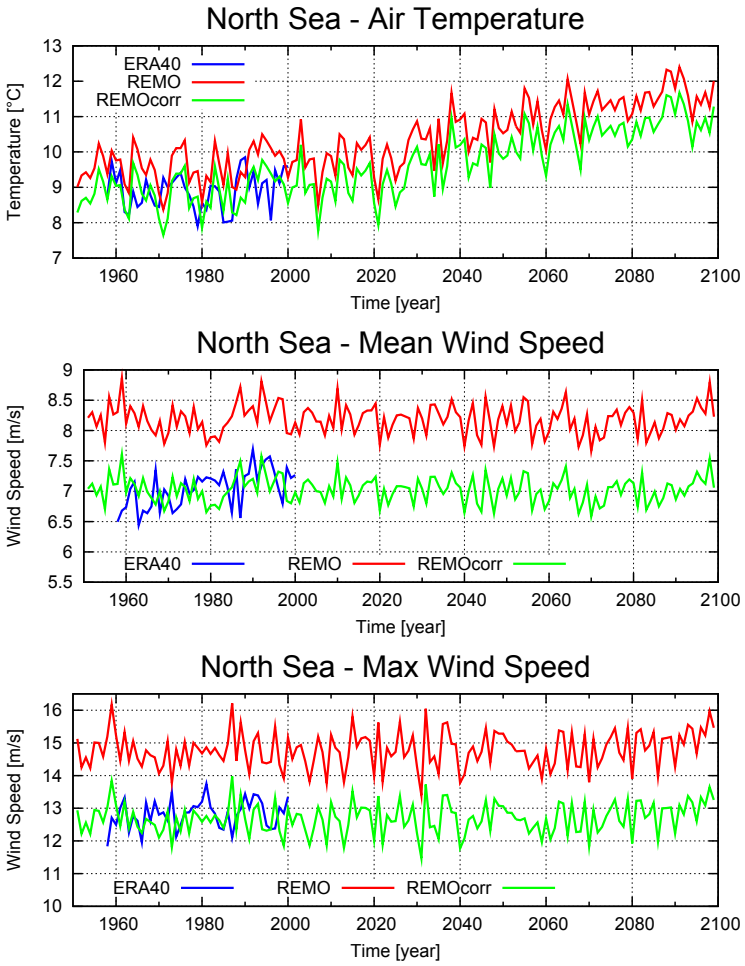

Figure 2.25: Time series of spatially averaged annual means of atmospheric parameters. Red: Uncorrected REMO data. Blue: ERA40 data. Green: Bias corrected REMO data.

(Fig. 2.25) is statistically insignificant, entailing the multiplicative scheme, in this respect, not to pose a deficiency. As already mentioned, wind directions and sea surface pressure are excluded from the correction scheme at all. The wind fields refer to winds at a height of 10 m above ground, where the respective wind vectors are derived by REMO from the pressure field of the lowest model layer with a layer thickness of about 100 m. The diagnostic treatment relativizes the critical independent correction of wind speed from surface pressure. Accordingly, the variables wind stress and sea surface pressure are incorporated decoupled in the HAMSOM model. Since the additive scheme does not change the temporal variability of any underlying time series, but also the extent of the multiplicative scheme changes the variability to a mere negligible amount, the power spectra shown in Fig. 2.16 remain widely unaffected by the bias correction.

In Siegismund and Schrum (2001) a statistical analysis of two-dimensional wind vector fields is introduced. In combining the wind speeds and their relative frequency of occurrence at predefined wind directions, the so-called wind density function quantitatively addresses the angular distribution of various wind conditions. It is understood as a representation of the predominant wind condition for a given domain and time period. In Fig. 2.29 the wind density functions for the whole North Sea as well as its two components

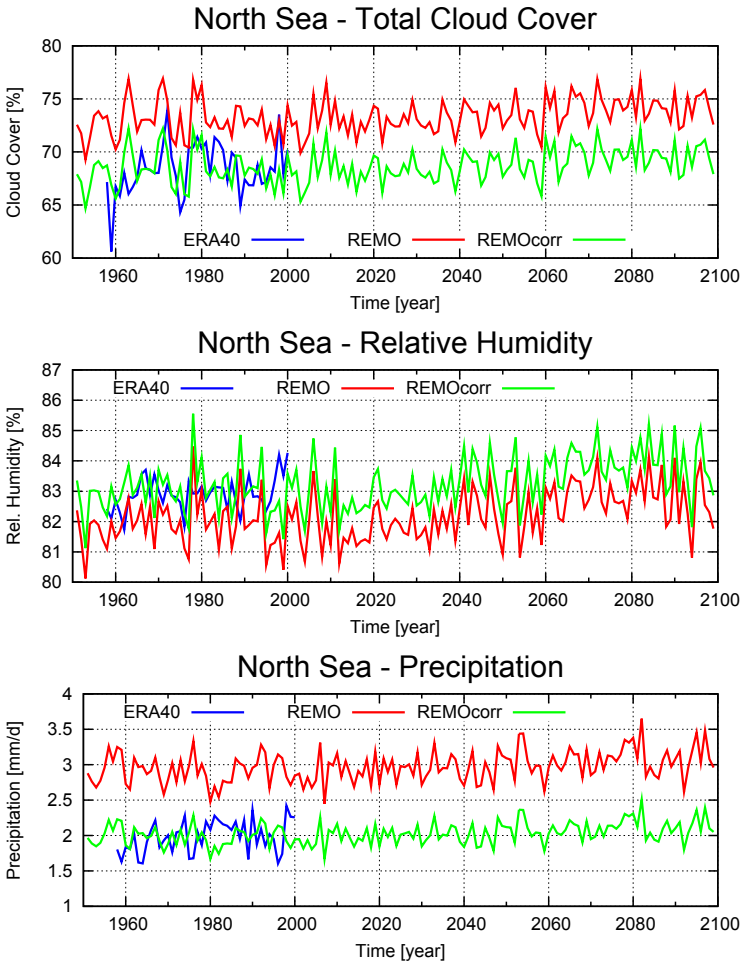

Figure 2.26: Analogous to Fig. 2.25.

wind speed and relative frequency of the bias corrected REMO and the respective ERA40 wind fields are compared on a seasonal scale. A high wind density at a given direction arises from either a high mean wind speed at that particular direction or a high frequency of occurrence of wind blowing from that direction (or both of it). Wind directions are distinguished in the analysis as 5° sectors, bringing about any curve in the diagrams to consist of 72 samples. The physical unit m/s is carried by the wind density for mathematical reasons and shall not be interpreted as ordinary speed.

The ERA40 wind density functions shown in Fig. 2.29 well reflect the predominant westerly and south-westerly wind conditions over the North Sea, in particular for the more stormy seasons autumn and winter. The diagrams distinctly show a more uniform distribution of wind speeds than of relative frequency, underlining similar wind speeds in the North Sea to potentially occur at all directions. Whereas the integrated relative frequency of each season sums up to 100% per definition, the lowest and highest wind speeds in summer and winter, respectively, yield minimum and maximum wind density functions. Relative to ERA40, the REMO wind densities show an overestimation of westerly and south-easterly wind conditions and an underestimation of south-westerly ones. Since the wind speeds are reduced in the course of the bias correction, the overestimation, accordingly, is more pronounced for the uncorrected wind speeds (not shown). The standard deviation of

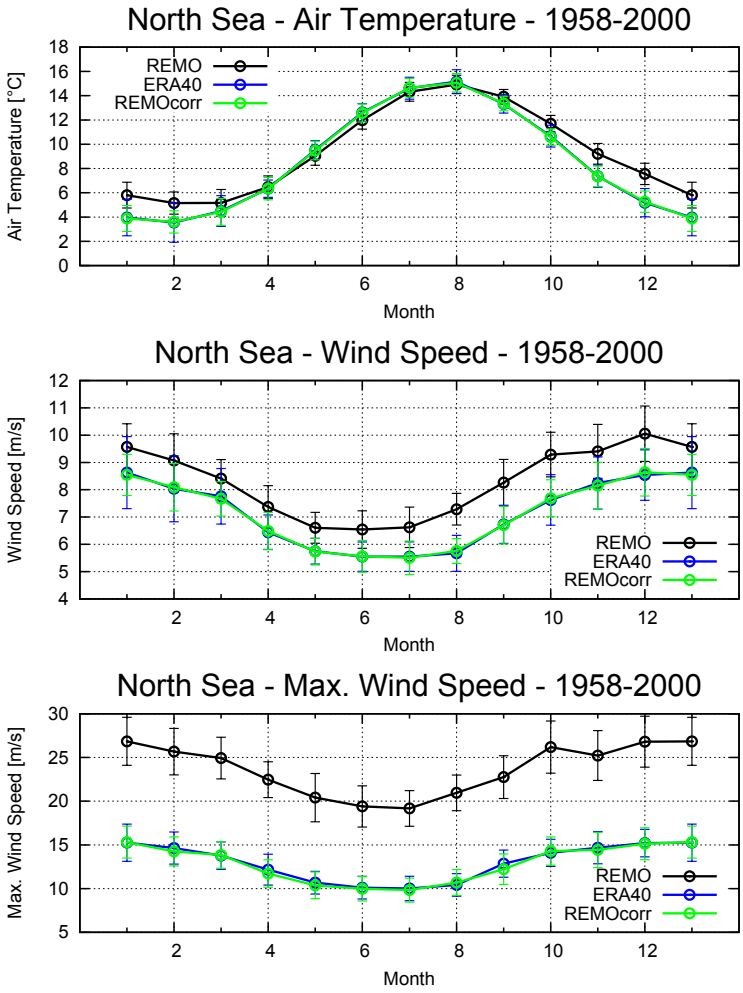

Figure 2.27: Monthly means of spatially averaged atmospheric parameters for the period 1958-2000. Black: Uncorrected REMO data. Blue: ERA40 data. Green: Bias corrected REMO data. Standard deviation is represented by vertical error bars.

the monthly wind density functions used to calculate the mean of 1958-2000 depicted in Fig. 2.29 are shown in Fig. 2.30. Since neither curve in Fig. 2.29 can take negative values, smaller means necessarily have smaller standard deviations, which therefore largely follow the qualitative shape of the means. Implications of the deviating wind conditions of REMO and ERA40 on the general circulation of the North Sea are discussed in chapter 3, where the HAMSOM model was driven with the two data sets for the period 1958-2000.

The application of bias correction methods in climate research is controversially discussed by the scientific community. Advocating approaches range from simple additive corrections of the mean or variance in e.g. Lenderink et al. (2007), across local intensity scaling in e.g. Schmidli et al. (2006), to more advanced quantile mapping methods in e.g. Li et al. (2010), while critical general objections are raised in e.g. Ehret et al. (2012). Added value is conceded to the linear bias correction applied in this study in virtue of the following considerations, which may not fully hold for other bias correction methods than the linear one used in the present study.

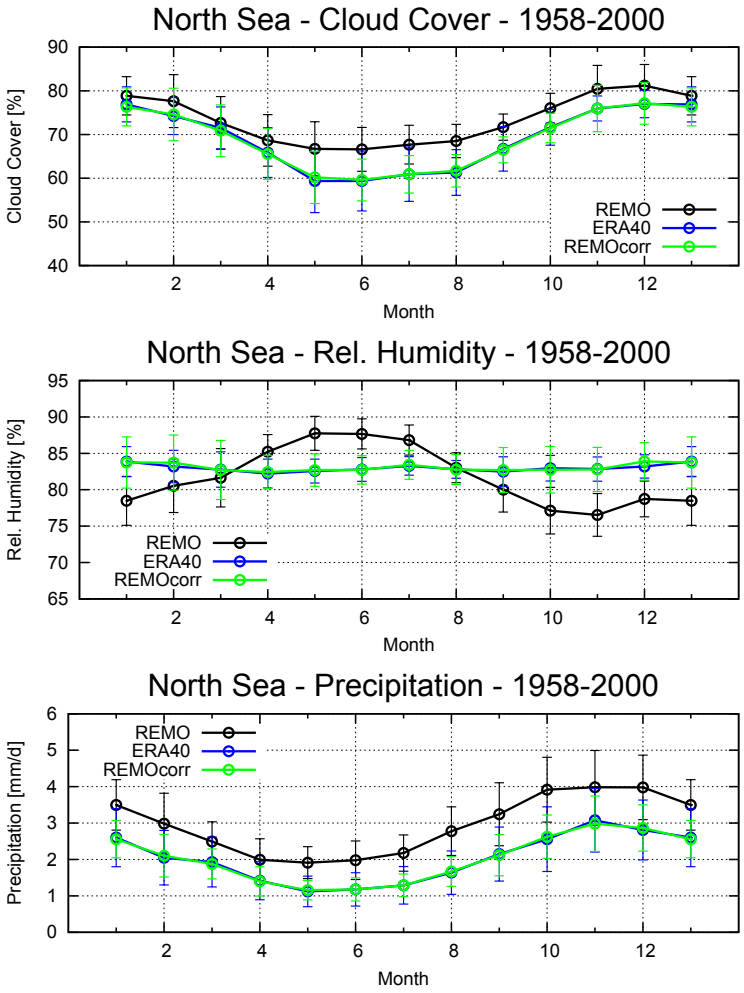

Figure 2.28: Analogous to Fig. 2.27.

(1) The main argument against any postprocessed modification of physical parameters from model output is that the physical consistency of the modified data is no longer guaranteed (Ehret et al., 2012). In modifying individual physical parameters, generic conservation laws like e.g. the conservation of mass are violated. However, the bulk formulas used by HAMSOM are empircal formulas derived from observations and do not expect a perfectly consistent set of forcing variables. The aim of applying a bias correction in this study is not to improve the atmospheric model output itself but rather to provide forcing data for the ocean model HAMSOM showing the same statistical characteristics for a given hindcast period as a well established observational reference data set.

(2) In using different methods for the discretization and implementation of the physics and dynamics, different models yield different results, while the differences in the results often amount to the same order of magnitude as both the ensemble mean and the sensitivity to critical parameters (Delhez et al., 2004). In this respect the extent of the parameter modification in the course of the bias correction is distinctly moderate. Moreover, as can be seen in Fig. 2.25 and 2.26, the long-term scenario trend of the variables is generally positive, but the sign of the correction is predominantly negative. Therefore, the extrapolation of the transfer functions (i.e. the δ-fields) from the reference period into the scenario period is not expected to lead to atmospheric conditions beyond physical limits.

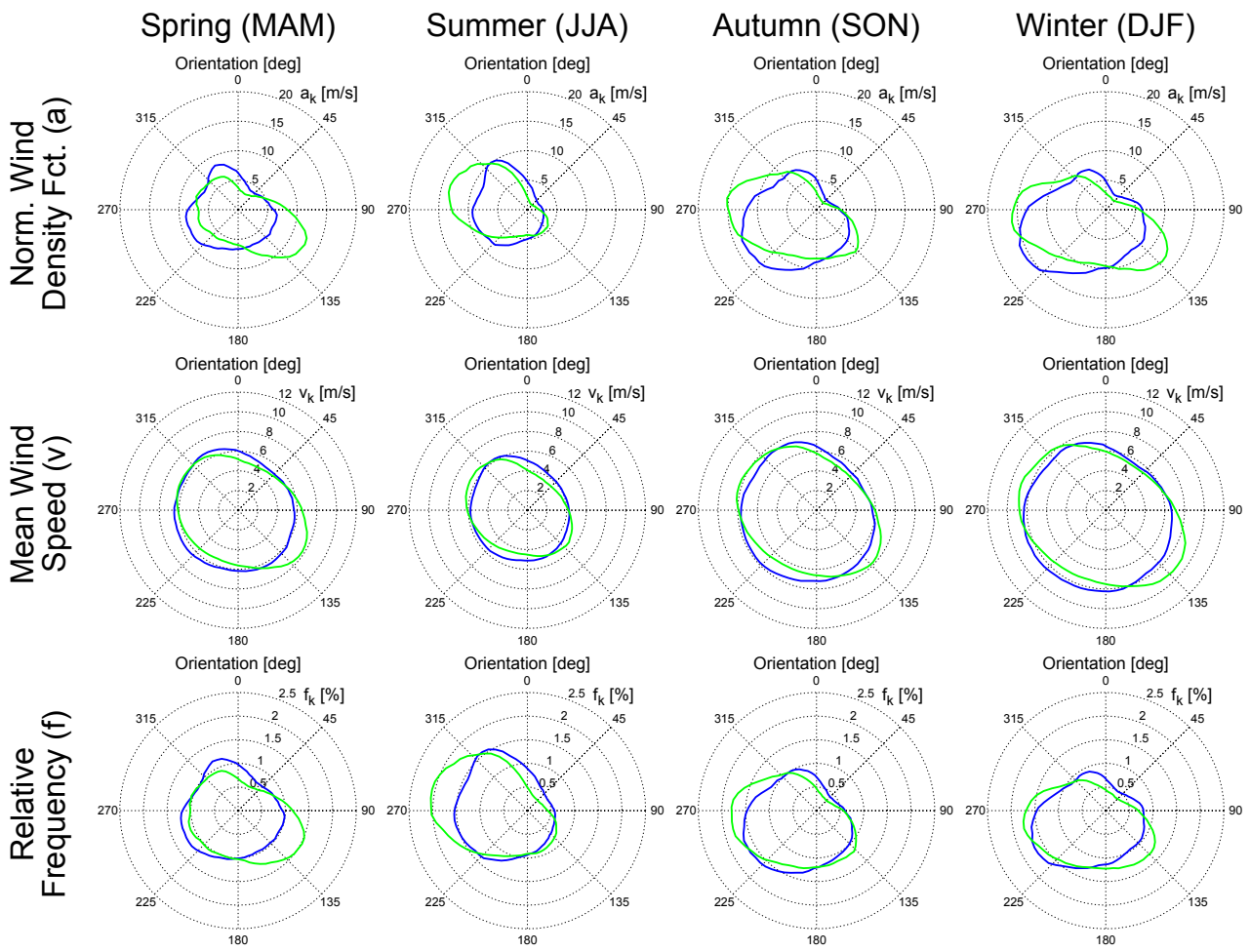

Figure 2.29: Normalized wind density functions (Siegismund and Schrum, 2001) for the whole North Sea as well as their two components, mean wind speed and relative frequency, on a seasonal scale of the period 1958-2000. Green: Bias corrected REMO data. Blue: ERA40 reanalysis data. Orientation angles of 0 deg correspond to northerly winds.

(3) In climate models the equations of fluid motion as a system of *discretized* differential equations describe finite temporal changes of state variables of a finite spatial control volume. As such, they deal with averages only, where the entailing loss of information at scales lower than the averaging scale inevitably leads to deviations from reality (Oreskes et al., 1994). Thereby, the averaged quantities obey their own statistical regularity. Surprisingly, even the second law of thermodynamics, which is supposed to be involved in any physical process at all, turns out as the prototype of a statistical regularity (Schrödinger, 1962). From a statistical point of view, it states that all physical incidents evolve from relatively unlikely conditions to more likely ones. And indeed, there are serious stances among physicists, mathematicians, and philosophers (e.g. Franz S. Exner, Erwin Schrödinger, John A. Wheeler) that endorse the only bottom-level principle of reality to be the stochastic law of large numbers. However, owing to the inherent statistical character of physical theories, they are never mathematically perfect and precise and hence, they are always consistent with a certain *range* of absolute parameter values.

(4) Under converging residuals of a model simulation, a successive refinement of the spatial grid resolution yields model results that converge on the corresponding grid-independent

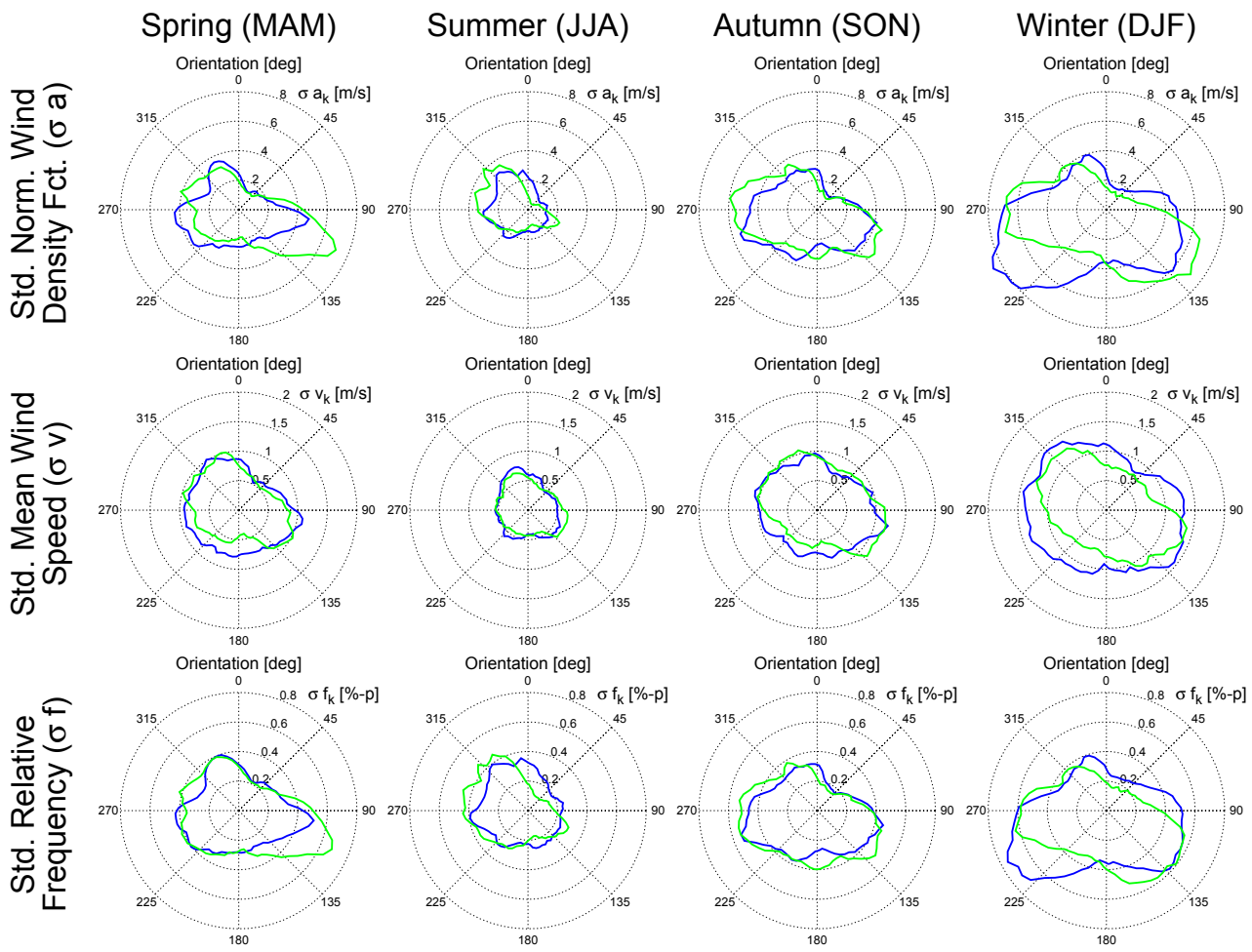

Figure 2.30: Standard deviation of the monthly wind density functions used to calculate the mean of 1958-2000 depicted in Fig. 2.29. Green: Bias corrected REMO data. Blue: ERA40 reanalysis data.

accurate solution (Ferziger and Perić, 2002). The loss of information due to finite sizes of control volumes mentioned in (3) can then be arbitrarily reduced by a refinement of the numerical mesh. However, as a representation of *phenomenological* determinism, the equations of fluid motion do not take into account microscopic degrees of freedom. With this, they cannot describe processes initiated by microscopic fluctuations that become unstable and amplified to macroscopic scales, which may even support *orderd* states as dissipative structures (Zeh, 2010). The standard example related to fluid dynamics is known as Bérnard´s instability, which describes the formation of convection cells in a horizontal layer of a liquid, optimizing the process of thermal equilibration between two reservoirs at different temperatures. In principal, though, a bias correction applied on appropriate spatial and temporal scales is indeed able to account for inadequate phenomenological representations in a model´s forcing data.

(5) Furthermore, the equations of fluid motion provide a mathematical system in which the number of unknowns is greater than the number of equations, enforcing the employment of turbulence closure schemes in numerical models. So, even if the equations are fulfilled by a single physical event, they still leave this event widely undetermined, again coming along with a tolerance range of absolute parameter values (Schrödinger, 1962).

(6) A well known source of inconsistencies between model results and reality arise from missing model implementations of dynamical interactions among various physical processes. For either there is no appropriate theory known or the available computer capacities are insufficient, potentially crucial interactions for addressing climate change such as interactions related to cloud physics, aerosols, vegetation, carbon and nitrogen cycles are usually not fully incorporated in climate models (Bader et al., 2008), even though they may not be judged negligible for the respective scale of interest. Therefore, if one relies in the reference data chosen for the bias correction as representation of physical reality, the modified model data can be regarded as fluctuations abount perfectly consistent equilibrium conditions. To put it provocatively, any model output then even *gains* consistency from the bias correction, since the modified model data is finally closer to reality which does not allow for any inconsistency at all.

(7) An other common argument against the application of a bias correction is the regime shift argument. It says that if at some future time the modeled climate changes into a different regime, the extent of the correction based on a certain reference regime is no longer appropriate for the new regime. The application of a bias correction thus implies stationarity of the correction function (Christensen et al., 2008). Processes sensitive to regime shifts are often related to the hydrological land-atmosphere cycle via the sensitivity of cloud cover and soil moisture (Hagemann et al., 2011), and to ice covered regions in general via the sensitivity of surface albedo (Maraun, 2012). A regime shift of climate is identified by the occurrence of a bifurcation point in the time series of atmospheric variables. A bifurcation point, in turn, is characterized by a conspicuous discontinuity in the variable´s temporal progression, that is, a sudden shift of its magnitude level or a distinct change of its long-term trend. However, considering the time series of the REMO variables in Fig. 2.25 and 2.26, there is no indication for a climatic regime shift in the North Sea. Also the spatial patterns of the variables do not undergo substantial qualitative changes as indicated by the comparison of time series of five representative locations across the North Sea, not shown here (northern North Sea, central North Sea, Southern Bight, German Bight, Skagerrak). It is therefore not expected the individual δ-fields of the bias correction to be inappropriately extrapolated into the scenario period. Nevertheless, nonlinear characteristics of the model bias as a function of e.g. air temperature or precipitation cannot be ruled out completely.

(8) Different models not only yield different results, as mentioned in argument (2), but also more than one model implementation and even more than one setup of preferences within an individual model can produce very similar results. This particularly holds for comparatively short time scales, where assumptions and simplifications in the model´s principal hypothesis may cancel assumptions and simplifications in some auxiliary hypothesis (Oreskes et al., 1994) - an issue referred to as the non-uniqueness problem. A match of model results and observations on just a short period thus cannot be regarded as a quality proof of the model. Therefore, the bias correction in this study is based on monthly climatological means as statistically representative long-term model characteristics. Moreover, monthly based bias corrections fully preserve observed annual and seasonal statistics (Rojas et al., 2011), whereas daily based corrections may negatively influence the

variance of monthly means (Haerter et al., 2011). Basing the correction upon monthly climatological means also assures that meso-scale atmospheric processes, which cannot be accounted for by the coarser grid resolution of ERA40, are largely retained in the REMO data.

(9) While the correction of many forcing variables do have a mere quantitative implication, some physical phenomena in the ocean *existentially* rely on absolute variable values. The thermocline, for instance, simply does not develop in the North Sea when wind speeds are too strong. The structure of the general circulation in the North Sea is sensitively affected by sea surface gradients along the northern boundaries. The long wave and latent surface heat fluxes are nonlinearly related to the air and water temperatures. Thus, model simulations with uncorrected forcing variables off their respective validity ranges easily result in unreasonable hydrodynamic and hydrographic representations of the North Sea.

(10) Regardless of the given conceptual arguments, the modifications of atmospheric parameters in the course of the bias correction demonstrated in Fig. 2.25 to 2.28 are ever made in a conservative direction. The whole range of *relative* humidity can be acquired by an air parcel of any air temperature. Nevertheless, the corrected air and dewpoint temperatures are incorporated in the correction of relative humidity. Moreover, cloud cover is reduced as consistently is the precipitation rate, while in particular these variables are associated with the largest uncertainties in climate models, anyway (Bader et al., 2008). The increase of relative humidity in combination with decreasing cloud cover and precipitation can be understood as a local increase of the critical relative humidity for cloud formation in the REMO model. Wind speeds are reduced factorially in order to warrant conservation of mass in the atmosphere and to retain the spatial structure of the wind fields. Wind stress and sea surface heat fluxes are recalculated from the corrected variables. Hence, obviously inconsistent atmospheric conditions, like clear blue sky in combination with heavy rainfall or the like, are not induced by the bias correction.

(11) The same correction method was applied to the MPIOM data at the open lateral boundaries (see below) with respect to World Ocean Atlas 2001 climatologies (Boyer et al., 2005). Besides the account for the MPIOM model bias, the correction of the lateral boundary conditions also restores the consistency of the modified atmosphere and the ocean along the boundaries.

(12) Epistemologically considered, the quantitative models of physics, referred to as physical theories, are just mathematical constructions for the calculation of observable state of affairs (Schrödinger, 1962). In this sense the whole setup of a numerical model (from its initialization, across the mathematics in the source code, the forcing data, the computing system, to the bare model results) can be understood as a theory of its individual scientific discourse. Climate models represent theories of the Earth´s climate and the HAMSOM model represents a theory of the hydrodynamics in the North Sea. In the end the question whether a theory is successful reduces to the question whether the data that the theory is intended to describe is indeed sufficiently compressed by the theory, to be verified in

the course of the evaluation of the theory (Genz, 2004). However, that a theory is able to compress observational data is not a sufficient requirement for its validity but a *necessary* one. In accordance with experimental practice in physical sciences, any physical theory needs to be confirmed by measurements for being accepted, since the goal of scientific theories is *empirical adequacy* (Oreskes et al., 1994). In numerous studies in collaboration with the University of Hamburg, Institute of Oceanography, the HAMSOM model already *is* evaluated with respect to reanalysis data at best scientific discretion. Thus, the successful evaluation judges the transformation of any forcing data into the model´s reference range on the basis of reanalysis data almost *essential* to obtain reliable results. Insofar, the bias correction shall be deemed as an extension of the model´s mathematical construction in order to calculate observable state of affairs more accurately. As a consequence, the future scenario run is initialized by the bias corrected control run as a more realistic state of the ocean and atmosphere. To put it provocatively once more, the bias correction can be regarded as a pragmatic necessity, which does not *increase* the reliability of the scenario run but virtually constitutes its *foundation*.

For the given arguments the applied linear bias correction is assessed as being tenable within the presented conception. Nevertheless, most of the current bias correction approaches, including the presented one, are carried out separately across space, time, and variable, so that their application remains to be taken with a pinch of salt and must be carefully decided for each individual model study. In particular, be aware that the uncertainty of a scenario run, to be understood as the range of possible future outcomes, is not reduced by the application of a bias correction. But notwithstanding, relative to the quality of the chosen reference system, the simulated ocean-atmosphere system is shifted into a more realistic state, while the trend and variability of the forcing variables are retained and therefore, added value is conceded to the bias correction method for purely pragmatic reasons. As illustrated in Fig. 1.4, it is indeed common practice for model and scenario intercomparisons to normalize the various time series by shifting them into a specific reference level. This is in fact the same technique as the bias correction applied in this study. While not being an argument to justify the bias correction, it though points out its pragmatic value. Finally, a HAMSOM simulation driven with direct ERA40 forcing is analyzed in chapter 3 in order to evaluate the corrected REMO forcing.

Lateral Open Boundaries - WOA-01

The same additive correction method as for the meteorological forcing is also applied to the MPIOM data at the open lateral boundaries. Thereby, monthly climatologies from the World Ocean Atlas 2001 (WOA-01) provided by Boyer et al. (2005) is used as reference data. In Fig. 2.31 and 2.32 the proceeding of the correction is exemplified for water temperature and salinity at the northern boundary, respectively. The MPIOM water temperature is corrected along the northern boundary on average by about -1.5 °C throughout the year, whereas the salinity undergoes an increase up to +1.4 psu at the Norwegian Coastal Current but a slight decrease of about -0.3 psu elsewhere. Similar cooling and freshening is invoked at the western boundary. Thereby, deeper waters are generally stronger cooled

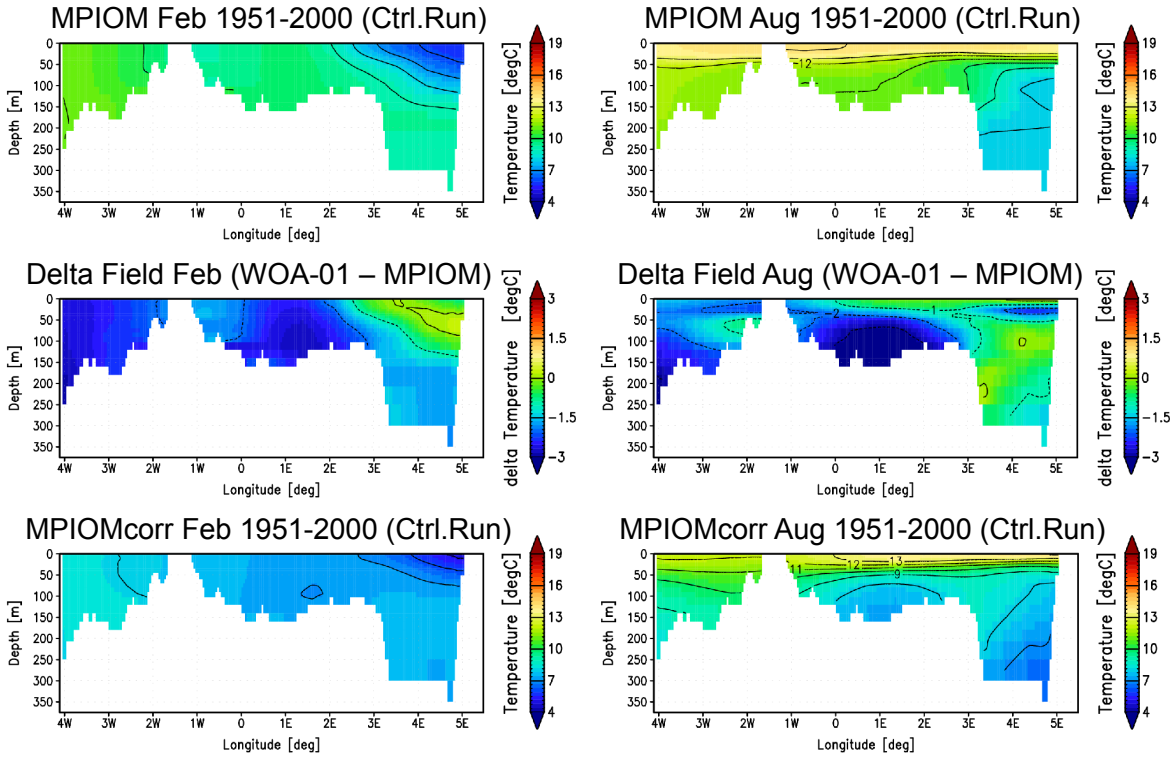

Figure 2.31: Proceeding of the additive bias correction scheme for water temperature at the northern boundary for February (left part) and August (right part). Upper part: Uncorrected, though spatially interpolated MPIOM data. Middle part: Corresponding δ-fields as the difference between WOA-01 and MPIOM. Lower part: Corrected MPIOM data obtained from imposing the respective δ-fields onto the monthly MPIOM time series. Isolines increment is 1 °C. Since both data sets refer to a monthly scale, the corrected MPIOM means are identical to the spatially interpolated WOA-01 data which are therefore not shown.

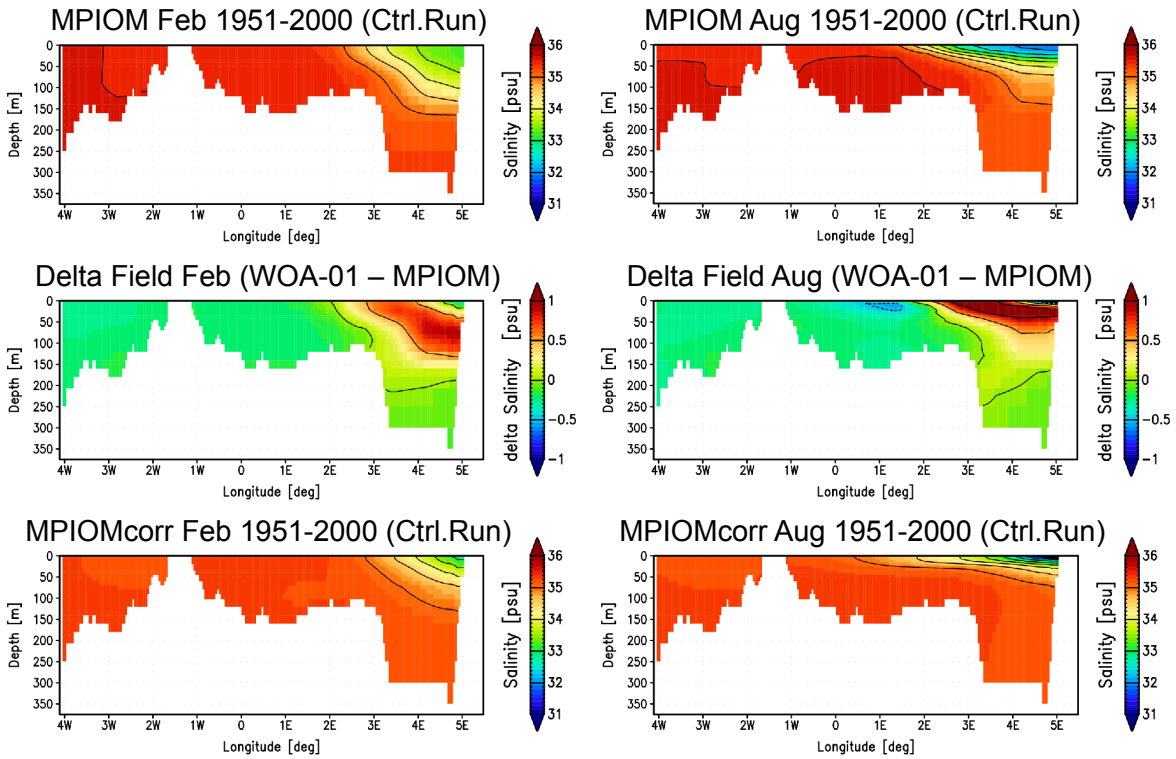

Figure 2.32: Description analogous to Fig. 2.31 for salinity. Isolines increment is 0.5 psu.

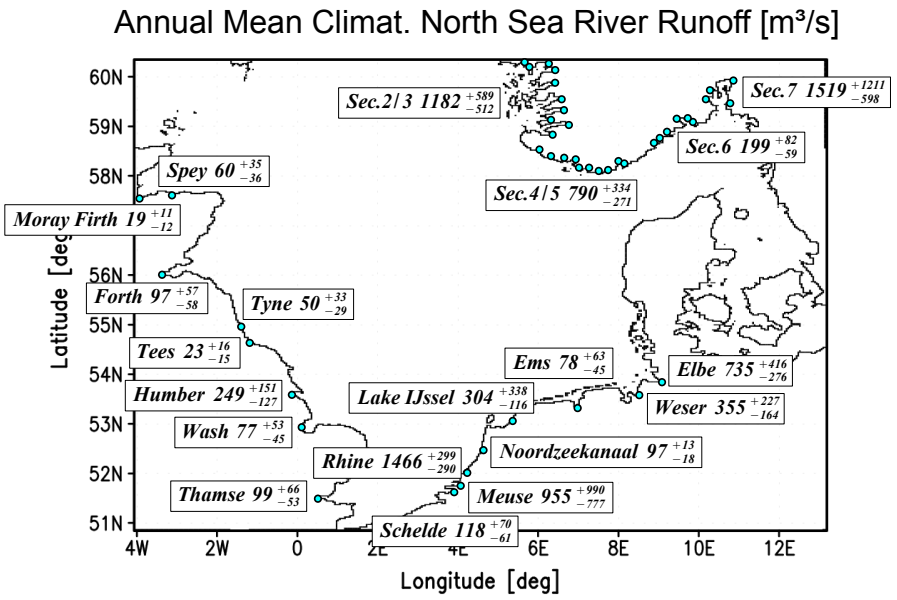

Figure 2.33: Map of the 46 North Sea rivers incorporated in HAMSOM and respective runoff fluxes. Numbers refer to annual climatological runoff means in m³/s according to Damm (1997) and O'Driscoll et al. (2012). Maximum positive and negative deviations from the mean are given too. The Norwegian sections are designated after Damm (1997) as well.

than surface waters, bringing about that no artificial vertical instabilities are introduced. But neither is the surface salting of the Norwegian Coastal Current strong enough causing the vertical haline stratification to collapse. At the southern and eastern boundaries, the MPIOM water temperature is decreased in summer by up to -2 °C but fits well with WOA-01 in winter. The salinity is increased by about +0.4 psu at the southern boundary, while at the eastern boundary, it undergoes a total adoption of the annual cycle, since the MPIOM salinity is almost zero in this region. Hence, the salinity at the eastern boundary is treated climatologically constant on a monthly scale for the whole 150-year simulation period. Sea surface elevation, the third prescribed ocean variable, is modified according to the descriptions in the following sections.

2.3 River Runoff

For the North Sea region no other fresh water runoff than the one descending from the Baltic catchment area is incorporated in the ECHAM5/MPIOM simulation. Coastal runoff data are nevertheless calculated from a hydrological model (Hagemann and Dümenil, 1998a,b) and provided by the MPI-M. However, the grid resolution of the data is almost 2°, which is regarded as too coarse to infer appropriate runoff data for individual rivers. Riverine discharge along the North Sea coasts is thus incorporated in HAMSOM as monthly climatological means. Respective runoff fluxes of 46 rivers are gathered by Damm (1997) and O'Driscoll et al. (2012), where a map of locations and mean runoffs is exhibited in Fig. 2.33.

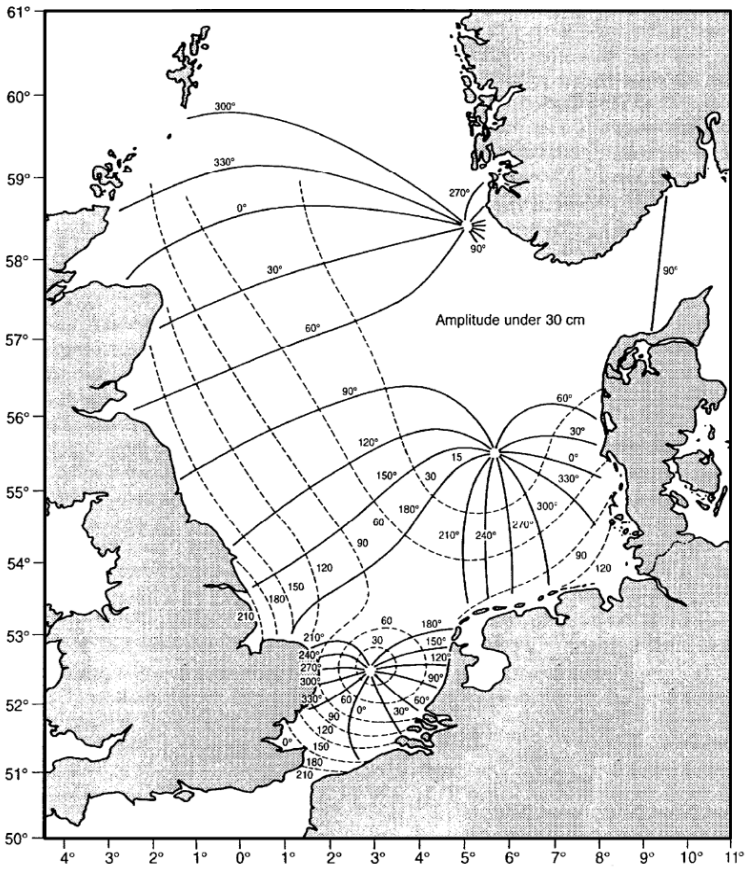

Figure 2.34: Amphidromic system of the semi-diurnal M_2 tide in the North Sea (Dyke, 2007). Solid lines: Co-phase lines. Dashed lines: Co-range lines [cm].

2.4 M_2 Tide

Since the MPIOM data are provided as monthly means, tidal oscillations are not reflected by the variable sea surface elevation. To account for tidal mixing and residual flow in HAMSOM, semi-diurnal lunar tidal oscillations as provided by the Oregon State Tidal Inversion Software (OTIS) are added onto the sea surface elevation prescribed at the open boundaries. In this study the HAMSOM model runs with a forcing time step of 10 minutes and thus, tidal oscillations can be resolved properly. Further partial tides are not included, since the model output is stored as mean values over two M_2 periods, i.e. 24.84 hours, representing approximate daily averages. In the North Sea the M_2 constituent already gives rise to about two thirds of the equilibrium tidal amplitude (Klein et al., 1994). With this, major dynamical effects due to tides are nevertheless sufficiently well simulated. The amphidromic system of the M_2 tide in the North Sea is shown in Fig. 2.34. As described in the introduction (section 1.2.3), the North Sea tide is a co-oscillating response to the tide generated in the North Atlantic Ocean (Banner et al., 1979). Tidal waves enter the North Sea through the northern entrance and through the English Channel. As progressive Kelvin waves, they are mainly adhered to the coast passing the North Sea in cyclonic sense. Bottom friction causes the waves to gradually lose energy, indicated by the successive decay of tidal amplitude (see Fig. 2.34). At the northern and southern boundaries, the maximum M_2 amplitude amounts to about 1.2 and 2 m, respectively.

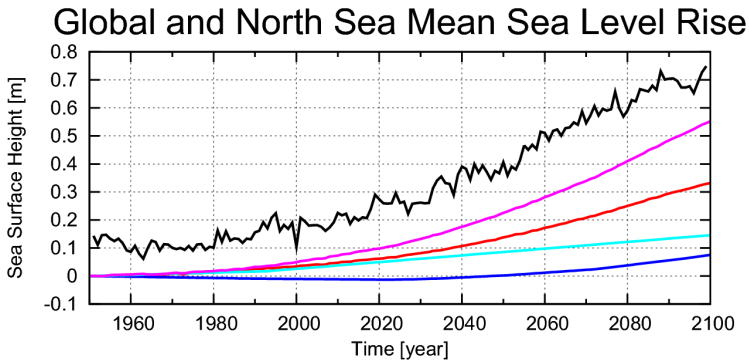

Figure 2.35: Components of global mean sea level rise and resulting mean sea surface height for the North Sea simulated by HAMSOM. Red: Global thermo- and halo-steric expansion. Light blue: Global deglaciation. Dark blue: Balance of Greenland and Antarctic ice dynamics. Magenta: Total global sea level. Black: North Sea mean sea level.

2.5 Global Sea Level Change

Change of the global mean sea level in the 21st century is mainly determined by steric expansion of the ocean due to global warming and by increasing fresh water supply from melting off the two permanent ice sheets over Greenland and the Antarctic and from inland deglaciation (Solomon et al., 2007). The mean sea level in the North Sea is furthermore determined by the regional distribution of globally added melt water masses due to gravitational effects, by barotropic and baroclinic ocean dynamics due to changing density distributions, and by glacial isostatic adjustment, that is, the vertical rebounding of the Scandinavian earth crust since the last ice age. However, the extent of the various regional effects differs to a larger amount between different climate models than between the simulated individual scenarios and therefore adheres to relative high uncertainties (Slangen et al., 2012).

Since the MPIOM is a volume-conserving model, it cannot account for a global rise of the mean sea level due to thermal expansion. Moreover, sea level change due to increasing fresh water supply from melting off the Greenland and Antarctic ice sheets and from inland deglaciation are not incorporated. For the HAMSOM simulations estimations of the different components of global sea level rise are thus continually added onto the sea surface elevation at the open boundaries. Respective time series are shown in Fig. 2.35. Steric expansion is thereby calculated from the global MPIOM temperature distribution, contributing about 60% of the total sea level rise. Global deglaciation for the A1B scenario is extrapolated from observations given in Solomon et al. (2007) sec. 5.5.6, contributing about 25%. However, the observed 0.8 mm/y for 1993-2003 are heuristically increased for the scenario period to 1.2 mm/y to take into account an expected exponential progress. The balance between Greenland and Antarctic ice dynamics is estimated in a model study by Jungclaus et al. (2006b), finally contributing about 15%. The negative balance up to the year 2050 arises from accumulation of snow and ice in the Antarctic as a consequence of higher precipitation rates in the generally moister A1B climate. The offset of the North Sea mean sea level simulated by HAMSOM of about 0.1-0.2 m above reference level (see Fig. 2.35) results from the halo-steric effect due to riverine discharge and Baltic outflow

and from wind induced surges in the southern and eastern North Sea. Since the model run is initialized with a spin-up period of three years, the offset is already present in 1951. Owing to the mentioned uncertainties, regional deviations of the global mean sea level rise are not accounted for in the present study. The total mean sea level rise of about 0.51 m from the period 1990-1999 to 2090-2099, as resulting from the three global components, nevertheless fits well with the projected IPCC ensemble mean for the North Sea region of approximately 0.4-0.6 m given in Slangen et al. (2012) in which estimations of all regional components but ocean dynamics are included. Sea level rise is incorporated in the HAM-SOM simulation primarily to account for potentially higher storm surges in the scenario period. Moreover, a changing sea level influences the speed of barotropic gravity waves like tides and seiches (Taylor, 1922) and should therefore not be ignored in a hydrodynamic study.

2.6 Baltic Sea Outflow

So far, the model setup consists of the following components: both the atmospheric forcing and the open lateral boundary conditions are bias corrected relative to reanalysis and climatology data, respectively. Climatological fresh water supply from 46 North Sea rivers is incorporated. The semi-diurnal lunar tide is imposed at the open lateral boundaries as well as an estimation for the global mean sea level change. A test run under these conditions was performed. Considering mean volume transports in the eastern boundary region, measurements at the Danish passages as given in Damm (1997) indicate monthly net Baltic outflow into the North Sea throughout the year with an annual mean of about 14900 m^3/s. In treating the eastern lateral boundary as an open boundary, unfortunately, it cannot do justice to the upsurge capacity of the semi-enclosed marginal Baltic Sea. Respective transport analysis of the test run thus revealed monthly net North Sea outflow into the Baltic for the whole summer season, yielding an annual mean Baltic discharge of just 1800 m^3/s (see Fig. 2.36). In reality, however, the Baltic conveys a substantial amount of fresh water into the North Sea, more than the total North Sea riverine discharge, and hence, it constitutes an important fresh water source for the Skagerrak/Kattegat region and the Norwegian Coastal Current.

In order to circumvent the deficiencies of the open eastern boundary and in turn, to warrant the appropriate magnitude and seasonality of Baltic outflow, the eastern boundary was taken as a closed lateral boundary with an additional volume flux across this boundary, which is normally used for grid cells representing river input. For determining the volume flux, coastal fresh water runoff taken from the hydrological model mentioned in section 2.3 is used to calculate monthly discharge of the entire Baltic catchment area for the control and scenario period. The obtained time series are then adapted to the aforementioned annual mean by subtracting a constant offset deduced from the period 1951-1960, while both the seasonality and the monthly variability are well represented. The maximum discharge now occurs in April in accordance to the snow melting in spring (see Fig. 2.36). The time series shown in Fig. 2.37 indicates a slight increase of Baltic discharge for the 21st century of about +780 m^3/s. The narrow gray area about the regression line repre-

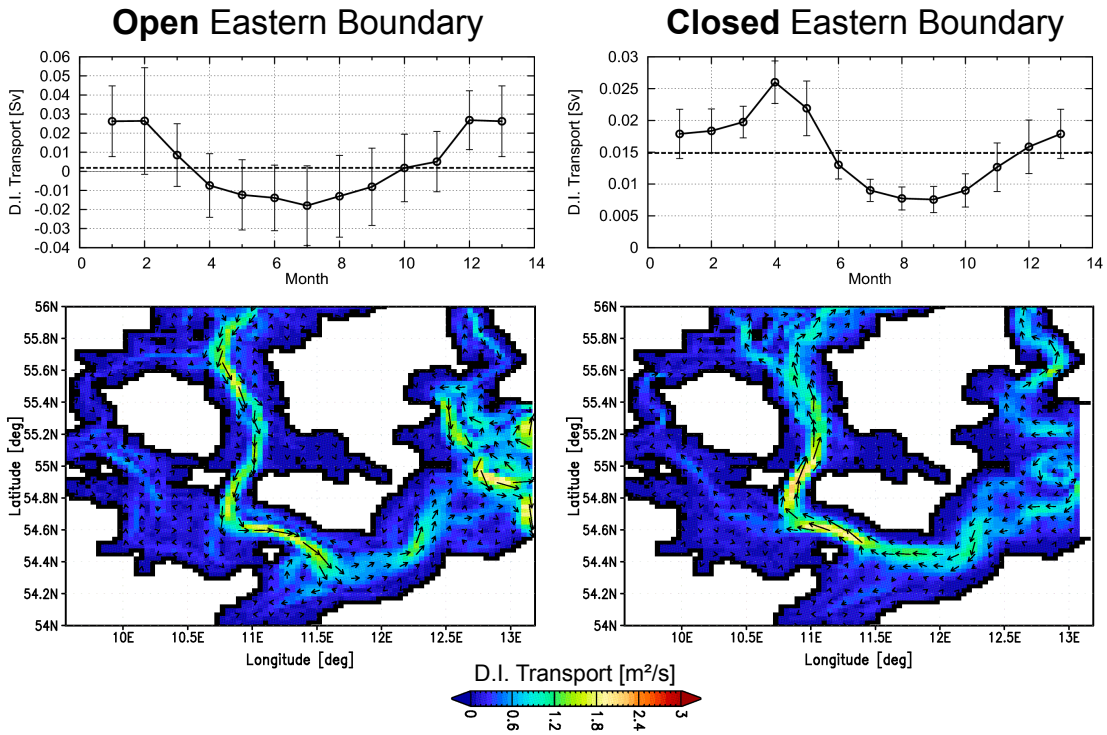

Figure 2.36: Depth-integrated volume transports of open (left part) and closed (right part) eastern boundary. Upper part: Monthly mean transports of 1951-1960 with standard deviation (error bars) and annual mean (dashed line). Lower part: Monthly mean transports at the eastern boundary region for April 1951-1960.

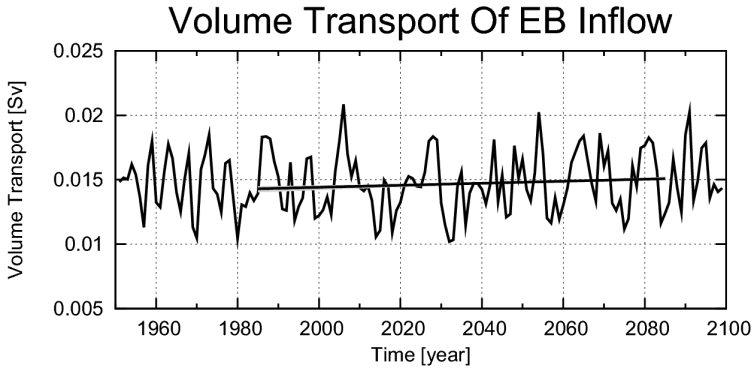

Figure 2.37: Annual mean Baltic discharge and 100-year linear trend. The narrow gray area about the regression line represents the statistical range of the trend. For a more detailed description see section 4.1.

sents the statistical range of the given linear trend, to be explained in more detail in section 4.1. The Baltic discharge is released into the model domain along a set of grid cells located at the closed eastern boundary at which the respective volume transports are prescribed. As illustrated in Fig. 2.36, this measure reverses the spurious southward flow through the Danish passages into a northward flow.

As originating from precipitation and snow melting, the Baltic discharge ought to be released as pure fresh water. The natural water exchange dynamics between the Baltic and North Sea and associated mixing dynamics of fresh Baltic runoff with salty North Sea water, however, cannot be simulated adequately by the confined eastern boundary region,

initiating the mixing with salty waters not until the fresh waters enter the Kattegat. The Baltic discharge in the model is therefore described using monthly climatological salinities of WOA-01.

2.7 SSH Modification at the Northern Boundaries

As mentioned in the introduction (section 1.2.4), the general circulation in the North Sea is driven by tidal currents, surface wind stress, baroclinic density gradients, and barotropic pressure gradients. The resulting geostrophically balanced cyclonic circulation is also reflected by respective sea surface gradients along the open boundaries, which account for the barotropic component of the resulting net currents. The shape of the sea surface elevation at the open boundaries thus determines both the magnitude and direction of the currents entering or leaving the domain and hence, it exerts great influence on the magnitude and structure of the general circulation pattern. In particular, the sea surface gradients along the northern boundaries (i.e. the northern and the western boundary) constitute a decisive regulatory parameter.

The comparison of volume transports through various sections with observations and other model results shows that the general circulation is by far too weak when using above-mentioned boundary and forcing data. But also its structure lacks of the distinct northern inflow at the western edge of the Norwegian Trench as well as of the cyclonic gyre in the Skagerrak (Rodhe, 1996; Svendsen et al., 1996). The main reason for these discrepancies can be attributed to the coarse horizontal grid resolution of the relevant MPIOM version that cannot properly resolve the specific SSH shape across the Norwegian Trench. An other reason is that the MPIOM was run without tides. Though tidal oscillations are largely canceled out on monthly scales, non-linear interactions of tidal currents with wind- and density-driven currents still give rise to significant sea surface elevations (Backhaus et al., 1986). The differences of two MPIOM runs with and without tidal oscillations incorporated are shown in Fig. 2.38 by courtesy of B. Klein (Bundesamt für Seeschifffahrt und Hydrographie, Hamburg). Even on an annual scale, the SSH gradients along the northern (~60°N) and western (~4°W) HAMSOM boundaries are more pronounced in the tidal run and the spatial structure is generally more detailed.

In Sündermann et al. (1996) a 50-year hindcast run including tides was realized with the large-scale Northwest European Continental Shelf Sea model (NECS) forced with NCEP/NCAR reanalysis data. The NECS domain spreads meridionally about 47°N-64°N and zonally about 16°W-14°E and thus, comprises the entire HAMSOM domain of the North Sea. The comparison of climatological means between the NECS run and the MPIOM run further highlights the substantial differences of SSH in the vicinity of the northern HAMSOM boundaries. However, the deviations are small at the very north-western edge of the HAMSOM domain, located in deep waters off the Continental slope and at distance from coasts where the global MPIOM is indeed expected to yield reliable results.

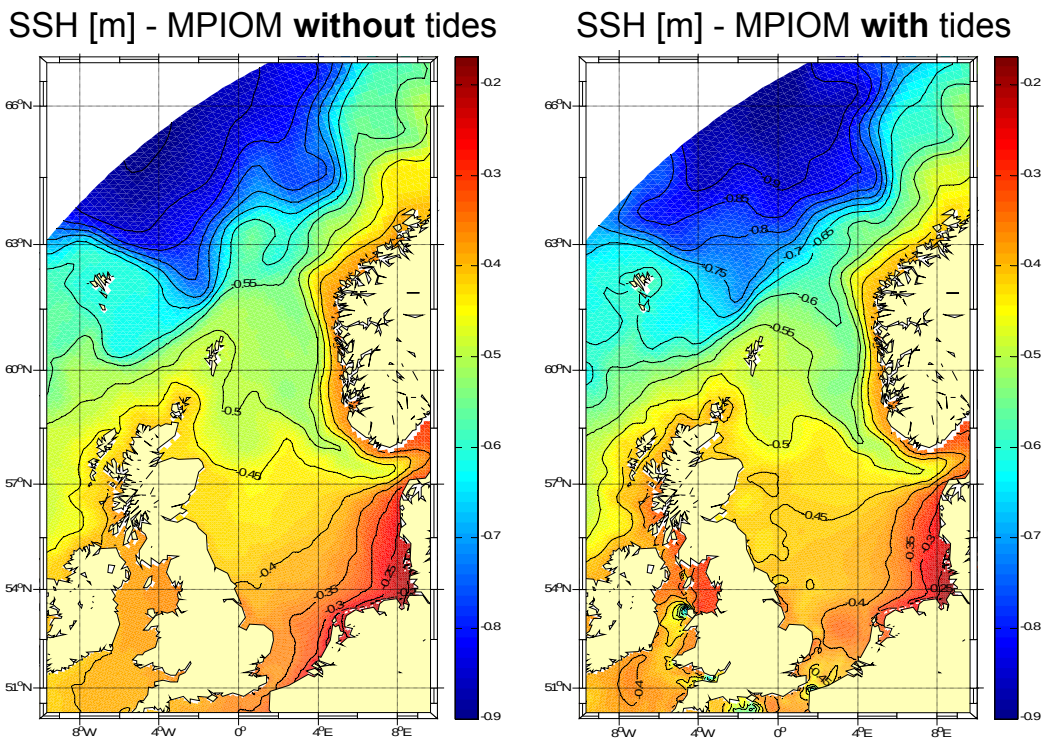

Figure 2.38: Annual mean SSH of 2007 from MPIOM forced with NCEP/NCAR. Left: MPIOM run without tides. Right: MPIOM run with tides. (By courtesy of B. Klein, Bundesamt für Seeschifffahrt und Hydrographie, Hamburg)

In order to provide for appropriate SSH boundary conditions and by that, to allow for the HAMSOM model to spin up the characteristic cyclonic general circulation in the North Sea, the SSH extracted from MPIOM is modified at the northern and western boundaries by incorporating monthly climatological SSH extracted from NECS. Thereby, the level of the climatological SSH is determined by the MPIOM SSH of the outermost north-western HAMSOM grid cell, while the shape of SSH along the northern and western boundaries is continuously adapted to the NECS model. The overall SSH level and its temporal variability are thus retained from the MPIOM time series. In Fig. 2.39 SSH and current speeds at the northern boundary are exemplified from HAMSOM runs with MPIOM SSH and NECS SSH. In both models the shape of the depicted SSH is widely persistent throughout the year, whereas its level and local gradients are subject to seasonality. Note that the two SSH curves match at the western end of the boundary, as intended. The NECS SSH, however, is characterized by distinctly stronger gradients, inducing a strong inflow at the edge of the Norwegian Trench and a narrower, though enhanced outflowing Norwegian Coastal Current. The annual mean inflow to the east of the Shetland Islands and the Norwegian outflow are thus significantly amplified (see Fig. 2.39). It becomes clear now that the variability of the MPIOM SSH at other locations than the western end of the boundary is not projected onto the NECS SSH, since the spatial structure of the circulation and hence, the horizontal SSH gradients of the two models are qualitatively so different. Adopting the local variabilities anyhow would impose SSH dynamics of an inappropriate current regime onto the SSH of the new NECS regime. Nevertheless, by keeping the shape of the monthly climatological NECS SSHs, the HAMSOM scenario run is deprived of a degree of freedom. However, the variability of the general circulation is still subject to the variability of surface

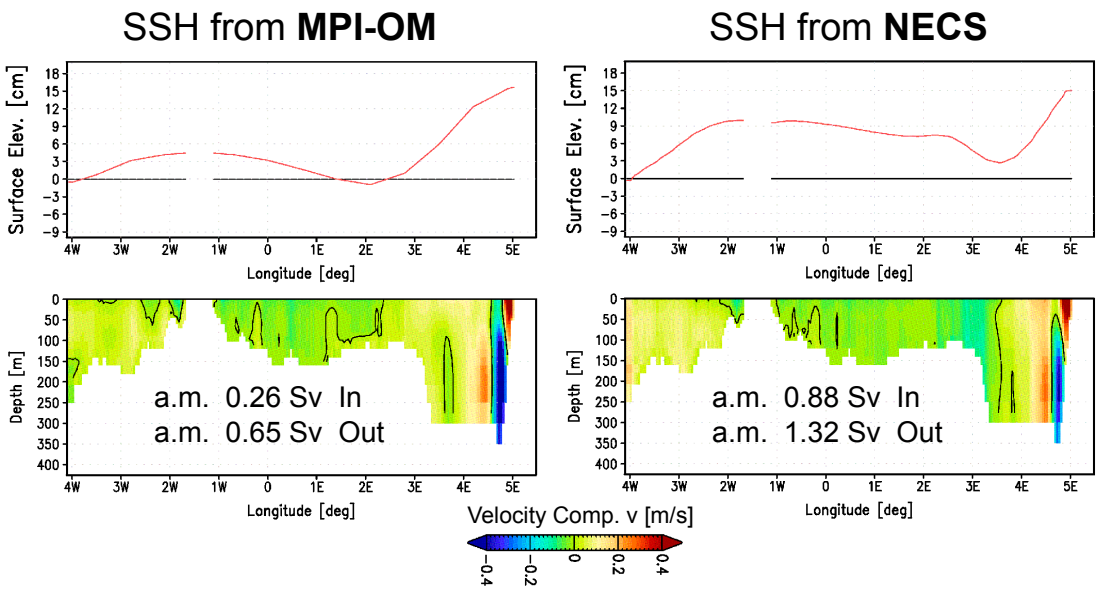

Figure 2.39: Vertical Section at the northern boundary from HAMSOM runs with MPIOM SSH (left part) and NECS SSH (right part) for November 1951-1960. Upper part: SSH. Lower part: Meridional velocity component; + northward, - southward. Annual mean volume transports for 1951-1960 are given for the inflow to the east of the Shetland Islands (a.m. In) and the Norwegian outflow (a.m. Out).

wind stress, baroclinic density gradients, and barotropic pressure gradients in the interior of the domain. Be aware that no variability of the simulated general circulation arise from tides, since the only incorporated tidal constituent is M_2 (see section 2.4). Anyway, on climatological scales, other partial tides are irrelevant for the variability of the general circulation. Besides, further analysis indicate that the mean MPIOM SSH gradients at the northern HAMSOM boundaries do not undergo a significant change in the scenario period. The replacement with climatological SSH gradients does therefore not contradict any long-term SSH trend of the original MPIOM scenario run.

Further sensitivity studies affirm the Fair Isle Current entering the North Sea via the western boundary to be a decisive driver for the cyclonic sense of the Skagerrak recirculation. In regulating the strength of the Dooley Current, it is important to redirect northerly inflowing water masses south-eastwards alongside the Norwegian Trench. The south-eastward flow, in turn, feeds the northward flowing Jutland Current and finally guides it eastward into the Skagerrak. By that, the south-eastward flow along the Norwegian Trench distinctly contributes to the cyclonic sense of the Skagerrak recirculation. If the Dooley Current is too weak, on the contrary, the northerly inflow just spreads diffusely over the northern North Sea and consequently, the south-eastward flow along the Norwegian Trench is substantially attenuated. Most of the Jutland Current then directly joins the Norwegian Coastal Current without entering the Skagerrak, giving rise to a persistent anticyclonic recirculation in the Skagerrak. In the NECS model, unfortunately, the salinity to the north of Scotland is significantly overestimated owing to insufficient river runoff. The resulting underestimated halo-steric expansion of the water column thus causes the SSH gradient at the western boundary of the HAMSOM domain to be underestimated, too. However, via geostrophic adjustment, the latter is proportional to the strength of the Fair Isle

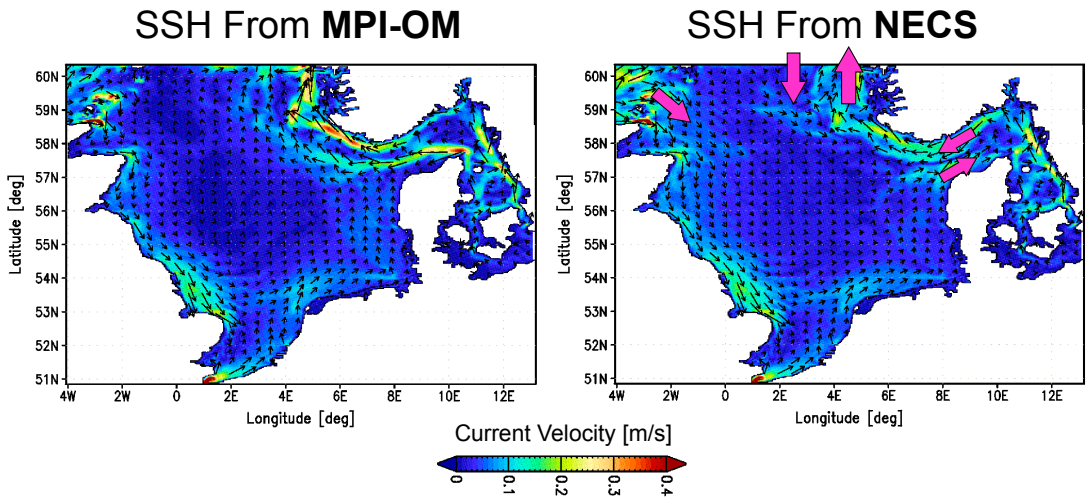

Figure 2.40: Mean surface current velocities of HAMSOM runs with MPIOM SSH (left) and NECS SSH including the rise of the western boundary slope (right) for April 1951-1960.

Current. The underestimated SSH gradient at the western boundary therefore provokes an inadequate recirculation in the Skagerrak.

As a final modification, the SSH gradients along the western boundary are empirically doubled in order to provide cyclonic recirculation in the Skagerrak by enhancing the Fair Isle and Dooley Current. The doubling of the gradients entails an increase of SSH that approximately corresponds to halo-steric expansion induced by a salinity drop of about -0.7 psu in the western boundary region, as being the magnitude of the salinity overestimation in the NECS model, approximately. Surface current velocities of HAMSOM runs with MPIOM SSH and NECS SSH including the additional rise of the western boundary slope are exemplified in Fig. 2.40. The simulated general circulation in the North Sea now renders all important structural features and the volume transports lastly reach similar values given in ICES (1983), Eisma and Kalf (1987), Smith et al. (1996), Svendsen et al. (1996), Lenhart and Pohlmann (1997), OSPAR (2000), and Hjøllo et al. (2009). Transport magnitudes and various cross-correlations are discussed in chapter 3.

Chapter 3

Model Evaluation

The final model setup is evolved from the modifications described in the previous sections, consisting of the following components. Both the atmospheric forcing and the open lateral boundary conditions are bias corrected relative to reanalysis and climatology data, respectively. Climatological fresh water supply from 46 North Sea rivers is incorporated. The semi-diurnal lunar tide is imposed at the open lateral boundaries as well as an estimation for the global mean sea level change. The eastern boundary is treated as a multiple river input at which Baltic discharge into the North Sea is prescribed. The sea surface height (SSH) gradients along the northern and western open boundaries are used as climatological corrections on a monthly scale. This setup was finally used to perform the dynamical downscaling run for the North Sea for the control period 1951-2000 and with this, to evaluate the model results.

As mentioned in the introduction, the physical state of the North Sea is highly influenced by the conditions of the atmosphere. To assure that the bias correction of the atmospheric forcing does not lead to unreasonable hydrographic and hydrodynamic conditions in the North Sea, e.g. owing to neglected non-linearities or induced accumulation effects, HAMSOM was run with direct ERA40 forcing, too, with otherwise identical model setup. Sea surface temperature (SST) and salinity (SSS) of the two runs are compared in Fig. 3.1 and 3.2 for February and August 1958-2000, respectively, where the term REMOcorr refers to the bias corrected REMO forcing. Meaningful parameters of the thermocline concerning duration, depth, and intensity are given in Tab. 3.1. Temperature and salinity isolines are very similar as are the thermocline parameters, widely ruling out the introduction of unreasonable physical effects by virtue of the bias correction.

Annual mean volume transports through various transverse sections (Fig. 3.3) and corresponding standard deviations are given in Fig. 3.4. While the transports well agree in the central and southern North Sea, the transports from the REMOcorr driven run are about 10% weaker in the northern North Sea than from the ERA40 driven run, which can be attributed to the deviating wind conditions shown in Fig. 2.29. To be well confirmed by EOF analysis in section 4.2.1, westerly winds over the North Sea enhance the general cyclonic circulation, while easterly winds weaken or occasionally even reverse it. The strongest impact thereby occurs on northerly inflows and on the circulation along the Norwegian Trench, entailing the pronounced south-easterly component of the REMO wind fields to weaken the respective mean volume transports. Nevertheless, the resulting net transports are still within the range given in ICES (1983), Eisma and Kalf (1987), Smith et al. (1996), Svendsen et al. (1996), Lenhart and Pohlmann (1997), OSPAR (2000), and Hjøllo et al. (2009), as obtained from both model results and observations (see Tab. 3.3). Moreover, the northern inflow/outflow dynamics as well as the recirculation in the Skagerrak are highly cross-correlated throughout the year, whereas the southern and eastern inflows widely obey independent dynamics, as also confirmed by Hjøllo et al. (2009). Transport variabilities of the REMOcorr and ERA40 runs, given as standard deviations in Fig. 3.4, well agree for all locations.

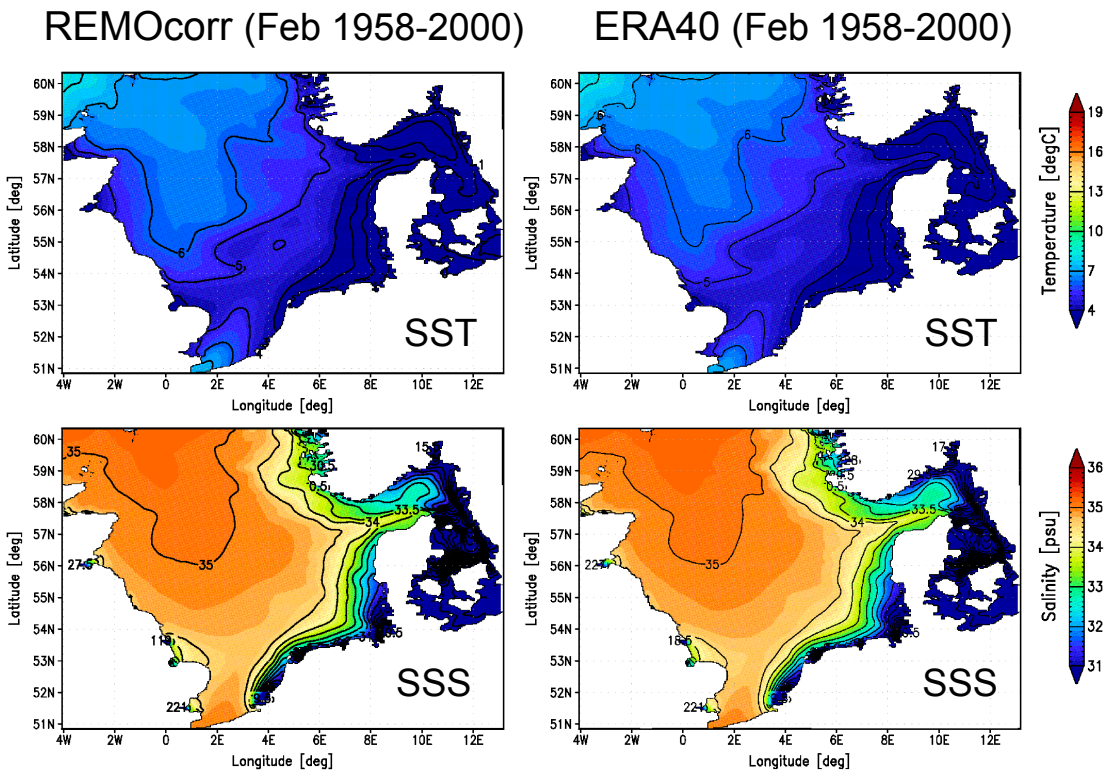

Figure 3.1: Monthly mean SST (upper part) and SSS (lower part) of February 1958-2000 from HAMSOM runs driven with bias corrected REMO data (left part) and ERA40 data (right part).

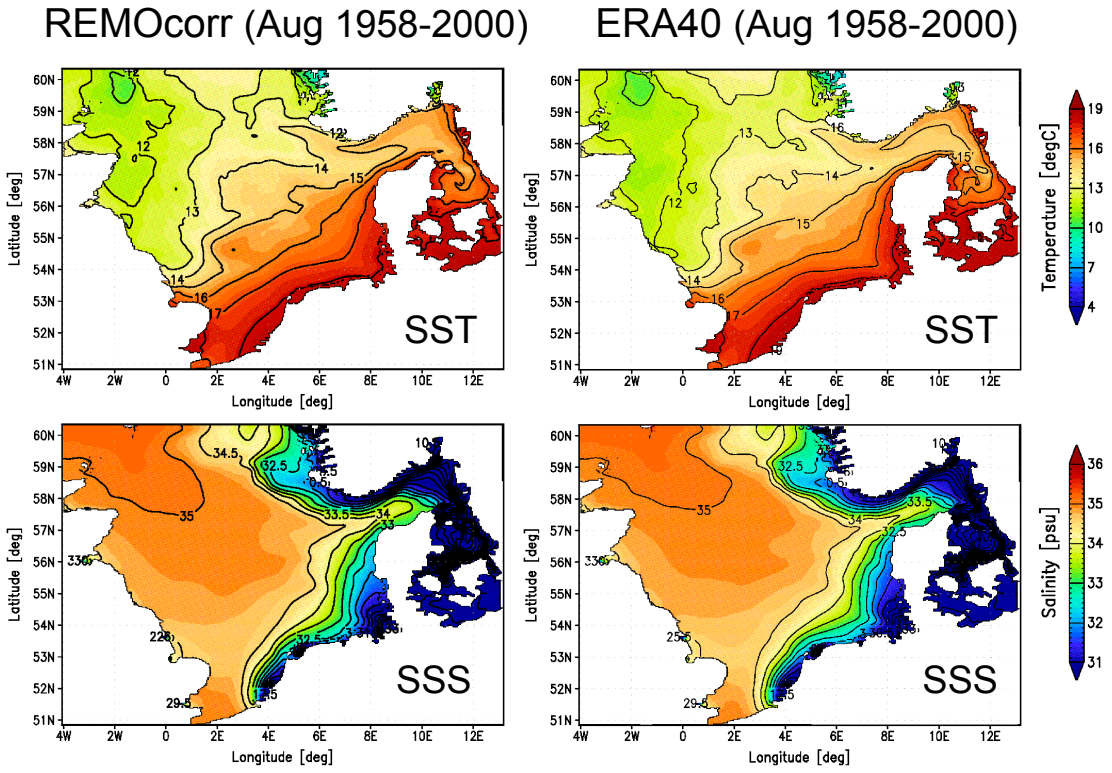

Figure 3.2: Analogous to Fig. 3.1 for August 1958-2000.

Some other basic analysis of the actual control run (i.e. driven with the corrected REMO data instead of ERA40) are carried out in order to further evaluate the final model setup. Intimately linked to the general circulation are associated residence and flushing times.

Parameter	REMOcorr	ERA40
Mean Start Day [JD]	122	120
Mean End Day [JD]	269	271
Mean Depth [m]	16	16
Max Depth [m]	35	36
Mean Intensity [°C/m]	0.19	0.20
Max Intensity [°C/m]	0.31	0.35
Mean Days of Int $>$ 0.2 °C/m	63	62
Annual Mean SST [°C]	9.3	9.2
Annual Mean Vol-Avr T [°C]	8.0	8.0

Table 3.1: Mean thermocline parameters for 1958-2000 from HAMSOM runs driven with bias corrected REMO data (left column) and ERA40 data (right column).

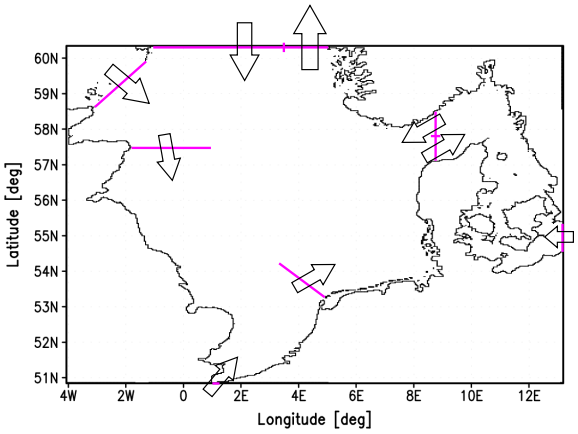

Figure 3.3: Transverse sections and main flow directions used for calculating net volume transports.

The residence time refers to the time that a water parcel stays in a certain region. Respective residence times until a parcel passes the entire North Sea region can be estimated from integrating depth-averaged current speeds along individual stream lines, where the latter are calculated from depth-integrated volume transports. As shown in Fig. 3.5, resulting mean residence times range from 0.5-1 year in the northern North Sea to 3-4 years for water masses entering the domain via the Fair Isle Passage in the north-west but passing through the southern North Sea. Similar residence times from model studies are given by Maier-Reimer (1979), Prandle (1984), and Blaas et al. (2001). The flushing time refers to the time needed for the total inflowing volume transport into a certain domain to add up to the volume of that domain. According to the model results, the mean flushing time of the North Sea amounts to 1.13 years, where a similar value can be inferred from model studies given by Lenhart and Pohlmann (1997).

As known from several observation and model studies (e.g. Hurrell, 1995; Becker and Pauly, 1996; Visbeck et al., 1998), the North Atlantic Oscillation (NAO) has a strong influence on European weather conditions in the winter season and hence, on the atmospheric forcing of the North Sea. Its phase is indicated by the NAO index. Positive phases are associated with stormy and wet winters in the North Sea region that are accompanied by high precipitation rates but mild temperatures. Negative phases, on the contrary, are associated with dry and cold winters. Time series of various atmosphere and ocean parameters

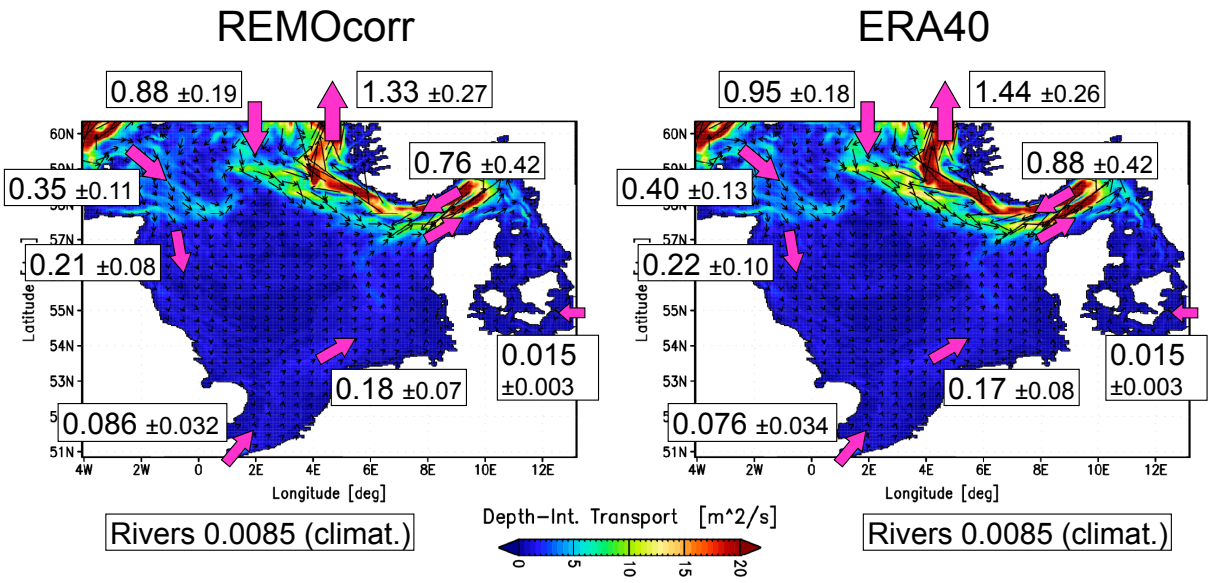

Figure 3.4: Annual mean volume transports [Sv] and standard deviations of 1958-2000 for various locations. Left: HAMSOM driven with bias corrected REMO data. Right: HAMSOM driven with ERA40 reanalysis data.

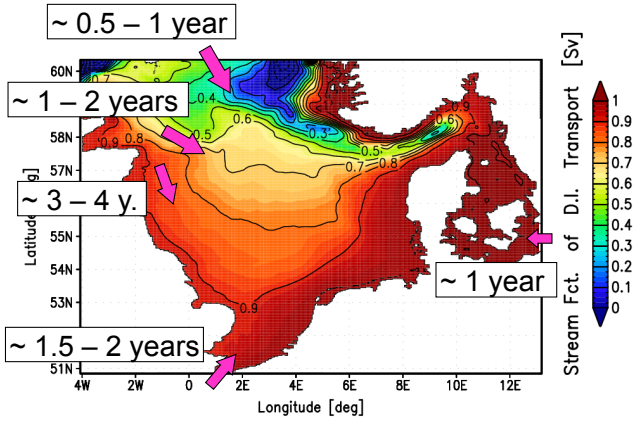

Figure 3.5: Stream function of depth-integrated annual mean volume transports of 1951-2000 and associated North Sea residence times.

accordingly reflect the NAO influence via respective correlations with the NAO index. From the global model run ECHAM5/MPIOM, the NAO winter index is calculated relative to the mean sea level pressure difference between Iceland and the Azores (Rogers, 1984) of DJF 1900-2000 and depicted in Fig. 3.6. NAO variabilities in observations range from interannual scales of 2-5 and 8 years up to multi-decadal scales of about 70 years (Hurrell and van Loon, 1997; Loewe and Koslowski, 1998). On the one hand, such time scales can indeed be found in the frequency analysis of the NAO model index, also shown in Fig. 3.6. On the other hand, the figure does not suggest any typical harmonic oscillation, as supported by Hurrell and Deser (2009) who state that there is little evidence for the NAO to vary on any preferred time scale. Large changes can occur from one winter to the next, as well as from one decade to the next.

Winter NAO model correlations of spatially averaged atmosphere parameters and corresponding confidence levels are given in Tab. 3.2. In accordance to the mentioned phase-

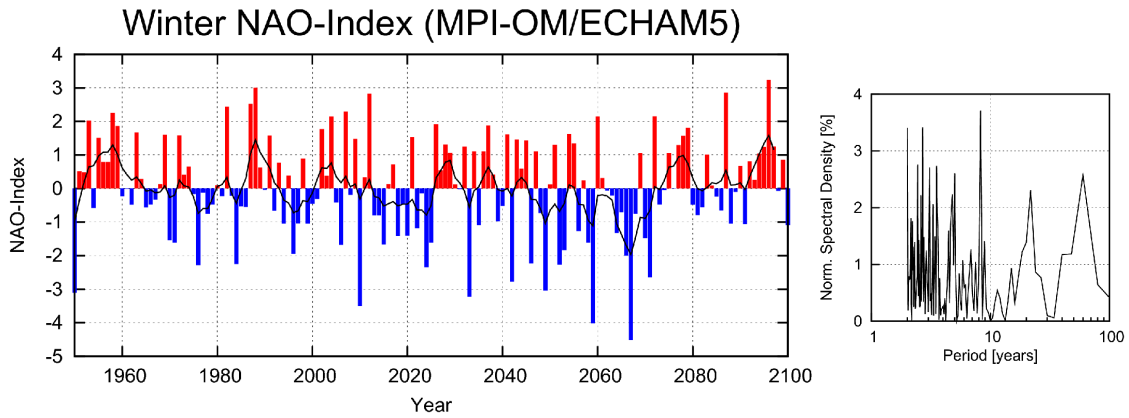

Figure 3.6: Left: NAO index for winter (DJF) as extracted from ECHAM5/MPIOM and 5-year running mean (black line). Right: Corresponding frequency spectrum.

NAO correlations and confidence levels		
Air Temperature	+0.45	99%
Wind Speed	+0.28	95%
Rel. Humidity	+0.30	97%
Precipitation	+0.32	98%

Table 3.2: Winter NAO model correlation coefficients of spatially averaged atmosphere parameters of the North Sea for 1951-2000 and corresponding confidence levels.

associated weather conditions, air temperature, wind speed, relative humidity, and precipitation are positively correlated with the NAO index. In analyzing observational weekly SST charts of the North Sea, Dippner (1997) calculated an NAO correlation with the 1st Principal Component of SST of +0.71 (P=98%), which amounts to +0.30 (P=97%) in the present model results. However, the SST correlation in the model is not supposed to be higher than the NAO correlations of the meteorological forcing. Besides, in being a complex phenomenon sensitive to large-scale ocean-atmosphere interactions, the driving mechanisms of the NAO variability are yet sparsely understood. It is therefore not surprising that the correlations in the model are weaker than in observations. Rather, the correct sign of the correlations as well as their high statistical significance indicate the NAO signal to be well reflected.

Furthermore, a positive NAO correlation holds for the general circulation in the North Sea, as given in e.g. Schrum and Siegismund (2002) and Winther and Johannessen (2006). Derived from the model results, NAO correlations with volume transports at various locations are depicted in Fig. 3.7. The only negative correlation shows up at the northern inflow, possibly related to specific wind conditions, which in turn annihilate the correlation at the Norwegian outflow. Depth-integrated volume transports and associated stream functions are exemplified in Fig. 3.8 for a positive and negative NAO phase. In agreement with findings from Schrum and Siegismund (2002), in positive phases the stream lines are considerably closer in the central and southern North Sea as well as in the Skagerrak, indicating an enhanced circulation.

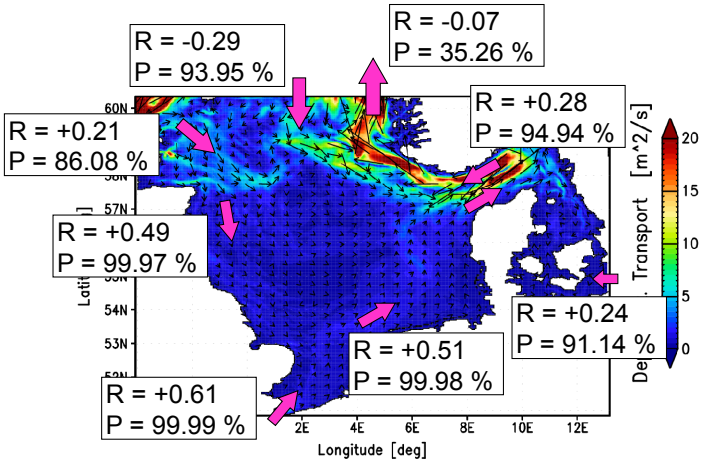

Figure 3.7: NAO correlation coefficients R and confidence levels P of volume transports for 1951-2000 at various locations. Colors and small black arrows indicate annual mean depth-integrated volume transports. Magenta arrows indicate the annual mean flow direction to which the sign of the correlations are related.

The progression of the NAO index in the 21st century may suggest a slight long-term decrease up to the 2060s, followed by a steady increase for the last 30 years. However, be aware that a long-term NAO trend does not reflect long-term trends of the correlated variables. The NAO index is calculated from pressure *differences*, which are independent of the absolute pressure level. As such, it reflects *anomalies* of a mean pressure difference, which do not contain information about any long-term trend of the underlying air pressure time series. It can therefore neither explain the continuous temperature increase in the North Sea due to global warming. What it *does* explain are the pure *anomalies* of the correlated variables, obtained from detrended time series.

Total surface heat flux is understood as the sum of the four components: solar incoming short wave radiation, emitting long wave radiation, sensible heat flux, and latent heat flux, as calculated via bulk formulas from SST and atmospheric state variables (Pohlmann, 2006). The annual cycle of the four components and their total is depicted in Fig. 3.9 as spatially averaged monthly means of 1951-1980. A positive sign reads as heat input into the ocean, and a negative sign as heat loss to the atmosphere. The variables that enter the respective bulk formulas are given next to the diagrams. The stronger net surface heat loss in winter than the net heat uptake in summer reveals the North Sea as a sink of heat for the North Atlantic Ocean, as already found by Becker (1981) and Michaelsen et al. (1998). Though being sensitive to the magnitude of the single heat flux components, the model results sum up to an annual mean surface heat loss of -13.6 W/m². Integrated over the North Sea area, this value corresponds to about -8100 GW. The difference of about 293 W/m² total heat flux between its maximum in June and its minimum in December is composed of about 200 W/m² (68%) short wave radiation, 45 W/m² (15%) latent heat flux, 40 W/m² (14%) sensible heat flux, and 8 W/m² (3%) long wave radiation. The variability of the total surface heat flux is smaller in summer than in winter because of the fact that the thermocline inhibits intrusion of surface heat flux variations to deeper layers.

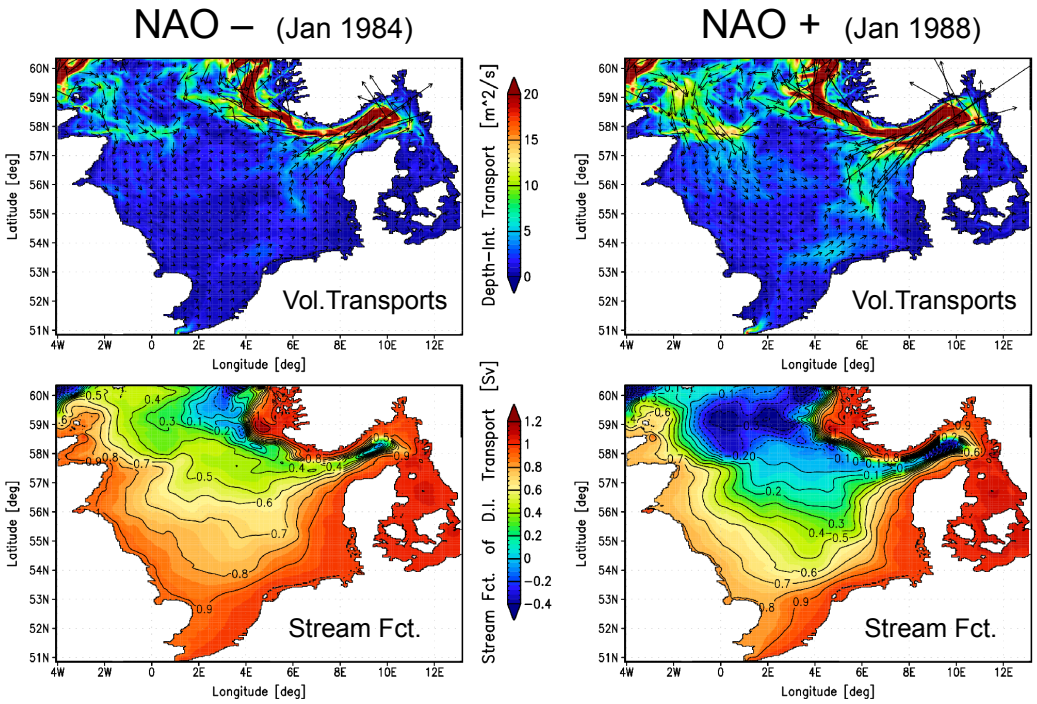

Figure 3.8: Left part: January 1984 as an example of a negative NAO phase (see Fig. 3.6). Right part: January 1988 as an example of a positive NAO phase. Upper part: Depth-integrated volume transports. Lower part: Corresponding stream function.

The spatial distribution of total surface heat flux is shown in Fig. 3.10 as annual and seasonal means of 1951-1980, which qualitatively agree with calculations by Becker (1981) from observational data. While in the southern North Sea the annual mean surface heat flux is largely balanced, it reaches maxima up to -50 W/m² in the northern North Sea because of inflow of warm Atlantic waters in winter, lower solar radiation at higher latitudes, and generally higher cloud cover. The distribution of total surface heat flux in winter is clearly dominated by bathymetry and the related effect of differential heating. In summer, however, the maximum positive surface heat flux off the British coast is induced by a weak latent heat flux due to low wind speeds and comparatively low SST. The highest summer SST, by contrast, occurs in the shallow waters along the Continental coast, where the heat is not mixed into deeper parts of the ocean and with this, the sensible heat flux is almost zero, but the latent heat flux is strong, giving rise to the minimum total surface heat flux in this region.

In Fig. 3.11 relative frequency of occurrence, depth, and intensity of the thermocline are shown to demonstrate various spatio-temporal characteristics of the temperature-induced stratification in spring and summer. As suggested by Pohlmann (1996c, 2006) and Meyer et al. (2011), the threshold of the climatological mean vertical temperature gradient for identifying the thermocline is set to 0.1 °C/m. The relative frequency of the thermocline is thus the number of days per month with a maximum vertical temperature gradient exceeding threshold, relative to the total number of days of the considered month. The thermocline depth is defined as the mean depth of the daily maximum vertical temperature gradients, provided they exceed the threshold, and analogously, the intensity is defined as their mean magnitude.

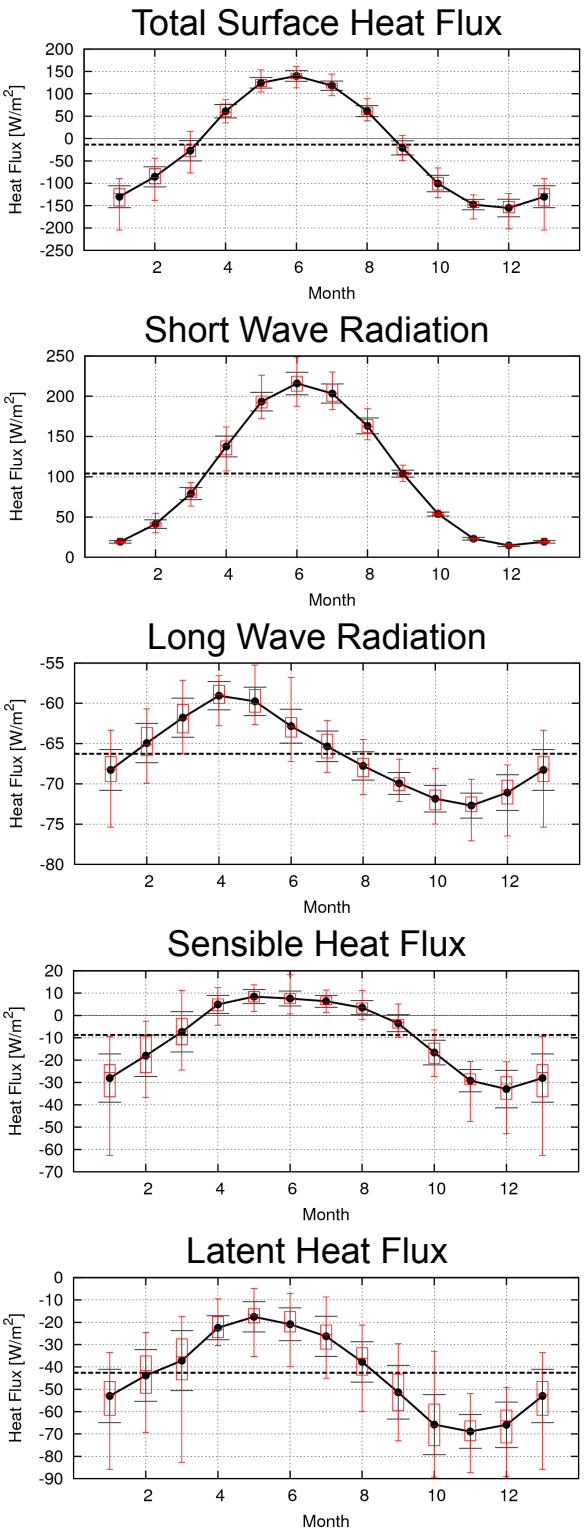

Figure 3.9: Annual cycle of total surface heat flux and its four components, given as spatially averaged monthly means of 1951-1980 (black dots). Annual means are given to the right as well as the variables that enter the bulk formulas. Dashed lines: Annual means. Black error bars: Standard deviation of the underlying time series of monthly means. Red boxes: Lower quartile, median, and upper quartile. Red whiskers: Minimum and maximum.

In the relative frequency plots of Fig. 3.11 the onset of the thermocline in spring, its presence over summer, and its decay in autumn are well reflected. The maximum spatial extension as shown in in the figure is also recognized in the position of fronts drawn

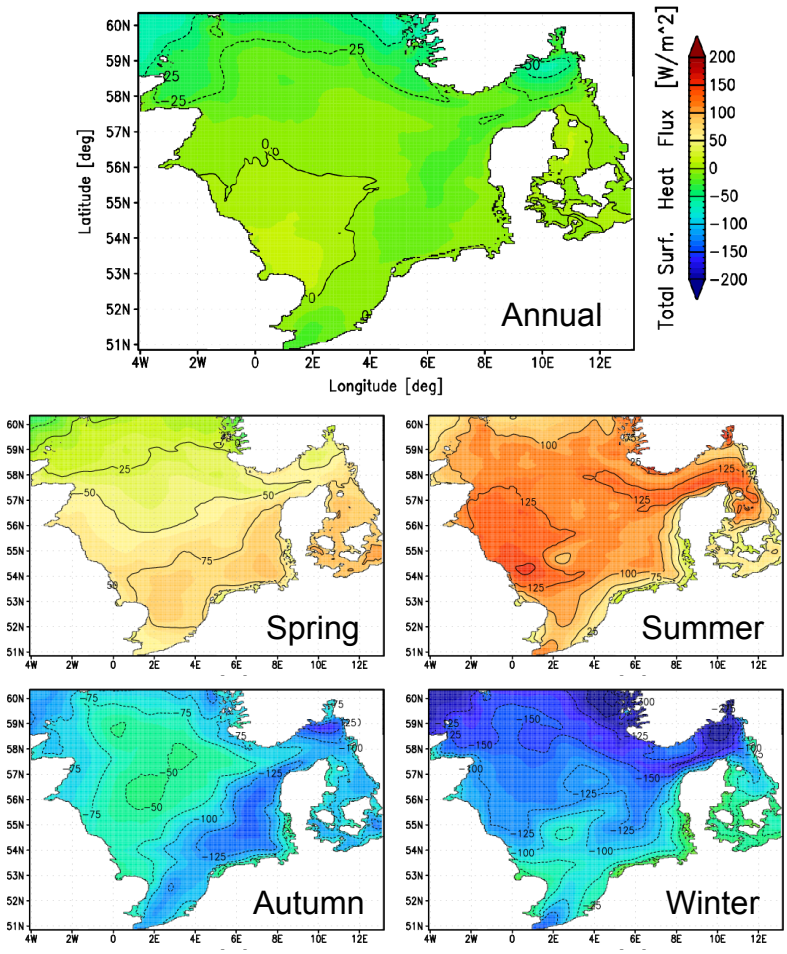

Figure 3.10: Annual and seasonal mean total surface heat flux of 1951-1980. Positive values refer to a heat input into the ocean, negative values refer to a heat loss to the atmosphere. Seasons refer to months MAM for spring, JJA for summer, SON for autumn, and DJF for winter.

from satellite infra-red images presented in Otto et al. (1990) (therein Fig. 3.6). In the north-western North Sea extensive tidal mixing in the Pentland Firth and Fair Isle Passage prevent the development of a stable stratification, whereas the extension in the shallow southern North Sea is restricted by tidal mixing due to the influence of bottom friction (Pohlmann, 1996b). The tidal front thereby roughly follows the 35 m isobath, which can be derived from the critical parameter H/u_t^3, where H represents the water depth and u_t the mean amplitude of the semi-diurnal tidal current (Simpson and Hunter, 1974; Luyten et al., 2003). The depth and intensity plots indicate, respectively, the deepening of the thermocline in autumn from essentially 15-20 m down to about 30-40 m caused by increasing wind speeds, and the strongest vertical temperature gradients to occur around June and July. Be aware that vertical gradients up to 5 °C/m as usually recorded in field studies cannot be properly resolved by a vertical grid resolution of 5 m of the HAMSOM surface layers (Pohlmann, 2006). Nevertheless, strong gradients in the model, indicated by the black isolines in the intensity plots referring to 0.2 °C/m, hold for about 63 days per year on average.

Total surface fresh water flux results from the balance of fresh water input via precipitation from the atmosphere into the ocean and fresh water loss via evaporation at the sea

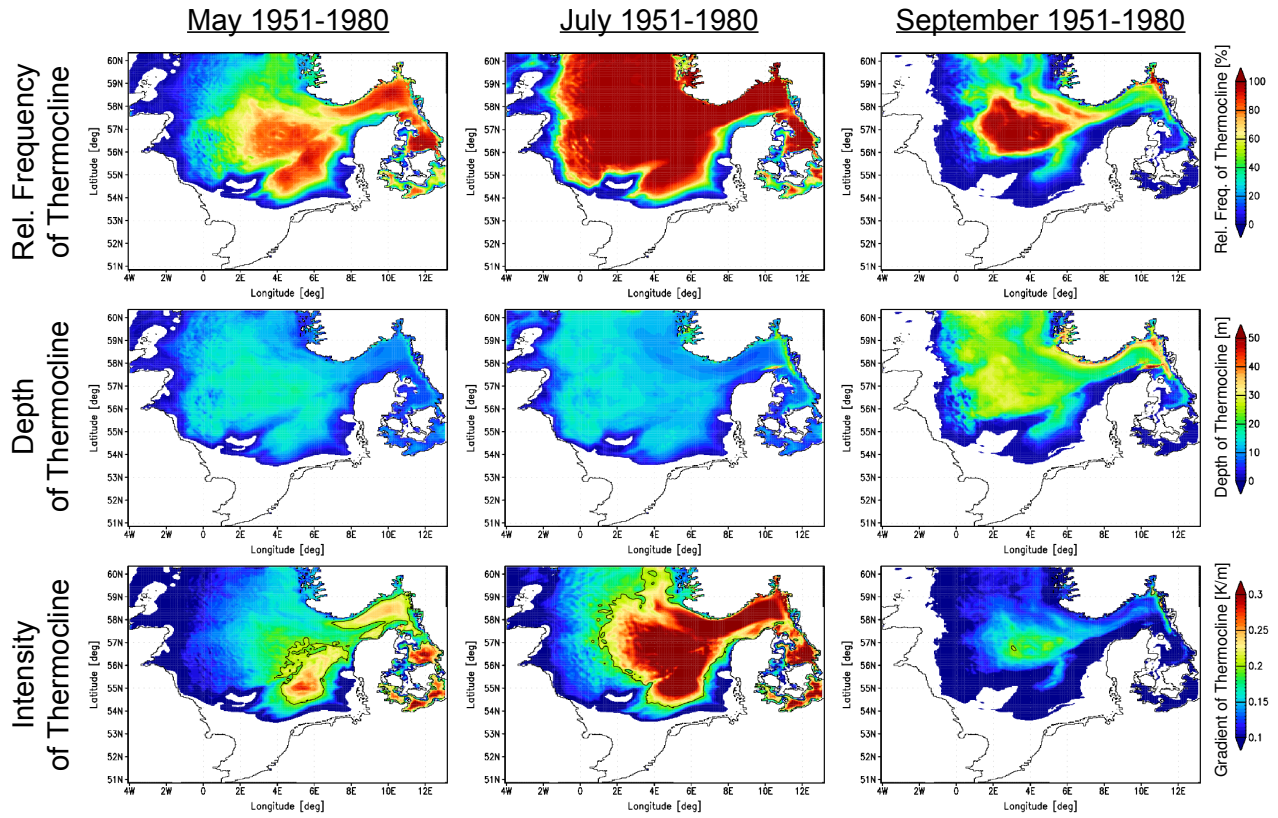

Figure 3.11: Mean relative frequency of occurrence (upper row), depth (middle row) and intensity (lower row) of the thermocline for May, July and September of 1951-1980. Black isolines in the intensity plots refer to 0.2 °C/m.

surface to the atmosphere. Precipitation is thereby composed of large scale and convective precipitation, whereas evaporation is a function of SST, air temperature, wind speed, and relative humidity (Pohlmann, 2006). The annual cycle of spatially averaged total surface fresh water flux in the North Sea as well as its two components extracted from HAMSOM results of the period 1951-1980, are shown in Fig. 3.12. Signs read as positive for fresh water input and negative for fresh water loss. The seasonalities of precipitation and evaporation show qualitatively opposing progressions with minimum precipitation and maximum evaporation in spring and summer, and maximum precipitation and minimum evaporation in autumn and winter. Though subject to strong temporal variability, mean precipitation rates are generally in excess of mean evaporation rates throughout the year, yielding a positive annual mean net surface fresh water flux into the North Sea of about +0.54 mm/d. The corresponding total fresh water input integrated over the North Sea area amounts to about +3800 m^3/s, which agrees well with data provided by the European Center for Medium range Weather Forecast (ECMWF) as given in Damm (1997). The value is of the same order of magnitude as the Continental river runoff and hence, surface fresh water fluxes indeed considerably influence the salinity of the North Sea.

The spatial distribution of total surface fresh water flux is shown in Fig. 3.13 as annual and seasonal means of the period 1951-1980. Off the Norwegian coast, precipitation rates are higher than evaporation rates for all seasons. Even though for the whole North Sea precipitation is lower in summer than in winter, a weak (strong) evaporation in summer

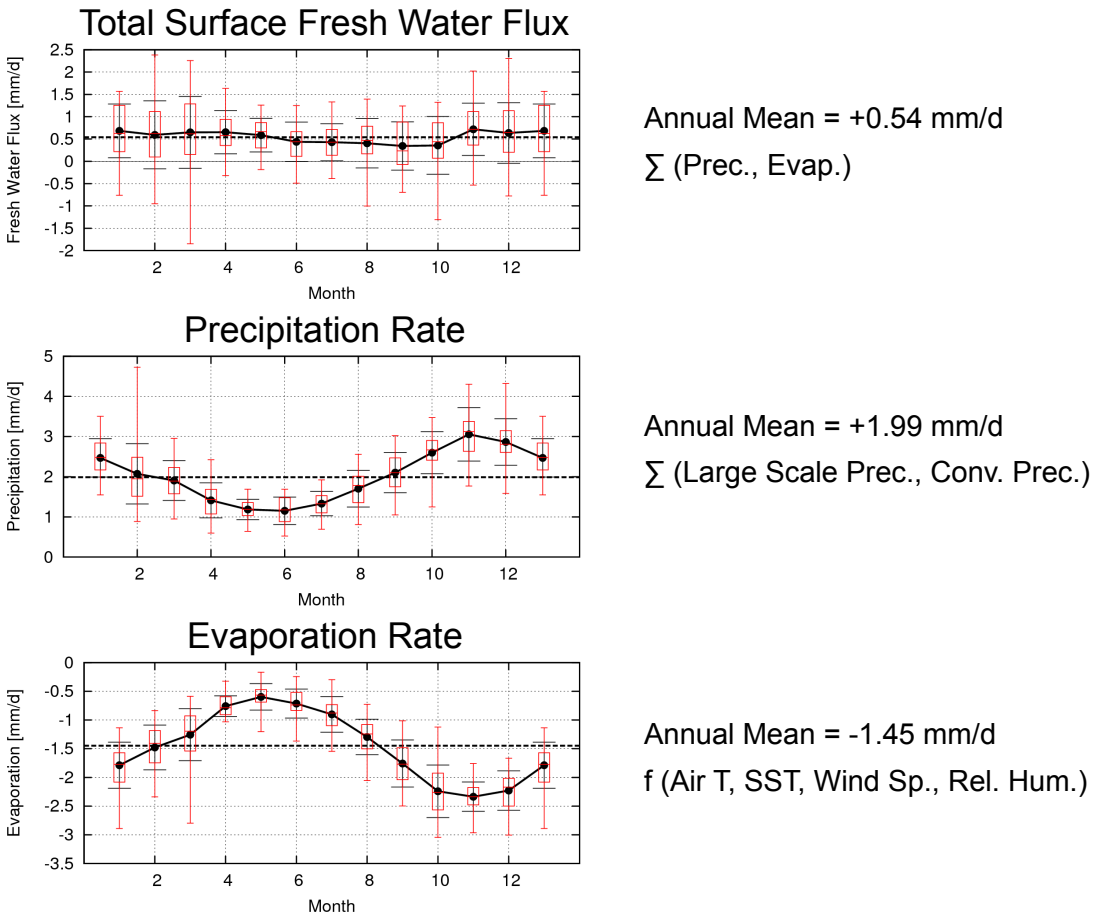

Figure 3.12: Annual cycle of total surface fresh water flux (upper part), as well as its two components precipitation rate (middle part) and evaporation rate (lower part), given as spatially averaged monthly means of 1951-1980 (black dots). Error bars, boxes and whiskers analogously to Fig. 3.9.

(winter) off Norway due to low (high) wind speeds and comparatively cool (warm) SST still gives rise to a persistently positive net surface fresh water flux. Along the Continental coast and in the eastern boundary region, however, in contrast to precipitation, evaporation is high in summer but low in winter because of comparatively low air-sea temperature differences. Mean total fresh water fluxes in the southern and eastern North Sea thus follow a pronounced seasonality, while their annual mean is nevertheless widely balanced.

As the sections thus far are aimed to elaborate a reliable dynamical downscaling of the North Sea, the bare model results from MPIOM and HAMSOM are finally opposed to high resolution climatological data from Janssen et al. (1999) in order to evaluate the model system. The distribution of water temperature and salinity at the sea surface and at the northern boundary are shown in Fig. 3.14 to 3.17, where the maximum and minimum means of the annual cycle are exemplified, respectively. The annual cycles and the variability of their underlying volume-averaged monthly means are depicted as well. The HAMSOM results emphasize the added value of the high horizontal grid resolution of the regional model when comparing with the MPIOM results. The temperature fields and their seasonality widely agree with the climatologies. But also the salinity fields show generally good agreement. The deviation of the annual means of about 0.3 psu (dashed lines) result from water masses of too low salinity in the deep of the Norwegian Trench. Albeit the

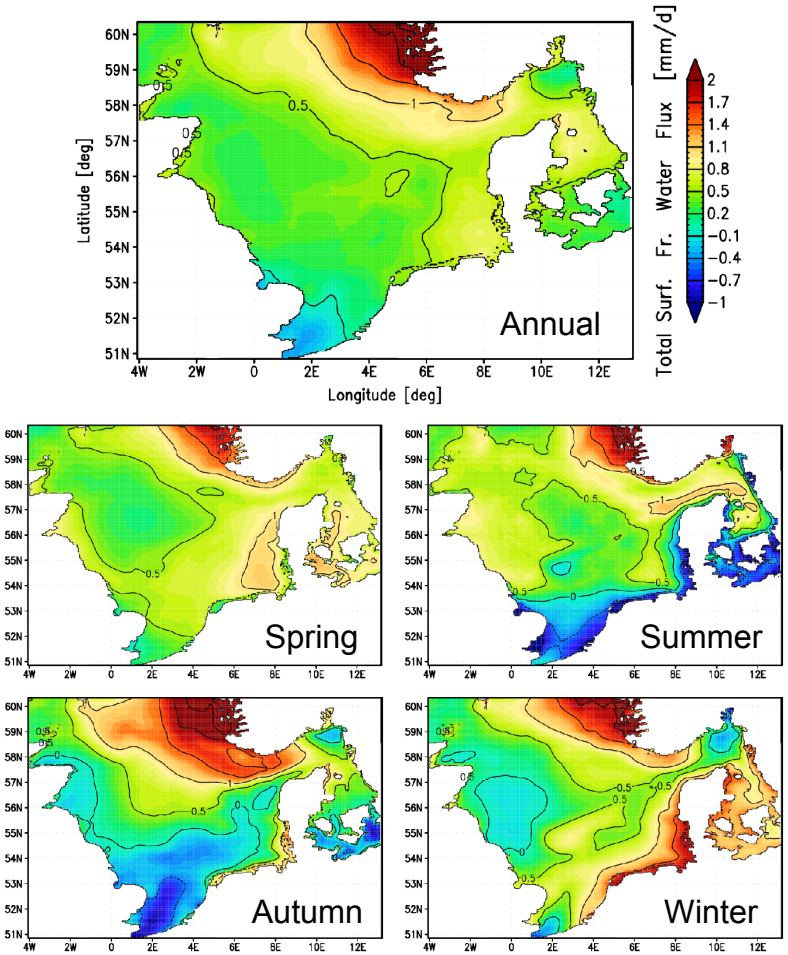

Figure 3.13: Annual and seasonal mean total surface fresh water flux of 1951-1980. Positive values refer to a fresh water input into the ocean, negative values refer to a fresh water loss to the atmosphere. Seasons refer to the same months as in Fig. 3.10.

mathematical treatment of the open lateral boundaries is subject to continuous improvement (e.g. Chen et al., 2012), it is not yet able to initiate a shear flow with inflow conditions in deep layers and outflow conditions at the surface, causing the vertical inflow/outflow structure at the northern boundary across the Norwegian Trench to lack of a faithful representation. Besides, the comparatively high SSS in the Skagerrak arises from suboptimal vertical exchange dynamics in the HAMSOM version of the present study, which have already been improved recently by others. The strongest monthly mean surface flow field, the corresponding meridional velocity component at the northern boundary, and the annual cycle of the total volume transport passing the North Sea are shown in Fig. 3.18. Again, the meso-scale grid resolution of HAMSOM enables a detailed representation of the general circulation. Mean volume transports through various sections are given in Tab. 3.3 and compared with the range from observations and model studies to be found in the literature. The annual mean volume throughput of the North Sea simulated by HAMSOM amounts to about 1.33 Sv. The MPIOM result, by contrast, amounts to just about 0.65 Sv as appearing substantially underestimated.

The regional ocean model HAMSOM driven with boundary conditions derived from the global ocean model MPIOM and atmospheric forcing derived from the regional atmosphere

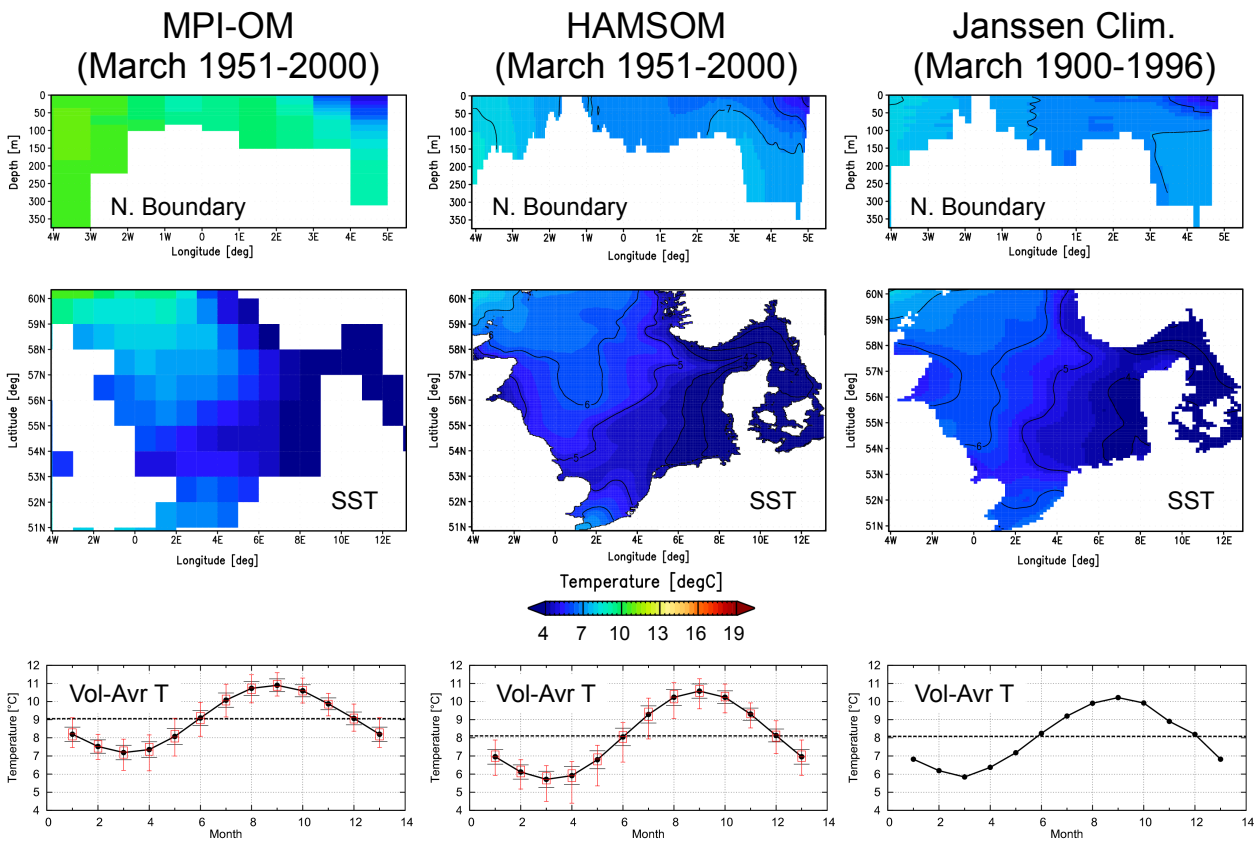

Figure 3.14: Comparison of sea water temperature for March between MPIOM, HAMSOM, and Janssen climatology. Upper part: Vertical section at the northern boundary. Middle part: SST. Lower part: Annual cycle of volume-averaged monthly means. Error bars analogous to Fig. 3.9.

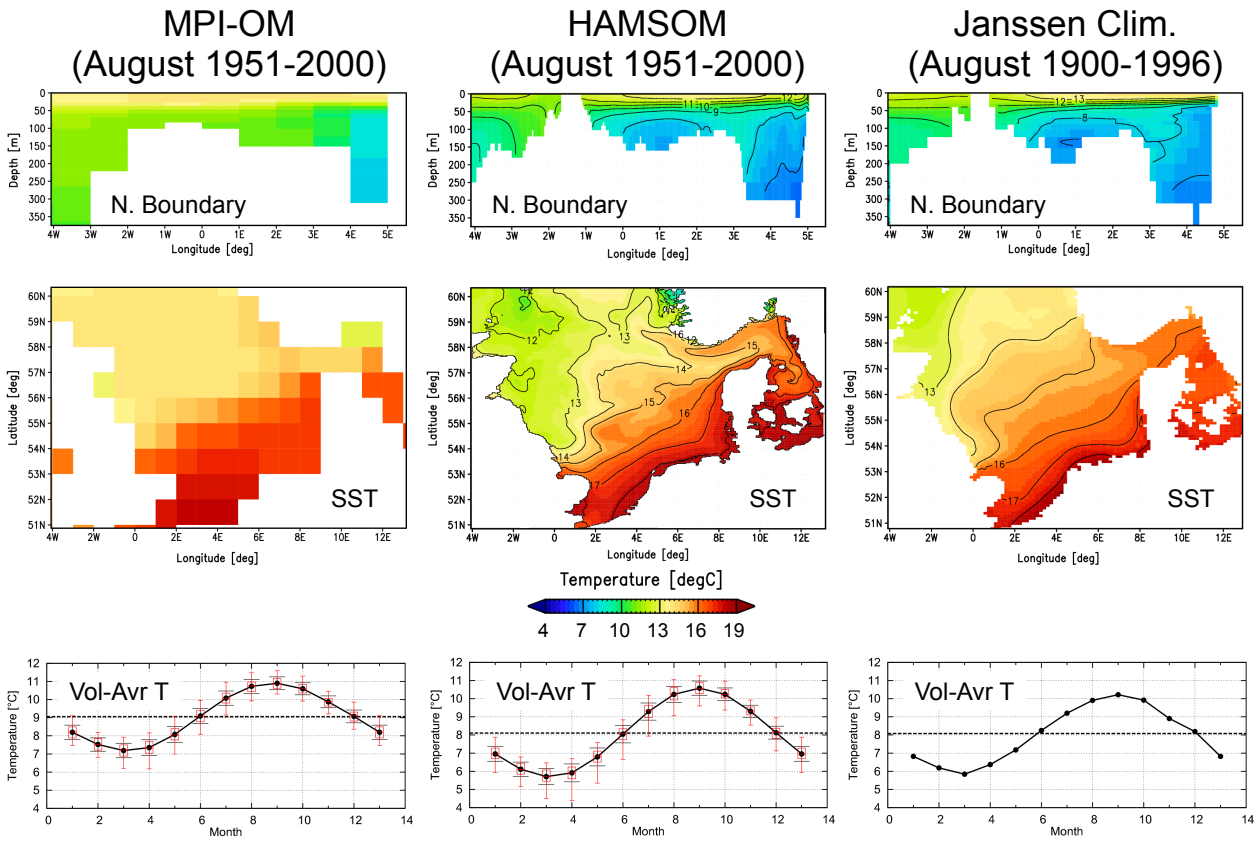

Figure 3.15: Comparison of sea water temperature for August between MPIOM, HAMSOM, and Janssen climatology. Description analogous to Fig. 3.14.

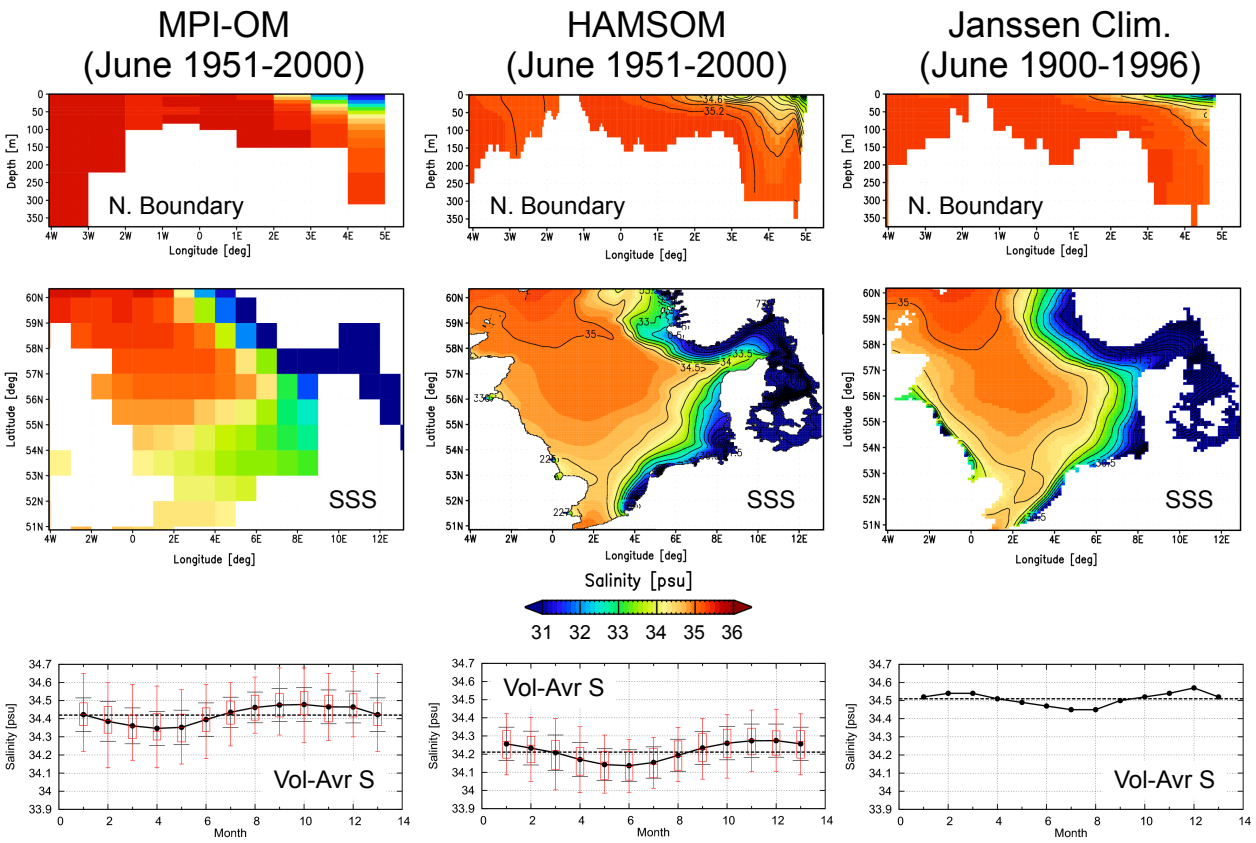

Figure 3.16: Comparison of salinity for June between MPIOM, HAMSOM, and Janssen climatology. Description analogous to Fig. 3.14.

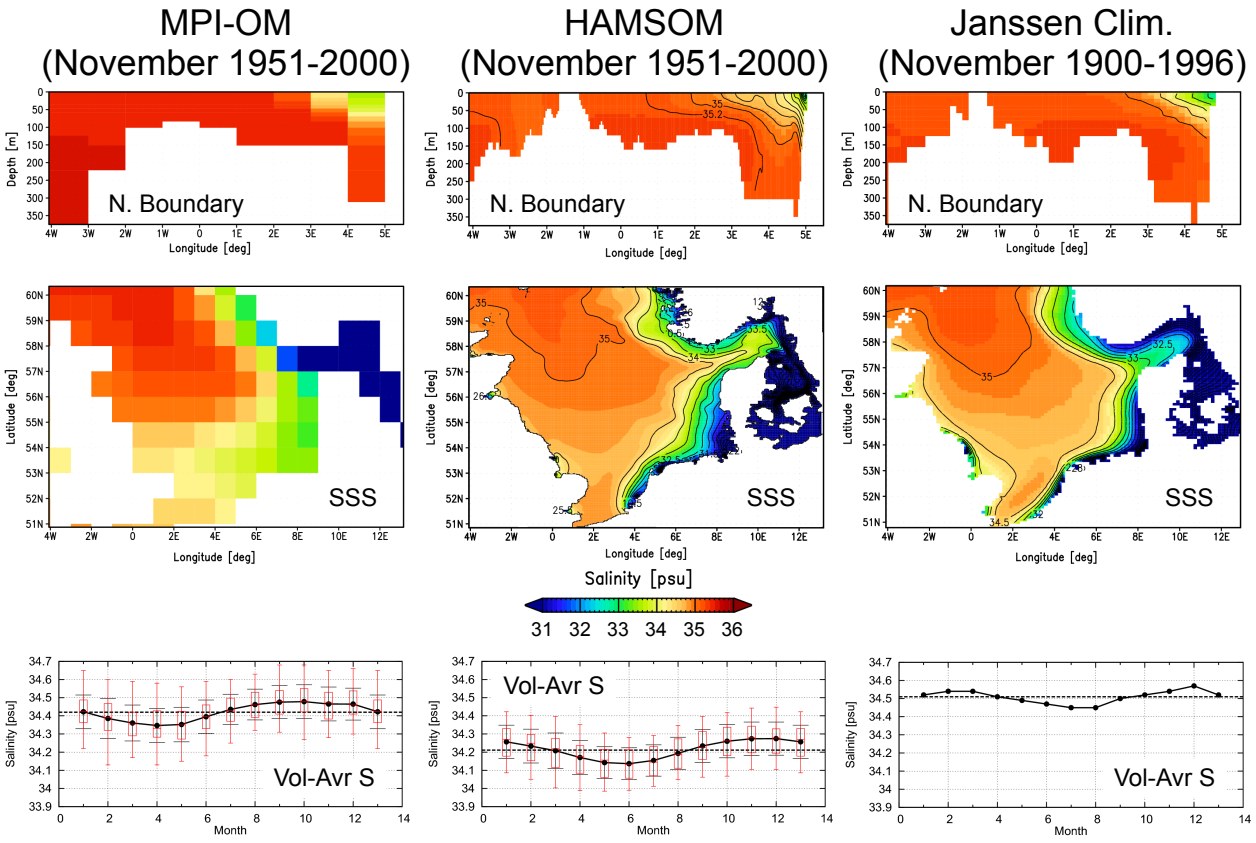

Figure 3.17: Comparison of salinity for November between MPIOM, HAMSOM, and Janssen climatology. Description analogous to Fig. 3.14.

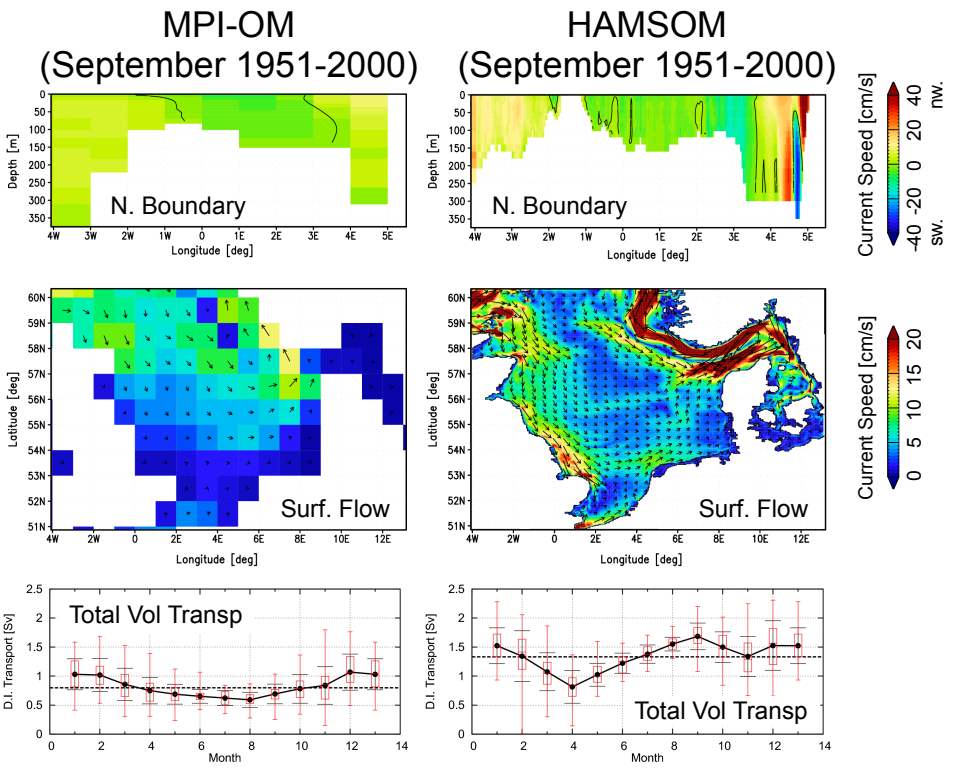

Figure 3.18: Comparison of the general circulation for September between MPIOM, HAMSOM. Upper part: Meridional velocity component at the northern boundary (+ northward, - southward). Middle part: Surface flow field. Lower part: Annual cycle of the total volume transport passing the North Sea and the variability of its underlying monthly means. Error bars analogously to Fig. 3.9.

model REMO shows high level of skills in simulating the current temperature and salinity distribution in the North Sea as well as the characteristic features of the general circulation. The dynamical downscaling gives improvements in the mean ocean climate and its spatial and temporal variability patterns. The application of a bias correction on the forcing data was necessary to reproduce reasonable hydrodynamic conditions in the North Sea with HAMSOM. The straightforwardness of the specific bias correction method especially accounts for maintaining the variability as well as the long-term trends of the original uncorrected data. In its application to scenario studies, information of the correction basis (ERA40 and WOA-01) is thereby projected into the future to the smallest extent, compared to more sophisticated methods. Finally, an ocean model setup intended to regionalize an IPCC scenario run by the incorporation of results from two other numerical models (MPI-OM and REMO) into the HAMSOM model is successfully elaborated.

Mean Volume Transports [Sv]	**HAMSOM**	**Literature (range)**
Northern Boundary Inflow	0.88	0.67 - 1.71
Orkney-Shetland Inflow	0.35	0.30 - 0.70
English Channel Inflow	0.08	0.06 - 0.17
Skagerrak Outflow	0.84	0.50 - 1.50
Baltic Inflow	0.015	0.014 - 0.016
Norwegian Outflow (total)	1.33	1.00 - 2.33

Table 3.3: Volume fluxes in the North Sea from HAMSOM model results and from model results and observations given in ICES (1983), Eisma and Kalf (1987), Smith et al. (1996), Svendsen et al. (1996), Lenhart and Pohlmann (1997), OSPAR (2000), and Hjøllo et al. (2009).

Chapter 4

Model Results and Discussion

4.1 A1B Scenario Run

After the devised model setup is affirmatively evaluated in the previous chapter, the control run of 1951-2000 is now extended with the A1B scenario run up to the year 2099. As explicated in section 1.3, the A1B scenario was chosen for the projected forecast in this study, since taking into account the global carbon dioxide emissions according to all of the individual 40 future scenarios that entered the IPCC ensemble project, the median of global carbon dioxide emission in 2100 as well as the median of the resulting global surface warming are covered by the range of the A1B scenario group. If the IPCC were to construct one scenario to be representative for the entire range of all scenarios, the outcome were thus probably very similar to the A1B marker scenario.

As mentioned in section 1.1, a period of at least 30 years is suggested by the World Meteorological Organization to analyze climate change. Though SST or transport anomalies in the ocean are indeed recognizable on 30-year scales, inquiry of significant climatic change in the world oceans often requires time scales in the order of 10^3 years because of the higher heat capacity and total mass of sea water than of atmospheric air. The North Sea, however, as being a semi-enclosed shallow shelf sea, suffers strong impact of atmospheric forcing, which allows for a hydrographic memory in the water column of just less than one year. The meteorological 30-year reference time frame can thus be adopted for the North Sea without hesitation. To address any climate change signal, in the present study two 30-year periods, 1971-2000 from the end of the control run and 2070-2099 from the end of the scenario run, are used to encompass the 100-year period subject to detailed analysis. It is common practice in climate research to quantify climate change signals from slice mode analysis, i.e. as the difference between the means of such two 30-year time slices. However, in doing so, no information about the significance of the putative change is accessible since the variability of the parameter time series is not taken into account, while misleading conclusions are easily drawn from simply focussing on the largest absolute changes. The most intelligible method to account for statistical significance is linear regression analysis, where the calculated slope of the regression line can be used to quantify the climate change signal as well as to associate a confidence level with the presumed linear trend. Fortunately, the time series of most variables at hand can indeed be well approximated by white noise combined with a linear trend. However, the slope of a regression line is somewhat sensitive to the specific sample values close to the ends of the considered time series. For many variables, therefore, a regression line spanning from say 2001 to 2099 nevertheless does not represent a robust climate change signal for the 21st century. In order to take advantage of both the climatological 30-year time scale and linear regression analysis, the set of 30 100-year regression lines that start at every single year of the period 1971-2000 and consequently end at the corresponding year of 2070-2099 are used for the definition of a robust and meaningful climate change signal. The median slope and the median confidence level of this set are thereby regarded as being representative for the change of the variables in the 21st century, and the upper and lower quartiles are used to estimate the robustness of the deduced trend and significance. The calculation of the representative linear 100-year trend is referred to in this study as *median regression*

analysis. Be aware that mean and standard deviation are inappropriate parameters here, since adding the standard deviation of the confidence levels to their mean easily yields a confidence level range that exceeds the 100% bound.

In depicted time series the median slope is combined with the median intercept to construct the representative regression line, which is set into the 100-year period 1986-2085 as being the center of 1971-2000 to 2070-2099. The respective quartiles are then used to draw the statistical range about the median in terms of a narrow gray area. Thereby, the medians of the regression parameters slope, intercept, and confidence level are determined independently of each other in order not to select one particular regression line but rather to obtain a representation of the whole set of 30 linear trends.

4.1.1 Atmosphere

Time series of the atmospheric forcing variables are shown in Fig. 4.1 and 4.2 for spatially averaged annual means but also for summer and winter if the seasonality is pronounced enough for the time series to be well distinguished in the graphics. Corresponding regression analysis is given to the right of the figures with the medians followed by the upper and lower quartiles in squared brackets. As already caught a glimpse from the time series shown in section 2.2.3, all atmospheric parameters except wind speed undergo significant increase in the scenario period. The mean air temperature thereby increases by about +1.8 °C in summer but by about +2.3 °C in winter (spatial seasonal distributions are shown in Fig. 4.25). As will be discussed by means of the surface heat fluxes in section 4.1.3, the stronger warming in winter turns out to be the major driver for the total warming of the North Sea in the 21st century. Cloud cover increases by about +2.1 %-points with maximum increase in summer and minimum in winter, relative humidity increases by about +1.4 %-points with maximum in summer and minimum in spring, and precipitation increases by about +0.2 mm/d with maximum in autumn and minimum in summer. In general, the driving atmosphere thus changes into a warmer and wetter climate. Though most of the absolute changes are indeed small numbers, the implications on the surface heat fluxes add up to considerable changes of the North Sea heat budget. Regional changes of the mentioned atmospheric parameters are therefore addressed in section 4.1.3 by analyzing surface heat fluxes.

The wind field, however, constituted as a highly variable vector field, directly influences both local currents and the general circulation of the North Sea but also key parameters of the thermocline. Characteristics of the wind fields and respective changes are thus analyzed in more detail. As well known, the mean wind speeds, shown in Fig. 4.3, are generally higher in the northern North Sea than in the southern and eastern North Sea, with maximum mean wind speeds up to 10 m/s in winter. As indicated by the time series of wind speed (Fig. 4.1), for spatial averages there is no significant change of wind speeds in the 21st century. Nevertheless, according to the maps of linear 100-year trends and associated confidence levels (Fig. 4.4 and 4.5), slight decreases show up in the north in winter and spring and in the south and west in summer. The maps of trends and confidence levels

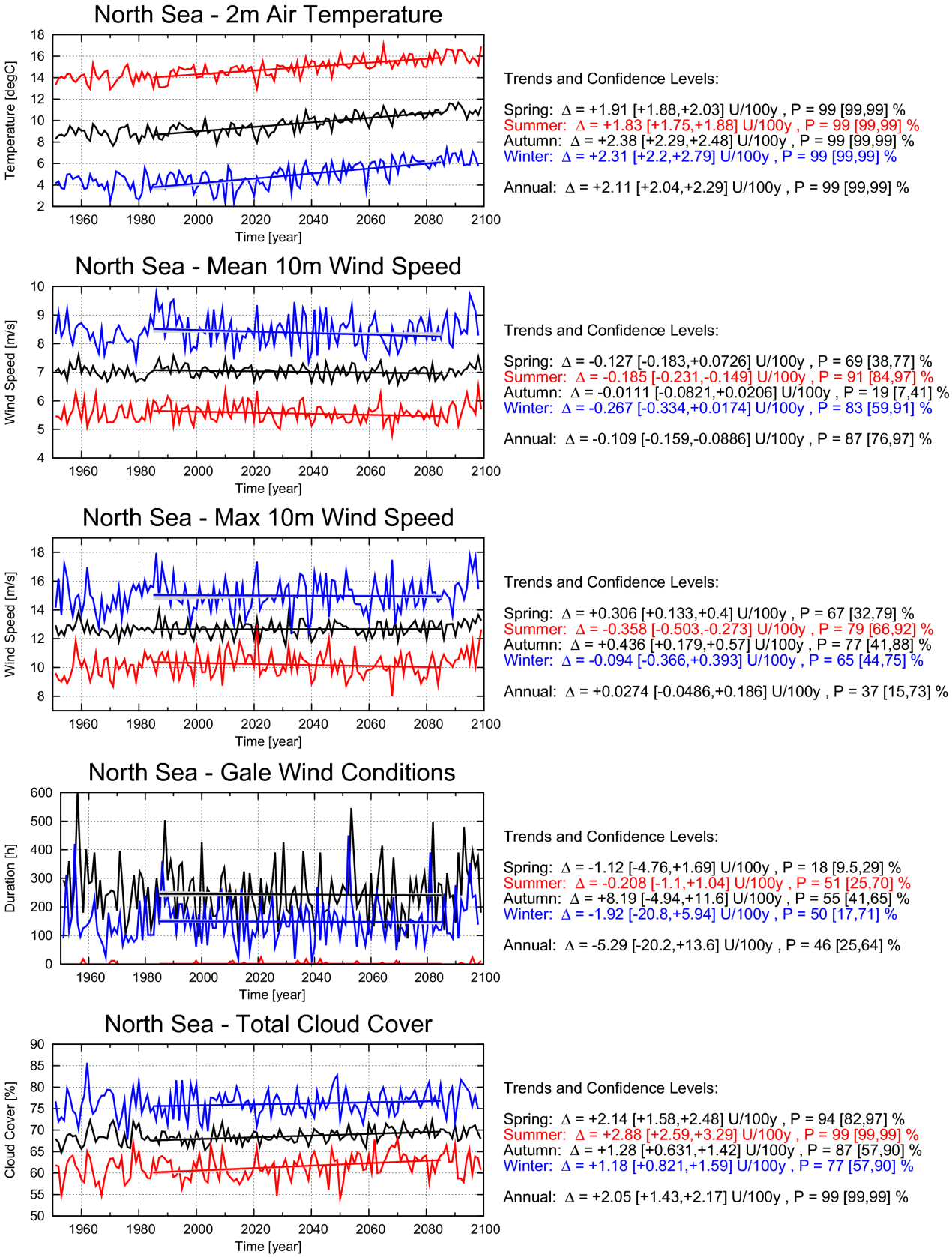

Figure 4.1: Time series of spatially averaged atmospheric forcing variables. Black: Annual mean. Blue: Winter mean (DJF). Red: Summer mean (JJA). Straight lines: Median 100-year linear regression line of the respective time series. Gray area: Range between the upper and lower quartile. Regression analysis is given to the right with medians followed by upper and lower quartiles in brackets.

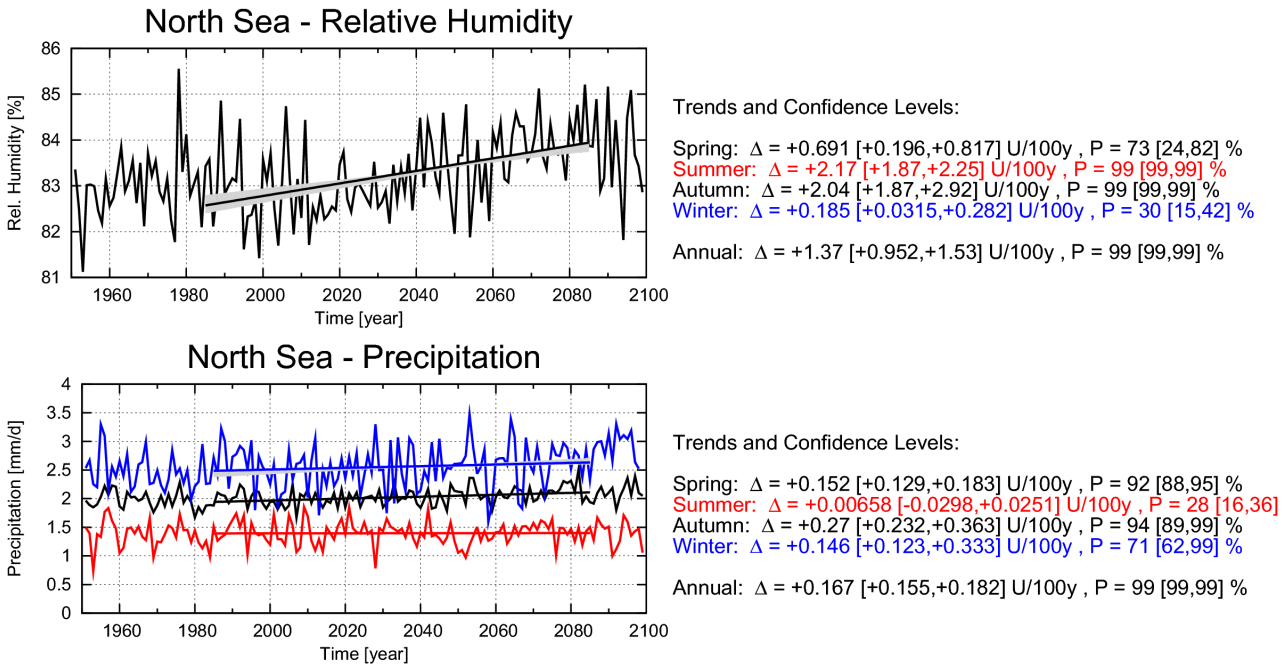

Figure 4.2: Analogous to Fig. 4.1.

are always calculated with the same median regression analysis as for the representative trends of the time series of spatially averaged means. The maximum wind speed, defined as the highest spatially averaged 6-hourly mean wind speed, nevertheless shows a slight increase in spring and autumn (Fig. 4.1). The combination of lower mean wind speeds in spring, summer, and autumn but higher maximum wind speeds in autumn directly affects the mean and maximum depth of the thermocline, to be discussed in section 4.1.4. The distribution of the duration of gale wind conditions is shown in Fig. 4.6, where gale winds are defined as wind speeds equal to or greater 17 m/s. The spatial structure is similar to the mean wind speeds, with maximum gale wind conditions up to 130 h per season in winter in the northern North Sea but almost no gale conditions in summer. The trends and confidence levels (Fig. 4.7 and 4.8) indicate a slight decrease in the region of maximum gale conditions west of Norway in spring and winter by about -25 h corresponding to -40% in spring and -20% in winter, and a slight increase in the same region in autumn by about +15 h corresponding to +40%. From the decrease of annual mean wind speeds, the decrease of annual gale wind conditions, and the increase of annual maximum wind speeds, it can be inferred that the temporal variability of the wind speeds is getting larger in the 21st century. Larger in a way that, on the one hand, calm wind conditions tend to occur more often, but on the other hand, stormy events tend to occur with higher wind speeds.

To account for wind directions too, the wind density function after Siegismund and Schrum (2001) introduced in section 2.2.3 lends itself for further trend analysis of the wind field. When calculating wind density functions for each season, a time series is obtained for each of the 72 wind directions accounted for. In applying again median regression analysis, two wind density functions can be constructed (one from the start of the representative regression line in 1986 and one from the end in 2085) that illustrate the 100-year change. The respective wind density functions and their components mean wind speed and rela-

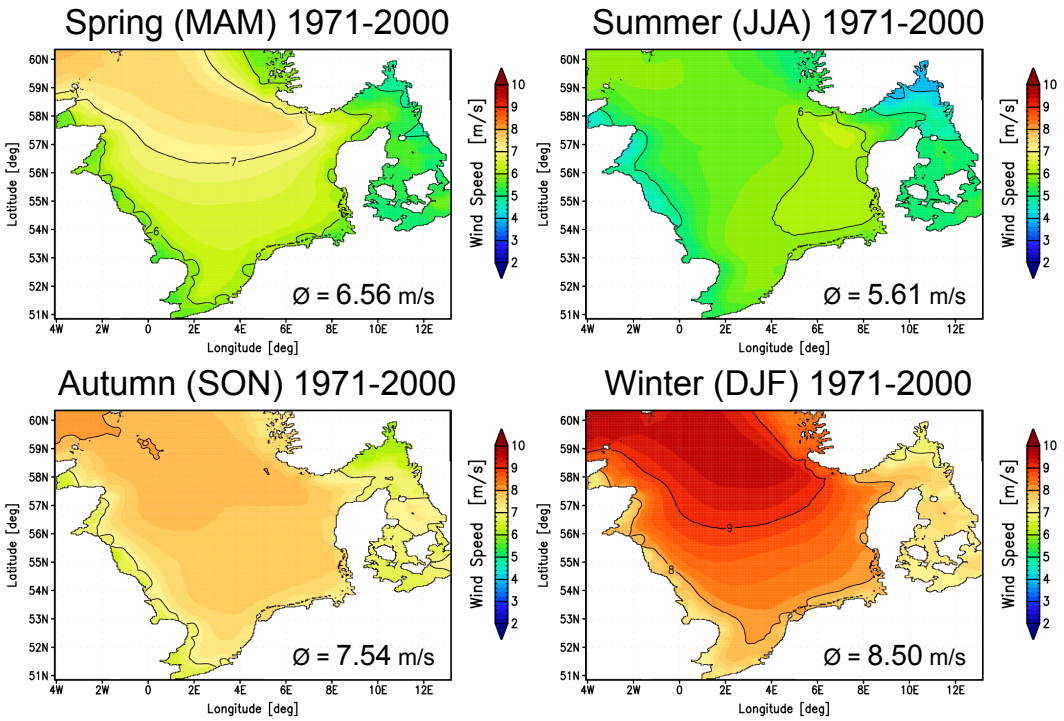

Figure 4.3: Seasonal mean wind speed of 1971-2000 with spatial averages to the lower right.

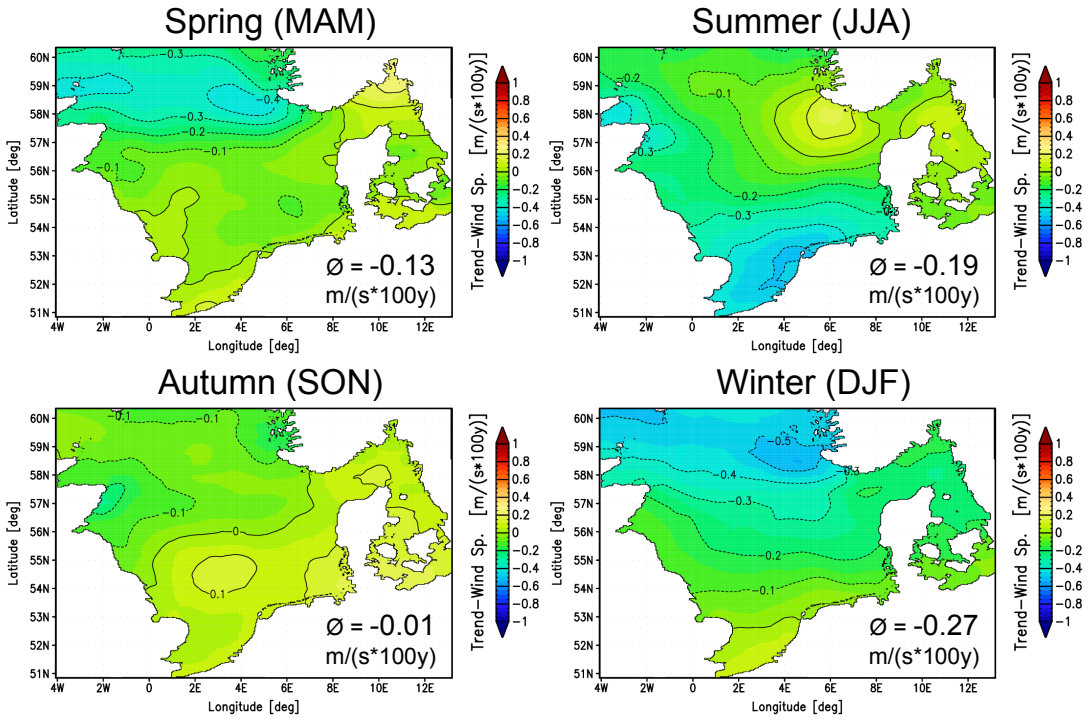

Figure 4.4: Representative linear 100-year trends of mean wind speed for the 21st century with spatial averages to the lower right.

tive frequency are depicted in Fig. 4.9, where the trends are indicated by the difference between two curves 1986 and 2085. Additionally, the confidence levels of the given trends are inserted as gray lines, where the center of each diagram refers to 0% and the outermost dashed circle to 100% confidence. From this analysis the decreasing mean wind speeds throughout the year are also indicated. Moreover, a change from south-easterly wind direc-

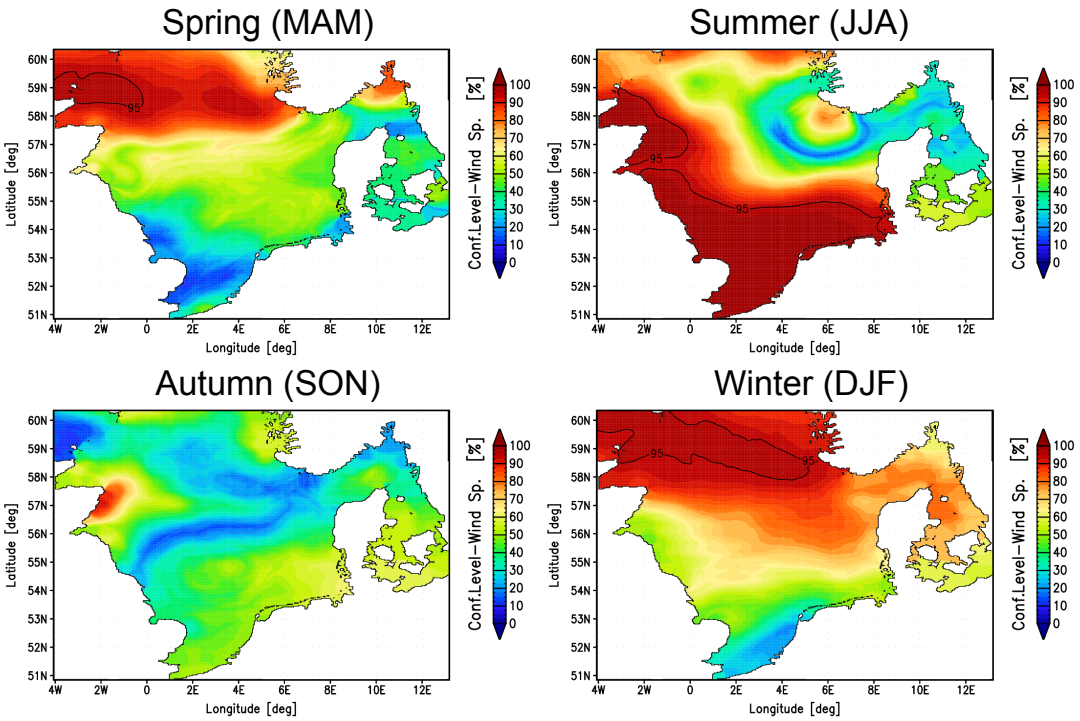

Figure 4.5: Confidence levels associated to the linear trends shown in Fig. 4.4.

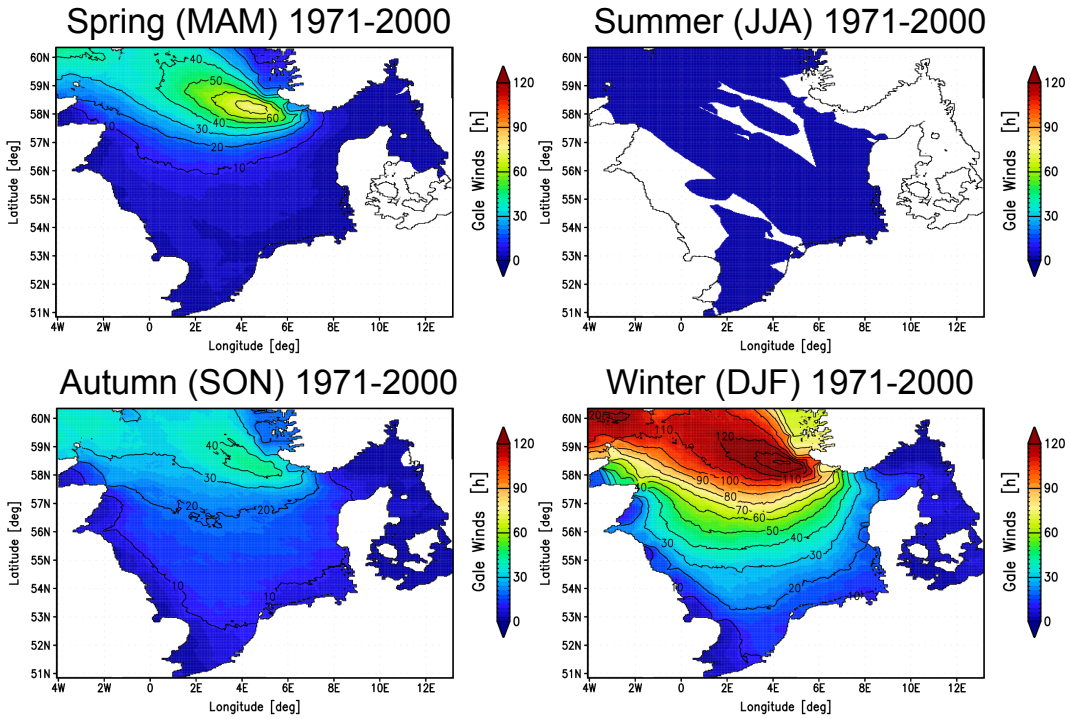

Figure 4.6: Seasonal mean duration of gale wind conditions of 1971-2000.

tions to more north-westerly ones is indicated in spring and a higher occurrence of westerly wind directions is indicated in summer and autumn. The most conspicuous change in the composed wind conditions represented by the wind density functions is though indicated in spring.

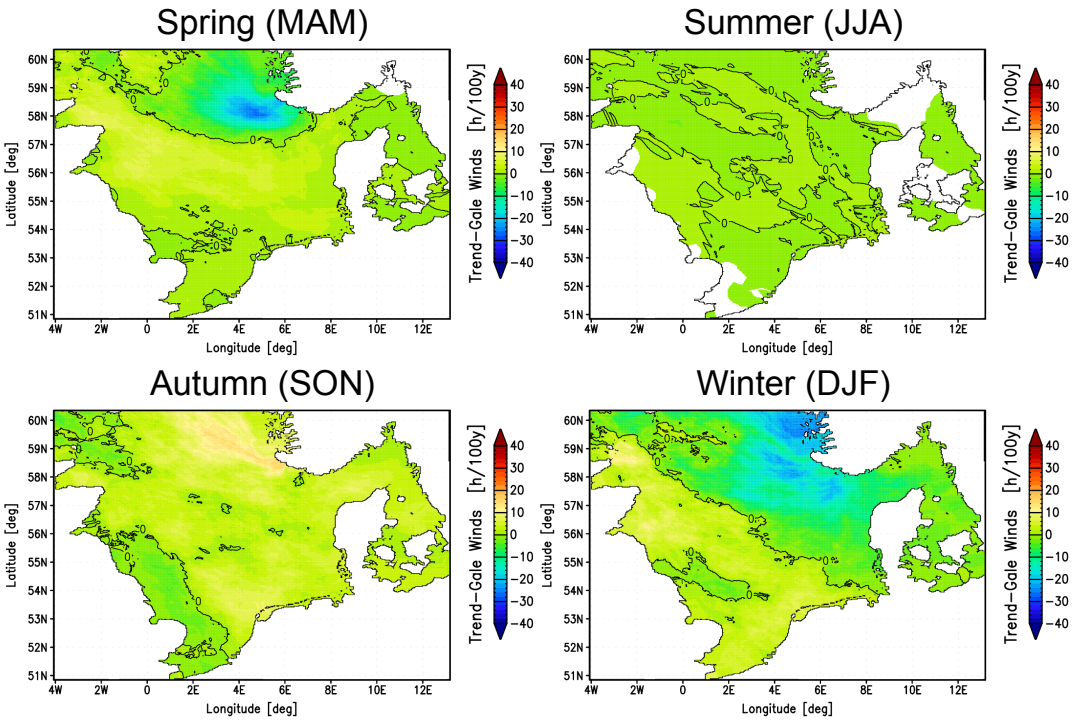

Figure 4.7: Representative linear 100-year trends of gale wind conditions for the 21st century.

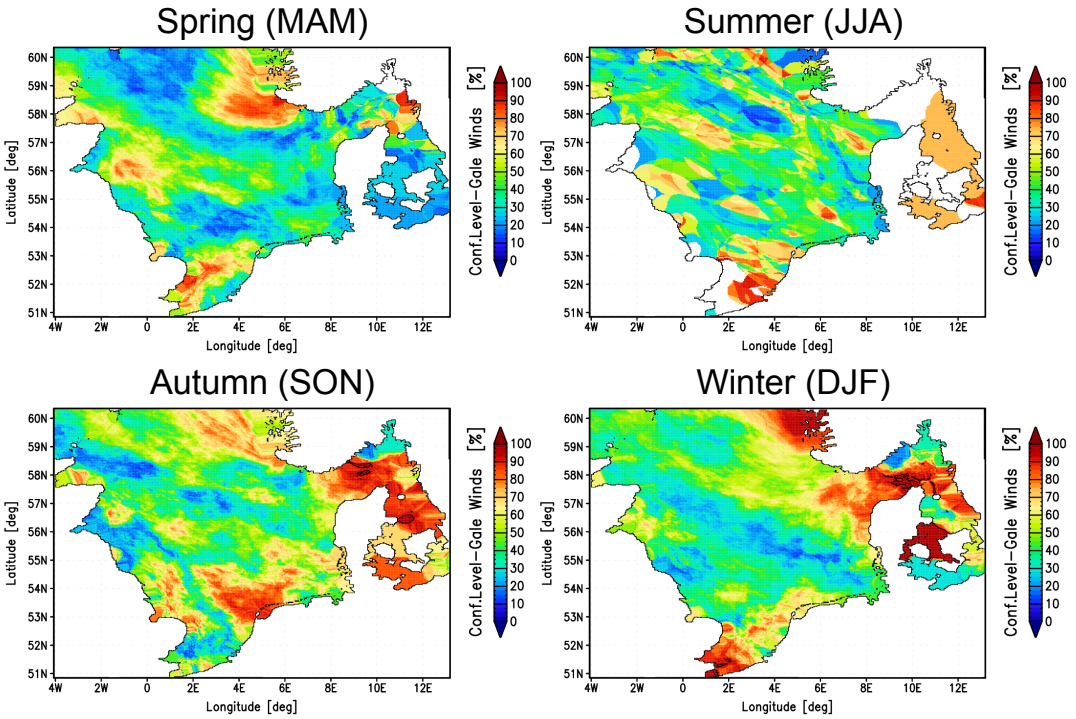

Figure 4.8: Confidence levels associated to the linear trends shown in Fig. 4.7.

However, circulation wind patterns are not recognized by the wind density function, since in the analysis the detected wind directions at different locations are not comprised relative to each other. An algorithm was applied to scan the wind fields for cyclonic, anticyclonic, and uniform wind patterns as well as for remaining undefined conditions which fit none of the former. According to this analysis the North Sea wind fields as simulated by REMO are composed of relative frequencies of about 5% cyclonic wind patterns, 2% anticyclonic,

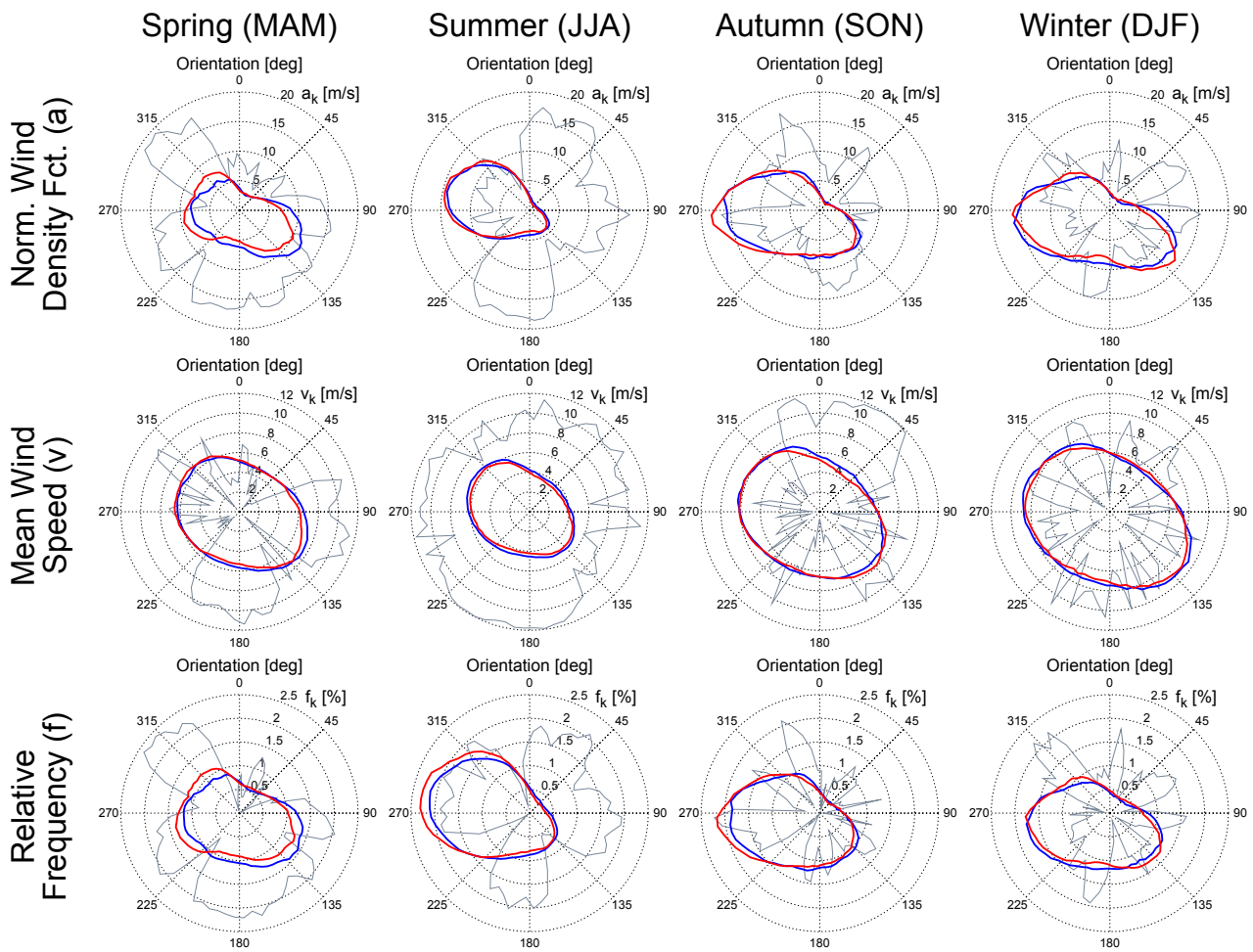

Figure 4.9: Representative linear 100-year trends of wind density and its components wind speed and relative frequency. Blue: Start of the regression line in 1986 as representation of 1971-2000. Red: End of the regression line in 2085 as representation of 2070-2099. Gray: Confidence level of the linear trends with the center of the graphics referring to 0% and the outermost dashed circle to 100% confidence.

53% uniform, and 40% undefined. A comparison with other studies, however, turns out to be difficult since the results sensitively rely upon the specific cyclone tracking algorithm at hand. The uniform wind patterns are further subdivided into eight wind directions and transferred to Hofmueller diagrams of the scenario period, shown in Fig. 4.10. Qualitatively they agree well with the relative frequencies calculated in the course of the wind density analysis. The trends given in Fig. 4.11 again point out the significant transition of easterly to north-westerly winds in spring and the cumulation of westerlies in summer. But also the standard deviations qualitatively coincide with the REMO ones given in Fig. 2.30, finally affirming the wind density approach as an appropriate method for analyzing wind fields over the North Sea. Time series of the relative frequency of cyclonic and anticyclonic circulation patterns are shown in Fig. 4.12. Though wind speeds are highest in winter, the cyclone density is often highest in spring. While the 100-year trends given in the graphics do generally not reach statistical significance, that is, a two-sided confidence level equal to or greater 95%, a steady increase of cyclone density in winter until the 2060s is followed by a distinct decrease in the last 30-40 years of the scenario period. This progression is also indicated by the NAO index shown in Fig. 3.6, since strong winter NAO phases (positive

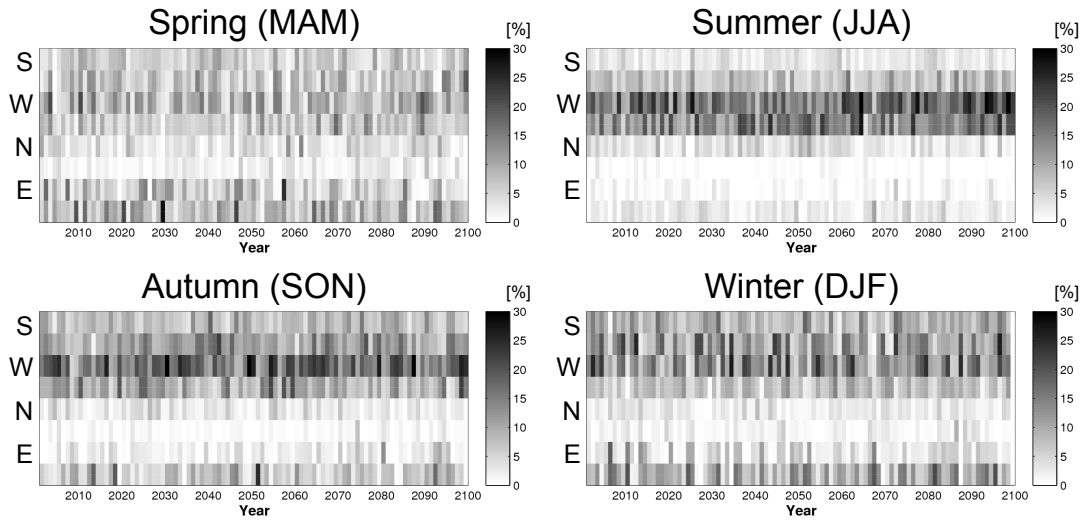

Figure 4.10: Annual relative frequency of occurrence of uniform wind patterns for 2001-2099.

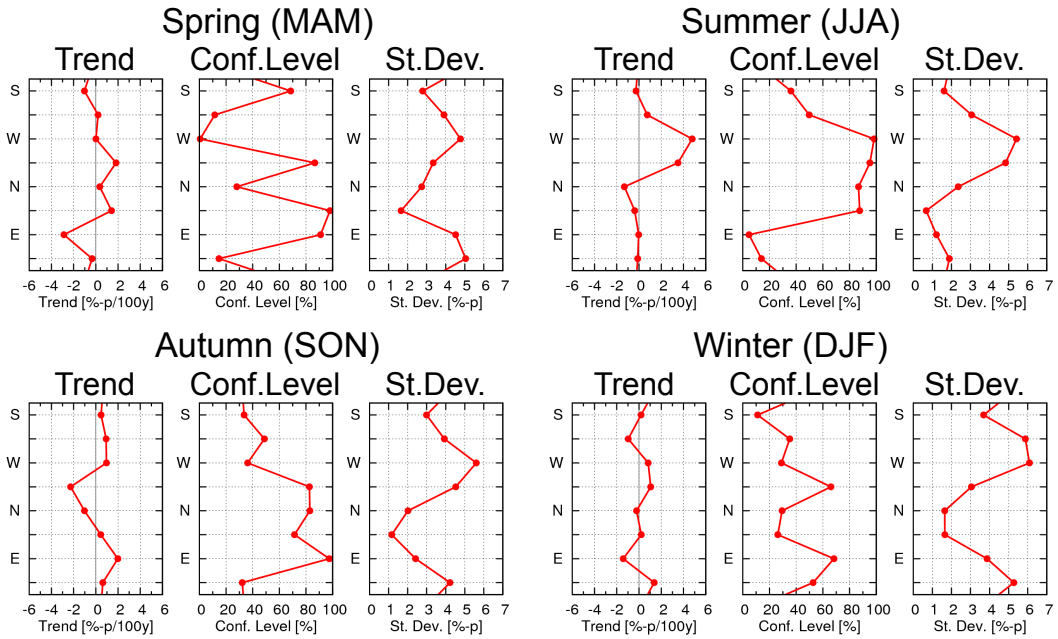

Figure 4.11: Linear trends, associated confidence levels and standard deviations of the relative frequency of uniform wind patterns shown in Fig. 4.10.

and negative) entail intensification of both cyclone density and intensity over midlatitudes of the East Atlantic and Europe (Vyazilova, 2012). Consequently, the time series of local maximum wind speeds in the North Sea for winter (not shown) is qualitatively similar to the cyclone density depicted in Fig. 4.12.

4.1.2 General Circulation

In Fig. 4.13 the flow field of the general circulation in the North Sea is represented by depth-averaged velocity vectors with maximum seasonal depth-averaged current speeds up to 30 cm/s north of Denmark at the main inflow into the Skagerrak. Seasonal mean net volume transports through various transverse sections (see Fig. 3.3) and corresponding standard deviations are given in boxes. As being the only mean net outflow of the North

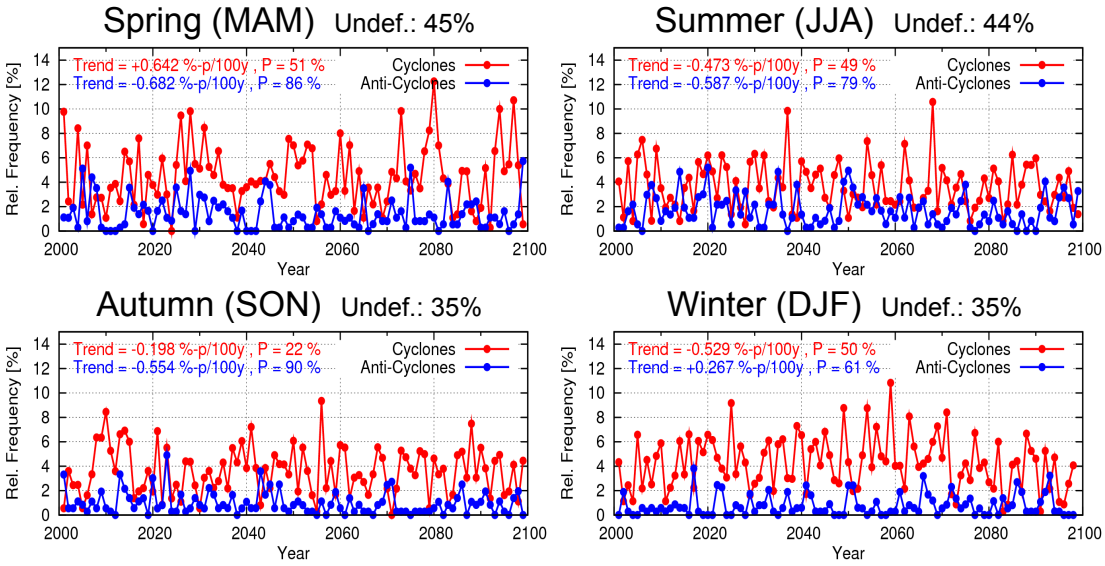

Figure 4.12: Annual relative frequency of occurrence of cyclonic and anticyclonic wind patterns for 2001-2099. Linear trends and associated confidence levels are given in the graphics. Mean relative frequency of undefined wind patterns are given in the titles.

Sea, the Norwegian Coastal Current passing the northern boundary balance all inflows and can therefore be used as an indicator of the strength of the general circulation. However, note that the given volume transports do not exactly balance each other up to the order of 10^{-2} Sv. Riverine discharge and the balance of precipitation versus evaporation account for an additional annual mean freshwater input of about +0.012 Sv. Moreover, the given values represent seasonal averages over three months, while the residence times in the North Sea range from 0.5 to 4 years (see Fig. 3.5). Local changes in sea level due to varying wind conditions or water densities influence the magnitude of the volume transports through the open boundaries. In accordance to the wind density analysis given in Fig. 2.29, the circulation is strongest in autumn (1.50 Sv) with comparatively strong and stable westerly winds, but weakest in spring (0.95 Sv) with comparatively weak and variable south-easterly winds. Nevertheless, the Fair Isle Current in the north-west and the English Channel flow in the south are strongest in winter. The inflow at the northern boundary is calculated through a fixed section from the east of the Shetland Islands to the western side of the Norwegian Trench at 3.6°E, which marks the transition from northern inflow to Norwegian coastal outflow.

Representative linear 100-year trends and associated confidence levels of the seasonal depth-averaged current speeds are shown in Fig. 4.14 and 4.15. Be aware that the global mean sea level rise is included in the given transport trends. However, comparing the trends of depth-averaged current speeds with depth-integrated volume transports reveal the influence of the global sea level rise on transport trends to be negligibly small, even in the shallow southern North Sea. Thus, trends of depth-averaged current speeds are finally chosen to illustrate changes of the general circulation, since they provide a more intelligible quantity for plotting spatial distributions than two-dimensional transport rates given in m^2/s. Moreover, the given trends represent changes of the current speeds of seasonally mean flow fields independent of the mean current directions. The transport trends given

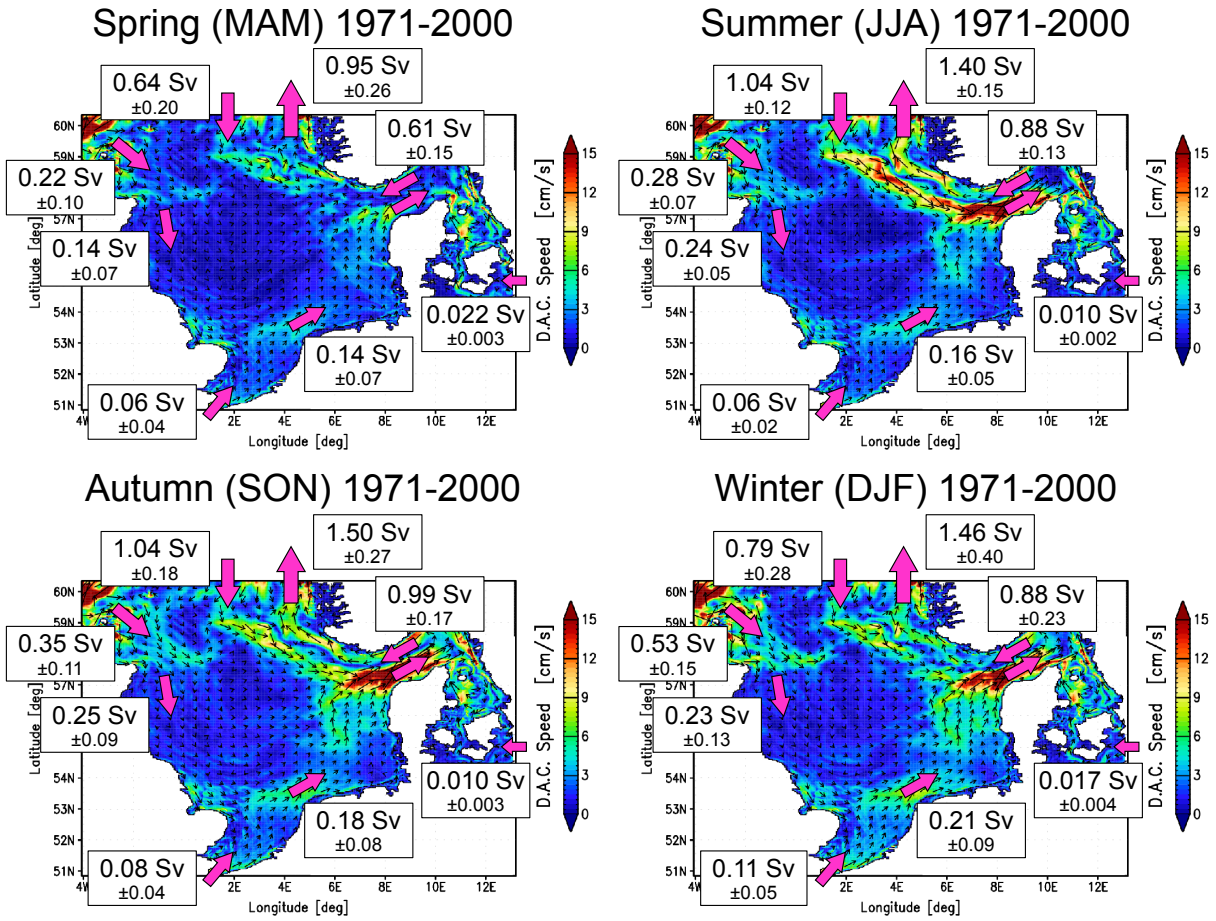

Figure 4.13: Seasonal mean depth-averaged current speeds and velocity vectors for the period 1971-2000. Boxes: Net volume transports at various transverse sections (see Fig. 3.3) and standard deviations. Magenta arrows: Main flow directions of the given net volume transports.

in the boxes of the figures, on the contrary, represent the net volume transport through fixed lateral cross sections, bringing about that a certain change of current speeds does not necessarily entail a proportional change of volume transport. However, changes of the flow field by comparing current velocity vectors or stream functions of 1971-2000 and 2070-2099 are hardly recognized by eye and therefore not shown. The combination of trends of both current speeds and volume transports thus gives a more conceivable alternative to address changes of the general circulation. In Fig. 4.14 positive transport trends are designated by red arrows, negative trends by blue arrows.

The change to more westerly wind conditions in spring indicated by respective changes of the wind density function (Fig. 4.9) gives rise to an enhanced general circulation of about +14% and a considerable increase of northern inflow by about +21%. Even though the Dooley Current is slightly weakened, the increased northern inflow entails an enhanced recirculation in the Skagerrak by about +12%. In summer and autumn, however, the increase of northern inflow is weak so that the significant decrease of the Fair Isle and Dooley Current (Fig. 4.15) is strong enough to reduce the recirculation in the Skagerrak by about -9% and -12%, respectively. Besides, the generic decrease of wind speed in summer lowers the general circulation in particular in the southern North Sea, involving a significant decrease of southern inflow through the English Channel by about -38%. The increase

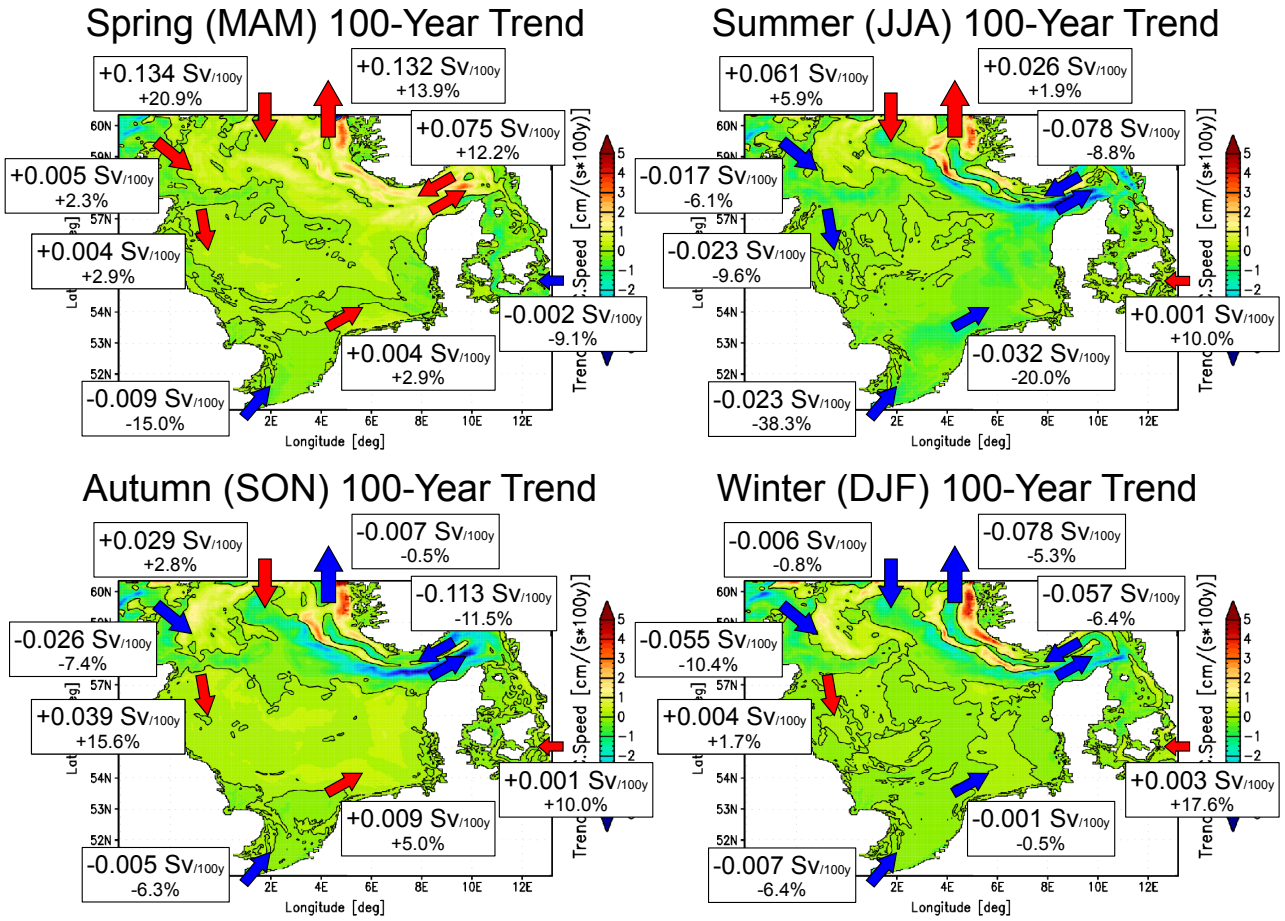

Figure 4.14: Representative linear 100-year trends of depth-averaged current speeds and selected volume transports. Respective changes relative to the mean transports of 1971-2000 (Fig. 4.13) are given in percent. Positive transport trends are indicated by red arrows, negative trends by blue arrows. Black isolines refer to 0 Sv/100y.

of Norwegian outflow in summer thus indicates the northern inflow to reverse largely into the Norwegian Coastal Current, whereas in autumn, the northern inflow is guided more westward leading to enhanced current speeds and volume transports in the central and southern North Sea, albeit the southern inflow is slightly, though insignificantly, reduced as well. Interestingly, the westward shift of northern inflow in autumn causes the south-eastward flow along the Norwegian Trench to decrease that much that a greater part of the Jutland Current is able to join the Norwegian Coastal Current without entering the Skagerrak, finally reducing the recirculation in the Skagerrak despite an enhanced Jutland Current. In winter it is mainly the attenuation of the Fair Isle and Dooley Current by about -10% that entail the reduction of the Skagerrak recirculation, while the circulation in the central and southern North Sea remains widely unchanged. The strong increase of Baltic discharge in winter by about +18% can be attributed to higher precipitation rates at concurrently warmer temperatures in winter, ponding less precipitation on land in terms of snow and ice. Consequently, the snow melting runoff in spring time is reduced as well, resulting in lower Baltic discharge. However, the induced change of the baroclinic component of the cyclonic surface flow in the Skagerrak is not strong enough in the model to determine the change of the depth-integrated flow by compensating the different order of magnitudes of the Baltic discharge and Skagerrak recirculation rate, since the trends of the

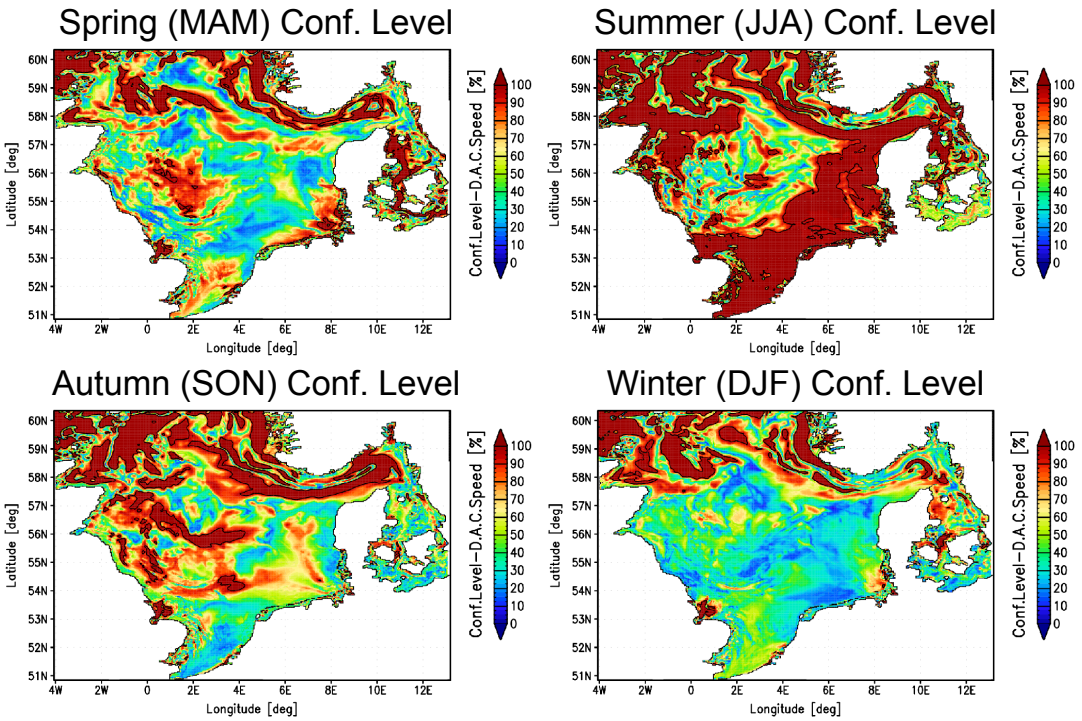

Figure 4.15: Confidence levels associated to the linear trends of depth-averaged current speeds shown in Fig. 4.14. Black isolines refer to 95% confidence indicating statistical significance.

two are of inverse signs for all seasons. Further seasonal analysis of the general circulation with respect to current anomalies and the influence of anomalies of the predominant wind conditions are discussed in section 4.2.1 by means of EOF analysis.

Fig. 4.16 finally summarizes the seasonal changes in depicting respective means and trends on the annual scale. The decreasing Fair Isle Current by about -7% and the increasing northerly inflow by about +6% lead to a slight increase of current speeds in the central North Sea but to considerable decrease of the Skagerrak recirculation by about -5%. The attenuation of southerly inflow by about -14% gives rise to slightly lower current speeds in the southern North Sea. However, statistically significant changes with a confidence level of at least 95% are recorded only in the northern North Sea as far as into the Skagerrak, though high confidence levels are also reached in the Southern Bay. The stream function obtained from vertically integrated mean advective transports is shown in the lower left part of Fig. 4.16. Be aware that the given values of the stream function cannot explicitly be read as transport rates at certain locations. Rather, the difference between the values of two arbitrary stream lines represents the volume transport in Sv that passes through the region enclosed by the two stream lines. Close stream lines thus account for higher transport rates than wide stream lines. The signs of the stream function values are thereby chosen in accordance to the common meteorological convention, where the flow direction is identified with the lower stream function value situated to its left (e.g. Etling, 2008). The figure highlights the great influence of the northerly inflow via the Fair Isle Current and to the east of the Shetland Islands on the strength of the Dooley Current and the south-easterly flow along the Norwegian Trench, which finally guides the Jutland Current into the Skagerrak. More than 70% of these two northern inflows do not propagate

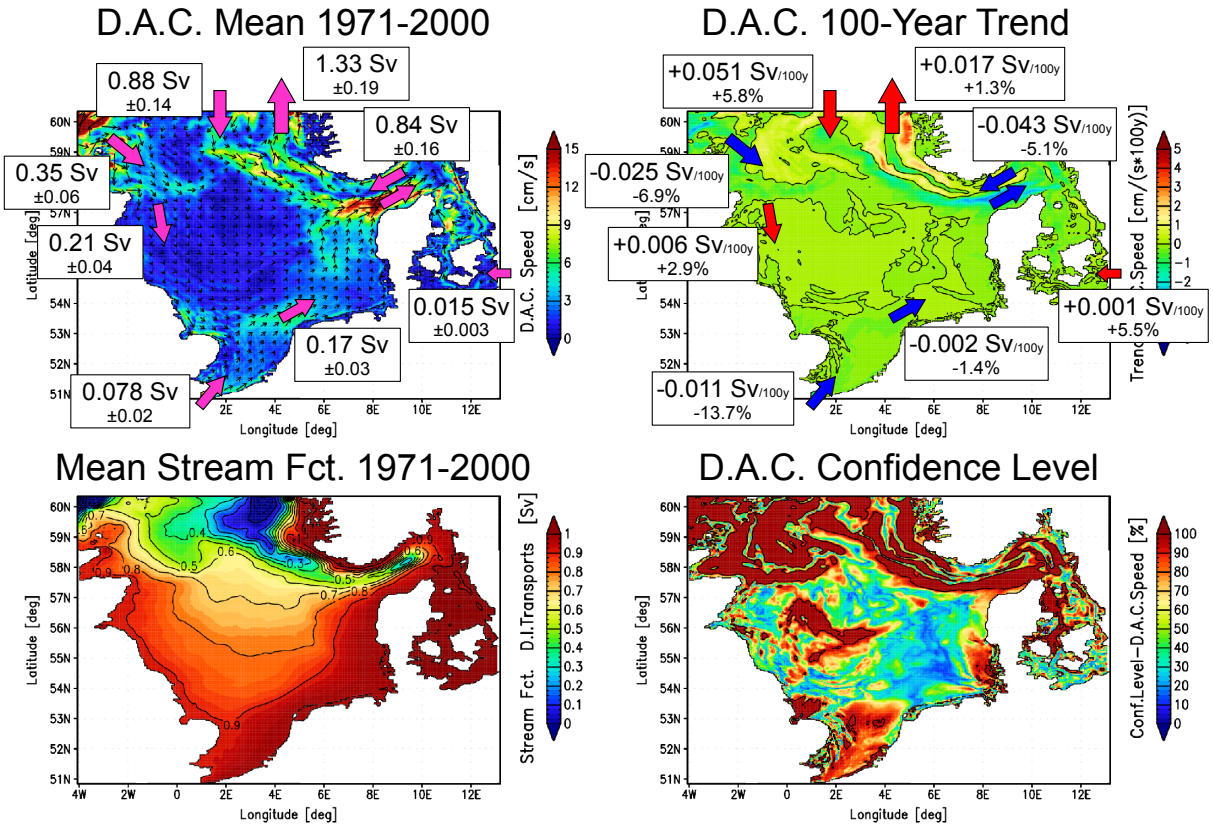

Figure 4.16: Annual mean depth-averaged current speeds and associated linear trends and confidence levels, analogous to Fig. 4.13 to 4.15. Lower left part: Stream function of the annual mean depth-integrated volume transports.

farther south than 57°N, whereas a great part of the northern inflow at the western side of the Norwegian Trench reverses into the Norwegian Coastal Current without flushing the Skagerrak.

4.1.3 Heat Fluxes and Water Temperature

The heat content E [J] of a fluid parcel is generally obtained from the change of heat energy ΔE with respect to a certain reference value. The latter is most often associated with a heat content of 0 J at 0 °C, as also in the present analysis for maintaining comparability with other studies. A physically more appropriate reference heat content though were associated with -2 °C, as being approximately the freezing point of sea water with salinity of 35 psu at one atmospheric pressure (e.g. Pickard and Emery, 1990). Below that threshold temperature, the North Sea water is expected to be fully frozen and therefore cannot be regarded as a Newtonian fluid anymore. From an oceanographer´s view, the heat content relative to -2 °C thus represents the maximum amount of heat energy that can potentially be extracted from the North Sea. The change of heat energy is given by

$$\Delta E = cp \cdot m \cdot \Delta T \tag{4.1}$$

where cp [J kg^{-1} K^{-1}] is the specific heat of sea water and m [kg] is the mass of water being warmed or cooled by the temperature difference ΔT [K] (e.g. Gill, 1982). With cp according to Feistel (1993) at mean water temperature and salinity of 1971-2000 and at

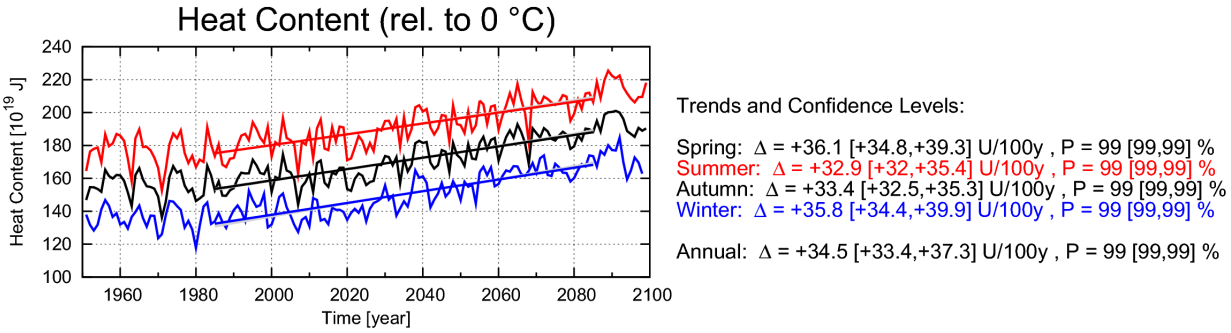

Figure 4.17: Total annual and seasonal heat content of the North Sea relative to -2 °C. Representative 100-year trends and associated confidence levels are given to the right with statistical ranges in brackets.

atmospheric pressure (3984 J kg^{-1} K^{-1}), the mean normalized heat content for the control period 1971-2000 of about 33.3e+06 J/m³ (relative to 0 °C) yields a total heat content of the North Sea, of about 157e+19 J (see Fig. 4.17). The minimum in winter amounts to about 29.1e+06 J/m³ and 138e+19 J, respectively, and the maximum in summer to about 37.6e+06 J/m³ and 178e+19 J. In general, the main sources for the heat content of the North Sea are composed of the surface heat fluxes and the advective heat fluxes through the open lateral boundaries. As already mentioned in chapter 3, the annual mean surface heat flux obtained from bulk formulas amounts to about -13.6 W/m², which integrated over the entire North Sea area entails a mean net heat loss of about -8.1 TW. This quantity can be easily calculated in absolute numbers, since in the process of surface heat exchange no advective mass transport is involved. However, in order to determine the advective heat transport ΔQ_{ad} [W] through the open boundaries, equation (4.1) needs to be modified to account for the in- or outflowing transport rates by replacing m with the term sea water density ρ [kg/m³] times current speed perpendicular to the transverse sections v [m/s] times area of the transverse sections A [m²].

$$\Delta Q_{ad} = cp \cdot \rho \cdot v \cdot A \cdot \Delta T \tag{4.2}$$

The magnitude of ΔQ_{ad}, however, is highly sensitive to the dominating volume transport $v \cdot A$ as well as to the chosen reference temperature in $\Delta T = T - T_{ref}$. Nevertheless, the commonly used reference temperature of 0 °C proves to be a reasonable choice for the North Sea. The lowest water temperatures in winter are quite close to this value, entailing the Atlantic inflow to reliably represent a source of heat throughout the year. The obtained annual mean advective heat transports through the open lateral boundaries are given in the left part of Fig. 4.18. Positive and negative signs indicate heat input and output, respectively. Additionally, the mean temperatures of the in- or outflowing water masses are also given, which must be distinguished from the mere mean temperatures *at* the boundaries (not quoted). As expected, the largest advective heat input is constituted by the strong Atlantic inflow through the northern boundary, while the English Channel flow conveys a much smaller amount of heat into the North Sea because of its low volume flux. The crucial choice of the reference temperature can be envisaged by considering the calculated *heat outflow* along the Norwegian coast. In fact, on average the Norwegian

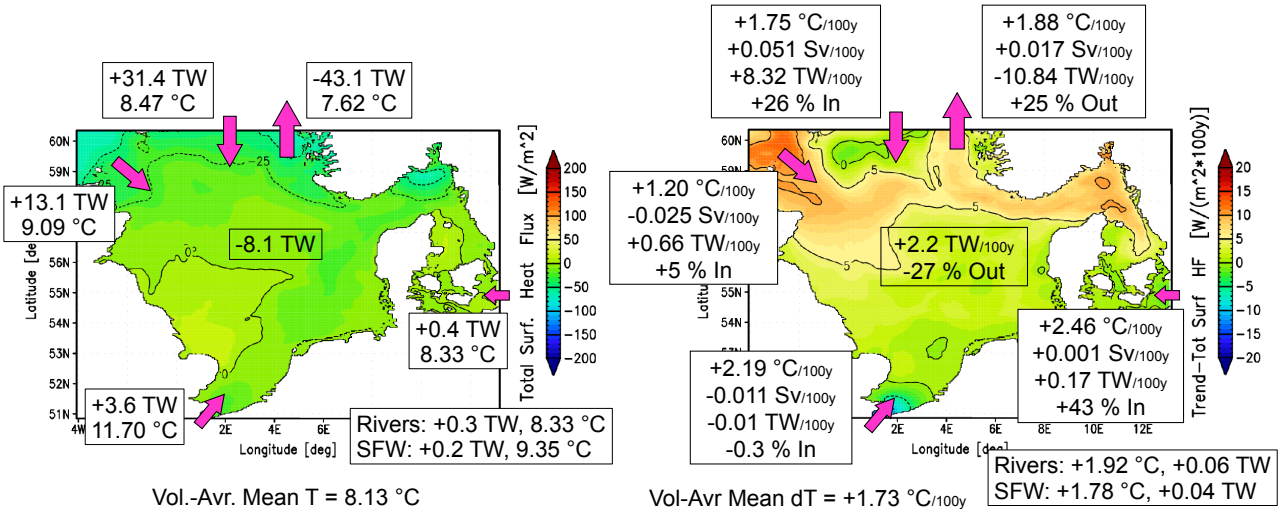

Figure 4.18: Left part: Annual mean total surface heat flux of 1971-2000 (colors), and advective heat transports through the open lateral boundaries relative to 0 °C and mean temperatures of the respective in- or outflowing water masses (boxes). Right part: Representative linear 100-year trends of the annual mean total surface heat flux (colors), and of the temperature of the in- and outflowing water masses, the net volume transports, the advective heat flux relative to monthly volume-averaged North Sea temperatures, and the advective heat flux relative to the mean of 1971-2000 (boxes).

outflow ought to act as a *source of heat* for the North Sea, since in spring, summer, and autumn, water masses ever cooler than the North Sea mean temperature permanently leave the domain, thus indirectly transporting heat into the system. The sensitive choice of reference temperature pertaining to the magnitude of advective heat transports does hardly allow for the advective heat fluxes to be equilibrated by the surface heat fluxes. Moreover, note that the large magnitudes of the annual mean advective heat fluxes in comparison to the annual mean total surface heat flux, also given in the figure, do not indicate a dominating influence of advective boundary heat fluxes on the heat content of the North Sea. The surface heat flux is subject to a pronounced seasonality with monthly means ranging between ±150 TW, while the total advective heat flux does not even change its sign throughout the year, to be discussed below.

Representative trends of the annual advective and surface heat fluxes for the 21st century are shown in the right part of Fig. 4.18. The numbers given in boxes read as the temperature change of the in- or outflowing water masses, the change of net volume transport, the change of advective heat flux relative to running monthly mean North Sea temperatures, and the change of advective heat flux relative to the mean of 1971-2000 shown in the left part of the figure. Be aware that positive changes of heat flux components do not necessarily indicate a warming of the North Sea like e.g. the positive change of heat content does as long as the influence of the increasing North Sea volume due to global sea level rise is negligible. Rather, they describe a change of the aspired dynamical equilibrium between the North Sea, the atmosphere, and adjacent oceans. Even though the temperature of the in- and outflowing water masses is increasing everywhere in the course of global warming, the weakening of the English Channel flow, for example, causes a slight reduction of the associated advective heat flux. The northern inflow, however, carries more

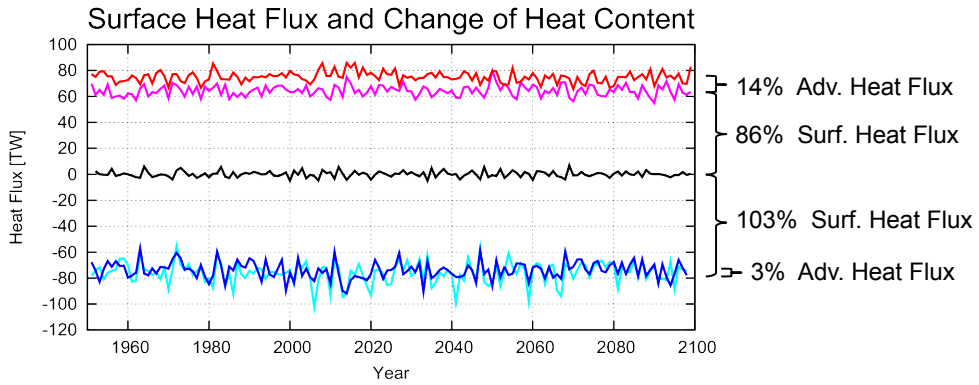

Figure 4.19: Total North Sea surface heat flux (in positive, out negative) and changes of the total heat content. Black: annual change of total heat content. Red: summer (JJA) change of total heat content. Dark blue: winter (DJF) change of total heat content. Magenta: summer total surface heat flux. Light blue: winter total surface heat flux.

heat into the North Sea by about +26%. Both water temperature and volume transport are also increasing at the Norwegian outflow, resulting in an enhanced advective heat flux by about +25%. Again, the changes of heat fluxes quoted in Fig. 4.18 do not sum up to a balanced heat budget, because of their dependence on the arbitrarily chosen reference temperature, where the imbalance is neither equilibrated by the change of the total North Sea heat content given in Fig. 4.17.

In Fig. 4.19 annual and seasonal changes of the North Sea heat content are shown as well as seasonal total surface heat fluxes. The warming of the North Sea by about 0.02 °C/year corresponds to an imbalanced heat budget of just about 0.12 TW, which is hardly recognizable in Fig. 4.19. Nevertheless, the calculated long-term mean of the annual changes of heat content (black line) over the 21st century well reflects the imbalanced heat budget and with this, the warming of the North Sea. Note that to a very good approximation, the quantities shown in Fig. 4.19 are *independent* of any chosen reference temperature, since only temperature *differences* are involved in their calculations. Any imbalance between the total surface heat flux and the change of heat content of the water column can therefore be identified as the total advective heat fluxes through the open lateral boundaries independent of a reference temperature, too. For the North Sea the remaining contributions from river runoff, surface fresh water fluxes, and mean sea level rise, which are also included in the change of heat content, turn out to be negligibly small on the considered scales.

In summer, the influence of air-sea heat exchange is largely restricted to the upper 30 m, allowing for the Atlantic inflow to influence the temperature of deeper layers. Fig. 4.19 indicates the Atlantic inflow in summer to represent a heat input, since below the thermocline, Atlantic inflow is typically warmer than the North Sea waters. In winter, however, the water column is vertically well mixed so that any advective heat transferred from the Atlantic Ocean into the North Sea is exposed to the heat exchange at the sea surface and hence, Atlantic inflow does not essentially contribute to the change of the North Sea heat content in winter. Nevertheless, the total surface heat flux in winter is slightly stronger negative than the corresponding change of heat content, consistently indicating the warm

Atlantic inflow to represent a heat input for the North Sea in winter, too. From averaging summer and winter means over the control period 1971-2000, the relative contributions of surface and advective heat fluxes amount to 86% and 14% in summer, respectively, and 103% and 3% in winter, where the predominant influence of the atmospheric forcing hardly changes under the A1B scenario. The dominating influence of local air-sea heat exchange on the water temperature and heat content of the North Sea is concluded in numerous other studies (e.g. Colebrook and Taylor, 1979; Otto et al., 1990; Becker and Pauly, 1996; Hjøllo et al., 2009), quantified to a similarly strong influence than in the present study.

The trend of the annual total surface heat flux integrated over the entire domain adds up to an increase of about +2.2 TW, corresponding to a reduction of the net heat loss at the sea surface to the atmosphere by about -27%. Trend analysis of the four surface heat flux components and of atmospheric parameters reveals the maximum change in the north-western North Sea to be induced by a weaker latent heat flux in this region due to locally lower wind speeds and higher relative humidity for all seasons. The strong change along the Norwegian Trench and in the Skagerrak, however, is primarily induced by a weaker negative sensible heat flux in winter due to decreasing air-sea temperature differences. The negative trend in the Southern Bight can be attributed to a stronger latent heat flux in winter caused by slightly increasing wind speeds, while the sensible heat flux is not affected, since air-sea temperature differences in this region hardly change because of the strong temperature increase of the English Channel flow.

As can be seen in Fig. 3.10, the seasons spring and summer are characterized by a positive total surface heat flux, i.e. a heat input from the atmosphere into the ocean, whereas autumn and winter are characterized by a negative total surface heat flux, i.e. a heat transfer from the ocean to the atmosphere. Averaging the two respective seasons yields semi-annual surface heat flux components as given in Tab. 4.1. In the first column the four components incoming short wave radiation, outgoing long wave radiation, sensible heat flux, and latent heat flux, as well as the total surface heat flux are quoted with an arrow indicating the direction of the magnitudinal change which coincides with the literal implications given in the third column. The representative linear 100-year trends given in the second column, however, carry the definite signs of the changes in accordance with the signs of the respective heat flux components as defined in Fig. 3.9. The trends are also given in percent relative to the means of 1971-2000. In the last column the driving quantities involved in the bulk formulas for the individual heat flux components are listed, again quoted with a trend-indicating arrow. Those driving quantities whose trends finally give rise to the direction of the corresponding heat flux trends are underlined. Respective values can be found in Fig. 4.1 and 4.2, while relevant values are given in the text, too.

In the following paragraphs any literal changes refer to the trend´s absolute magnitudes rather than to their actual signs. The numbers in Tab. 4.1 indicate that in the warm seasons spring and summer the increase of cloud cover (+2.51 %-points) induces a reduction of short wave radiation by about -5.54 W/m², which is in fact strong enough to account for a negative trend of the total surface heat flux of about -1.42 W/m². In the cold sea-

Component	Trend [W/(m²*100y)]		Implication	Drivers (Winning Drivers)
Spring+Summer:				
SW Rad ↓	**-5.54**	(3.4 %)	**less heat input**	solar rad., albedo, cloud c.↕
LW Rad ↑	-0.50	(0.8 %)	more heat loss	cloud c.↑, air temp.↕, SST ↑
Sens HF ↑	+1.58	(36.5 %)	more heat input	wind sp.↓, rel.hum.↑, ΔT(air-sea)↕
Lat HF ↓	+3.04	(11.8 %)	less heat loss	wind sp.↓, rel.hum.↑, air temp.↑
Tot HF ↓	**-1.42**	(1.8 %)	**less heat input**	
Autumn+Winter:				
SW Rad ↓	-0.83	(1.9 %)	less heat input	solar rad., albedo, cloud c.↕
LW Rad ↓	+0.02	(0.1 %)	less heat loss	cloud c.↕, air temp.↕, SST ↑
Sens HF ↓	**+6.78**	(31.7 %)	**less heat loss**	wind sp.↓, rel.hum.↑, ΔT(air-sea)↓
Lat HF ↓	+2.37	(3.4 %)	less heat loss	wind sp.↓, rel.hum.↑, air temp.↑, ΔT(air-sea)↓
Tot HF ↓	**+8.34**	(7.7 %)	**less heat loss**	
Annual Tot HF ↓	+3.46	(25.8 %)	less heat loss	

Table 4.1: Representative 100-year trends of semi-annual surface heat flux components calculated from Bulk formulas. Involved quantities are given in the last column with underlined winning drivers whose trends finally give rise to the direction of the corresponding heat flux trends. Upward and downward pointing arrows indicate the qualitative direction of the given changes.

sons autumn and winter, however, the decrease of air-sea temperature difference induces a substantial reduction of the sensible heat flux by about -6.78 W/m² providing for a strong decrease of the total surface heat flux by about -8.34 W/m². In other words, in spring and summer there is slightly less and less heat input into the North Sea, whereas in autumn and winter there is distinctly less heat loss to the atmosphere. Looking at the time series of SST for summer and winter, the corresponding representative 100-year trends, and the associated time series of air temperature in Fig. 4.20, the following conclusion can be drawn. Because of the stronger warming trend of air temperature in winter (+2.31 °C) than of SST in summer (+1.54 °C), the temperature drop from summer to winter becomes less intense from year to year so that the air-sea temperature difference in winter becomes continuously smaller, indicated by the slight convergence between the blue SST curve and its associated green air temperature curve. Hence, as a consequence, the sensible heat flux is accordingly reduced, contributing to the lower total heat transfer from the North Sea to the atmosphere in autumn and winter. The reduction of heat input in spring and summer, on the contrary, gives rise to an increasing air-sea temperature difference in summer, indicated by the slight divergence between the red SST curve and its associated green air temperature curve, which in turn increases the sensible heat flux. Finally, the warming trend in winter is that strong that the North Sea nevertheless suffers a warming in summer too, even though the net heat input in summer is successively reduced.

Advective heat fluxes through the open boundaries, however, are not included in this consideration, since the influence of advective heat fluxes on the water temperature of the North Sea is estimated above to amount to less than 20% for the entire simulation period. Most of the northerly inflowing Atlantic waters merely recirculate the northern North Sea and Norwegian Trench. Their residence times thereby still take up to 2 years (see Fig. 3.5), entailing that they are subject to intense vertical mixing in winters, induced by heat exchange with the atmosphere at the sea surface. Moreover, as already mentioned, individually calculated advective heat fluxes only contribute to a *balanced* heat budget if the system at hand is in equilibrium state, unlike the 21st century state of the North Sea

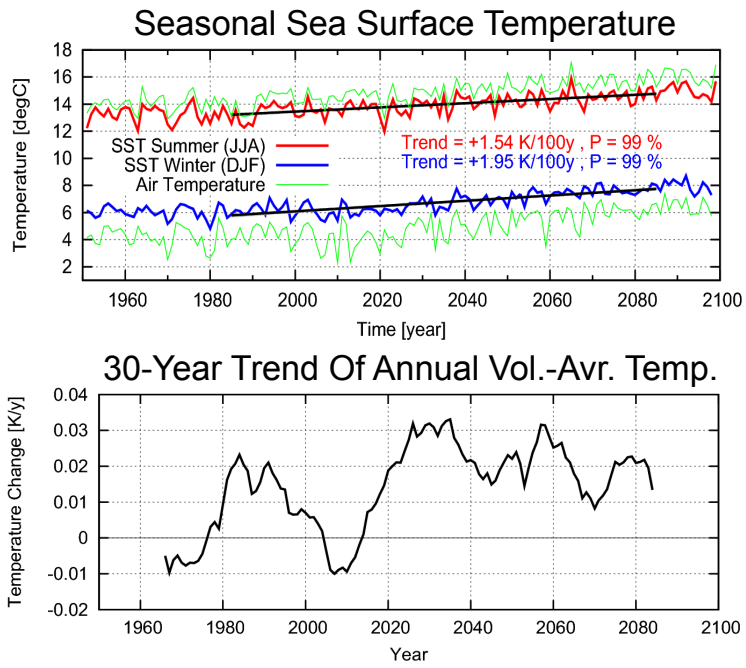

Figure 4.20: Upper part: Time series of SST for summer (red) and winter (blue), representative 100-year trends, and the associated time series of air temperature (green). Lower part: Running 30-year trends of the annual volume-averaged North Sea temperature.

of continuous warming and changing boundary volume fluxes. When changes of advective boundary heat fluxes are incorporated anyway and added to the respective changes of surface heat fluxes, the resulting changes of total heat flux in autumn and winter are still stronger than in spring and summer by a factor of about 2.4, again emphasizing the significant warming of the cold seasons. Finally, from the analysis of the surface heat fluxes given above, the strong warming of air temperature in winter is identified as the main driver for the total warming of the North Sea in the 21st century.

The running 30-year trends of the annual volume-averaged North Sea temperature, shown in the lower part of Fig. 4.20, indicate the strongest warming up to about +0.03 °C/y to occur until the 2030s followed by a gradual decrease of the warming intensity, hinting at an asymptotic progression of the temperature time series. The 100-year trend of the annual volume-averaged temperature by about +1.73 °C with a confidence level higher than 99% (Fig. 4.21), gives rise to an increase of the total heat content in the North Sea by about +34.5e+19 J, corresponding to +22% (Fig. 4.17).

Resulting seasonal mean SSTs for 1971-2000 are shown in Fig. 4.22, while spatial distributions of the representative 100-year trends of total surface heat flux and SST are shown in Fig. 4.23 and 4.24, respectively (seasonal depth-averaged water temperatures for 1951-2000 are shown in Fig. 4.49). Be aware that correlations between the total surface heat flux and SST on shorter time scales than the seasonal cycle hardly hold even when time lags are incorporated in the analysis. For sure, a change of surface heat flux reflects a proportional change of heat energy entering or leaving the sea surface. However, in prescinding from advective heat fluxes, unless the surface heat flux changes its sign, the temporal progression of SST does not change the sign of its gradient. A decrease of positive (ingoing) surface

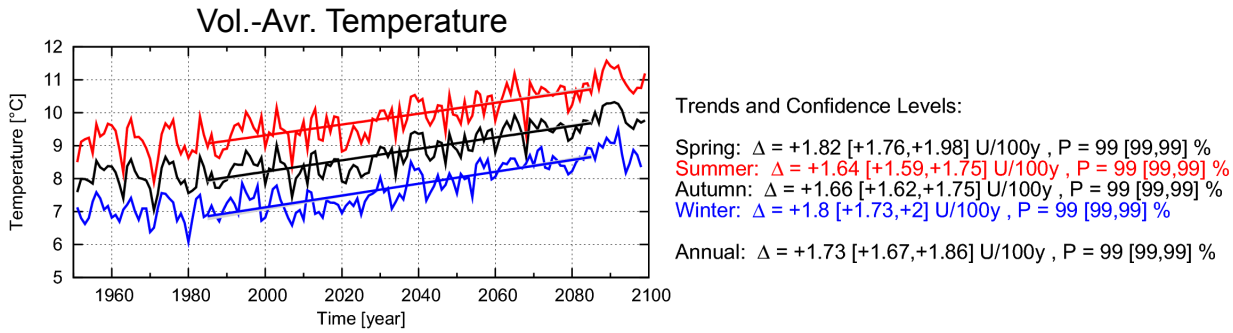

Figure 4.21: Time series of annual volume-averaged water temperature. Representative 100-year trends and associated confidence levels are given to the right with statistical ranges in brackets.

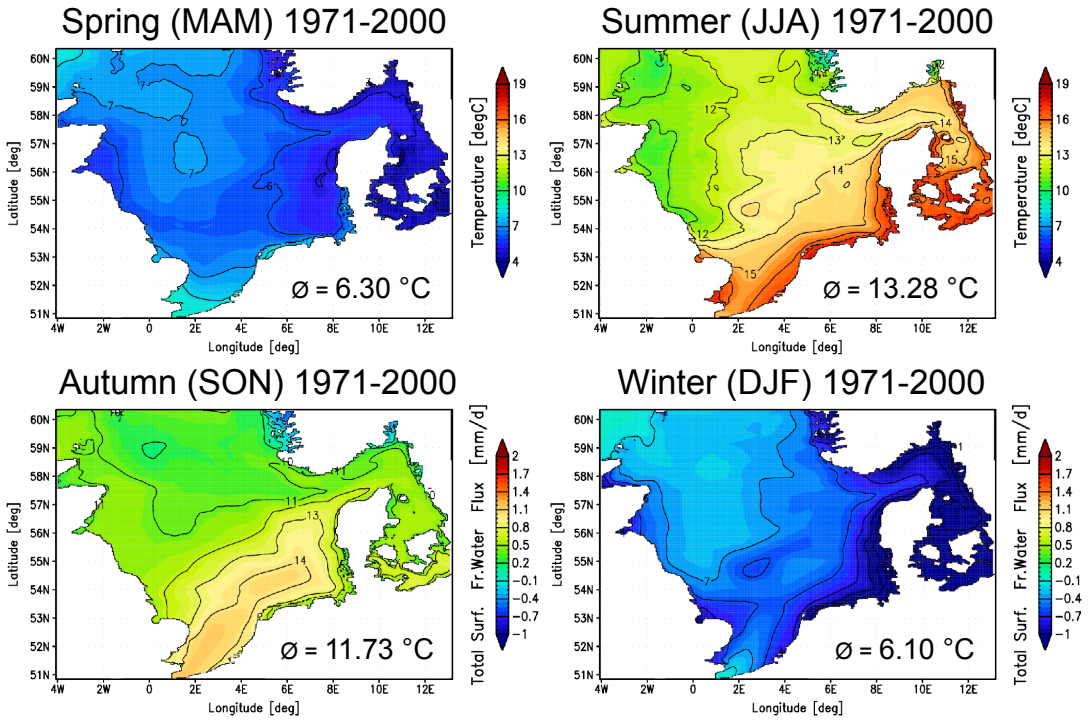

Figure 4.22: Seasonal means of sea surface temperature for 1971-2000.

heat flux, indicated by a *lower* but still positive value at time t_1 than at time t_0, causes the SST to still further increase, indecated by a *higher* SST value at time t_1 than at time t_0. Only if a change of surface heat flux involves the value to change its sign from t_0 to t_1, the change of SST is qualitatively oriented in the same direction. However, it is indeed the qualitative *change* from t_0 to t_1, i.e. a decrease or increase, that determines the correlation rather than the *magnitudes* of the respective values at t_0 and t_1, bringing about the time series of surface heat flux and SST to suffer an inherent mismatch.

The local intensity of SST warming in autumn and in particular in winter is highly influenced by the bathymetry via the effect of differential heating. Albeit in winter the water column is vertically well mixed, simple calculations show that in terms of heat it is never balanced with the atmosphere within one winter season at regions with water depths greater than about 35 m. The general climate warming thus entails a stronger warming of the water column in shallower regions. Moreover, since the SST obtained from the coupled

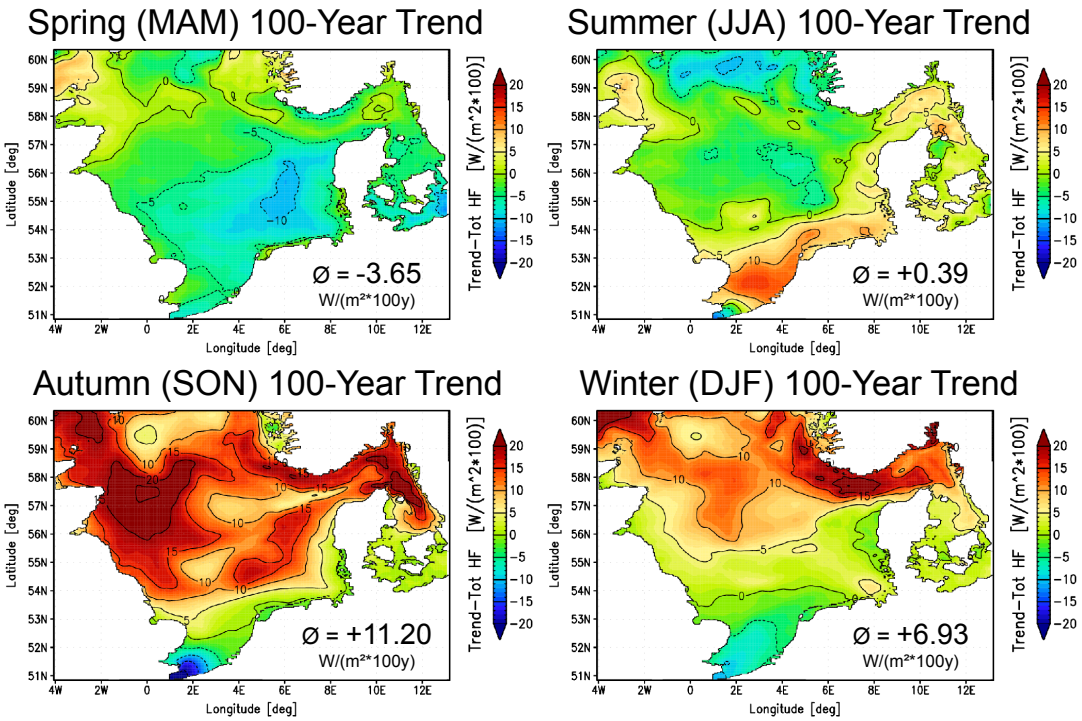

Figure 4.23: Seasonal representative 100-year trends of total surface heat flux.

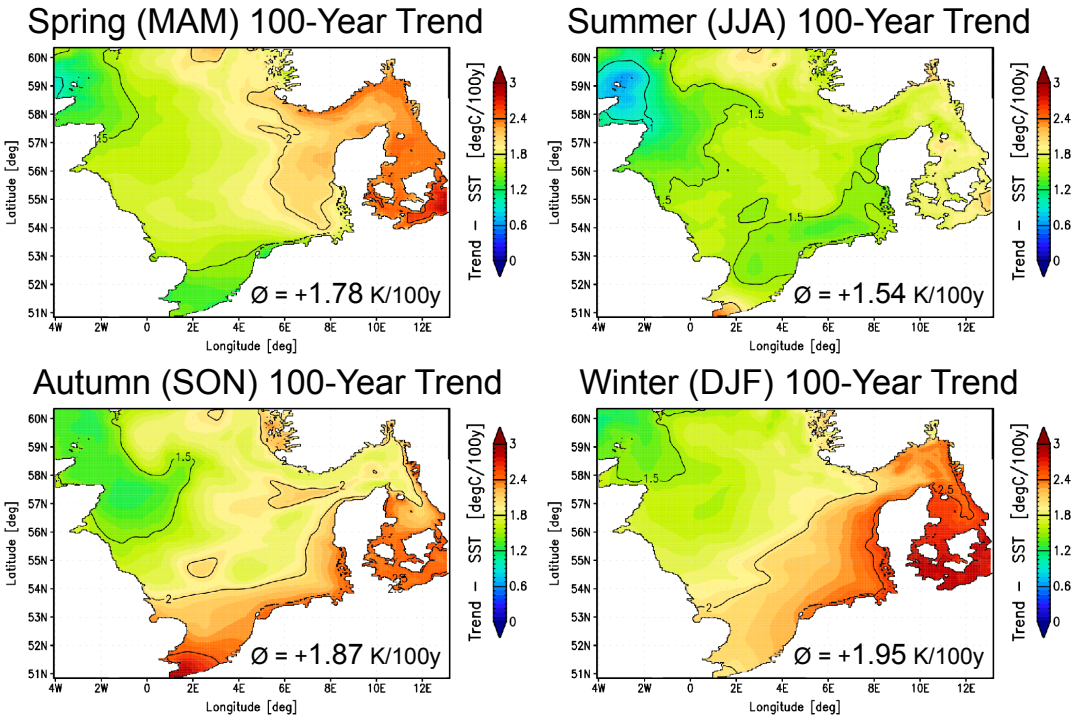

Figure 4.24: Seasonal representative 100-year trends of sea surface temperature.

global atmosphere-ocean model ECHAM5/MPIOM entered the REMO climate simulation, a similar bathymetry-influenced north-west to south-east gradient in the air temperature trends of autumn and winter caused by the coupled atmosphere-ocean dynamics is recognized in Fig. 4.25. In reentering the HAMSOM simulation, the air temperature trends provide to some extent for a positive temperature feedback in the model chain. In summer, however, the SST trends are much more uniformly distributed, since the warming in

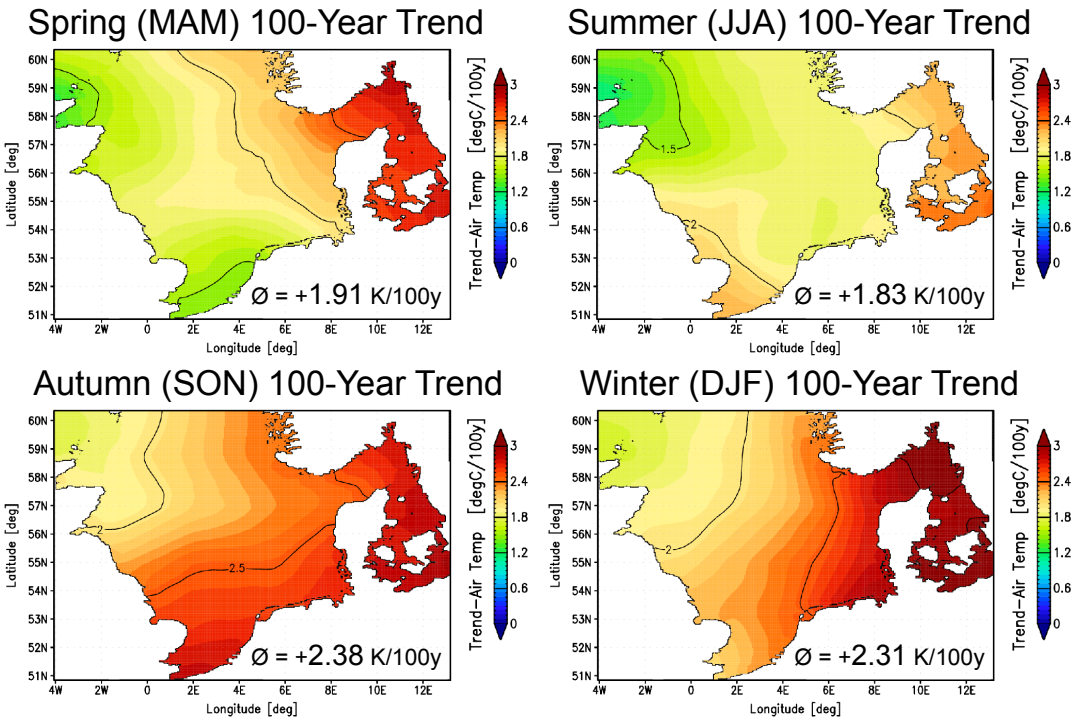

Figure 4.25: Seasonal representative 100-year trends of 2m air temperature.

summer is widely restricted to upper layers because of the development of the thermocline.

Although the individual trends of the heat flux components given in Tab. 4.1 do not differ qualitatively for each of the two merged seasons, their magnitudes are most pronounced in spring and autumn (Fig. 4.23), respectively. While both seasons spring and summer are characterized by a strong reduction of short wave radiation due to increasing cloud cover, the regionally positive trends in summer in the southern and eastern North Sea originate from an even stronger reduction of latent heat flux due to decreasing wind speeds and increasing relative humidity. And accordingly, both seasons autumn and winter are characterized by a strong reduction of sensible heat flux induced by decreasing air-sea temperature differences, whereas in autumn a strong reduction of latent heat flux due to lower wind speeds, higher relative humidity, and also decreasing air-sea temperature differences is additionally imposed. The trends of the total surface heat flux close to the southern boundary are dominated by the strong temperature increase of the southern boundary inflow for all seasons, which reduces the sensible heat flux in the warm seasons spring and summer but enhances it in the cold seasons autumn and winter. Further analysis of regional temperature anomalies and correlations are discussed in section 4.2.2 by means of EOF analysis.

4.1.4 Thermocline

As described in the introduction (section 1.2.7) and model evaluation (chapter 3), the most characteristic feature of the North Sea´s seasonality is the development of a strong thermal stratification in the central and northern North Sea over the warm seasons, referred to as the thermocline. In the following analysis the thermocline is again defined

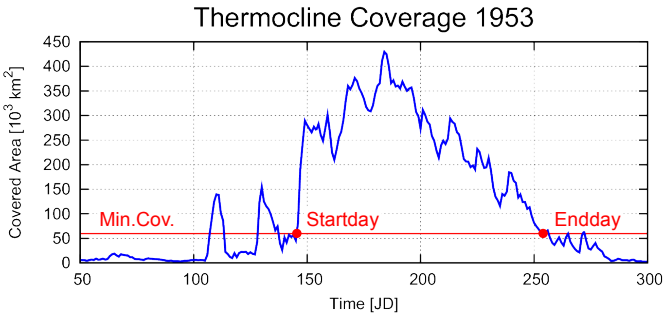

Figure 4.26: Typical time series of spatial thermocline coverage of the year 1953 with two early temporary thermocline periods. Start and end days of the thermocline main period are denoted. The minimum coverage area refers to one tenth of the total North Sea domain.

as the location of the maximum vertical temperature gradient equal to or greater 0.1 °C/m (Pohlmann, 1996c, 2006; Meyer et al., 2011). The development of the thermocline is initialized by increasing solar heat input in spring. Favorably warm and calm weather conditions occasionally induce the development of a very early thermocline which, however, is destroyed again after some days. In Fig. 4.26 a typical time series of the spatial thermocline coverage is exemplified, demonstrating the occurrence of even two early temporary thermocline periods. In summer the thermocline is most pronounced and reaches its maximum spatial coverage up to 400e+03 km² (see also Fig. 3.11). The increasing wind speeds in combination with the seasonally induced decreasing solar heat input finally destroy the thermocline in autumn. In the calculation of the thermocline duration a minimum coverage area of stratified conditions has to be exceeded. The size of the minimum coverage is deduced from the classification of distinct hydrographic regions in the North Sea by ICES (1983), whose mean size amounts to approximately one tenth of the total domain size.

The temporal progression of the thermocline duration for the 21st century is shown in the upper part of Fig. 4.27. The representative 100-year trends indicate a prolongation of the thermocline period by about +6 d in autumn, while the date of onset in spring does not undergo significant changes. The prolongation can be attributed to the slightly lower mean wind speeds in autumn and in particular to the substantially weaker heat loss to the atmosphere (see Fig. 4.23). Depth and intensity of the thermocline are identified with the the strongest vertical temperature gradient in the water column.

Time series of mean depth and mean intensity, as averaged over both the thermocline period and the daily spatial coverage, are shown in the middle and lower part of Fig. 4.27, respectively. The green curves refer to the upper and accordingly, lower bound of the section of the water column with a vertical temperature gradient higher than 0.1 °C/m, representing a more meaningful conception of the thermocline depth than the depth of the maximum temperature gradient. Nevertheless, the representative 100-year trend of the mean thermocline depth indicates a slight raising of the thermocline by about +0.2 m in the 21st century caused by the lower mean wind speeds in spring, summer, and autumn. By contrast, the maximum depth is dropping down by about +2.4 m because of higher maximum wind speeds and a more frequent occurrence of gale wind conditions in autumn. Since the bottom temperature in the North Sea in summer is determined by

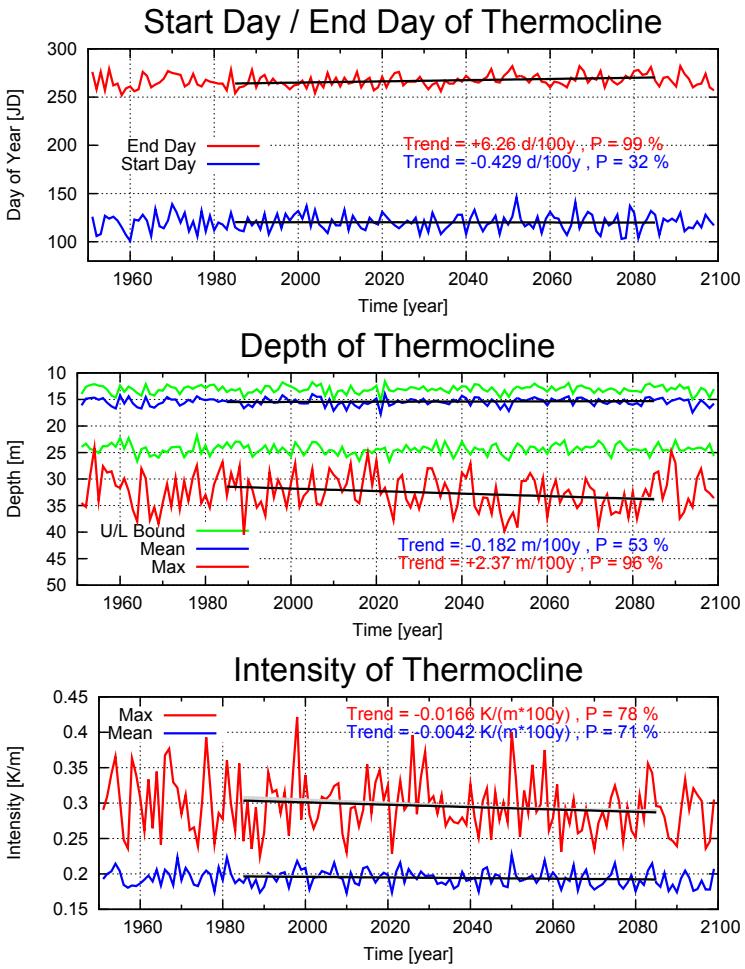

Figure 4.27: Upper part: Start and end day of the thermocline period, defined as the time at which the required minimum coverage area is exceeded. Middle part: Mean and maximum depth of thermocline as well as the lower and upper bound of the water column at which the required minimum temperature gradient is exceeded. Lower part: Mean and maximum intensity of the thermocline. Representative linear 100-year trends are also given.

the water temperature of the preceding winter, the stronger temperature increase in winter than in summer (Fig. 4.20 and 4.17) consequently entails a continuous weakening of the mean and maximum thermocline intensity by about -2% and -5%, respectively, as shown in the lower part of Fig. 4.27. Note that the representative confidence level of the trend of the mean thermocline depth does not reach statistical significance. The inferred causal relation with the similarly insignificant changes of wind speeds given in Fig. 4.1 therefore is not fully confirmed. However, some evidence can still be drawn from the indeed significant deepening of the maximum thermocline depth, which assignes additional significance to the changes of wind speed and hence, to the proposed causal relation. Likewise, the upper bound of the calculated confidence range of the decreasing SST difference between summer and winter (see Fig. 4.20) amounts to a confidence level of 99.8%, providing additional significance for the decreasing intensity of the thermocline.

As indicated by the upper part of Fig. 4.28, the highest intensities tend to occur early in the thermocline period where the cold water column, the strong increase of solar heat input, and relatively calm weather conditions favor maximum vertical temperature gradi-

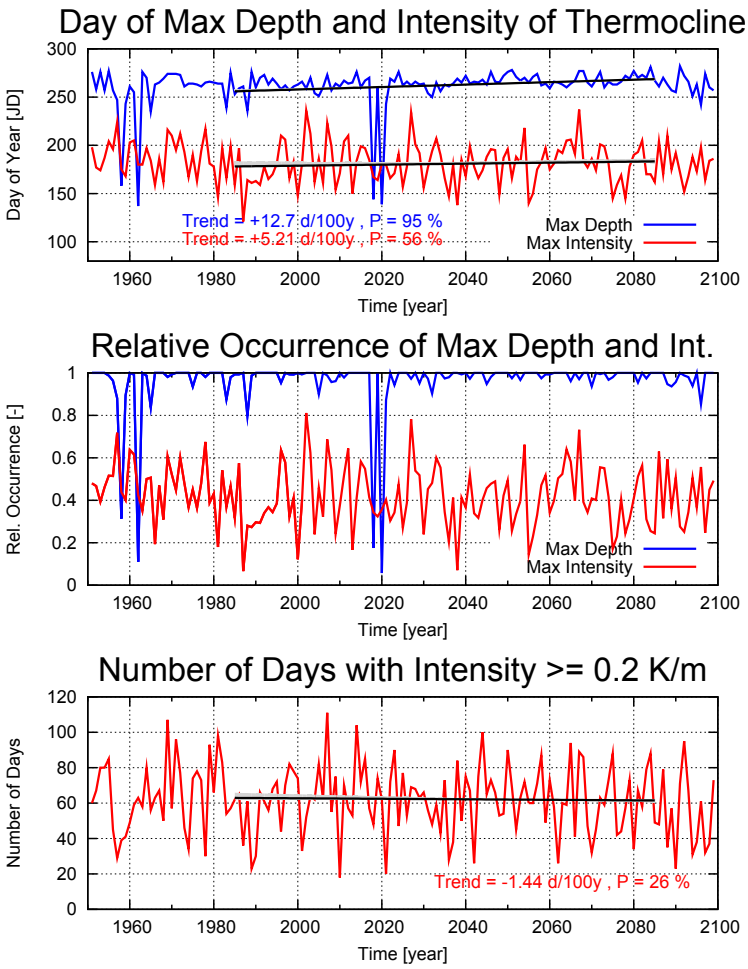

Figure 4.28: Upper part: Date of occurrence of maximum depth and intensity of the thermocline. Middle part: Date of occurrence of maximum depth and intensity relative to the thermocline period as specified by the upper part of Fig. 4.27. Lower part: Number of days of a strong thermocline intensity.

ents. However, the maximum depths of the thermocline tend to occur at the very end of the period, where increased wind speeds transfer more and more turbulent energy into the water column causing a deepening of the thermocline and a weakening of its intensity. In the middle part of Fig. 4.28 the occurrence of the maximum depth and intensity relative to the thermocline period is depicted, highlighting the maximum depth to preferably occur shortly before the thermocline erosion. It turned out that the few outliers in the figure are related to stormy wind conditions which last for about 3 to 5 days in succession. The calculated trend of the occurrence of maximum thermocline depth is apparently overestimated under the spurious influence of the outliers. Nevertheless, a slight delay can be recognized in accordance with the prolongation of the thermocline duration. The lower part of Fig. 4.28 finally indicates that the number of days with a strong thermocline intensity of more than 0.2 °C/m is not subject to significant change. Moreover, the spatial distributions of the thermocline depth, intensity, and relative frequency as depicted in Fig. 3.11 neither undergo significant change in the 21st century and are therefore not shown.

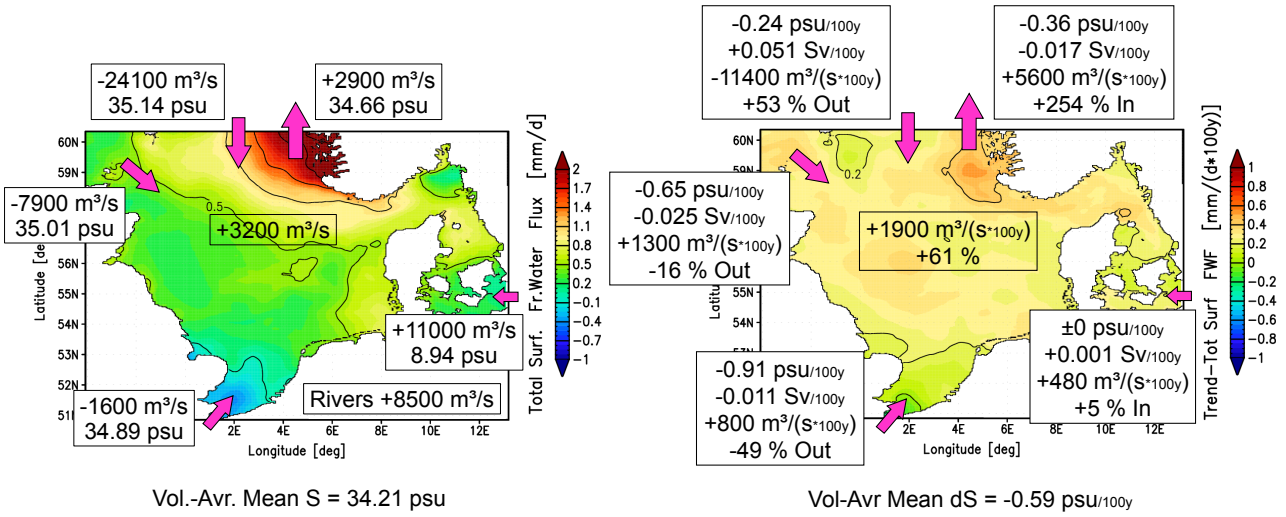

Figure 4.29: Left part: Annual mean total surface fresh water flux (colors), and advective fresh water transports through the open lateral boundaries relative to monthly volume-averaged salinities of 1971-2000 and mean salinities of the respective in- or outflowing water masses (boxes). Right part: Representative linear 100-year trends of the annual mean total surface fresh water flux (colors), and of the salinity of the in- and outflowing water masses, the net volume transports, the advective fresh water flux relative to monthly volume-averaged North Sea salinities, and the advective fresh water flux relative to the mean of 1971-2000 (boxes).

4.1.5 Fresh Water Fluxes and Salinity

As the equivalent to the advective heat flux ΔQ_{ad} (section 4.1.3), the advective fresh water flux is analyzed to address the influence of the boundary fluxes on the salinity of the North Sea. The advective fresh water flux ΔF_{ad} in m³/s is thereby calculated via

$$\Delta F_{ad} = \rho \cdot v \cdot A \cdot \left(1 - \frac{S}{S_{ref}}\right) \cdot \frac{1}{1000} \tag{4.3}$$

with ρ [kg/m³] sea water density, v [m/s] current speed perpendicular to the transverse section, A [m²] area of the transverse section, S [psu] salinity at the transverse section, S_{ref} [psu] reference salinity. The monthly mean advective fresh water transports are always calculated relative to S_{ref} as the running monthly mean salinities of the total North Sea. Any in- or outflowing water masses are thus assessed whether they finally increase or decrease the actual monthly mean North Sea salinity. As such, the annual mean advective fresh water transports given in the left part of Fig. 4.29 account for the relative contribution that the individual boundary fluxes make to the mean volume-averaged salinity of the North Sea on a monthly scale. The numbers therefore, in addition to their dependence on the reference salinity, neither strictly balance over all open lateral boundaries, nor do they justice to the total salt budget of the North Sea. The latter rather has to be based on the mass fluxes of salt entering and leaving the domain, which sum up to an annual mean throughput of about 47000 t/s. The mean salinities of the in- or outflowing water masses are also quoted in Fig. 4.29. As expected, relative to the monthly volume-averaged salinities, the calculation singles out the northern inflow as the greatest source of salty waters with a negative advective fresh water flux more than -24000 m³/s and a salinity of the inflowing water masses higher than 35 psu. Baltic and riverine discharge, on the contrary, constitute the greatest fresh water supply with fresh water fluxes of about +11000

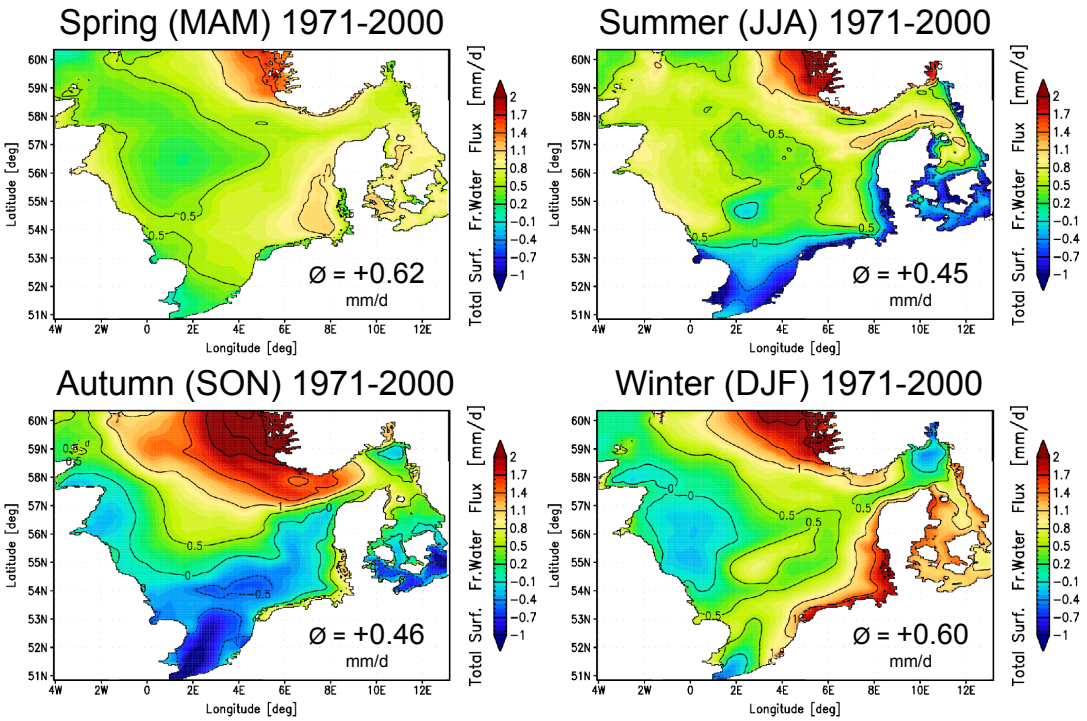

Figure 4.30: Seasonal distributions of mean total surface fresh water flux 1971-2000 and spatially averaged means.

and +8500 m³/s, respectively. The colors in the left part of Fig. 4.29 refer to the annual mean total surface fresh water flux given in mm/d as the balance of precipitation and evaporation. Positive and negative signs indicate net fresh water input or loss, respectively, i.e. more or less precipitation than evaporation.

Corresponding seasonal means are shown in Fig. 4.30. In the northern North Sea the net surface fresh water flux is characterized by higher precipitation than evaporation rates throughout the year, while both components are comparatively low in spring and summer but high in autumn and winter with a maximum up to +3 mm/d off the Norwegian west coast. In the southern North Sea, however, the seasonality of the two surface fresh water flux components give rise to inversed flux directions for summer and winter. In particular along the Continental coast the high SST in summer entails high evaporation rates because of a strong latent heat flux. At the same time, the precipitation rates are low, finally yielding negative total surface fresh water fluxes up to -2 mm/d. In winter, though, the latent heat flux along the Continental coast is weak, and so is the evaporation rate, but the precipitation rate is high, summing up to positive surface fresh water fluxes up to +2.5 mm/d.

The seasonal cycle of area integrated monthly means and associated variabilities of the total surface fresh water flux for 1951-1980 as well as of its components precipitation and evaporation are shown in Fig. 3.12. The predominantly positive total surface fresh water transports give rise to an annual mean of about +0.53 mm/d for 1971-2000, corresponding to about +3200 m³/s fresh water flux from the atmosphere into the North Sea.

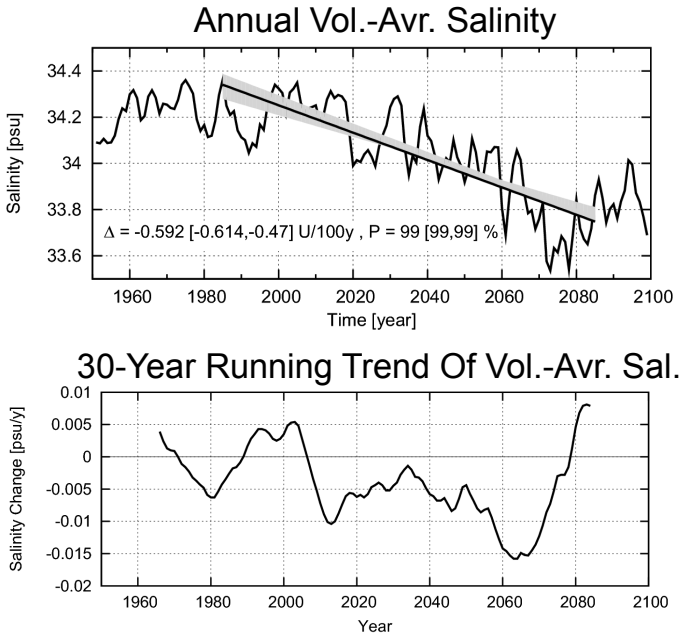

Figure 4.31: Upper part: Time series of annual volume-averaged salinity and representative 100-year trends. Upper and lower quartiles are given in squared brackets and are represented by the gray area about the representative trend (black line). Lower part: Running 30-year trends of the time series shown in the upper part of the figure.

Spatial distributions of the representative 100-year trends of annual mean total surface fresh water flux are shown in the right part of Fig. 4.29. The values in boxes read as changes of the salinity of in- and outflowing water masses, changes of the volume transports, induced changes of the advective fresh water fluxes relative to monthly volume-averaged North Sea salinities, and corresponding changes of fresh water in- and outflow relative to the means of 1971-2000 given in the left part of the figure. The strong salinity reduction of the Fair Isle Current and English Channel flow by about -0.65 and -0.91 psu, respectively, but also the weakening of their volume transports cause a distinct decrease of advective fresh water outflow. The salinity drop at the northern boundary inflow, however, is of lower extent than the drop of the total volume-averaged salinity. Moreover, its volume transport increases, causing the advective fresh water outflow through the northern boundary to increase by about +53%. Note that the mathematically strong increase of advective fresh water inflow via the Norwegian outflow by more than +250% results from the low mean of 1971-2000 but corresponds to an absolute change less than the change at the northern inflow to the east of the Shetland-Islands. The widely uniform increase of total surface fresh water flux of about +61% is induced by lower evaporation rates in summer by about -17% due to lower wind speeds and higher relative humidity, and higher precipitation rates in winter by about +25%.

Again, be aware that changes of the various fresh water fluxes merely account for respective changes of the aspired equilibrium condition of the North Sea salt budget but do not necessarily reflect changes of the volume-averaged salinity given in psu. Nevertheless, the salinity drop at all open lateral boundaries in combination with minor changes of associated inflowing volume transports and the increase of both Baltic discharge and surface

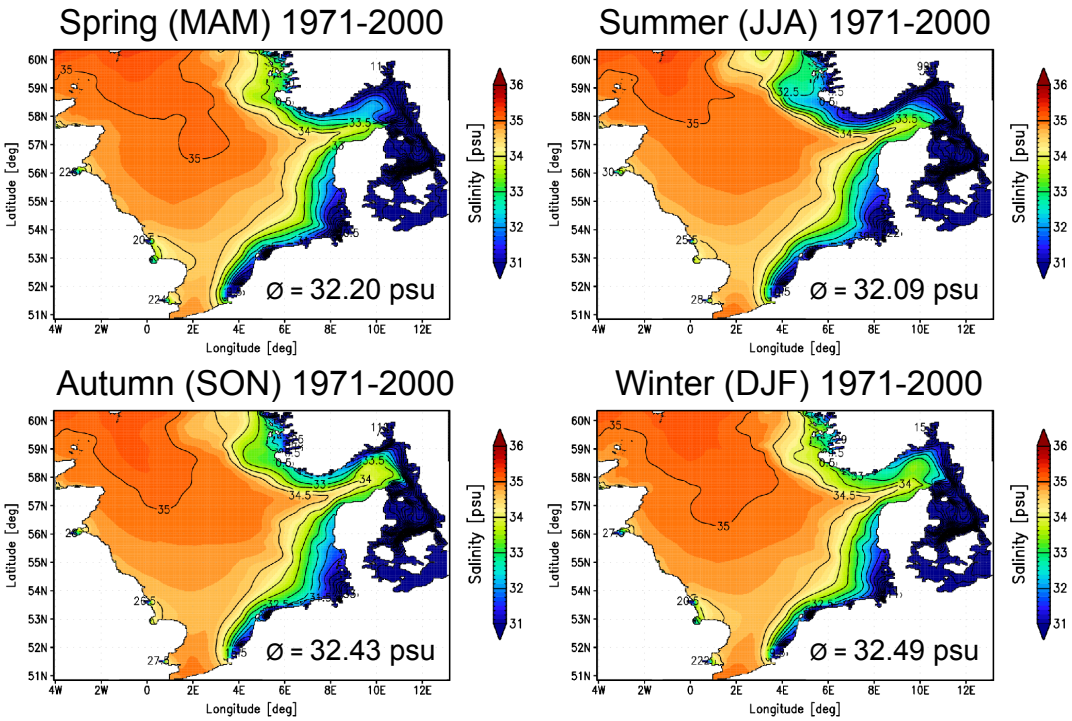

Figure 4.32: Seasonal means of sea surface salinity for 1971-2000.

fresh water flux lastly entail a drop of the volume-averaged North Sea salinity in the 21st century by about -0.59 psu (Fig. 4.31), corresponding to a drop of the total salt content by about -1%, whereby the volume increase of the North Sea due to the global mean sea level rise of about +0.54 m is incorporated. The running 30-year trend of the annual volume-averaged North Sea salinity shown in the lower part of Fig. 4.31 further differentiates the salinity drop into a continuous decrease up to the 2070s from about 34.21 to a minimum of about 33.53 psu, followed by an increase in the last 30 years of the 21st century.

The enhancement of the global hydrological cycle suggested by all IPCC models conveys more moisture from the tropics to the subpolar latitudes, leading to a substantial freshening of the North Atlantic north of 40°N and hence, of the northern and southern North Sea inflows. Spatial distributions of seasonal mean SSS for 1971-2000 and representative 100-year trends are shown in Fig. 4.32 and 4.33. The given trends largely reflect the salinity changes of the northern and southern boundary inflows with the weakest decrease of about -0.4 psu in the northern North Sea and the strongest decrease of about -0.8 psu in the southern North Sea. Both the spatial structure of the salinity trends in the North Sea and their magnitudes are not subject to a pronounced seasonality, with volume-averaged salinity changes between -0.57 psu in summer and -0.61 psu in winter. Be aware that the salinity of the eastern boundary inflow is fixed to monthly climatological means instead of using inappropriate salinities in the Baltic Sea simulated by the respective MPIOM model run (section 2.2.3). The salinity close to the eastern boundary, therefore, does not undergo any change until the Baltic discharge mixes with North Sea waters after the Danish passages. Nevertheless, from the Kattegat region onwards, Baltic discharge indeed influences the salinity via the trend and variability of its volume transport. As given in Fig. 4.14, the largest increase of Baltic runoff of about +18% is recorded in winter, consequently

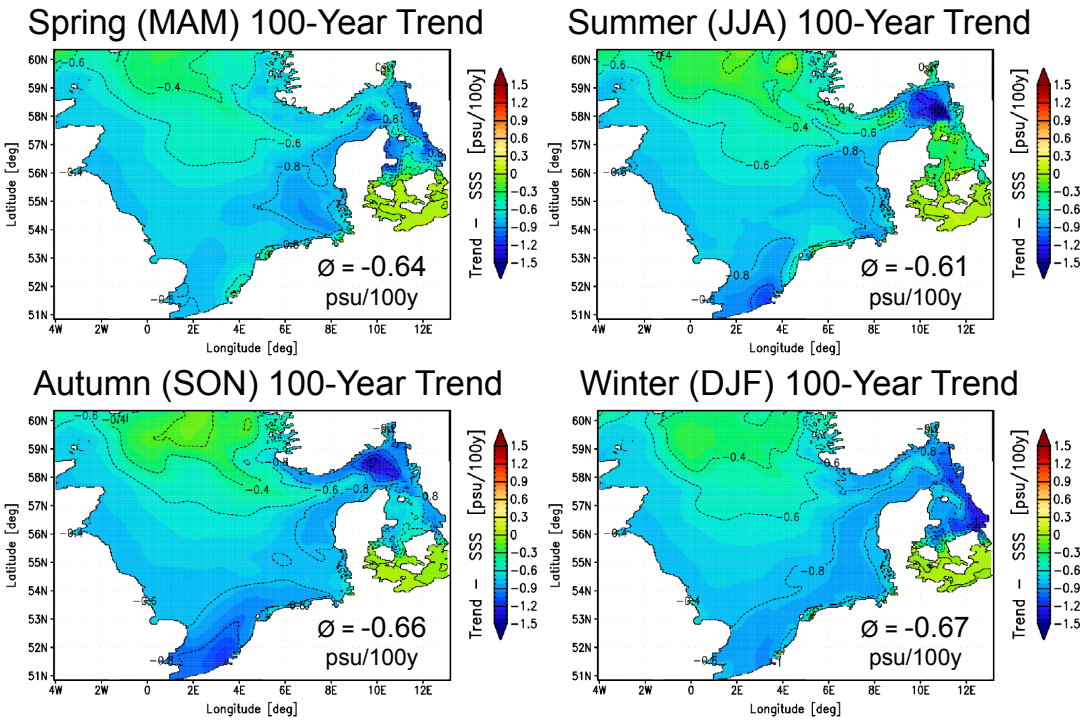

Figure 4.33: Seasonal representative 100-year trends of sea surface salinity.

accompanied by the largest salinity drop of the four seasons in the Kattegat.

The strong salinity decrease in the southern North Sea is primarily induced by the strong salinity decrease of the southern boundary inflow but also by the decrease of its volume transport throughout the year. A reduced southern boundary inflow induces the climatologically fixed river runoff along the Continental coast to propagate farther offshore and by that, to freshen a larger area. In accordance with the significant reduction of southern inflow in summer by about -38%, the two big Continental river plumes of the Rhine and Elbe are subject to pronounced salinity drops. The local maximum salinity decrease in the Skagerrak in summer and autumn can be attributed to the strong reduction of the Skagerrak recirculation in these seasons. A lower amount of saline North Sea waters intrude into the Skagerrak, while in turn, fresh Baltic discharge tend to accumulate and to lower the salinity. When higher riverine discharge into the Baltic and the North Sea in the course of expected higher precipitation rates and a generally wetter climate are taken into account (Bárdossy and Pegram, 2011), the salinity of the North Sea can be expected to decrease to an even higher extent (Schrum, 2001; Meier, 2006). Further analysis of regional salinity and surface fresh water flux anomalies are discussed in section 4.2.3 by means of EOF analysis.

4.1.6 T-S Diagrams

Finally, in Fig. 4.34 monthly T-S diagrams of 1951-1980 are constructed from the water temperature and salinity distributions, as a method to analyze typical seasonal features of distinct water bodies. The dominating aspect in the annual T-S cycle is clearly constituted by the rise and fall of the water temperature of the surface layers, to be identified in the

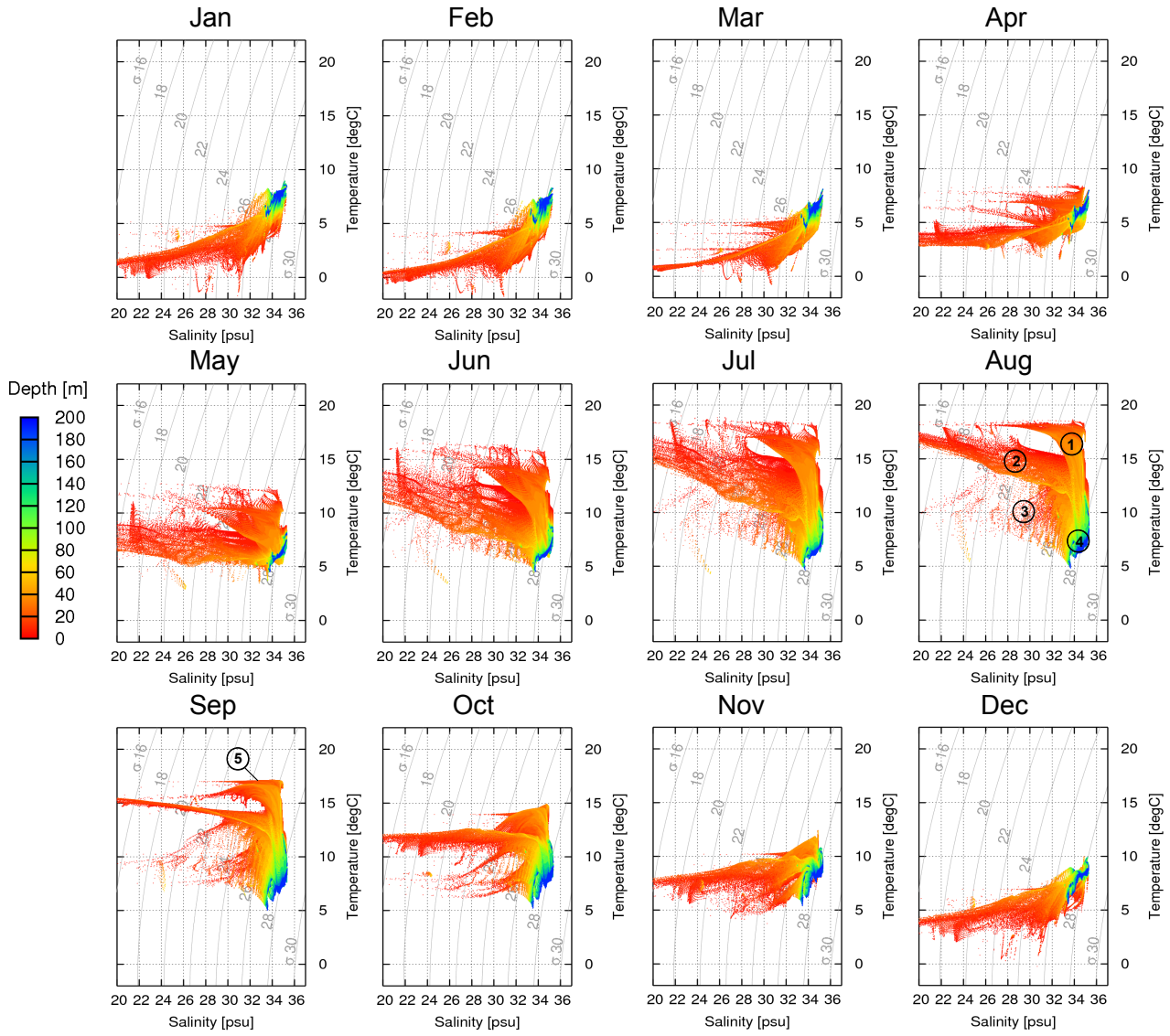

Figure 4.34: Monthly mean T-S diagrams of 1951-1980. Gray lines represent isopycnals of potential density. Colors refer to different water depths, where the blue end of the color bar refers to water depths greater or equal to 200 m. The inserted numbers refer to the formation of distinct water bodies as explained in the text.

figure by red color. While distinct water bodies are hardly recognized from the vertically mixed water column in winter, the stratified conditions in summer allows the specification of five characteristic water bodies by means of core layer analysis according to Wüst (1935). Tongue-like distributions of water properties are thereby used to identify distinct water bodies by defining core properties from local minima or maxima of property distributions. Apart from a few Continental estuaries, the T-S distributions in winter single out the mixed condition of the water column to represent mainly one continuous hydrographic formation in the North Sea. In summer, however, several tongue-like distributions are formed in the T-S diagrams, most clearly pronounced in August. The warmest water body is represented by the thermally stratified bulk of the central and northern North Sea (1), where surface layers with a depth up to about 30 m (red) acquire higher temperatures than underlying deeper layers up to about 70 m (orange). A low salinity water body is constituted by the thermo-haline stratified Baltic discharge and surface waters of the Kattegat

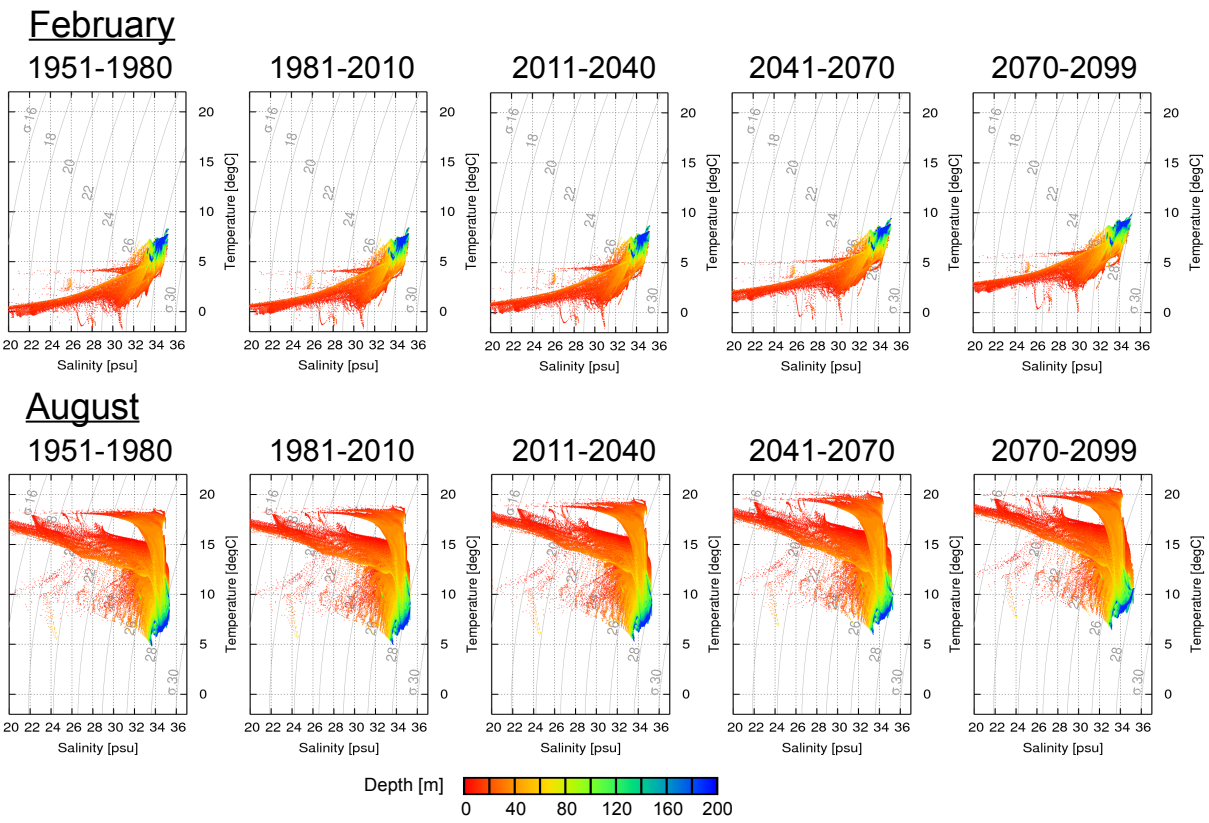

Figure 4.35: T-S diagrams of February and August of successive 30-year slices from 1951 to 2099.

and Skagerrak region (2), where surface layers (red) show higher temperatures and lower salinities than deeper layers (orange). (3) specifies a water body of low surface temperatures and low salinities to be identified with the Norwegian Fjords, where the high amount of cloud cover restricts incoming short wave radiation and the high amount of precipitation and accordingly, the strong coastal fresh water runoff lower the salinity. Deep waters of the northern North Sea and the Norwegian Trench at depths greater than about 100 m (green and blue) are represented by (4), where cool and salty waters are subject to a very weak seasonality, consisting of rather homogeneous properties.

In September and October the destruction of the thermocline is indicated by the cooling of the surface layers (red) of (1) and (2), which indeed acquire lower temperatures than the underlying deeper layers (orange). The entailing higher densities finally introduce vertically unstable conditions. Besides, the cooling of the stratified surface layers in September uncovers the water body of the tidally mixed water column along the British and Continental coasts (5) in which the deeper layers (orange) show the same high temperature than the surface layers (red). Since the cooling of the mixed water column takes a longer time than the cooling of the surface layers in the thermocline region because of the effect of differential heating, the temperature decrease of the mixed waters is slightly delayed, bringing about the mixed water body (5) to become visible behind the stratified water body (1).

In Fig. 4.35 successive 30-year slices of T-S diagrams for the entire simulation period 1951-2099 are depicted for the coldest and warmest month of the year. The progression

clearly indicates that the general structure of the identified water bodies is widely maintained during the warming and freshening of the North Sea in the 21st century. In summer the T-S formation rises rather uniformly by about +1.64 °C, indicated by the time series of Fig. 4.21. In winter, however, the T-S formation becomes slightly flatter, since the SST suffers a stronger increase (+1.95 °C) than the deeper waters (volume-averaged increase +1.8 °C) because of differential heating. Moreover, the upper layers are stronger affected by the freshening of the North Sea, with a freshening about twice as much as the freshening of the deeper layers and a local maximum salinity decrease up to -1.2 psu. This effect holds for all seasons and can be attributed to the increasing fresh water supply from the atmosphere and the Baltic Sea, which tends to stay close to the sea surface.

4.1.7 Sea Surface Height

While SSH changes due to the uniformly imposed global sea level rise cause a significant increase of SSH over the entire North Sea by about +50 cm over 100 years (see Fig. 2.35), local changes of SSH result from changes in both the thermo-steric and halo-steric contribution as well as from changes in the wind-induced south-eastern surge and changes in the general circulation via the related geostrophic pressure compensation. Seasonal mean SSH of 1971-2000 and respective 100-year trends are shown in Fig. 4.36 and 4.37.

The effect of changes in the general circulation is best recognized along the Norwegian Trench (Fig. 4.37). The decreasing flow speeds in summer, autumn, and winter indicated in Fig. 4.14 induce weaker horizontal SSH gradients perpendicular to the flow direction because of the weaker pressure gradients of the geostrophically balanced current. The region of local SSH depression along the Norwegian Trench undergoes a stronger SSH increase than the SSH along the south-eastward flow aligned to the western side of the Norwegian Trench, consequently giving rise to the weaker horizontal SSH gradients. In spring, on the contrary, the enhanced general circulation induces the horizontal SSH gradients to increase, as indicated by the SSH depression along the Norwegian Trench to undergo a lower SSH increase than the adjacent speeding-up south-eastward flow.

Since the general circulation in the North Sea is largely determined by wind forcing (see section 1.2.4), SSH changes due to changes in the wind-induced south-eastern sea level surge are intimately linked to changes in the general circulation as well. As discussed in section 4.1.2, the increase of the general circulation in spring can be attributed to a respective increase of westerly wind conditions. Besides, relative to the other seasons, both the temperature increase and the salinity drop in the southern and eastern North Sea in spring are moderate, yielding the SSH increase due to steric effects to be moderate, too. Hence, in spring, the strong SSH increase in the southern and in particular in the eastern North Sea can be attributed to more frequent wind surges. The trends of the wind density function shown in Fig. 4.9 and associated wind speed and relative frequency plots indicate the increasing westerly wind conditions in spring to mainly result from a transition of south-easterly wind directions to more frequent westerly wind directions rather than from increasing westerly wind speeds. The entailing increasing wind surges are thus to

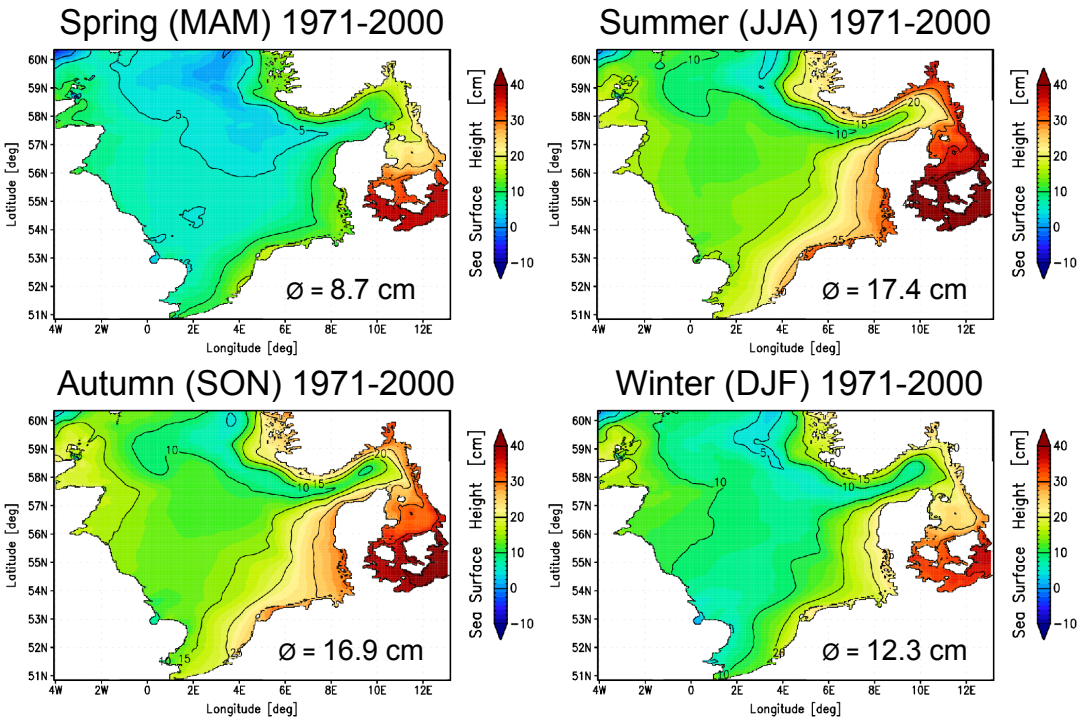

Figure 4.36: Seasonal means of sea surface height for 1971-2000.

be understood as higher mean sea level elevations, in contrast to higher maximum water levels from stronger storm surges.

Apart from the Norwegian Trench, the SSH changes in summer and winter are apparently dominated by the thermo-steric effect. As indicated by the temperature trends shown in Fig. 4.24, the bathymetry strongly influences the local warming of the water column in winter. Consequently, in the shallow southern North Sea where the temperature increase is stronger the SSH increases to a larger extent than in the deeper central and northern North Sea where the temperature increase is weaker. In summer, however, the spatially more uniform warming causes the water column along the shallow Continental coast to expand to a lesser extent than in deeper mixed regions and in the thermocline region farther north, reflected by respective SSH changes.

Moreover, indicated by the transport trends given in Fig. 4.14, the Baltic discharge of low salinity waters is increasing most strongly in winter. Thus, both the increasing volume transport and the resulting decrease of salinity from north of the Danish passages induce the strongest halo-steric SSH rise in the eastern North Sea to happen in winter, too. The striking SSH increase in the Skagerrak in summer and autumn can be attributed to the accumulation of low salinity waters in this region due to lower recirculation rates, discussed in section 4.1.5, as well as to the entailing weakening of the horizontal SSH gradient. The similar SSH rise in the Skagerrak in spring, however, apparently conflicts with both the *increasing* recirculation rate, which is supposed to *steepen* the horizontal SSH gradient, and the inconspicuous temperature and salinity trends. Closer analysis of the recirculation pattern in the Skagerrak though reveals that most of the enhanced inflow crosses the Skagerrak northwards right before the SSH trend anomaly. A restricted local

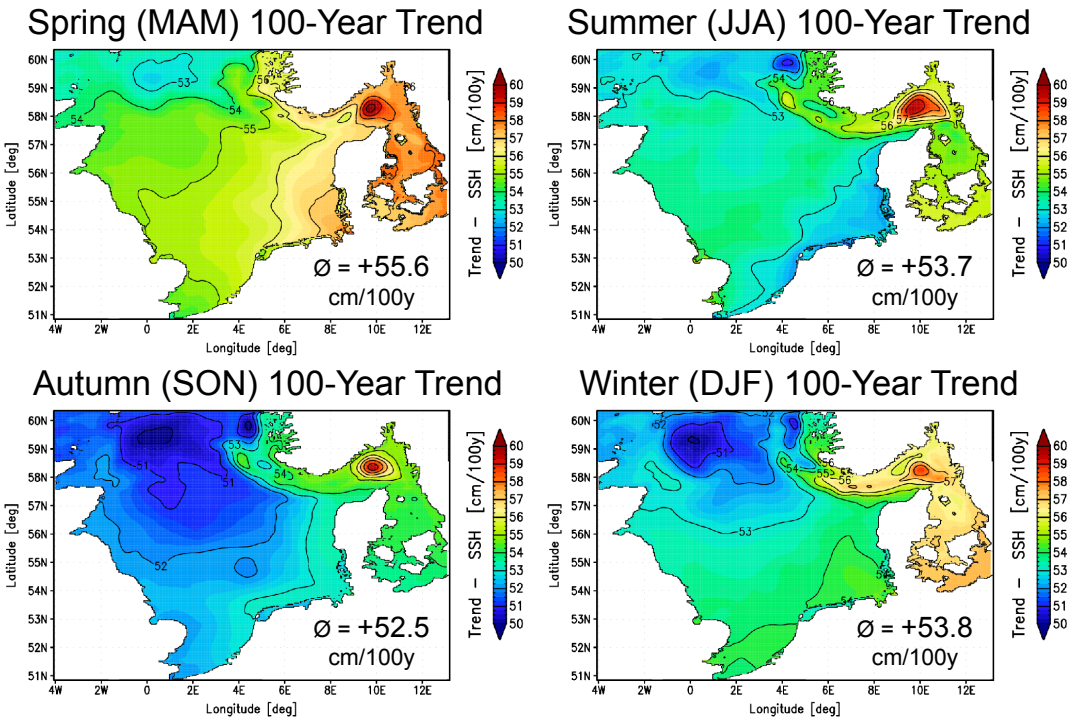

Figure 4.37: Seasonal representative 100-year trends of sea surface height. Divide the numbers given in cm/100y by 10 to obtain the often used unit mm/y.

SSH depression thus emerges to the west of the SSH trend anomaly, while the strength of the recirculation deeper into the Skagerrak is indeed weakened, consequently giving rise to the lower horizontal SSH gradients as indicated by the SSH trend anomaly. Further analysis of regional SSH anomalies and correlations are discussed in section 4.2.4 by means of EOF analyses.

4.2 EOF Analysis

The most important aspects of the probabilistic structure of time series can be examined either in the time-domain by studying autocorrelation functions, or in the frequency-domain by studying power spectra as applied in section 2.2.2 for the comparison of REMO and ERA40. By applying an autoregressive model, a certain behavior of the examined time series is presumed according to the chosen order of the autoregressive model. In order to appropriately fit an autoregressive process to a given time series, BIC (Bayesian information criterion; Schwarz, 1978) and AIC (Akaike information criterion; Akaike, 1973) statistics are often used to decide among potential orders of autoregressive models (von Storch and Zwiers, 1999; Wilks, 2005). Both criteria, however, yield to autocorrelation coefficients of 1 for lag-0 and 0 otherwise for any detrended, spatially averaged interannual time series considered in this study, indicating the data discussed in the previous sections to be best described as white noise about their long-term trends. To extract probabilistic information anyhow, regional correlations and variabilities are taken into account by the application of EOF analysis.

Empirical orthogonal function (EOF) analysis of weekly and monthly oceanographic data in the North Sea has already been discussed in the literature (e.g. Becker and Pauly, 1996; Dippner, 1997; Wiltshire et al., 2010). In considering such time series, however, the principal components (PCs) as well as the spatial EOF patterns are dominated by the strong seasonal cycle in particular of sea water temperature but also of salinity. In the present study EOF analysis is applied to interannual variabilities of each of the four seasons separately. In this context the analysis of depth-averaged temperatures reveals more spatio-temporal information than that of surface values, since the deeper regions are less influenced by atmospheric forcing and are therefore expected to obey different dynamics. Besides, since the magnitude of density anomalies is much smaller than of temperature anomalies, the analysis of depth-averaged temperature anomalies yields qualitatively similar information about heat content anomalies. Moreover, most of the fresh water discharge into the North Sea tends to stay at the sea surface. Any dynamics of deeper regions cannot be accounted for by analyzing mere surface values. Even though in general, the structures and magnitudes are more pronounced in the EOF patterns of surface salinity, the structures of the second and third EOF patterns of depth-averaged salinity described below become displaced by rather confused patterns when analyzing surface salinity, which are probably related to variable wind conditions. Thus, for both temperature and for salinity the EOF analysis is based on depth-averaged values. Anomalies of SSH and of the general circulation are also taken into account. In order to obtain pure anomalies by removing trends and means from the data, a third order polynomial least square fit over the entire simulation period 1951-2099 is subtracted from the time series of every grid cell.

The EOF patterns shown in the following sections represent rescaled EOF patterns of the control period 1951-2000 that reflect the variability of the parameter at hand by depicting the standard deviation of the principal components (PCs) multiplied by the unscaled EOF patterns. For salinity anomalies, additional patterns are provided that reflect the correlation coefficients between the unscaled EOF patterns and the associated PCs. In order to assign meaningful related physical processes to the different EOF patterns, further correlations between the principal components and various other time series, e.g. of volume transports and wind density functions, are taken into account. Nonetheless, the obtained correlation coefficients rarely exceed 0.6, emphasizing the complex interactions of the numerous physical processes involved in the North Sea dynamical system. Examples of pronounced anomalies from selected years are given as well. Finally, all PCs are extended until the year 2099 in order to address changes of the considered variabilities in the scenario period 2001-2099. Like in the previous sections, all analyses concerning the winter season are again based on averages over December, January and February, where the winter of a given year refers to December of that particular year and to January and February of the following year.

4.2.1 General Circulation

Considering interannual variabilities of the four seasons, the varying wind conditions in the North Sea and their interaction with the inflow of Atlantic waters through the open

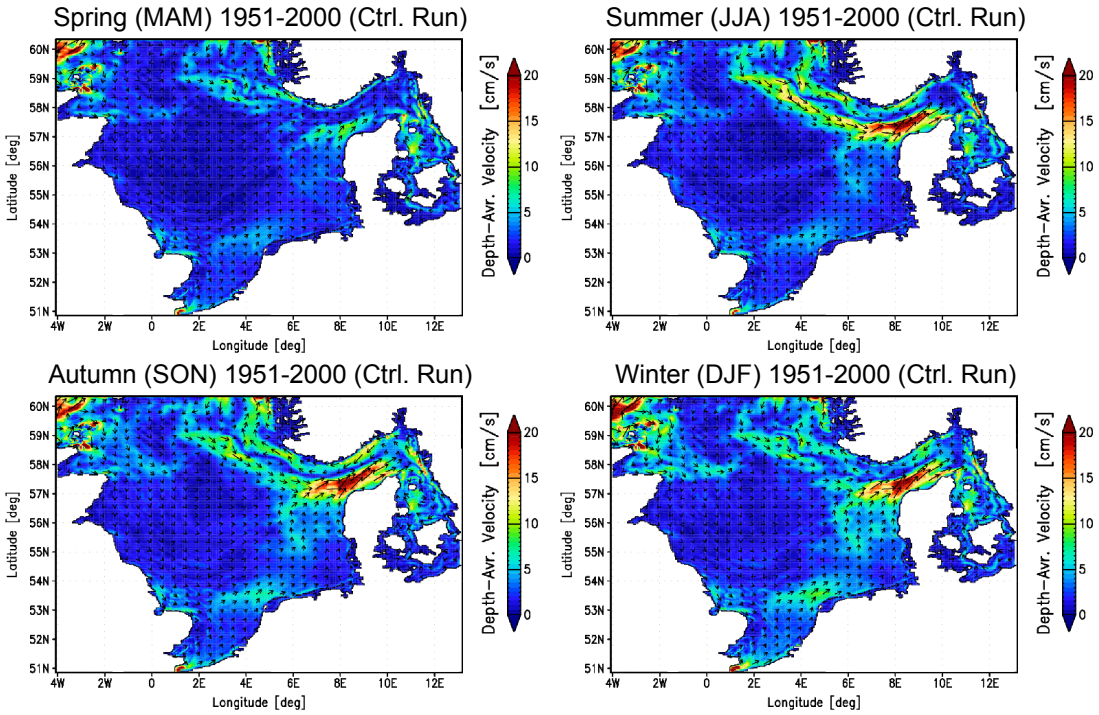

Figure 4.38: Seasonal mean depth-averaged current velocities for 1951-2000.

boundaries determine the variability of the general circulation, where the term 'circulation' is referred to in the following analysis by depth-averaged velocity vectors. In order to calculate the EOF patterns of the velocity vectors, the two vector components u and v are treated as independent scalar quantities, which they are usually not for natural fluid flows. However, at least the first and second PCs of u and v discussed in this study show high correlation coefficients ranging from +0.95 to +0.99 for the different seasons with confidence levels higher than 99%, which assures the resulting u and v EOF patterns to account for the same anomalies in the data. Therefore, the individual EOF patterns of u and v can be combined again to draw meaningful joint EOF patterns consisting of velocity vector anomalies. The so obtained first and second EOF patterns of the circulation are depicted in Fig. 4.39 and 4.40, respectively. Be aware that the direction of the vectors depends on the correlation with the corresponding PC. Thereby, the signs are chosen for a positive anomaly in the PC to refer to a velocity anomaly in the direction of the depicted EOF vectors and consequently, a negative PC anomaly to refer to an anomaly in the opposite direction. In order to indeed reconstruct an individual current field represented by an EOF and its PC, the respective anomaly vectors simply need to be added to the mean velocity vectors shown in Fig. 4.38. The magnitudes of the anomalies in the EOF patterns are rescaled into standard deviations of the current speed. The first EOF patterns of the circulation (Fig. 4.39) indicate the strongest variability to occur along the Norwegian Trench throughout the year with velocity anomalies up to ± 8 cm/s. Since the mean circulation is weakest in spring (see Fig. 4.38), the considerable wind speeds and their anomalies (see Fig. 2.29 and 2.30) give rise to pronounced anomalies of the circulation in the Norwegian Trench, whereas the low wind speeds in summer hardly affect the northern inflow and consequently give rise to a more stable circulation. In autumn and winter the general circulation in the North Sea as well as the current variability in the Norwegian Trench are

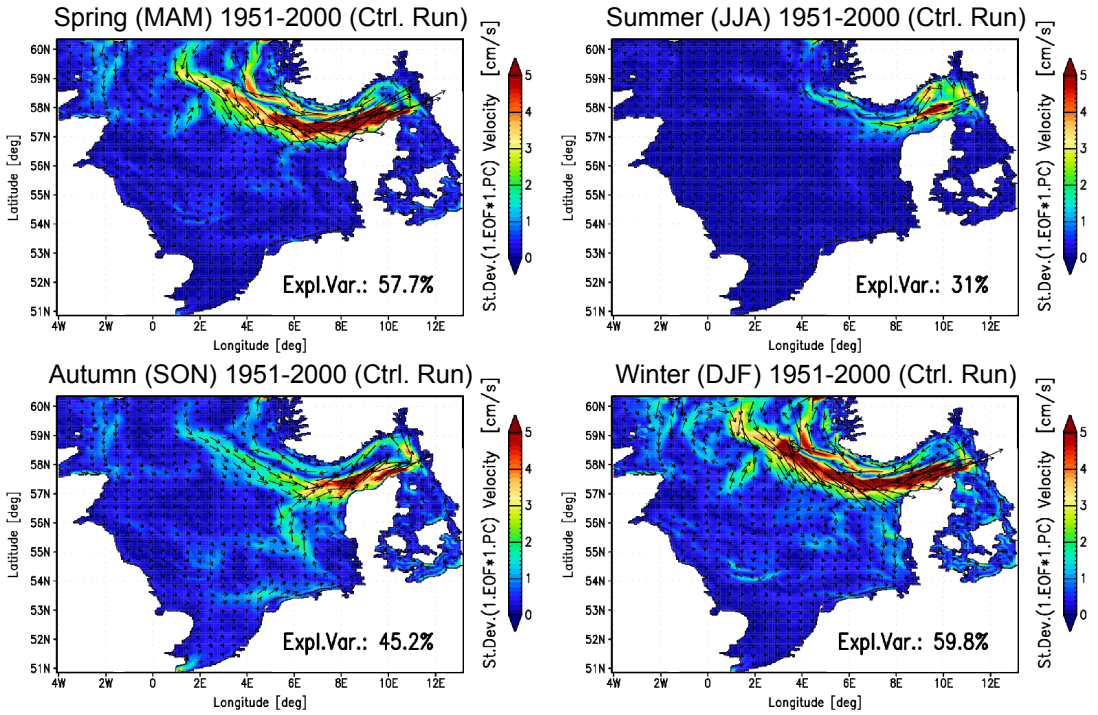

Figure 4.39: Rescaled first EOF patterns of depth-averaged current velocity.

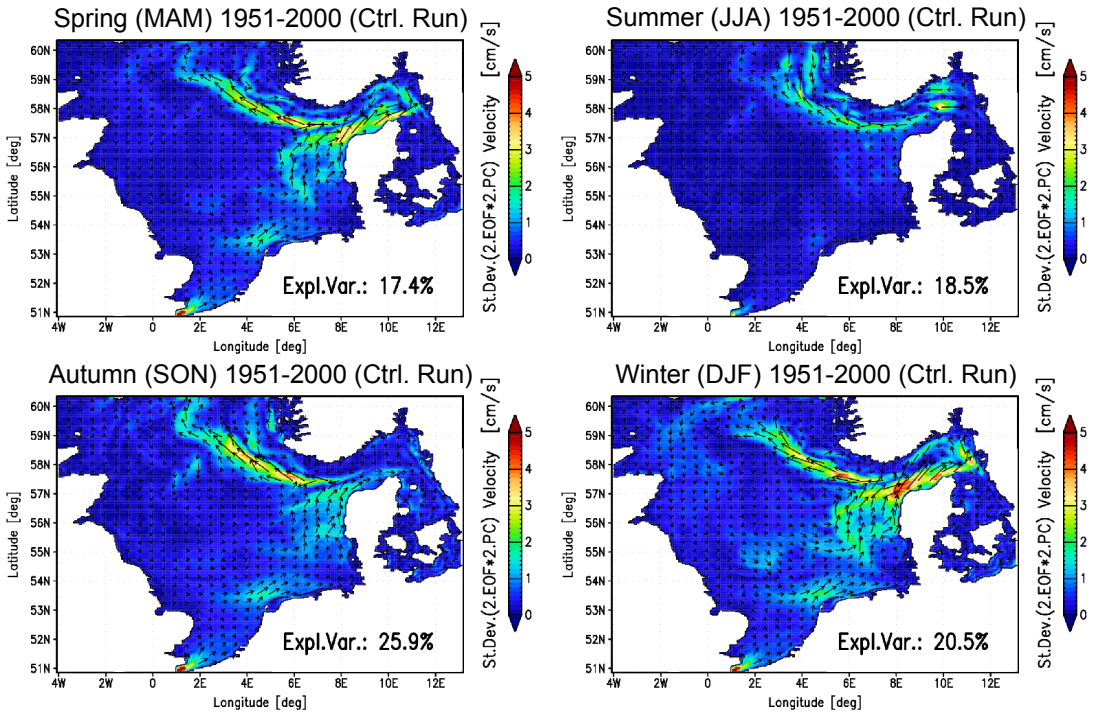

Figure 4.40: Rescaled second EOF patterns of depth-averaged current velocity.

comparatively strong. The proportions of the total variance that are explained by the first EOF patterns amount to 31-60%.

In order to understand and to quantify the relation between anomalies of the wind field and anomalies of the general circulation, the variability of the wind density function (see section 2.2.3) and its correlation with the first PC of the circulation are considered. For the

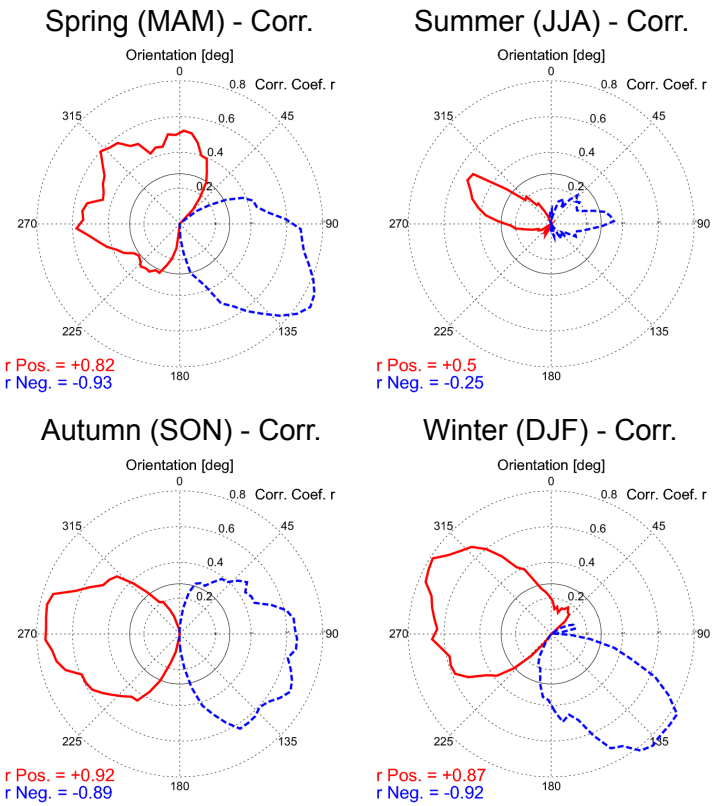

Figure 4.41: Correlations between the wind density functions and the first PCs of the circulation, analyzed for the period 1951-2000. Red solid lines represent positive correlations, blue dashed lines represent negative correlations. Solid black circles represent the 95% confidence level.

variability of the circulation to be related to varying wind conditions from different wind directions, both the magnitude of the anomalies at each wind direction and the correlation of the anomalies at each wind direction with the anomalies of the circulation need to be taken into account. Therefore, in extension to the wind density function devised by Siegismund and Schrum (2001) and depicted in Fig. 2.29, the effective variability $s_{eff}(wind, circ)$ of the wind field with respect to the circulation is introduced and referred to hereafter as the effective wind variability. It is defined as the product of the correlation coefficient $r_i(wind, circ)$ between the wind density function and the first PC of the circulation (Fig. 4.41) and the standard deviation $\sigma_i(wind)$ of the wind density function (Fig. 2.30), integrated over all wind direction sectors n.

$$s_{eff}(wind, circ) = \frac{1}{n} \sum_{i=1}^{n} | r_i(wind, circ) \cdot \sigma_i(wind) | \tag{4.4}$$

This quantity is designed to estimate the degree of interaction between the variability of the wind conditions and the variability of the general circulation. However, the effective wind variability carries the physical unit of wind speed and since the maximum possible standard deviations about a given mean wind density function are restricted by and hence, dependent on the individual magnitudes of the mean function, the effective variability needs to be regarded as a relative quantity. Accordingly, it is the most meaningful when comparing different time periods or different data sets of one and the same geographic region. In this sense a comparatively high effective variability indicates the variability of the

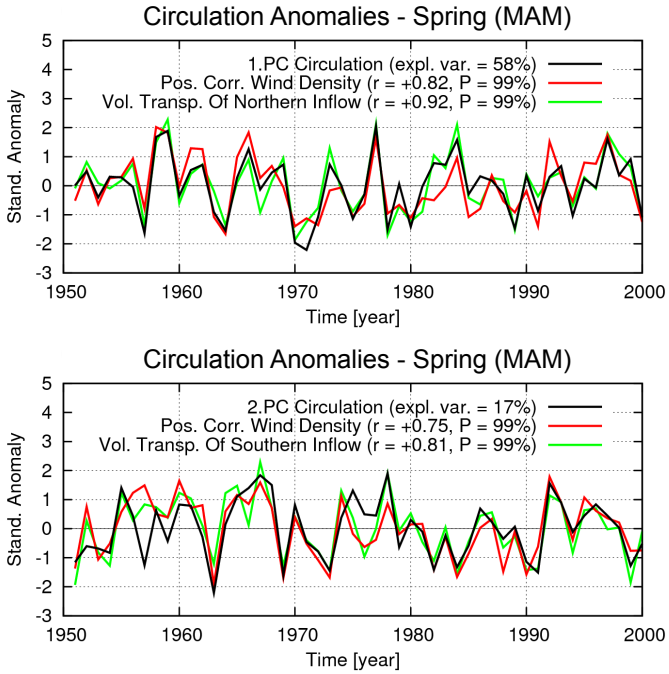

Figure 4.42: Black lines: PCs of depth-averaged current velocity. Red lines: Positive correlated wind density according to Fig. 4.41 and 4.44. Green lines: Inflowing net volume transports through the northern boundaries and the southern boundary. The inscribed correlations refer to the respective PC.

wind conditions to contribute more enhancingly (or less attenuatingly) to the variability of the circulation than in case of a comparatively low effective variability. As calculated from (4.4), the mean effective wind variability for spring, summer, autumn, and winter amounts to 1.50, 0.33, 1.58 and 1.95 m/s, respectively. The higher value for autumn than for spring indeed suggests the variability of the circulation to be higher in autumn, too. However, the corresponding eigenvalues of the EOF patterns, which are proportional to the variance of the data that is explained by the EOFs, rather indicate a higher variability in spring. In order to account for the higher variability in spring properly, the effective inflow variability $s_{eff}(inflow, circ)$ is introduced analogously, that is, the standard deviation $\sigma_i(inflow)$ of the n boundary inflows weighted by the correlation $r_i(inflow, circ)$ between the boundary inflows and the first PC of the circulation.

$$s_{eff}(inflow, circ) = \sum_{i=1}^{n} |\, r_i(inflow, circ) \cdot \sigma_i(inflow)| \tag{4.5}$$

Likewise, this quantity is designed to estimate the degree of interaction between the variability of the net inflowing volume transport through the open boundaries of the domain and the variability of the general circulation. Calculated from (4.5), the mean effective inflow variability for spring, summer, autumn, and winter amounts to 0.20, 0.07, 0.15 and 0.27 Sv, respectively. While the effective wind variability for spring is about 5% lower than for autumn, the effective inflow variability is about 33% higher, finally giving rise to a higher circulation variability in spring.

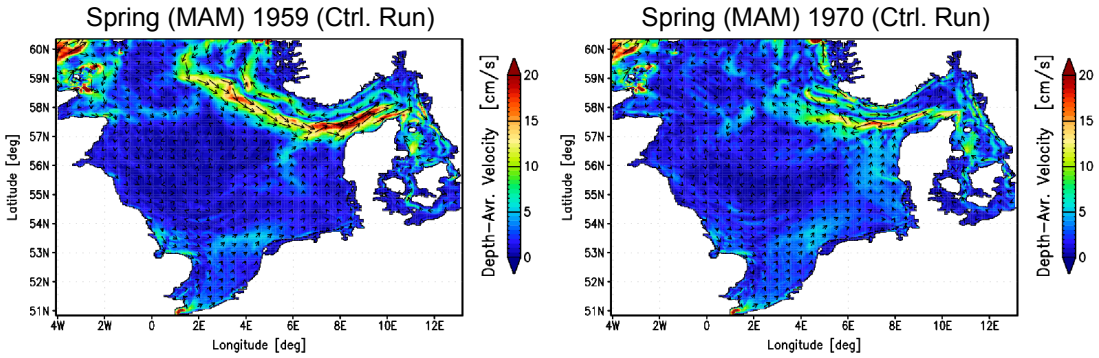

Figure 4.43: Examples of pronounced anomalies of the first PC of depth-averaged current velocity for spring (Fig. 4.42), where spring 1959 represents a positive, and spring 1970 a negative anomaly.

Fig. 4.41 shows seasonal correlations between the time series of the wind density function and the first PC of the circulation, where the red solid and blue dashed lines represent positive and negative correlations, respectively. The graphics clearly indicate a separation in positively correlated (i.e. circulation enhancing) westerly wind conditions and negatively correlated (i.e. circulation attenuating) easterly wind conditions in the North Sea model. Once the sign of the correlation for each wind direction is ascertained, the wind density function values of all equally correlated directions are summed up and correlated again with the first PC of the circulation in order to represent the total correlation of the dominating wind condition. The respective total correlations are inscribed to the lower left of the correlation graphics. Examples for a positive and negative circulation anomaly given in Fig. 4.43 are chosen from the standardized first PC shown in Fig. 4.42. In agreement with the circulation enhancing westerly and north-westerly winds, anomalies of the northern boundary inflow and the Fair Isle Current well contribute to the first circulation EOF with a positive correlation of +0.58 to +0.97 (P=99%), whereas the inflow through the English Channel remains fairly uncorrelated. Standardized anomalies of the positively correlated wind density function according to Fig. 4.41 as well as of the volume transports through the northern boundaries (i.e. the northern and the western boundary) are also shown in Fig. 4.42.

However, anomalies represented by the second EOF patterns of the circulation (Fig. 4.40) are induced by north-south oriented anomalies of the wind conditions. Fig. 4.44 again shows the correlation between the wind density functions and the second PC of the circulation. Since the second EOF patterns merely account for 17-26% of the total variance, both the effective wind variabilities and in particular the effective inflow variabilities are much lower than for the first EOFs. Nonetheless, the inflow through the English Channel becomes affected by the north-south wind anomalies with a positive correlation of +0.60 to +0.81 (P=99%) between English Channel flow anomalies and the second PC of the circulation, whereas the northern inflows are weakly negatively correlated. Consequently, the circulation in the southern North Sea and the strength of the Jutland Current are enhanced (weakened) up to ± 4 cm/s by southerly (northerly) winds, but the circulation in the Norwegian Trench is weakened (enhanced), as indicated by the second EOF patterns.

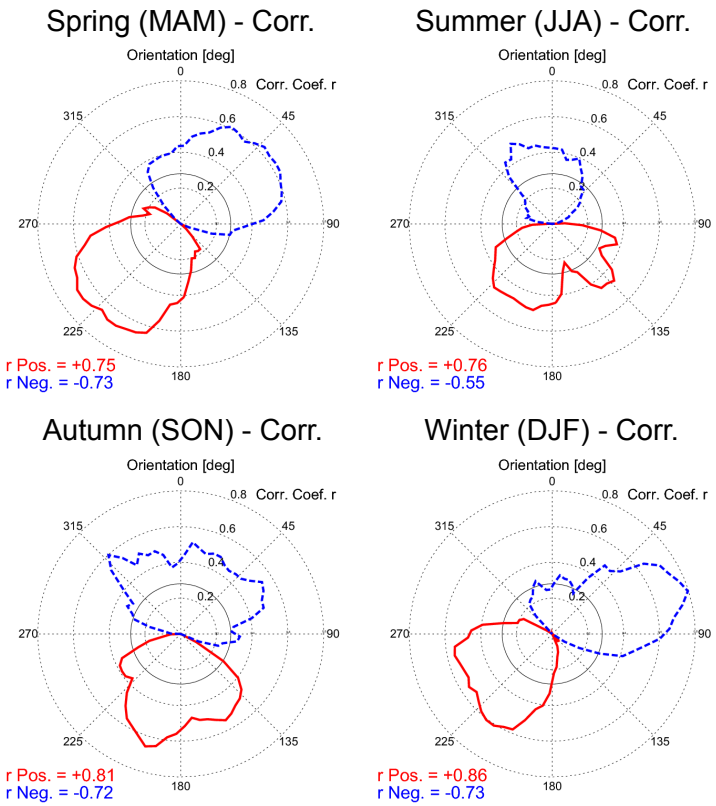

Figure 4.44: Correlations between the wind density functions and the second PCs of the circulation, analyzed for the period 1951-2000. Red solid lines represent positive correlations, blue dashed lines represent negative correlations. Solid black circles represent the 95% confidence level.

Be aware that in the EOF analysis mere *anomalies* of the variable at hand are considered, i.e. temporal means and trends are removed at every grid point in advance to the analysis. Hence, in the EOF patterns the dynamical behavior of different regions relative to each other is singled out independently of the long-term trends. The identification of a specific change in the wind density function to occur in a positively or negatively circulation-correlated sector according to Fig. 4.41 and 4.44 indeed *hints* at a change of the general circulation and associated boundary transports. However, it does not tell how much the *magnitudes* of the net volume transports are affected *from year to year*, which finally cause the long-term trends. Therefore, even though changes in the wind density function are able to reflect the most significant transport trends, the latter can not be reliably inferred from the former.

The evaluation of REMO wind conditions by comparison with ERA40 reanalysis data in section 2.2.3 revealed a higher occurrence of south-easterly wind conditions in the REMO data, represented by the wind density functions shown in Fig. 2.29. Remember that the wind directions are not modified in the course of the bias correction. In order to address the implication of the qualitatively differing wind conditions in the two data sets, the total variability of the circulation is calculated as the square root of the sum of all eigenvalues obtained from the EOF analysis. Considerably higher effective wind and inflow variabilities in spring yield a stronger total variability of the circulation of +13% in the REMO driven simulation, whereas lower effective variabilities in winter yield a weaker total variability

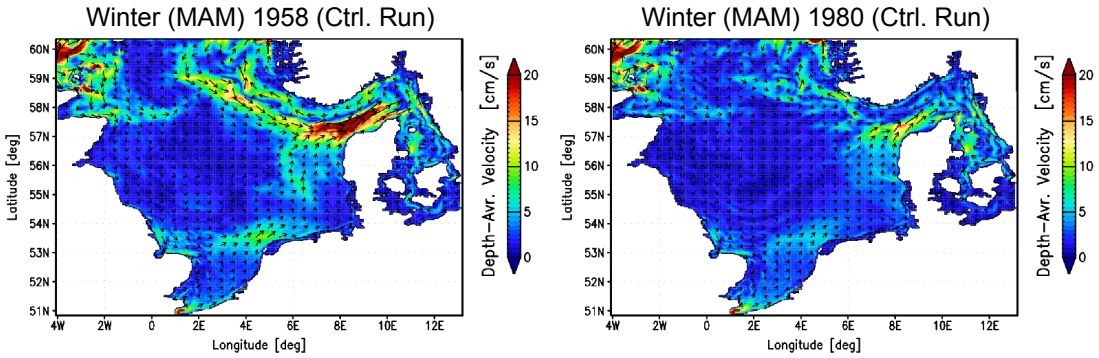

Figure 4.45: Examples of pronounced anomalies of the first PC of depth-averaged current velocity for winter, where winter 1958 represents a positive, and winter 1980 a negative anomaly.

of likewise -13%. The enhanced circulation variability in spring is even strong enough to occasionally reverse the seasonally mean south-easterly flow along the western side of the Norwegian Trench, as exemplified in Fig. 4.43, which is accompanied by a negative salinity anomaly in that region caused by displaced Skagerrak waters (Fig. 4.63). In the ERA40 driven simulation, however, negative circulation anomalies in spring merely weaken the mean circulation in the Norwegian Trench rather than reverse it, just like for the other seasons in both simulations. Pronounced winter circulation anomalies of the REMO driven simulation are demonstrated in Fig. 4.45. Nevertheless, after reducing the total variability of the mean circulation in spring by -13%, it is still larger than the total variability in autumn by about +9% so that the EOF results discussed in this section qualitatively still hold. Finally, the differing wind conditions in the REMO driven simulation give rise to weaker annual mean volume transports in the northern North Sea by about -10% with respect to the ERA40 driven simulation (see Fig. 3.4).

4.2.2 Water Temperature

In Fig. 4.46 to 4.48 spatial maps of the first three rescaled EOFs of depth-averaged sea water temperature are shown. The temperature variability in the North Sea is mainly governed by heat exchange with the atmosphere and to a lesser extent by variable water exchange with the adjacent North Atlantic. However, since the water temperature of the eastern North Atlantic is determined by the temperature and strength of the North Atlantic Current rather than by the condition of the atmosphere, the two components of heat exchange in the North Sea are fairly independent of each other. Hence, it can be expected the temperature variability induced by the dominant atmospheric heat exchange to be represented by the first EOF, whereas the influence of the water transports through the open boundaries, as being the complementary component, ought to be reflected by subsequent EOFs.

The first EOF patterns (Fig. 4.46) show a continuously increasing temperature variability from north to south with maximum deviations from the local mean temperature (Fig. 4.49) of ± 1 °C. However, most of the variability of the atmospheric forcing that influences the surface heat fluxes in the North Sea (like the variability of wind speed, relative humidity and air temperature) can be regarded as fairly uniformly distributed over the domain. The

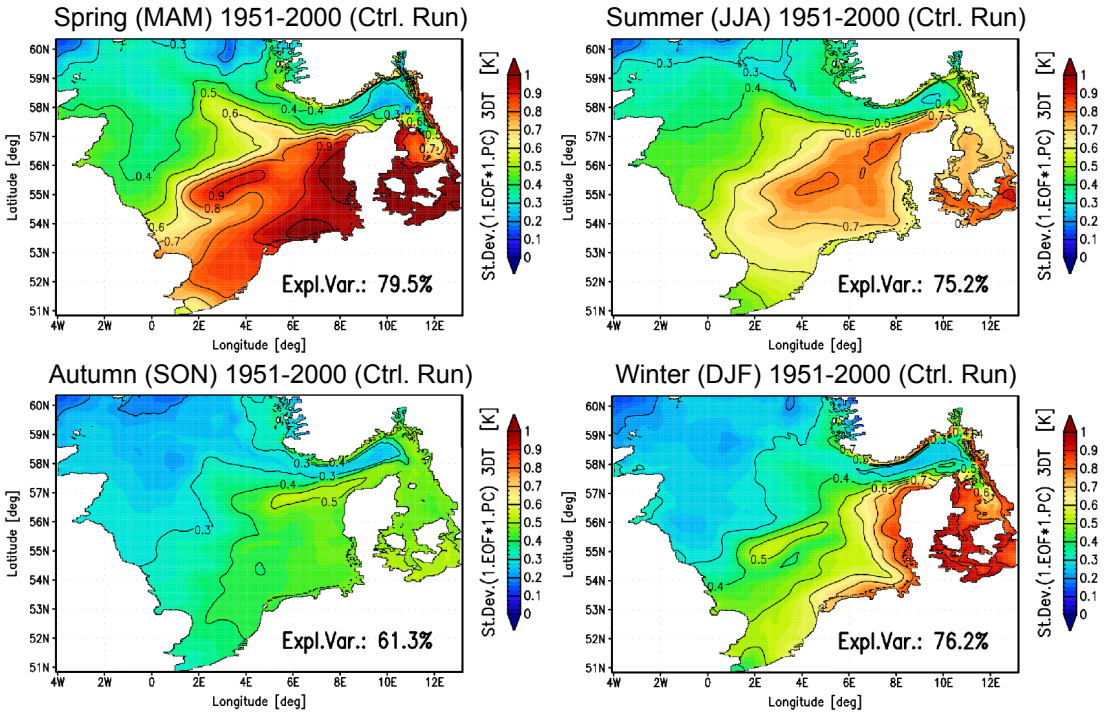

Figure 4.46: Rescaled first EOF patterns of depth-averaged sea water temperature.

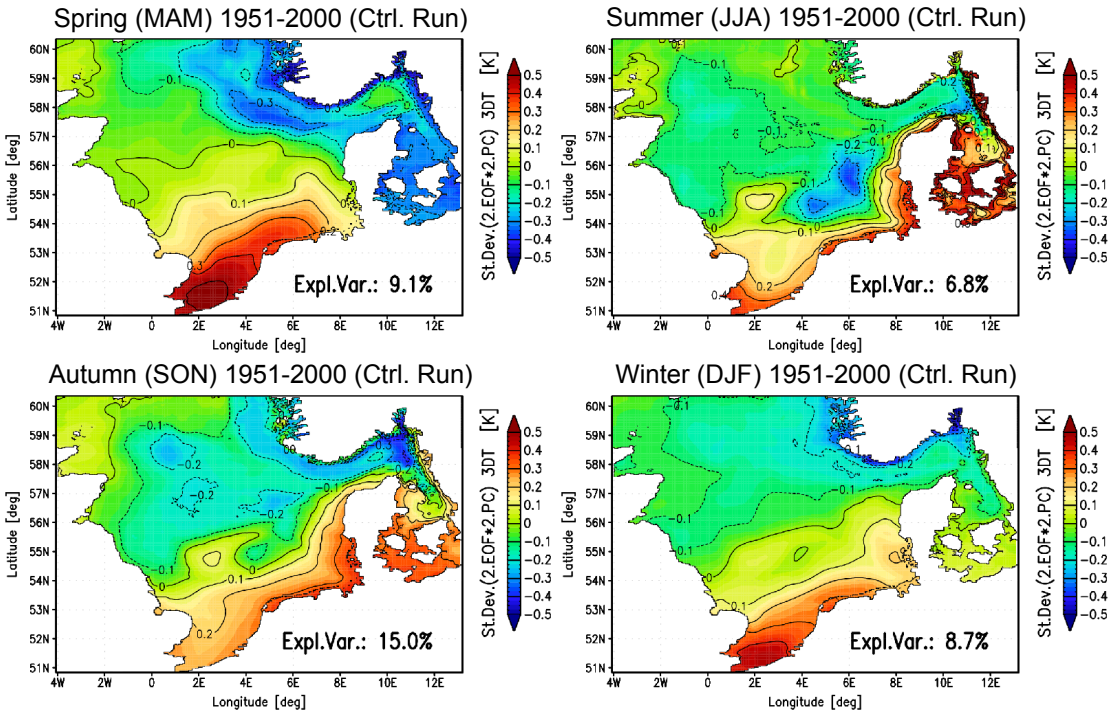

Figure 4.47: Rescaled second EOF patterns of depth-averaged sea water temperature.

stronger impact of atmospheric variabilities on the temperature variability in the southern North Sea is thus induced by differential heating in dependence on the bathymetry. The correlation between the first PC of sea water temperature and the time series of the spatially averaged 2m air temperature ranges from +0.76 to +0.93 (P=99%) for the different seasons. From comparing these time series in Fig. 4.50, examples of positive and negative temperature anomalies are selected to demonstrate anomaly patterns of the first EOF for

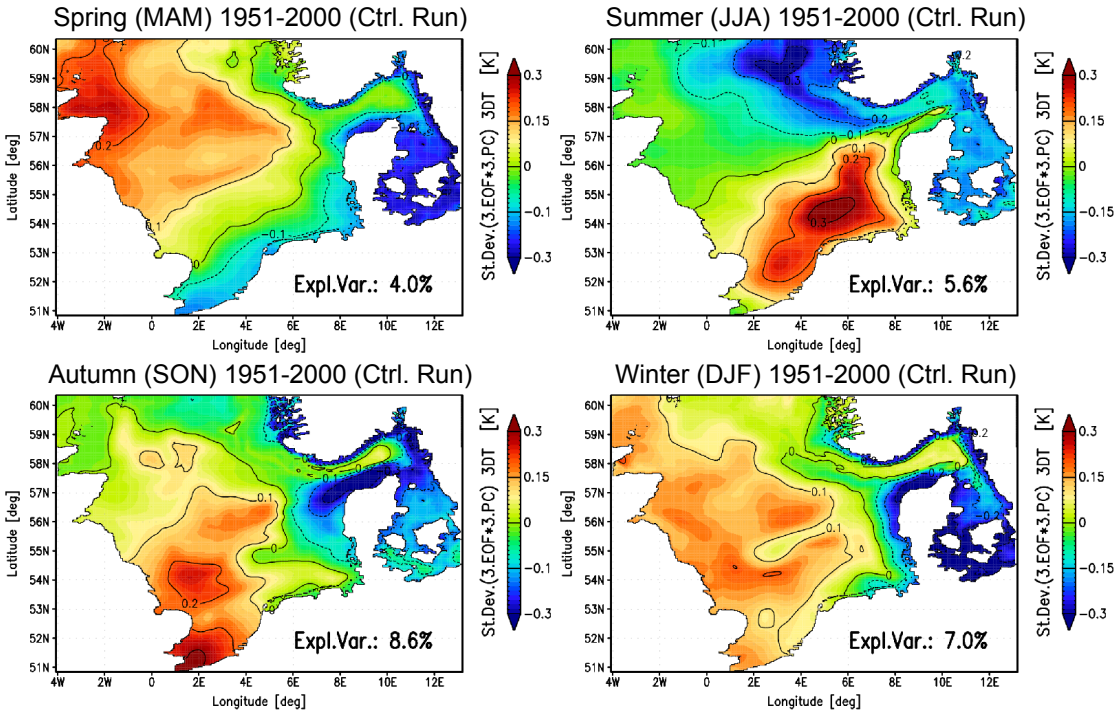

Figure 4.48: Rescaled third EOF patterns of depth-averaged sea water temperature.

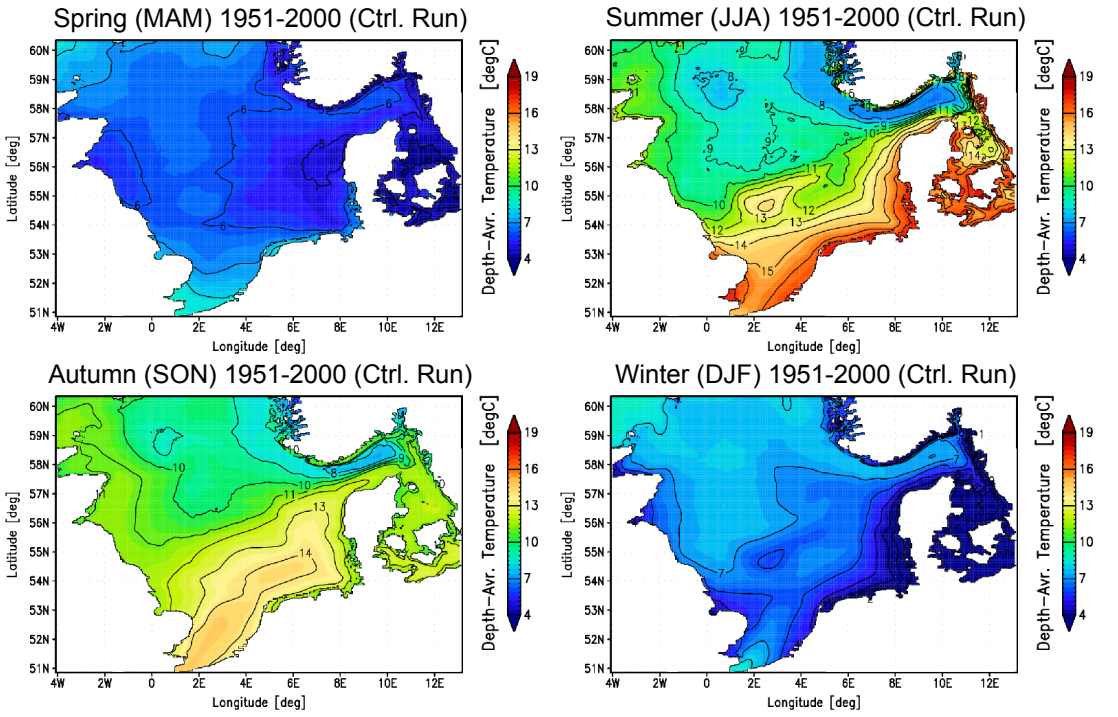

Figure 4.49: Seasonal mean depth-averaged sea water temperature for 1951-2000.

spring. However, the given examples always show the resulting temperature fields as the sum of all dynamics isolated by the distinct EOF patterns. The examples thus need to be chosen with care in order to indeed unveil the intended anomalies represented by a certain EOF. Fig. 4.51 shows spring 1959 representative for a positive, and spring 1951 for a negative anomaly of the first PC with respect to the control period 1951-2000.

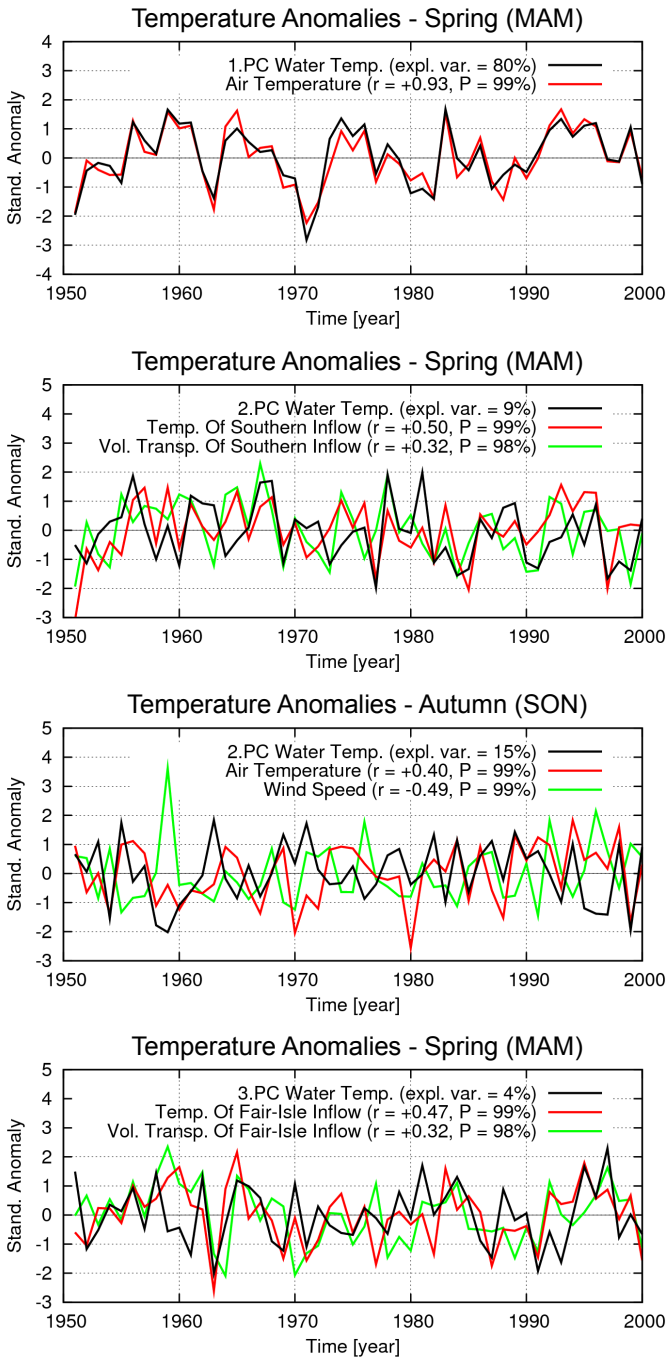

Figure 4.50: Black lines: PCs of depth-averaged sea water temperature. The descriptions of red and green lines are given in the figure's keys. The inscribed correlations refer to the respective PC.

Complementary to the first EOF patterns, the second EOF patterns of winter and spring (Fig. 4.47) more clearly highlight regions that undergo significant temperature variability caused by North Atlantic inflow. In winter the water column in the North Sea is vertically well mixed and cold, enabling the relatively warm inflowing North Atlantic waters to cause unambiguous anomalies. In summer, however, the water column is strongly stratified with warm waters in the upper 30-40 m but still cold waters underneath. Thus, for depth-averaged temperatures, the temperature ratio between inflowing North Atlantic waters and North Sea waters is less distinct in summer. Moreover, the variability of the inflowing volume transport is largest in winter and lowest in summer. With this, in the warm wa-

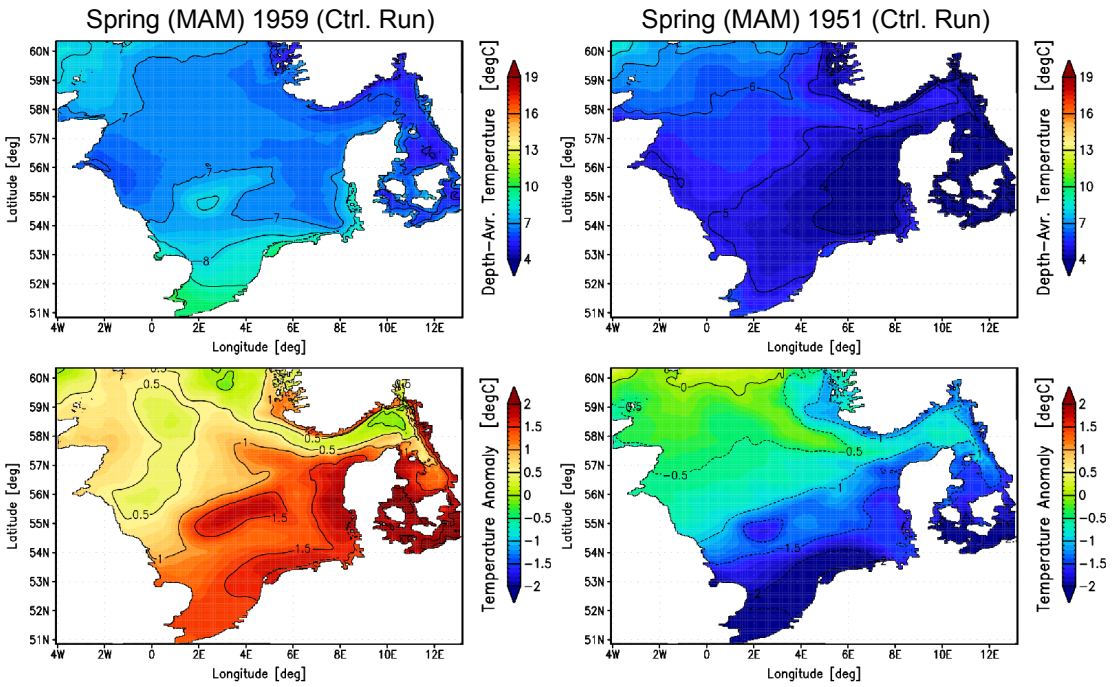

Figure 4.51: Examples of pronounced anomalies of the first PC of depth-averaged water temperature for spring (Fig. 4.50), where spring 1959 represents a positive, and spring 1951 a negative anomaly. Lower figures show deviations from the mean of the control period 1951-2000 (Fig. 4.50).

ter seasons summer and autumn the stratified water column gives rise to an additional variability mechanism represented by the second EOF patterns, where the third EOF patterns (Fig. 4.48) account for the same mechanisms that are represented by the second EOF patterns of the cold water seasons winter and spring.

In the second EOF patterns of winter and spring the Norwegian Trench and in particular the inflow through the English Channel stand out as the most significant regions with anomalies up to ± 0.3 and ± 0.5 °C, respectively. The opposed signs indeed indicate a negative correlation of temperature anomalies which account for about 9% of the total variance. In these patterns a warmer (cooler) (r=+0.50 to +0.62, P=99%) and stronger (weaker) (r=+0.32 to +0.60, P=98-99%) inflow through the southern boundary comes along with a cooler (warmer) (r=-0.32 to -0.38, P=98-99%) and weaker (stronger) (r=-0.22 to -0.50, P=88-99%) inflow through the northern boundaries of the domain. A strong (weak) southern inflow amplifies (attenuates) the transport along the Continental coast, which finally carries more (less) cold waters into the Jutland Current and the Norwegian Coastal Current via a positive correlation of r=+0.69 to +0.86 (P=99%) between the volume transports of the southern inflow and the Jutland Current. Hence, a positive (negative) transport anomaly of the English Channel flow causes a warm (cold) temperature anomaly in the southern North Sea but a cold (warm) temperature anomaly in the Norwegian Trench. Furthermore, the negatively correlated transport and temperature anomalies at the northern boundaries intensify the anomalies in the Norwegian Trench.

Examples of positive and negative temperature anomalies are selected from comparing the second PC with both temperature and volume transport anomalies of the English

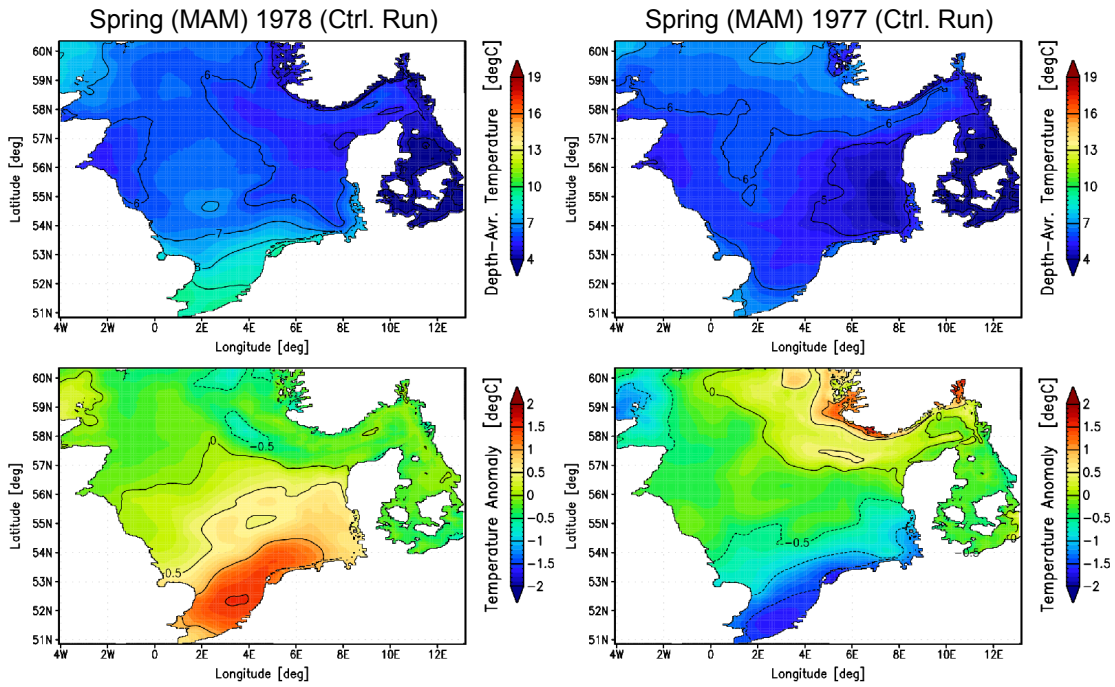

Figure 4.52: Examples of pronounced anomalies of the second PC of depth-averaged water temperature for spring (Fig. 4.50), where spring 1978 represents a positive, and spring 1977 a negative anomaly. Lower figures show deviations from the mean of the control period 1951-2000 (Fig. 4.50).

Channel flow, plotted in Fig. 4.50. Fig. 4.52 shows spring 1978 representative for a positive, and spring 1977 for a negative anomaly of the second PC with respect to the control period 1951-2000. The chosen examples also single out the difference between a transport anomaly and a temperature anomaly of the southern boundary inflow. The transport anomaly of spring 1978 causes the temperature anomaly of the Southern Bight to reach its maximum not until the inflow enters the general circulation, whereas the temperature anomaly of spring 1977 also influences the English Channel to the same extent.

Unlike for winter and spring, in the second EOF patterns for summer and autumn the zero contours conspicuously follow the contours of the spatial coverage of the well pronounced and decaying thermocline, respectively. Indicated by a weak but negative correlation in summer and autumn between air temperature and wind speed and accordingly, the depth of the thermocline, a cool (warm) air temperature anomaly is occasionally accompanied by a high (low) wind speed anomaly. However, comprehensive analysis of shear and buoyancy production in the water column with respect to thermal stratification in the North Sea by Pohlmann (1996b) revealed that under such weather conditions, the wind-induced shear production has a distinctly stronger impact on negative buoyancy production than the change of thermal forcing through the sea surface. Thereby, increased shear production and related higher negative buoyancy production entail a deepening of the thermocline due to transformation of turbulent kinetic energy into potential energy. Thus, under appropriate atmospheric conditions, the resulting drop (rise) of the thermocline due to higher (lower) wind speeds causes a larger (smaller) part of the water column to acquire warm surface temperature and in turn, a smaller (larger) part of the water column to keep cold bottom temperature, indeed summing up to a positive (negative) depth-averaged tempera-

ture anomaly in the thermocline region. Nonetheless, the involved air temperature anomaly needs to be moderate and the accompanying wind speed anomaly comparatively high in order for the depth-averaged temperature in the thermocline region in fact to change in the described way. The low proportion of mere 7% of the total variance in summer does justice to the special atmospheric conditions necessary for this effect. On the other hand, the stronger winds in autumn also coincide with a higher variability of wind speeds. Deviations of the thermocline depth from its mean are thus more pronounced in autumn than in summer and also more likely to occur. Consequently, the temperature anomalies depicted in the second EOF pattern as well as the corresponding explained variance are higher in autumn than in summer. Contrary to the positive (negative) depth-averaged temperature anomaly in the thermocline region, in the tidally mixed southern North Sea, however, the corresponding negative (positive) air temperature anomaly gives rise to a negative (positive) sea water temperature anomaly too, as indicated by the reversed signs in the EOF patterns.

In consistency with the given physical explanation, the correlations between the second PC for summer and autumn and respective time series of air temperature anomalies are significant and positive, amounting to +0.40 and +0.42 (P=99%), respectively, whereas no correlations hold for winter and spring anymore. Similarly, the correlations between the second PC for summer and autumn and respective time series of mean wind speed anomalies are significant and negative, amounting to -0.49 and -0.51 (P = 99%), respectively. The inversed signs of these two correlations are indeed necessary to induce the described temperature anomalies in the thermocline region. However, since both the warm waters of the upper layers and the cold waters of the deeper layers need to be taken into account, EOF patterns of SST (not shown here) rather than depth-averaged temperature, do not reflect these dynamics. Moreover, in representing a large scale phenomenon, the temperature anomalies tend to occur in the entire thermocline region. Local wind-induced current anomalies that may advectively change the vertical structure of the water column can therefore be ruled out as a driving mechanism.

Again, examples of positive and negative temperature anomalies are selected from comparing the second PC with anomalies of spatially averaged air temperature and wind speed, plotted in Fig. 4.50. Fig. 4.53 shows autumn 1955 for a positive, and autumn 1959 for a negative anomaly of the second PC with respect to the control period 1951-2000.

While the second EOF pattern for spring particularly emphasizes southern boundary anomalies, the respective third EOF pattern, shown in Fig. 4.48, well represents pronounced northern boundary anomalies. In this pattern an enhanced (attenuated) circulation comes along with a warmer (cooler) and stronger (weaker) northern inflow (mainly via the Fair Isle Current) but a cooler (warmer) southern inflow. In the third EOF pattern for summer a cooler (warmer) and weaker (stronger) northern inflow comes along with a stronger (weaker) southern inflow, giving rise to local temperature anomalies up to ± 0.3 °C. Once the positive surface heat flux from the atmosphere into the North Sea in spring has stopped the convection process in winter, the reaction of bottom water temperature on external heating in particular in the northern North Sea is restricted by low entrainment

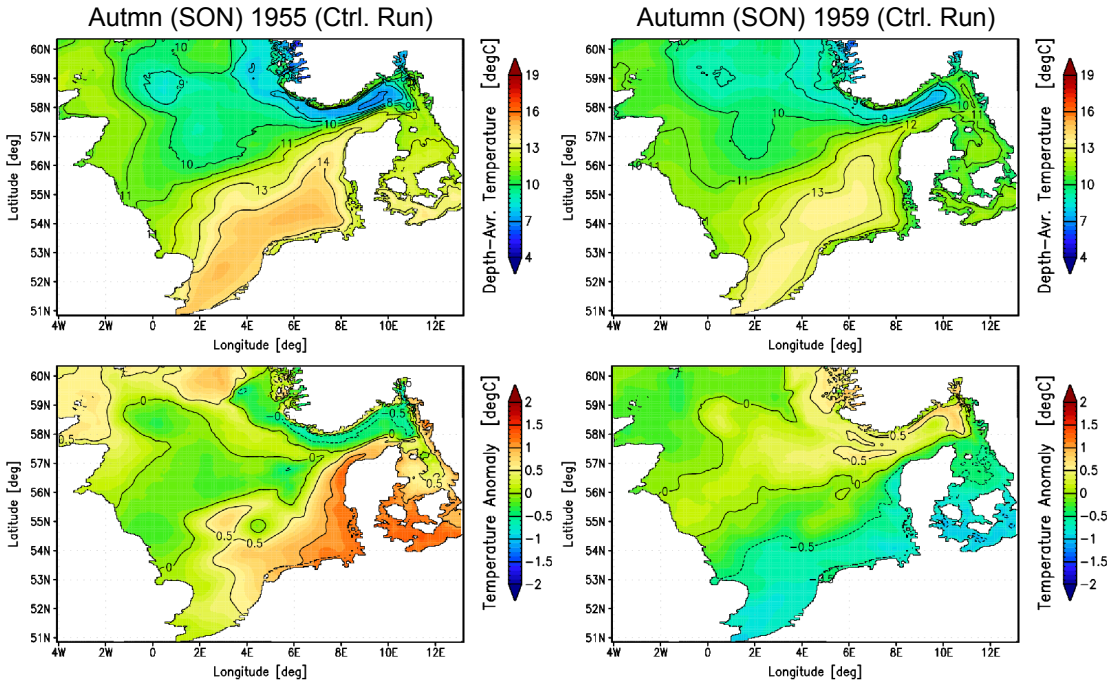

Figure 4.53: Examples of pronounced anomalies of the second PC of depth-averaged water temperature for autumn (Fig. 4.50), where autumn 1955 represents a positive, and autumn 1959 a negative anomaly. Lower figures show deviations from the mean of the control period 1951-2000 (Fig. 4.50).

rates through the thermocline. As represented by the second EOF for spring and the third EOF for summer, northern transport anomalies then show a strong impact on the depth-averaged water temperature, similarly reflected by respective correlations between the PCs and northern inflow. In autumn the third EOF pattern represents a warmer (cooler) but weaker (stronger) southern boundary inflow that comes along with a weaker (stronger) circulation, which transports less (more) warm southern North Sea waters into the Jutland Current. In winter, however, no distinct correlations between the third PC and various other quantities are found in order to draw a consistent and reasonable explanation for the EOF pattern. Anyway, the explained variance of the third EOF patterns merely amounts to 4-9%. The temperature anomalies in the Kattegat region are mainly caused by respective air temperature anomalies. Baltic inflow anomalies are ruled out as a source of temperature anomalies, since in the model, the temperature of Baltic discharge is always set to local water temperatures of the eastern boundary region.

The third PC for spring in comparison with anomalies of temperature and volume transport of the Fair Isle Current is shown in Fig. 4.50. However, the temperature fields even of spring 1965 and 1963 (Fig. 4.54), which exemplify pronounced positive and negative anomalies of the third PC, respectively, do not solely reflect the structures of the third EOF pattern. Rather, they are disturbed by interfering anomalies of the first and second EOFs, well demonstrating the power of EOF analysis to unveil and quantify hidden dynamics in the data. One could indeed calculate the anomalies given by the first and second EOFs for the two years and subtract them from the temperature field in order to uncover the hidden structures represented by the third and subsequent EOFs. From the associated

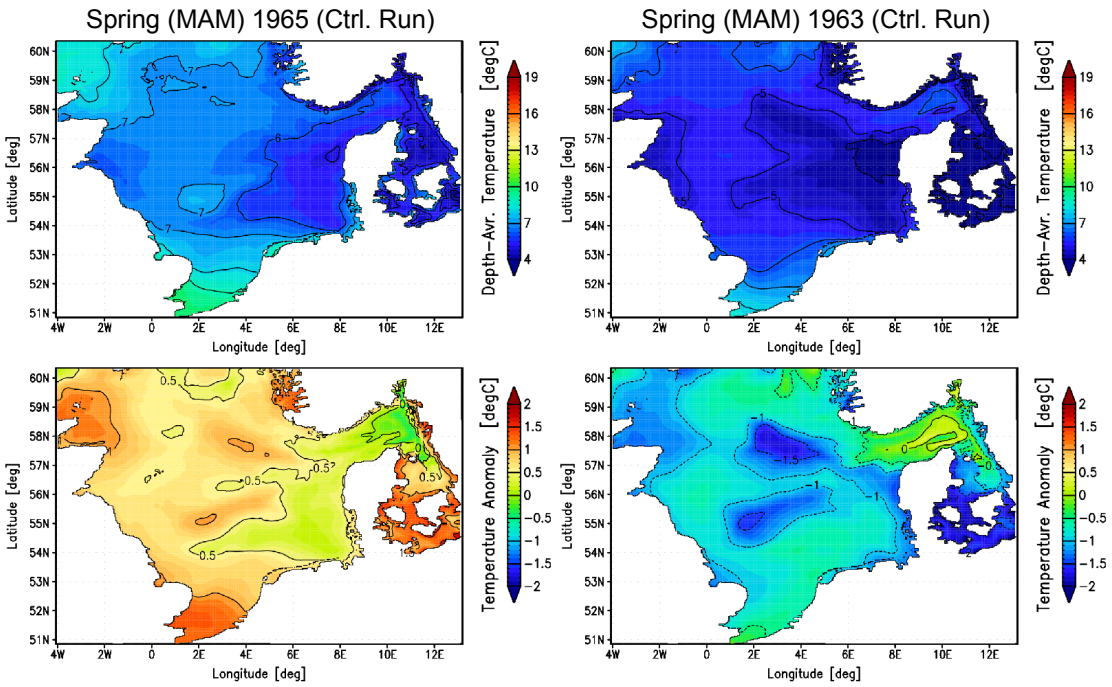

Figure 4.54: Examples of pronounced anomalies of the third PC of depth-averaged water temperature for spring (Fig. 4.50), where spring 1965 represents a positive, and spring 1963 a negative anomaly. Lower figures show deviations from the mean of the control period 1951-2000 (Fig. 4.50).

explained variances, however, a low relevance of the third EOFs to temperature anomalies in the North Sea can be deduced, anyway.

By comparing the explained variances of the first and subsequent EOF patterns, the analysis indicates the atmospheric influence on the North Sea water temperature to account for at least 76-82% and consequently, the influence of Atlantic inflow through the open boundaries to may account for the remaining 18-24%. However, inferred from significant correlations for all seasons, influences of the individual open boundaries are not clearly reflected by individual EOF patterns but rather are distributed over the whole lot of EOF patterns with higher order numbers, which can also represent atmospheric anomalies not accounted for by the EOF patterns considered thus far. The strong influence of atmospheric forcing on the temperature distribution and heat content in the North Sea estimated via EOF analysis additionally affirms the strong influence already calculated via the heat budget in section 4.1.3.

4.2.3 Salinity

Considering the same EOF patterns for the depth-averaged salinity, one clearly see at least two mutually independent mechanisms that govern the variable salinity in the North Sea. Firstly, the influence of Baltic discharge, which, according to the first EOF patterns, account for 46-66% of the total salinity variance in the North Sea. Secondly, the influence of Atlantic inflow through the open northern and southern boundaries, which, according to the second and third EOF patterns, account for at least 18-31% of the total variance. Contrary to the EOF patterns for temperature, the salinity patterns of a given order num-

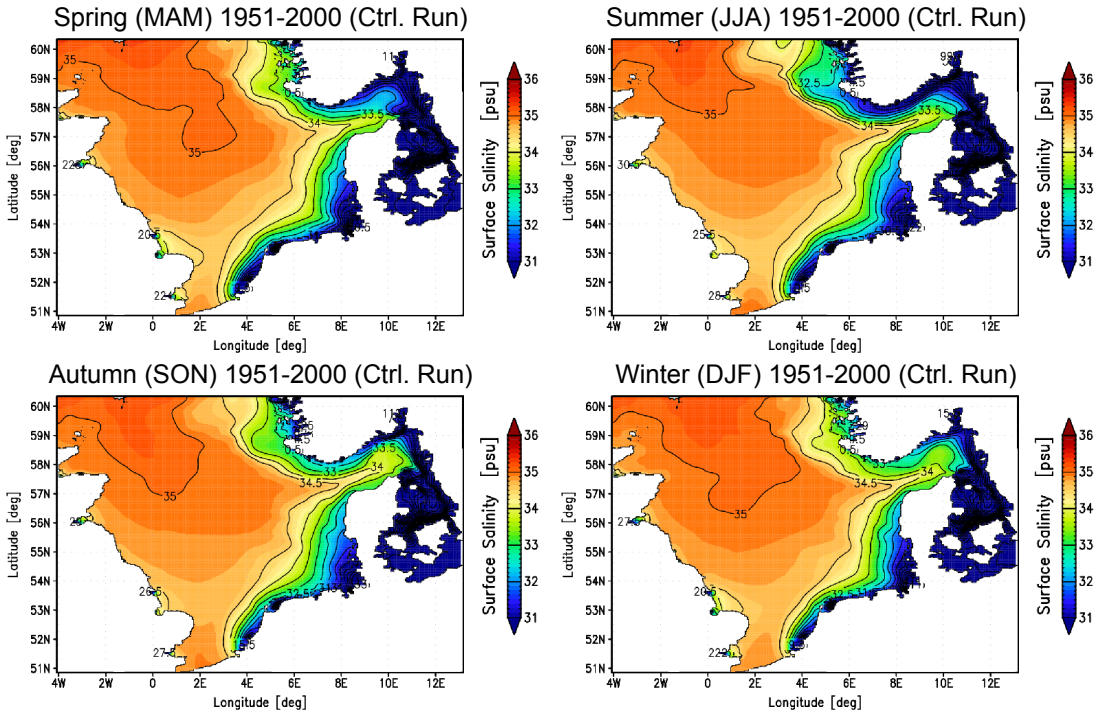

Figure 4.55: Seasonal mean surface salinity for 1951-2000.

ber are very similar throughout the year. However, as mentioned above, the circulation in the North Sea is weakest in spring (see Fig. 4.38), but the wind speeds are still moderate, easily giving rise to pronounced hydrodynamic and hydrographic anomalies. The spatial EOF patterns for spring are therefore often the clearest and most structured ones and consequently, salinity anomalies of single years are also most pronounced for spring. Salinity anomalies for selected years exemplified below therefore again focus on spring. Moreover, even though the anomalies represented by the EOF patterns are obtained from analyzing depth-averaged salinities, the magnitudes of the anomalies are highest at the sea surface. The mean salinity distributions in Fig. 4.55 as well as the given examples for pronounced anomalies show surface values only.

Unlike the range of sea water temperature, the salinity in the North Sea locally varies from nearly 0 psu in the vicinity of river mouths up to 35 psu in the open northern North Sea. Considering the EOF patterns again in a quantitative way by depicting the variability as the standard deviation of anomalies, the most highlighted region is almost always the Continental coast, since even a small salinity deviation that affects the river plumes of the Rhine and Elbe causes large absolute salinity anomalies in this region. To avoid misguided interpretations, the EOF patterns for salinity are additionally transformed into correlation maps (Fig. 4.59 to 4.61), reflecting correlation coefficients between the full salinity anomalies at each grid cell and the individual PCs. High correlations thus single out regions at which the time series of the full salinity anomalies show a high level of synchrony with the PC that they are correlated with. As such, the correlations represent the qualitative significance of the considered variability and hence, provide further information about the spatio-temporal structure of the salinity distribution in the North Sea.

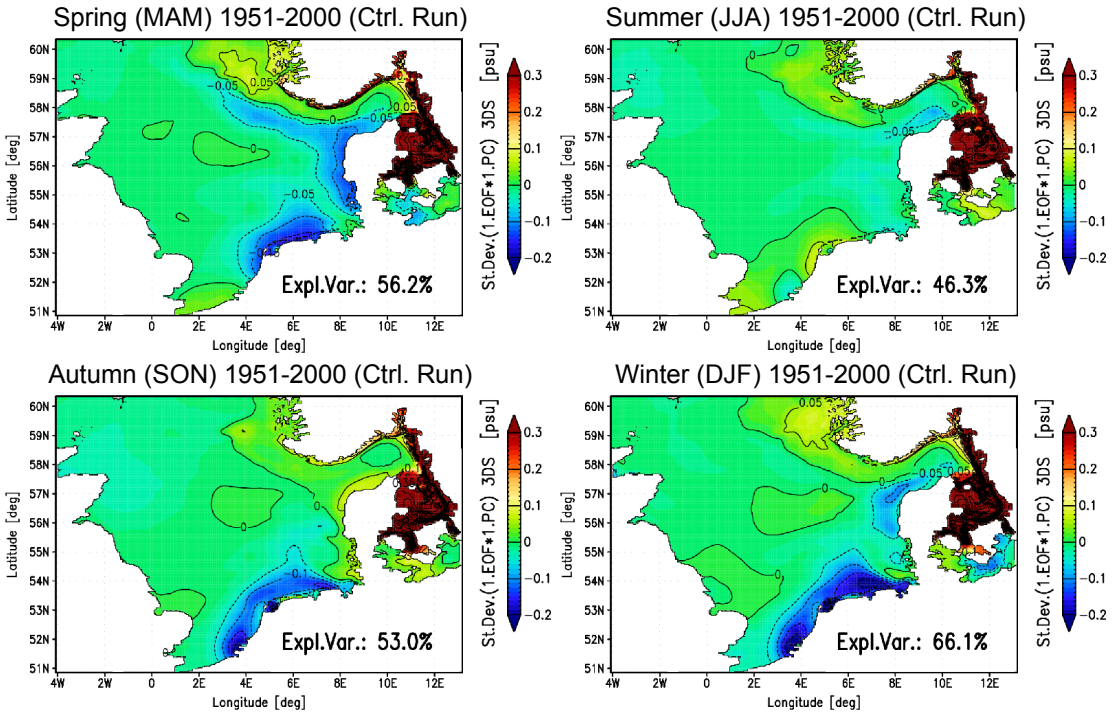

Figure 4.56: Rescaled first EOF patterns of depth-averaged salinity.

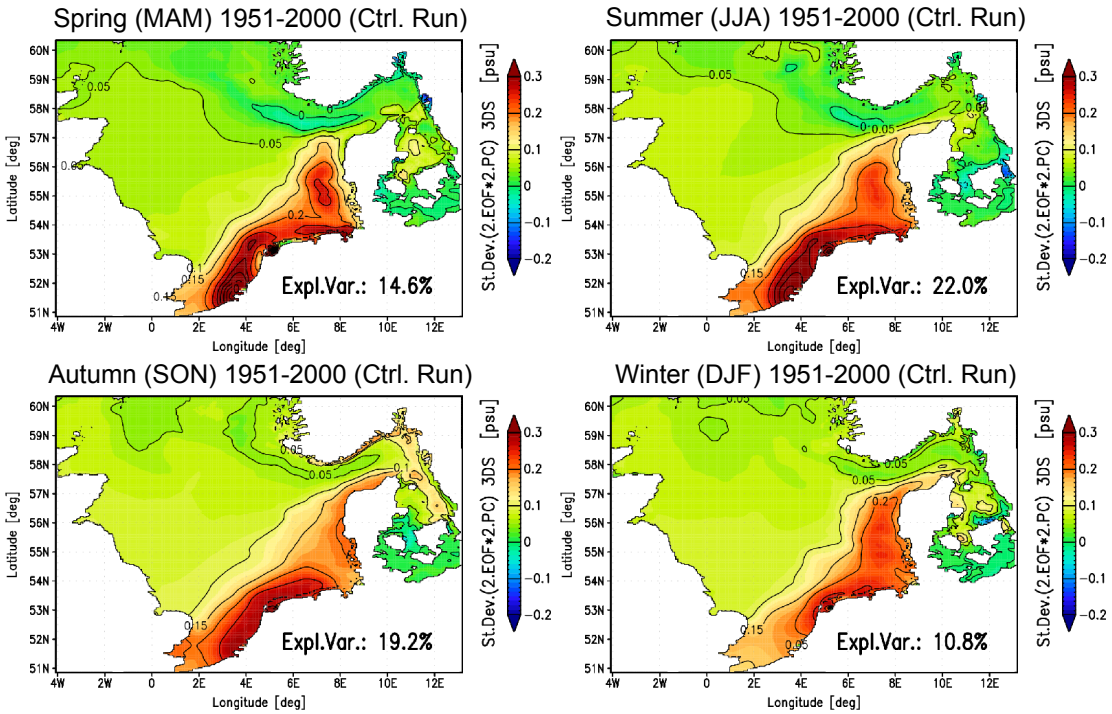

Figure 4.57: Rescaled second EOF patterns of depth-averaged salinity.

Contrary to the components of the surface heat fluxes, the surface fresh water fluxes (i.e. precipitation and evaporation, since condensation can be ruled out on seasonal averages) are quantitatively similar in the North Sea and therefore tend to almost cancel each other (Damm, 1997). In the present model the slightly predominant precipitation provides a positive net mean surface fresh water flux for the control period 1951-1980 of just +0.54 mm/d into the ocean (see chapter 3). The strength of the circulation which governs the ad-

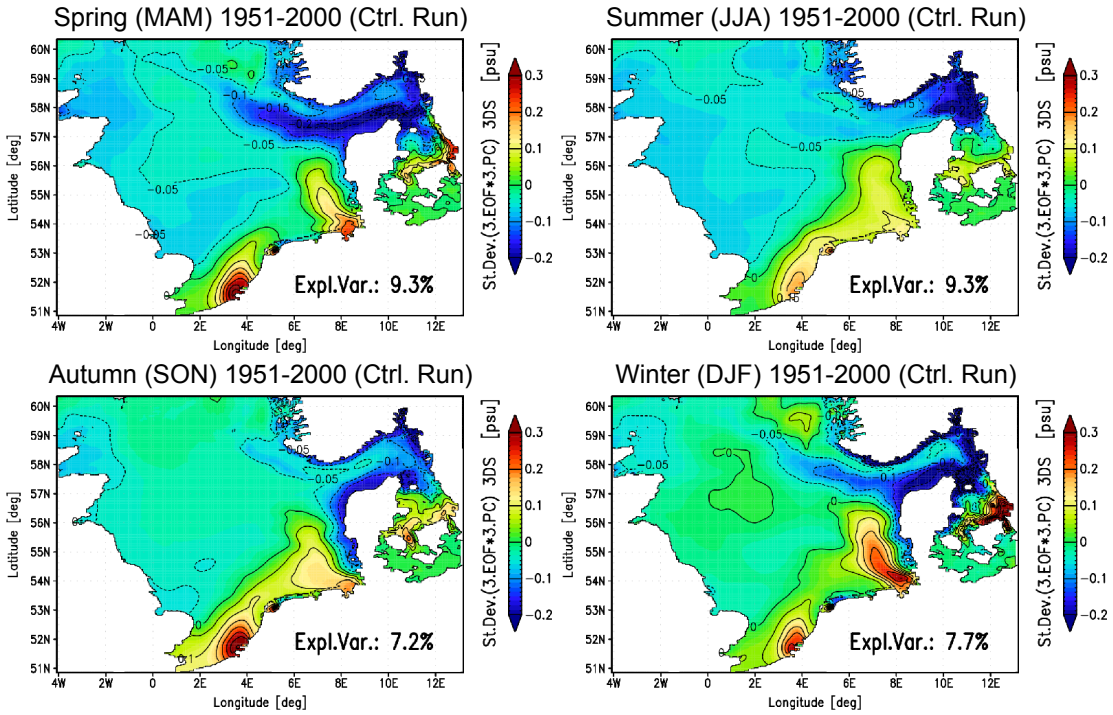

Figure 4.58: Rescaled third EOF patterns of depth-averaged salinity.

vective transports thus exerts a much greater influence on the salinity variability than on the temperature variability. For relating the circulation variability to the salinity variability, the first and second PCs of the circulation, discussed in section 4.2.1, are also incorporated in the salinity analysis.

Considering the first salinity EOF patterns shown in Fig. 4.56, which account for 46-66% of the total salinity variance, the high variability in the Kattegat highlights the region where the low-salinity waters discharging from the Baltic Sea are mixed with saline North Sea waters. The salinity in this region is determined by the variable inflow of Baltic waters (r=-0.60 to -0.94, P=99%) and by the strength of the circulation (r=-0.32 to -0.41, P=98-99%). Under a weak general circulation in the North Sea, the recirculation in the Skagerrak can be disturbed and even reversed into an anti-cyclonic sense. However, the less distinct the cyclonic recirculation in the Skagerrak, the more saline North Sea waters intrude into the Kattegat, causing a positive salinity anomaly there of up to +2.5 psu. As described in section 2.2.3, the salinity of Baltic discharge is interpolated from monthly climatological means, whereas the amount of discharge is extracted from the global MPIOM simulations as a function of time. Hence, the contribution of Baltic discharge to the salinity variability in the Kattegat merely emerges from the variable amount of discharge rather than from any salinity anomaly. Since the correlation coefficients of the transformed first EOF patterns shown in Fig. 4.59 are close to one in the Kattegat region, the corresponding anomalies are identified to represent almost the entire salinity variability in the Kattegat. Moreover, the first EOF patterns exclusively highlight variable regions that are correlated to some extent with the variable discharge of Baltic waters.

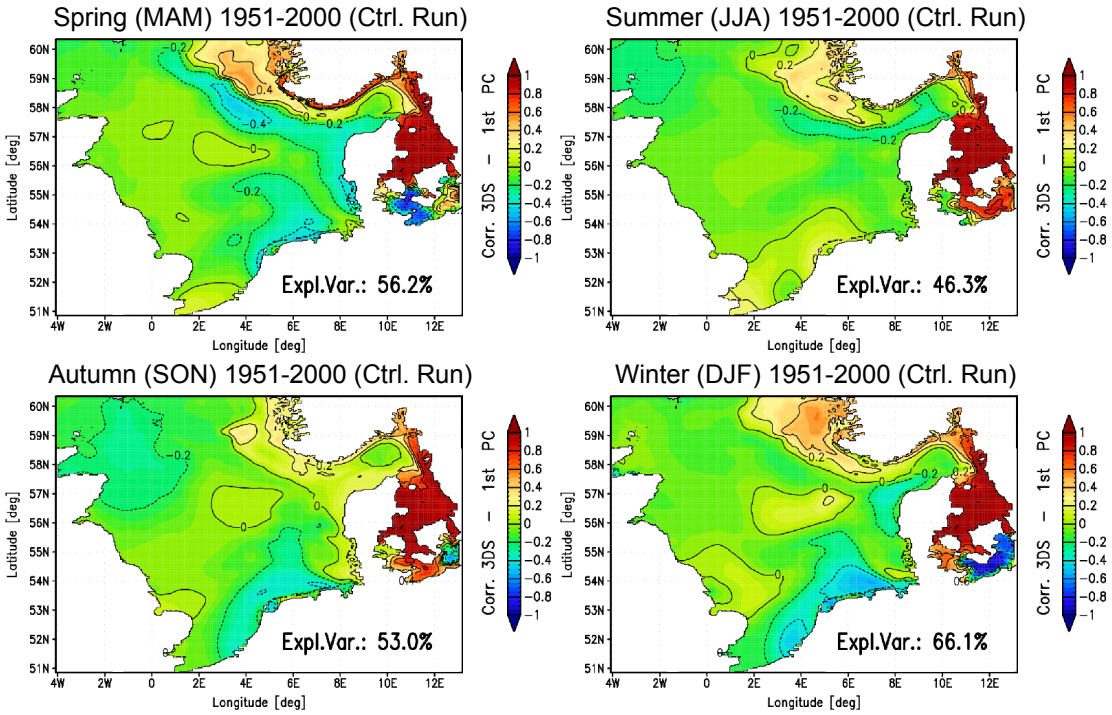

Figure 4.59: Transformed first EOF patterns of depth-averaged salinity, reflecting correlation coefficients between the full salinity anomalies and the PC.

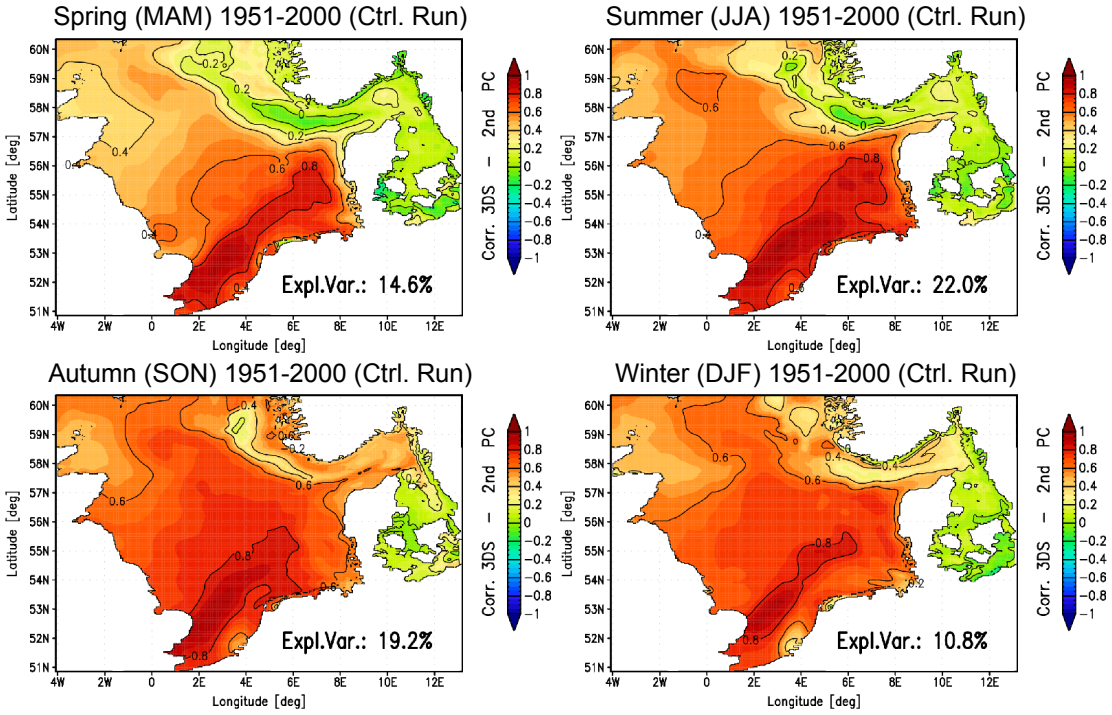

Figure 4.60: Transformed second EOF patterns of depth-averaged salinity, analogous to Fig. 4.59.

Well reflected by the first EOF patterns, the low-salinity waters in the Kattegat determine the salinity of the Norwegian coastal waters. The location of the salinity front that separates the fresh Norwegian Coastal Current from the saline central and northern North Sea is also clearly recognized, though best visible in spring and winter. As mentioned above, a negative salinity anomaly in these patterns is accompanied by an enhanced circulation but also by an enhanced saline inflow through the northern boundary along the western side

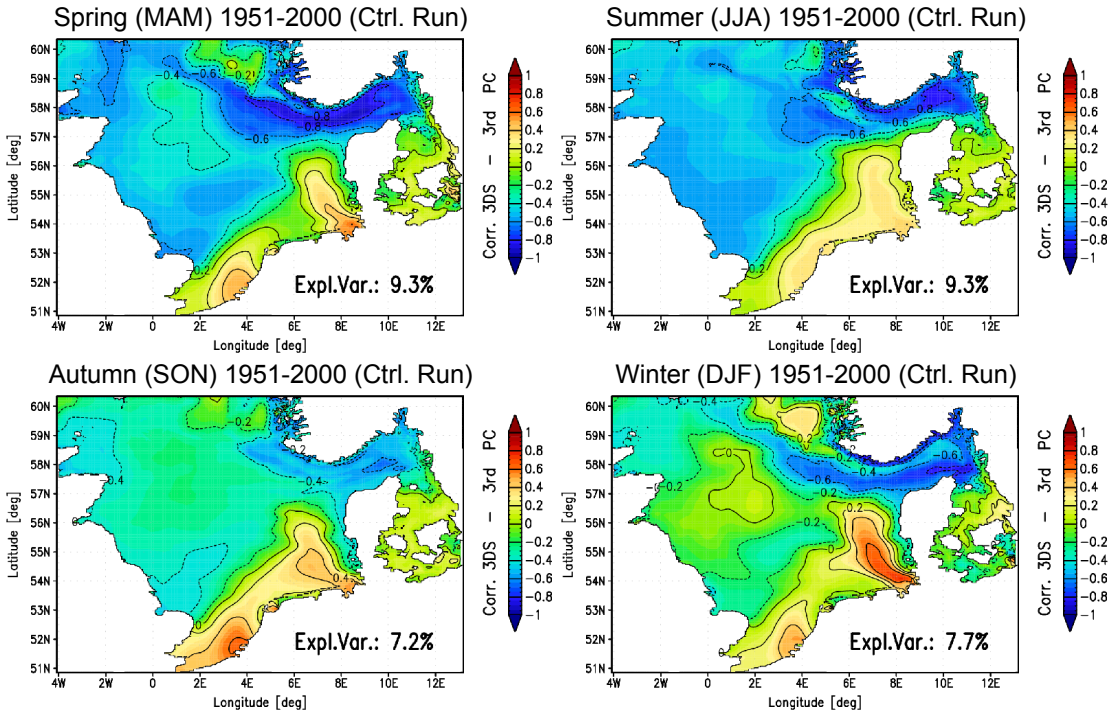

Figure 4.61: Transformed third EOF patterns of depth-averaged salinity, analogous to Fig. 4.59.

of the Norwegian Trench (r=-0.33 to -0.40, P=99%). From the corresponding time series shown in Fig. 4.62, spring 1959, depicted in Fig. 4.63, was chosen as an example for a negative anomaly of the first salinity PC, where Fig. 4.55 shows the mean surface salinity distribution of the control period 1951-2000. The comparison of isolines reveals an intensification of the salinity front in the Norwegian Trench (the isolines are closer) and hints at the positive salinity anomaly at the south-western side of the front, which penetrates into the Jutland Current. At the same time, more fresh water is entering the Norwegian Coastal Current, which occasionally spreads westward before leaving the domain northbound. On the one hand, an enhanced circulation increases the horizontal exchange of salinity across the front in the Norwegian Trench because of larger horizontal current velocity gradients, which cause larger shear and with this, more turbulence. While this effect indeed weakens the front, the permanent supply of fresh and salty water on the respective sides of the front, on the other hand, stabilizes the horizontal salinity gradient and thus, finally intensifies the salinity front in the Norwegian Trench under enhanced circulation conditions. The standard deviation of the salinity anomalies accounted for in the first EOF patterns indicate a mean variability in the Kattegat up to ± 1 psu, entailing a depth-averaged variability in the Norwegian Trench of ± 0.05 psu but a surface variability of ± 0.2 psu.

In turn, a positive salinity anomaly in the Kattegat intimately affects the salinity in the Skagerrak and the entire Norwegian Coastal Current, where the accompanying negative circulation anomaly indeed attenuates and widens the salinity front over a large area. An example for a positive salinity anomaly (spring 1970) is given in Fig. 4.63, where a strong easterly wind anomaly in combination with a weak northern boundary inflow causes a westward penetration of fresh Baltic waters into the North Sea domain (the corresponding circulation pattern is shown in Fig. 4.43). As mentioned in section 4.2.1, in the other

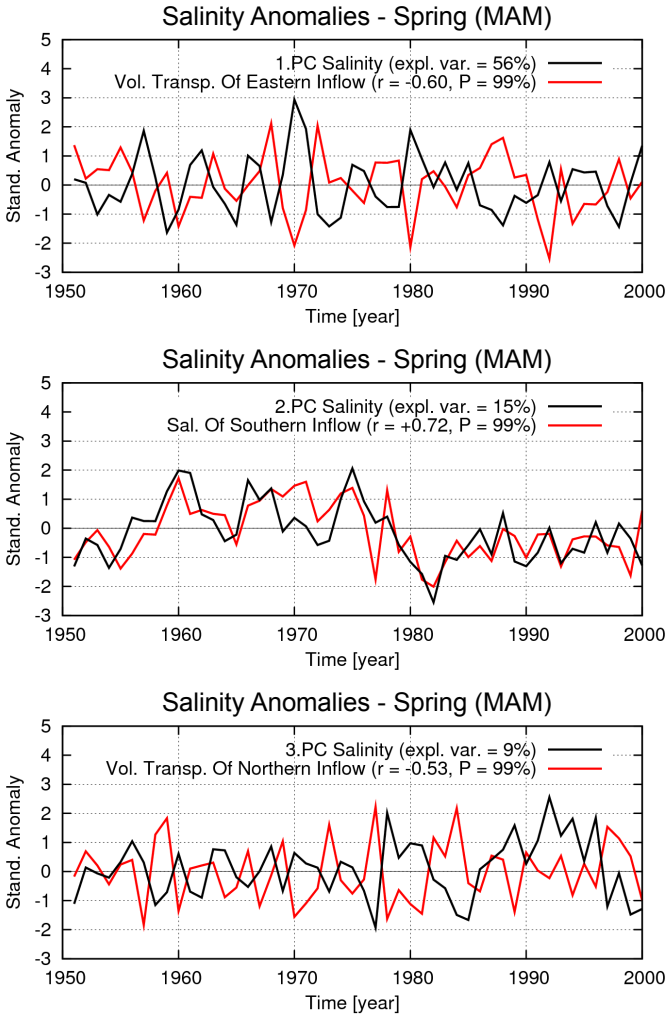

Figure 4.62: Black lines: PCs of depth-averaged salinity. The descriptions of red lines are given in the figure's keys. The inscribed correlations refer to the respective PC.

seasons, however, the general circulation is usually strong enough to resist easterly wind anomalies, where the northern inflow along the Norwegian Trench is just weakened rather than reversed. Moreover, riverine and Baltic fresh water supply peak out in spring time, too, because of snow melting on land. Consequently, positive salinity anomalies in the other seasons do not penetrate as far into the domain as in spring. Fig. 4.64 gives examples of positive and negative salinity anomalies for winter 1979/80 and 1958/59, respectively (the corresponding PC is not shown).

Besides, the region off the Continental and Danish coasts is also highlighted in the first EOF patterns, though negatively correlated to the salinity anomalies in the Kattegat and Norwegian Trench and most pronounced in spring and winter. Since river runoff in the simulation is interpolated from monthly climatological means, varying river runoff is precluded as a source for salinity anomalies. As indicated by Fig. 4.41, a weaker than mean circulation in the North Sea is caused either by weaker than mean westerly wind conditions or by easterly wind conditions. Similar correlations hold between varying wind conditions and the variability of the total boundary inflow, which is influencing the variability of the circulation, too. The salinity anomalies off the Continental and Danish coasts

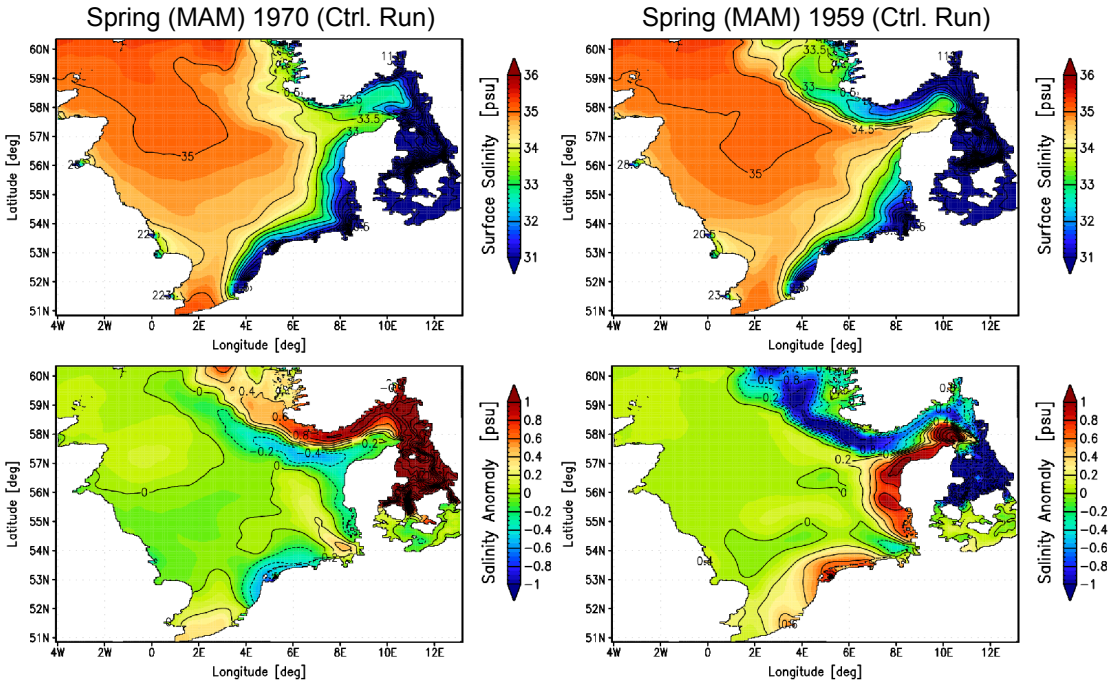

Figure 4.63: Examples of pronounced anomalies of the first PC of depth-averaged salinity for spring (Fig. 4.62), where spring 1970 represents a positive, and spring 1959 a negative anomaly. Lower figures show deviations from the mean of the control period 1951-2000 (Fig. 4.55). Extrema in the Kattegat region amount to ±2.5 psu.

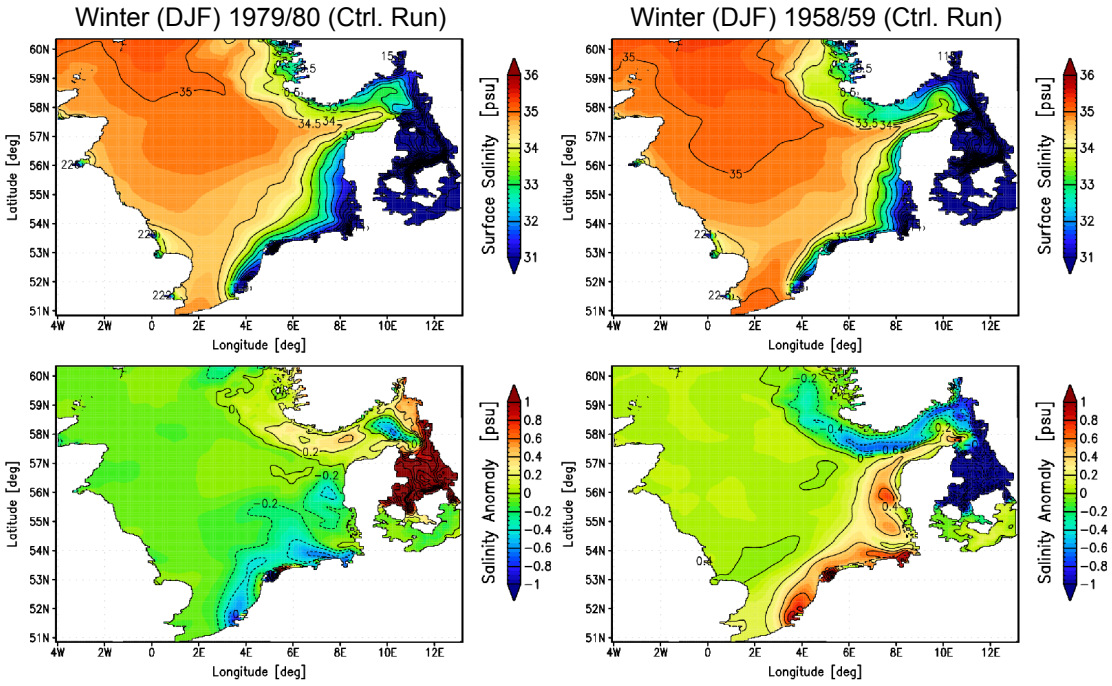

Figure 4.64: Examples of pronounced anomalies of the first PC of depth-averaged salinity for winter, where winter 1979/80 represents a positive, and spring 1958/59 a negative anomaly. Lower figures show deviations from the mean of the control period 1951-2000 (Fig. 4.55). Extrema in the Kattegat region amount to ±1.5 psu.

can thus be explained by negative and positive correlations between the first PC, and circulation enhancing westerly and circulation blocking easterly wind conditions, respectively. Negative circulation anomalies favor an accumulation of fresh riverine discharge in this

region, where positive circulation anomalies give rise to a stronger advective transport of saline North Sea waters towards the Continental coast. The Weser-Elbe river plume in the German Bight, however, is less affected by these dynamics, since for wind anomalies and corresponding circulation anomalies, the north-westward directed river runoff merely propagates either more northward or westward.

For easterly wind conditions in summer being comparatively sparse, the salinity anomaly off the Continental coast is hardly pronounced in the first EOF patterns for summer. Rather, the slightly positive correlation between the first salinity PC and the salinity anomalies of the southern boundary inflow give rise to the positively correlated Southern Bight, even though the strength of the southern inflow is slightly negatively correlated. The correlations close to the southern boundary for the other seasons, shown in Fig. 4.56 and 4.59, similarly reflect respective salinity anomalies of the inflowing English Channel water but also coincide with the signs of its transport anomalies. As discussed in section 4.1.2, the transport magnitudes of northern and southern boundary inflows are indeed affected differently by changing wind conditions. A direct correlation between northern and southern inflows rather reveals the southern boundary inflow to be fairly uncorrelated with the northern ones throughout the year. Despite varying wind conditions, the strength of the northern inflows are also governed by anomalies of the North Atlantic Current, whereas the strength of the southern inflow is governed by other drivers like the NAO or, more local, the wind fields and baroclinic density gradients. Analysis of the strength of the Gulf Stream and the North Atlantic Current in relation to NAO anomalies by Pingree (2005) showed the NAO to influence the North Atlantic Current only with a time lag of about six months. The independence of the two drivers at lag zero can thus account for the different inflow dynamics at the northern and southern boundaries of the North Sea. On the one hand, inferred from stream functions of depth-integrated volume transports in chapter 3, the NAO indeed influences the general circulation in the North Sea via influencing the wind forcing. However, in accordance to the independence of the North Atlantic Current, a significant correlation between the winter NAO index and the volume transports through the open boundaries was found in the present model results only for the southern boundary. Hence, although the first salinity EOF patterns are closely linked to anomalies of the northern boundary inflows, the independent correlations of the transport magnitude of the English Channel flow as well as of its salinity entail structurally different salinity anomalies in the southern North Sea, to be discussed in more detail below. The salinity anomalies of the southern inflow indicated by the first EOFs are eventually linked to large-scale atmospheric dynamics of northern Europe, causing respective anomalies of precipitation and/or snow melting in the catchment areas of the Baltic Sea and the English Channel. Nonetheless, most of the salinity variability of the southern boundary inflow is reflected by the second EOF patterns.

In addition to the dynamics of the Baltic discharge, the general circulation, the wind fields, and the boundary throughflows, which primarily influence the salinity distribution in the North Sea, the variability of the total sea surface fresh water flux as a secondary influence was also examined with EOF analysis. As shown in section 4.1.5, in the present model the mean net fresh water transfer from the atmosphere into the North Sea amounts

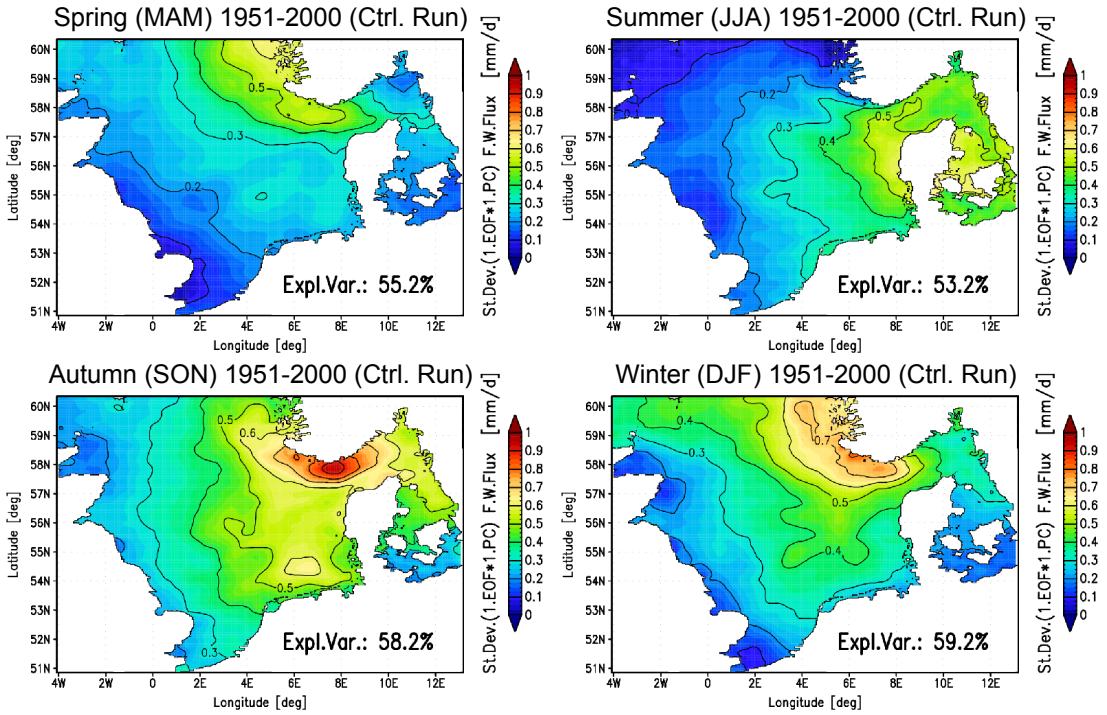

Figure 4.65: Rescaled first EOF patterns of total surface fresh water flux.

to about one third of the Baltic fresh water discharge. In the analysis the sign of the total fresh water flux was set for a positive anomaly to represent more-than-mean fresh water transfer into the ocean, that is, more precipitation and/or less evaporation.

The structures of both the first and second EOF patterns of surface fresh water flux (Fig. 4.65 and 4.66) show pronounced anomalies in particular along the Norwegian coast but also in the Kattegat. Together, the two patterns account for 66-74% of the total variance. The fresh water flux anomalies further amplify the salinity anomalies represented by the first salinity EOFs, since the PCs of fresh water flux show significant negative correlations with the first PCs of salinity up to -0.46 (P=99%). The second EOFs are even more amplifying than the first ones, since the difference between anomalies in the Norwegian Trench and in the open North Sea are larger in the second EOFs. A negative (i.e. a fresh) salinity anomaly in the Kattegat and Norwegian Trench can thus be accompanied by a positive (i.e. a fresh) surface fresh water flux anomaly of up to +1 mm/d in these regions.

In the second and third salinity EOFs, shown in Fig. 4.57 and 4.58, the strong influence of the English Channel water on the salinity of the southern North Sea is reflected. The second PCs are positively correlated in particular to the variability of the salinity of the southern boundary inflow (r=+0.71 to +0.78, P=99%), and just slightly correlated to the variability of its volume transport (Fig. 4.62). The third PC, on the contrary, is positively correlated in particular to the variability of the inflowing southern volume transport (r=+0.34 to +0.49, P=98-99%) but only slightly correlated to the variability of its salinity (as indicated by the low correlation coefficients close to the southern boundary shown in Fig. 4.61).

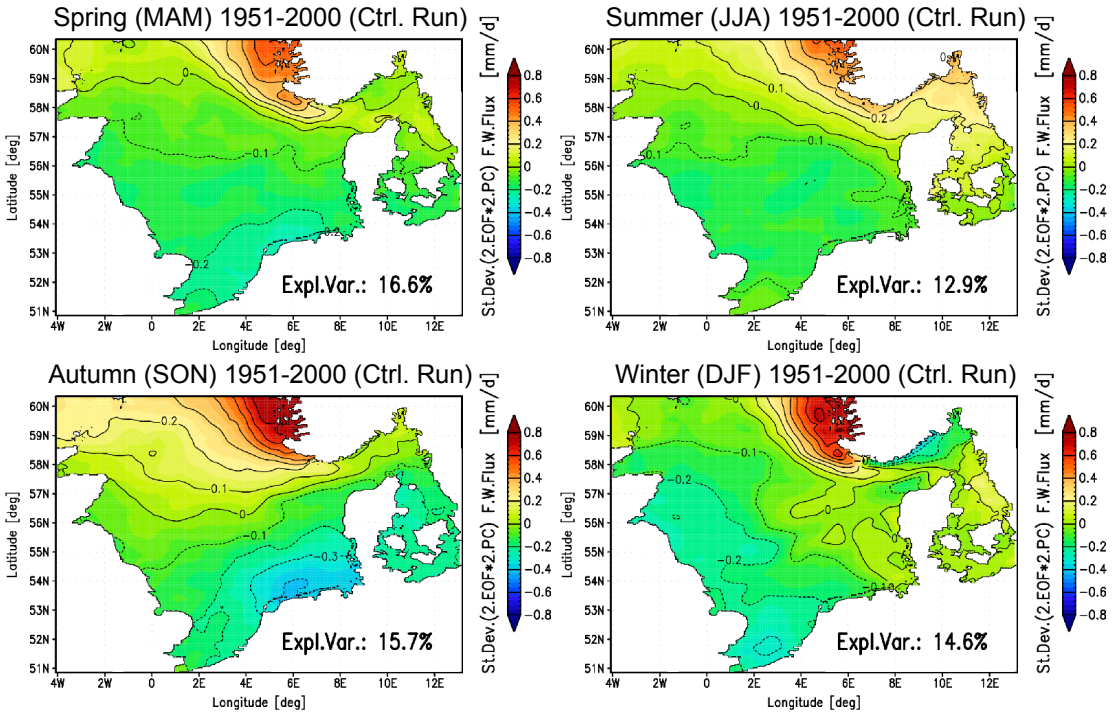

Figure 4.66: Rescaled second EOF patterns of total surface fresh water flux.

Remarkably, the second EOF patterns highlight salinity anomalies in the southern North Sea more homogeneously, whereas the third EOF patterns distinctly emphasize the two big Continental river plumes of the Elbe and Rhine. In particular, the qualitative difference between the second and third EOF patterns is represented more clearly by the associated correlation maps shown in Fig. 4.60 and 4.61, where the high correlation coefficients in the second EOFs single out the salinity anomalies of the southern boundary inflow as the dominating influence on the salinity in the southern North Sea. Positive salinity anomalies particularly increase the salinity of the frontal area to the north of the fresh Continental coastal waters where the correlation coefficients are the highest. The strengthening of the cross-frontal density gradient induces an increase of the along-frontal baroclinic flow (van Aken et al., 1987), amplifying the north-eastward propagation of the positive salinity anomaly. Negative salinity anomalies, on the contrary, decrease the along-frontal baroclinic flow because of the opposed effect of the same mechanism, bringing about a lower amount of still saline English Channel water to be advected north-eastwards and with this, giving rise to negative salinity anomalies in the southern North Sea. In summer the horizontal temperature gradient between offshore and coastal waters further amplifies the along-frontal baroclinic flow and thus, its influence on associated salinity anomalies. In winter, however, the reversed horizontal temperature gradient in the frontal area indeed weakens the baroclinic flow. Nevertheless, under a constant amount of river runoff, a pronounced salinity anomaly of the English Channel water causes a similar anomaly in the entire southern North Sea, whereas a pronounced anomaly of volume transport through the English Channel primarily causes a salinity anomaly in the Continental river plumes. A weak southern inflow opens the possibility for fresh river runoff to accumulate and to penetrate farther offshore. Consequently, less fresh water enters the Jutland Current, causing a positive salinity anomaly there. By contrast, a mere salinity anomaly of the En-

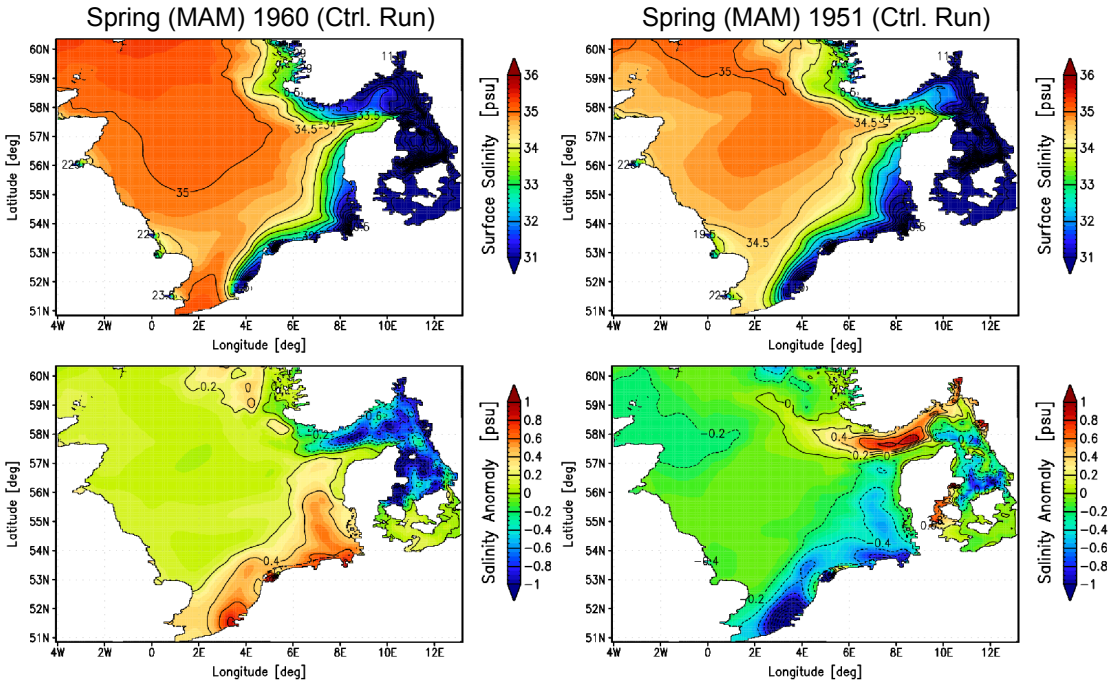

Figure 4.67: Examples of pronounced anomalies of the second PC of depth-averaged salinity for spring (Fig. 4.62), where spring 1960 represents a positive, and spring 1951 a negative anomaly. Lower figures show deviations from the mean of the control period 1951-2000 (Fig. 4.55).

glish Channel water affects the amount of salt transported into the southern North Sea, thus causing a salinity anomaly of the same sign in the Jutland Current, too.

An other dissimilarity between the second and third salinity EOFs holds for anomalies in the central and northern North Sea. Since the second salinity PCs do not show significant correlations with PCs of the general circulation, the anomalies in the central and northern North Sea represented by the second salinity EOFs arise from salinity anomalies of the northern inflows (r=+0.36 to +0.63, P=99%) rather than from anomalies of their volume transports. However, in the third EOF patterns the anomalies in the same regions and particularly in the Norwegian Trench arise from both salinity anomalies (r=-0.32 to -0.58, P=97-99%) in combination with transport anomalies (r=-0.19 to -0.70, P=81-99%) of the northern inflows. Consequently, the salinity anomalies represented by the third EOFs are also positively correlated with the second EOFs of the circulation (Fig. 4.40) and hence, largely induced by southerly and northerly wind anomalies as discussed in section 4.1.2. The second salinity EOF patterns account for 8-15% of the total variance, the third EOF patterns for 6-10%.

Chosen from the PC depicted in Fig. 4.62, examples of positive and negative salinity anomalies according to the second EOF pattern of spring are shown in Fig. 4.67. As indicated by the first salinity PC also shown in Fig. 4.62, spring 1960 is coincidentally accompanied by a fresh salinity anomaly in the Kattegat, whereas spring 1951, indicated by Fig. 4.42, is accompanied by a negative anomaly of the second circulation EOF (Fig. 4.40), enabling saline waters to enter the northern Skagerrak from the west. Examples of pronounced anomalies according to the third salinity EOF of spring are shown in Fig. 4.68,

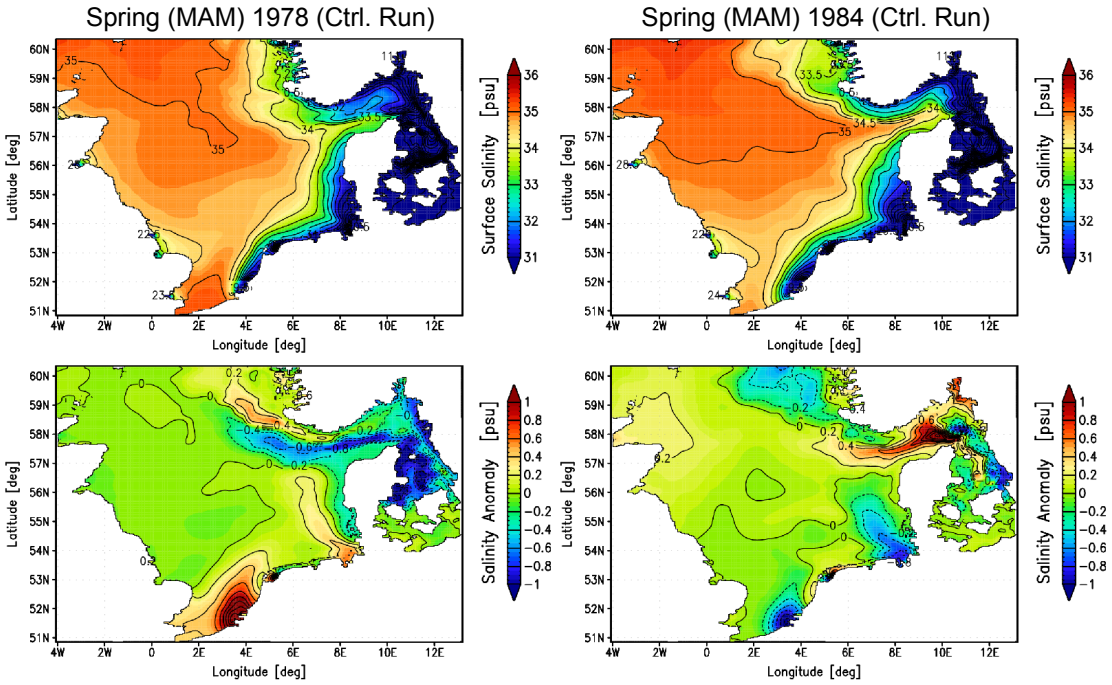

Figure 4.68: Examples of pronounced anomalies of the third PC of depth-averaged salinity for spring (Fig. 4.62), where spring 1978 represents a positive, and spring 1984 a negative anomaly. Lower figures show deviations from the mean of the control period 1951-2000 (Fig. 4.55).

where the salinity anomalies along the Norwegian Trench are again induced by respective anomalies of the second circulation EOF, though in this case, inferred from significant correlations.

4.2.4 Sea Surface Elevation

The first EOF patterns of sea surface elevation, shown in Fig. 4.70, clearly reflect the domain wide variability of the mean surface elevation (Fig. 4.69) induced by uniform anomalies of the SSH prescribed at the open boundaries. The correlation between the first PCs and the time series of spatially averaged SSH, as shown in Fig. 4.71 for spring, amounts to +0.99 (P=99%) for all seasons. Though at the open boundaries, the deviations from the mean elevation are indeed rather uniform, there is a continuously increasing variability from the northern North Sea towards the Continental coast. Moreover, a pronounced discontinuity occurs along the Norwegian Trench, in particular in spring and winter. As the response of the ocean to large scale anomalies of atmospheric pressure fields and wind conditions over the North Atlantic, these structures account for large scale wind-induced surges in the south-eastern North Sea and respective anomalies of the general circulation, well reflected by positive correlations with the first PC of the circulation (r=+0.26 to +0.71, P=93-99%) and hence, with anomalies of the northern inflows (r=+0.47 to +0.73, P=99%). However, the correlations for summer are much lower than those just given in brackets, as indicated by the associated EOF pattern, since in summer, wind condition anomalies are generally too low to cause pronounced local discontinuities in SSH variability. For the remaining seasons strongly varying wind conditions give rise to considerable wind induced surges in the south-eastern North Sea and particularly in the German Bight, entailing in-

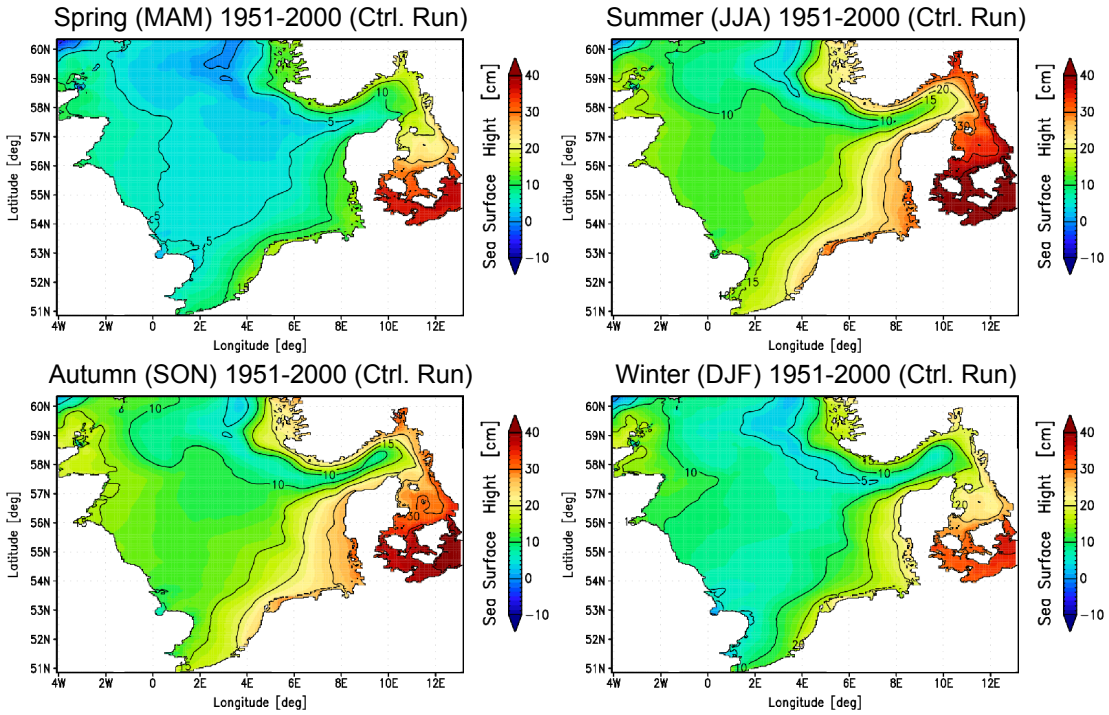

Figure 4.69: Seasonal mean sea surface elevation for 1951-2000.

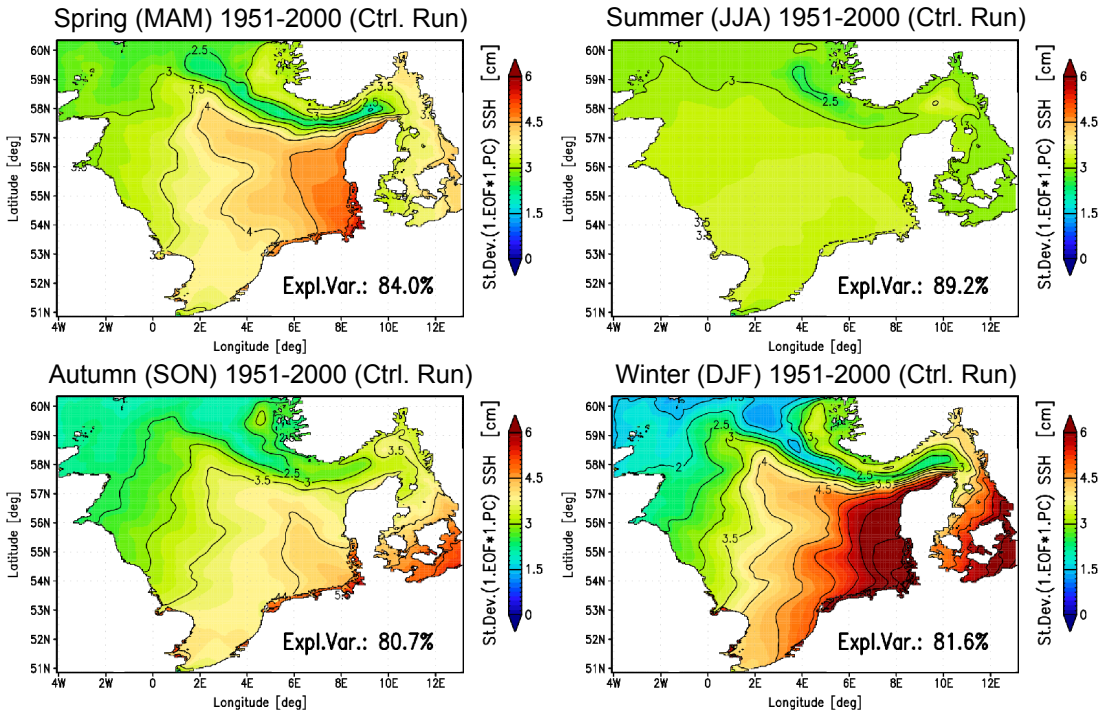

Figure 4.70: Rescaled first EOF patterns of sea surface elevation.

terannual SSH variabilities up to ±7 cm. Besides, the wind driven barotropic circulation in the North Sea is largely balanced by geostrophy (Furnes, 1980; Pingree and Griffith, 1980; Mork, 1981), where a stronger circulation causes stronger sea surface gradients. Consequently, since the variability of the general circulation is the largest in the Norwegian Trench (Fig. 4.39), the variability of SSH represented by the first EOF in this region is reduced.

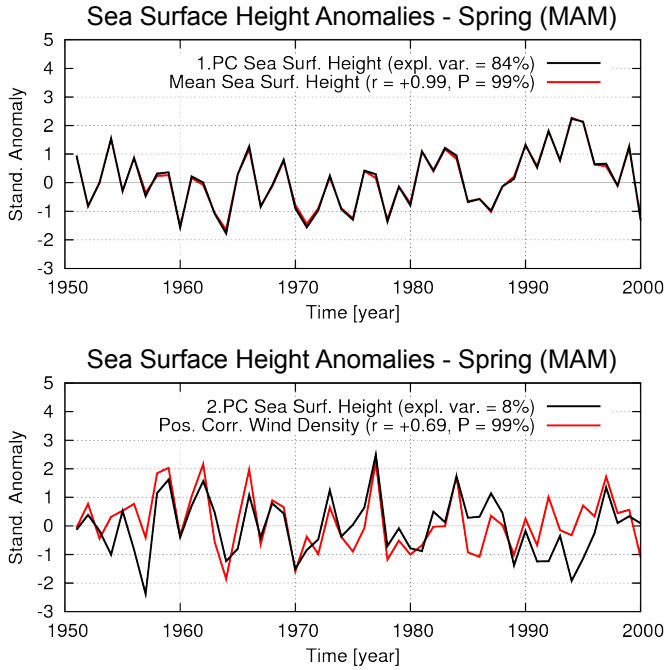

Figure 4.71: Black lines: PCs of sea surface elevation. The descriptions of red lines are given in the figure's keys. The inscribed correlations refer to the respective PC.

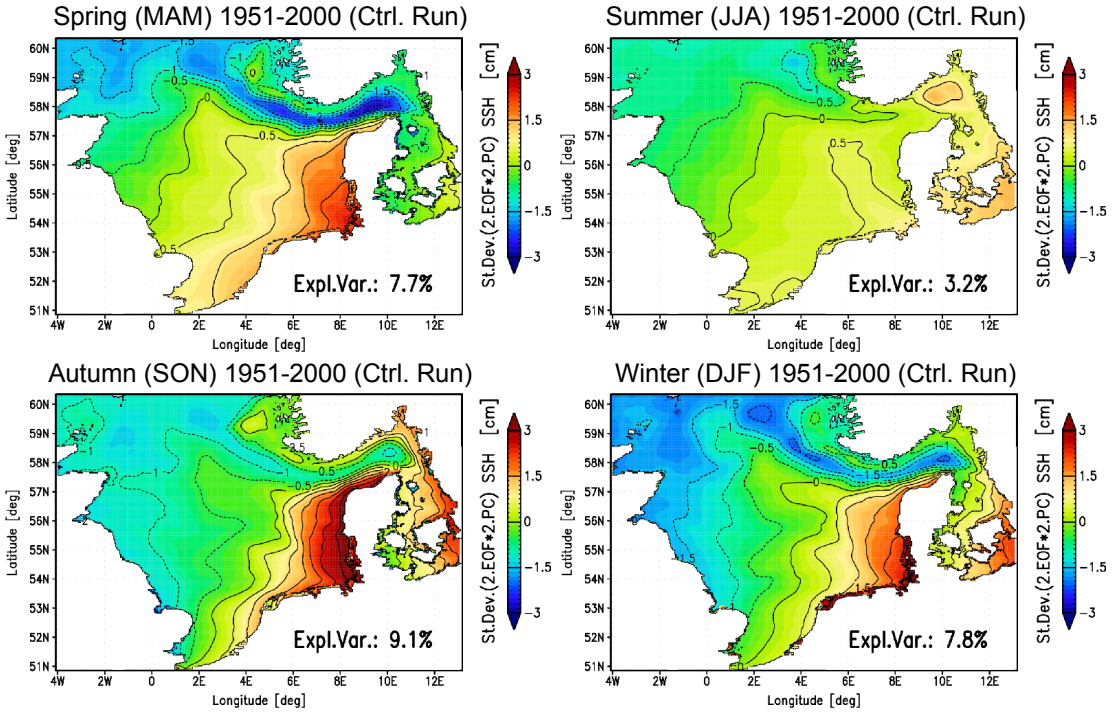

Figure 4.72: Rescaled second EOF patterns of sea surface elevation.

The very same local effects are reflected by the second EOF patterns, too (Fig. 4.72). However, whereas similar or even higher correlations hold for the first PCs of the general circulation (r=+0.61 to +0.91, P=99%) as well as for northern inflow anomalies (r=+0.55 to +0.76, P=99%), no correlations hold for anomalies of the spatially averaged sea surface elevation, indeed making the first and second EOF patterns mutually independent. Since the variability of the SSH prescribed at the open boundaries is extracted from the

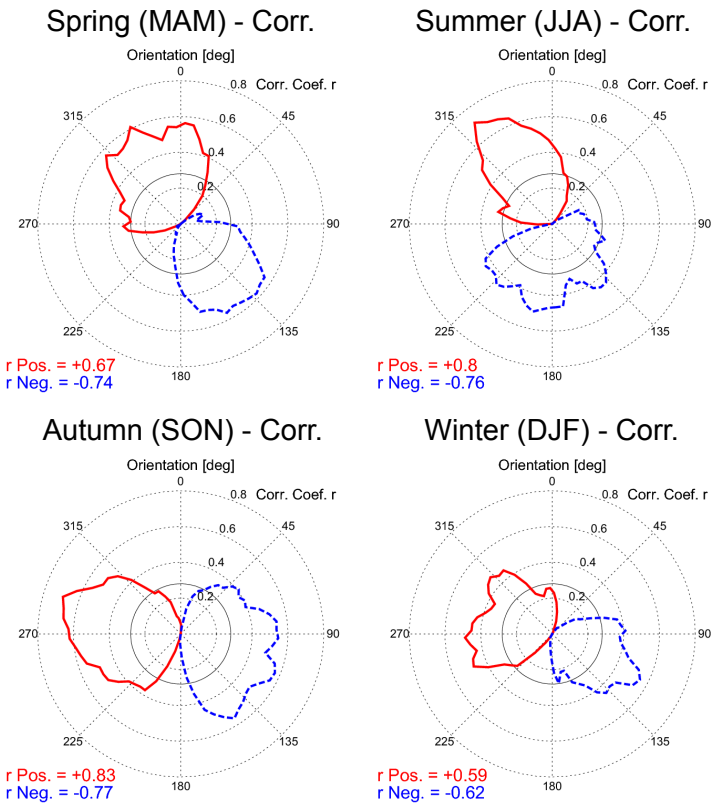

Figure 4.73: Correlations between the wind density functions and the second PCs of sea surface height, analyzed for the period 1951-2000. Red solid lines represent positive correlations, blue dashed lines represent negative correlations. Solid black circles represent the 95% confidence level.

global MPIOM simulation, the second EOF patterns exclusively account for the North Sea response to regional wind anomalies calculated by the regional atmosphere model REMO. Fig. 4.73 depicts correlations of the wind density functions and the second PCs of SSH, which again reflect the sensitivity of circulation anomalies and related SSH anomalies to north-westerly and south-easterly wind anomalies. Hence, without a superimposed dominating mean SSH anomaly, the signs of the anomalies in the Norwegian Trench and the southern North Sea are reversed in the second EOF patterns, merely accounting for 3-9% of the total variance. The high explained variance of the first EOF patterns of 81-89%, however, identifies SSH anomalies induced by large scale atmospheric anomalies to represent the most characteristic interannual SSH variability in the North Sea.

Since inflows through the northern and southern boundaries carry salty Atlantic waters into the North Sea, the circulation dynamics related to the variability of SSH are inevitably linked to local salinity variations. Large-scale storm surges in the south-eastern North Sea, for instance, weaken the southern boundary inflow, enabling Continental river runoff to generate a fresh salinity anomaly along the Continental coast, as accounted for by the third salinity EOFs. The halo-steric effect of the fresh water column, however, further amplifies the positive SSH anomaly and by that, influences the EOF patterns of SSH. Significant correlations indeed hold between the PCs of SSH and salinity (r=+0.28 to +0.66, P=95-99%).

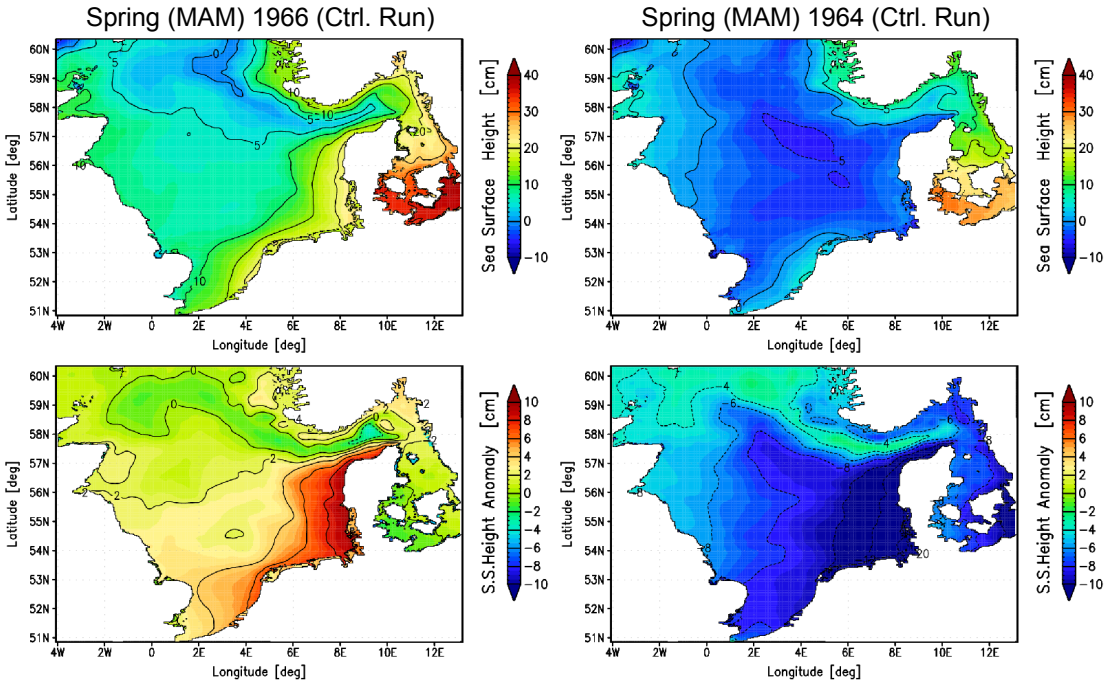

Figure 4.74: Examples of pronounced anomalies of the first PC of SSH for spring (Fig. 4.71), where spring 1966 represents a positive, and spring 1964 a negative anomaly. Lower figures show deviations from the mean of the control period 1951-2000 (Fig. 4.69).

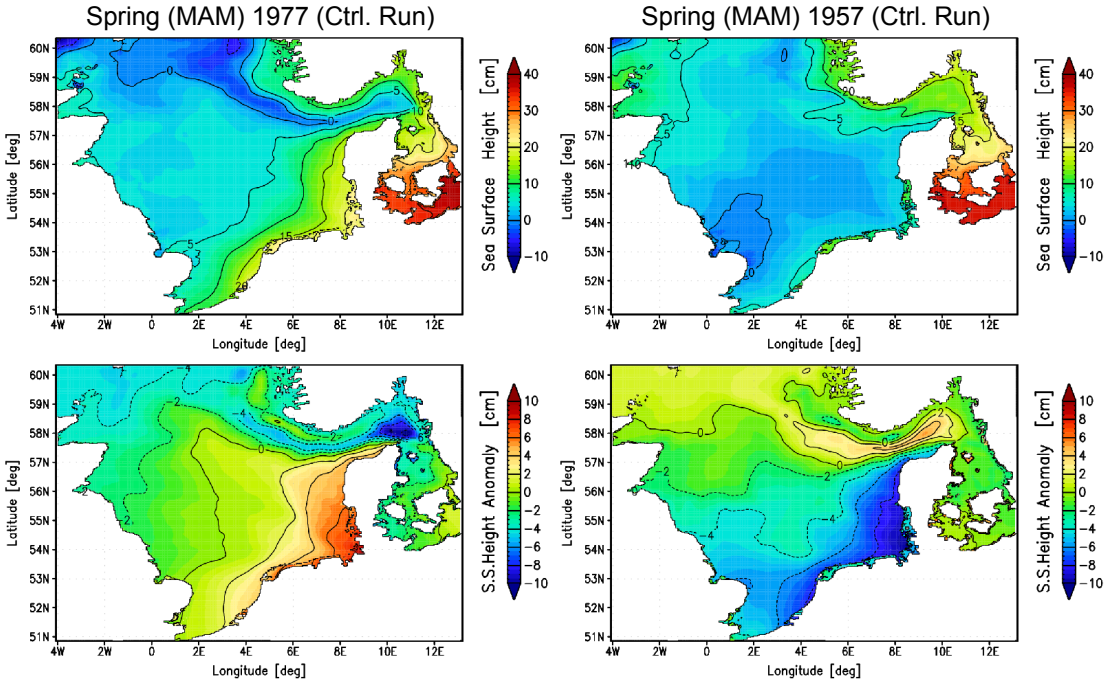

Figure 4.75: Examples of pronounced anomalies of the second PC of SSH for spring (Fig. 4.71), where spring 1977 represents a positive, and spring 1957 a negative anomaly. Lower figures show deviations from the mean of the control period 1951-2000 (Fig. 4.69).

The effective wind variability as well as the effective inflow variability introduced in section 4.1.2 were calculated with respect to circulation anomalies. Analogously, these quantities can be calculated with respect to any other meaningful anomaly. By substituting the PC of the circulation in equation (4.4) and (4.5) by a PC of the sea surface elevation, one

easily obtains effective wind and inflow variabilities related to SSH anomalies. Comparing such effective wind and inflow variabilities, from the second EOF patterns, higher effective variabilities are obtained for spring, summer, and autumn than from the first EOF patterns. Consequently, the maximum difference between the SSH variability in the German Bight and in the Norwegian Trench is higher in the second than in the first EOF patterns for these three seasons. For winter, however, both effective variabilities are higher from the first EOF pattern. Hence, in accordance with the introduced quantity, the maximum difference between the SSH variability in the German Bight and in the Norwegian Trench is higher in the first EOF pattern for winter, too.

Pronounced positive and negative anomalies of the first and second SSH PCs are chosen from Fig. 4.71 and exemplified in Fig. 4.74 and Fig. 4.75. Since the first EOF patterns account for large-scale wind induced SSH anomalies that come along with respective circulation and salinity anomalies, spring 1966 and 1964, shown in Fig. 4.74, demonstrate domain-wide positive and negative anomalies with outstanding peaks in the German Bight of more than ± 10 cm. Note that the anomaly patterns of these two examples are further intensified coincidentally by equally signed anomalies of the second SSH PC (see Fig. 4.71). Accounting for SSH anomalies induced by mere regional wind and circulation anomalies, spring 1977 and 1957, shown in Fig. 4.75, demonstrate second EOF anomalies of indeed similar structure to Fig. 4.74, while being devoid of a domain-wide piling up or down of the water level.

4.2.5 Scenario Period 2001-2099

All PCs are now extended until the year 2099 to address changes of the considered variabilities in the scenario period. The analysis reveals the spatial structure of the individual EOF patterns to remain essentially the same for the extended period as for the control period. The following analysis therefore comprehends the temporal progression of the PCs only. However, the extended PCs shown in Fig. 4.76 to 4.80 are standardized over the entire simulation period 1951-2099. Small quantitative deviations with respect to the previously given PCs of the control period can thus occur in the time series. In addition to the PCs, one green and two red curves are depicted in the graphics. The green curve represents the 30-year running mean of the PC and hence, accounts for climatological fluctuations of the variable at hand about its over all trend defined by a third order polynomial least square fit. The red curves represent the standard deviation of the continuous 30-year time slices, which approximately average to 1 over the 150 years since the PCs are standardized. Individual values of the green and red curves always refer to the center of the pertaining 30-year time slice. Fig. 4.81 and 4.82 finally show the spectral densities of the PCs, reflecting preferred harmonic periods of the anomalies represented by the various EOFs. For the sake of completeness the extended PCs and their spectra are exhibited for all EOFs already referred to in the preceding discussion.

Although in general, the spectral densities do not show pronounced distinct peaks, yet a tendency can be recognized for the circulation spectra as being blued (i.e. higher spec-

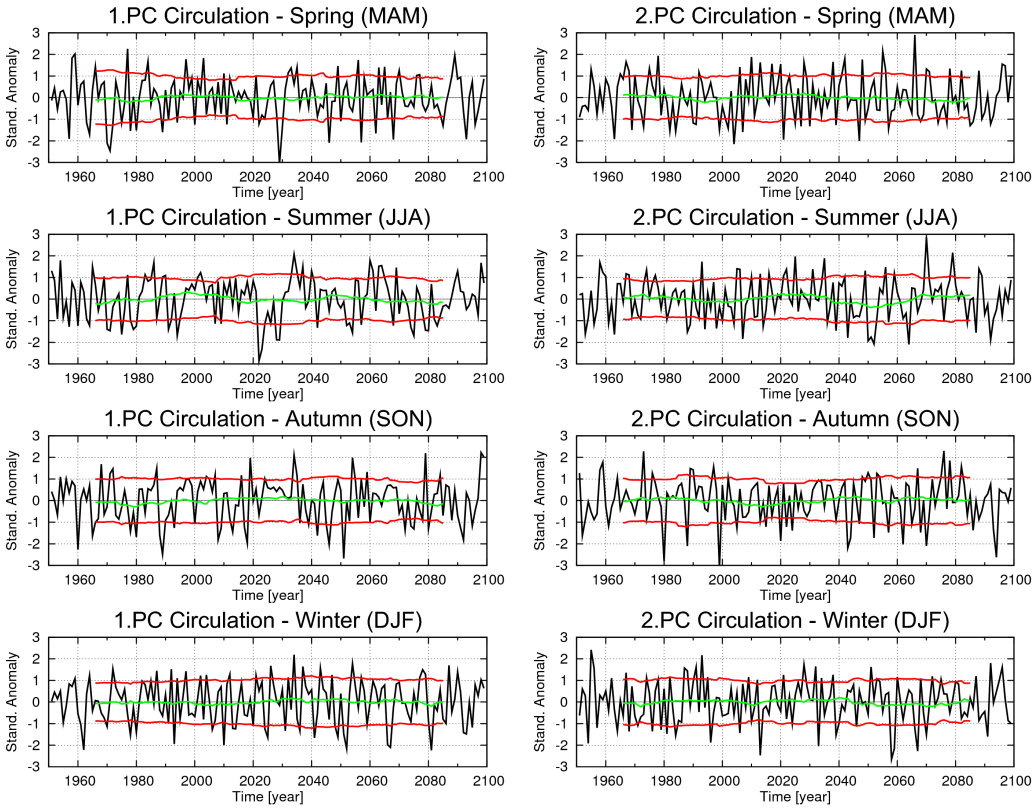

Figure 4.76: Black: First (left) and second (right) PCs of depth-averaged current velocity. Green: 30-year running mean. Red: St.Dev. of 30-year running time slices.

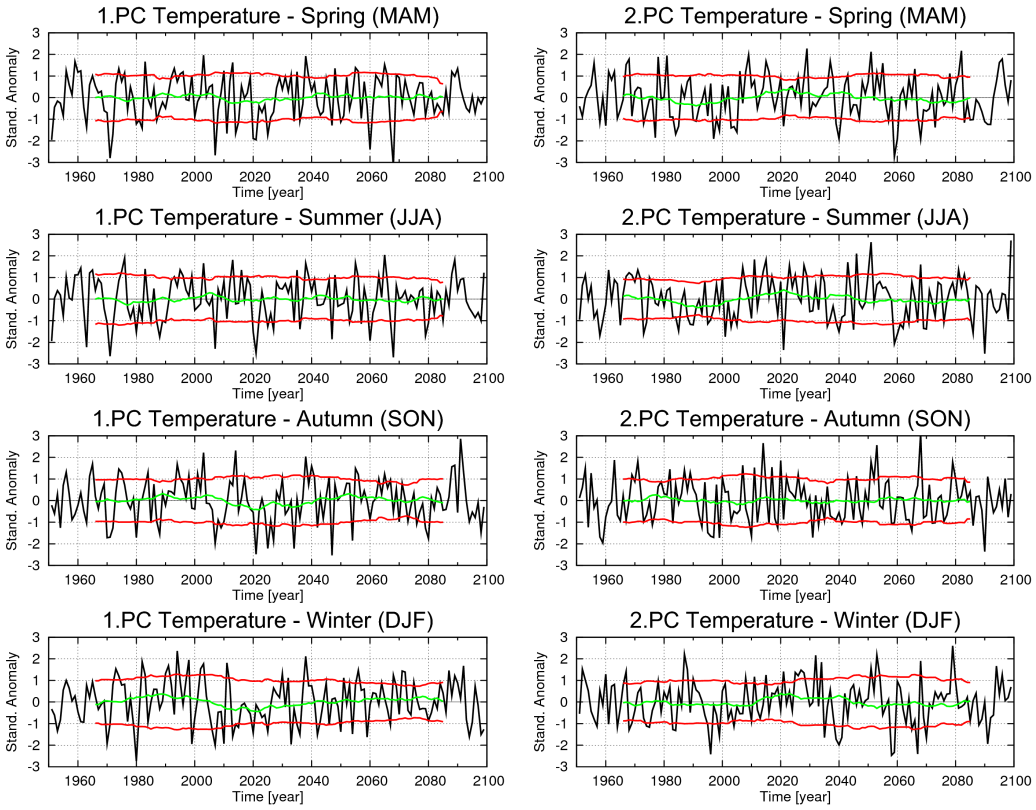

Figure 4.77: Black: First (left) and second (right) PCs of depth-averaged sea water temperature. Green: 30-year running mean. Red: St.Dev. of 30-year running time slices.

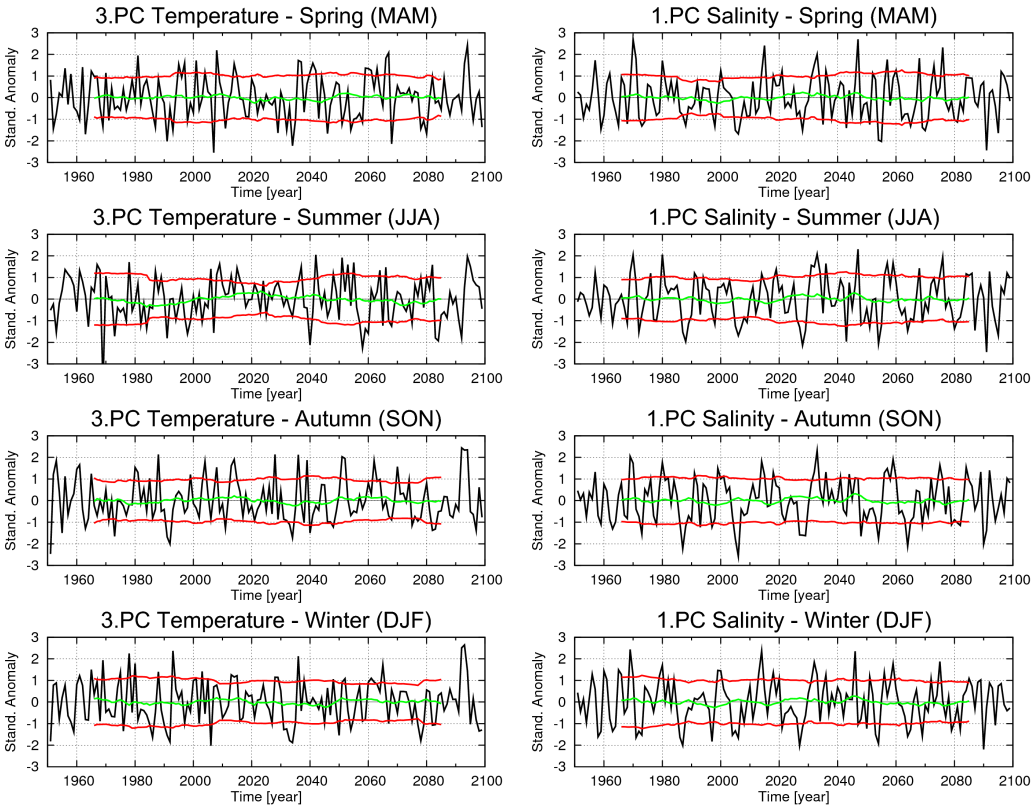

Figure 4.78: Black: Third PCs of depth-averaged sea water temperature (left) and first PCs of depth-averaged salinity (right). Green: 30-year running mean. Red: St.Dev. of 30-year running time slices.

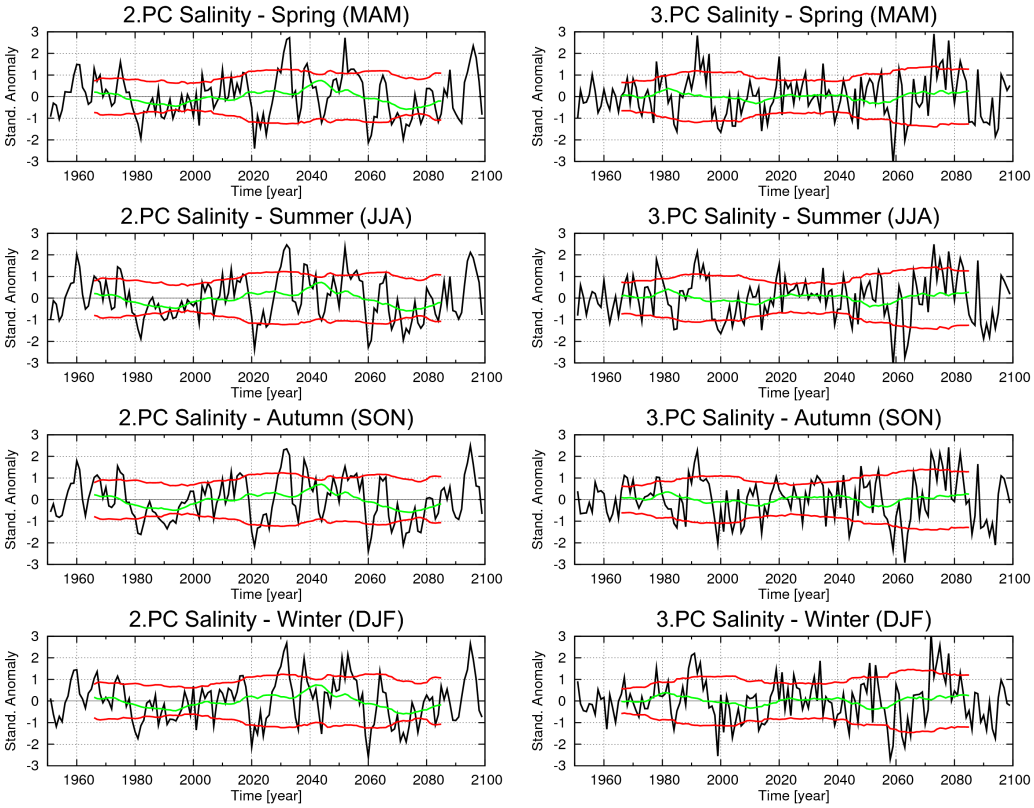

Figure 4.79: Black: Second (left) and third (right) PCs of depth-averaged salinity. Green: 30-year running mean. Red: St.Dev. of 30-year running time slices.

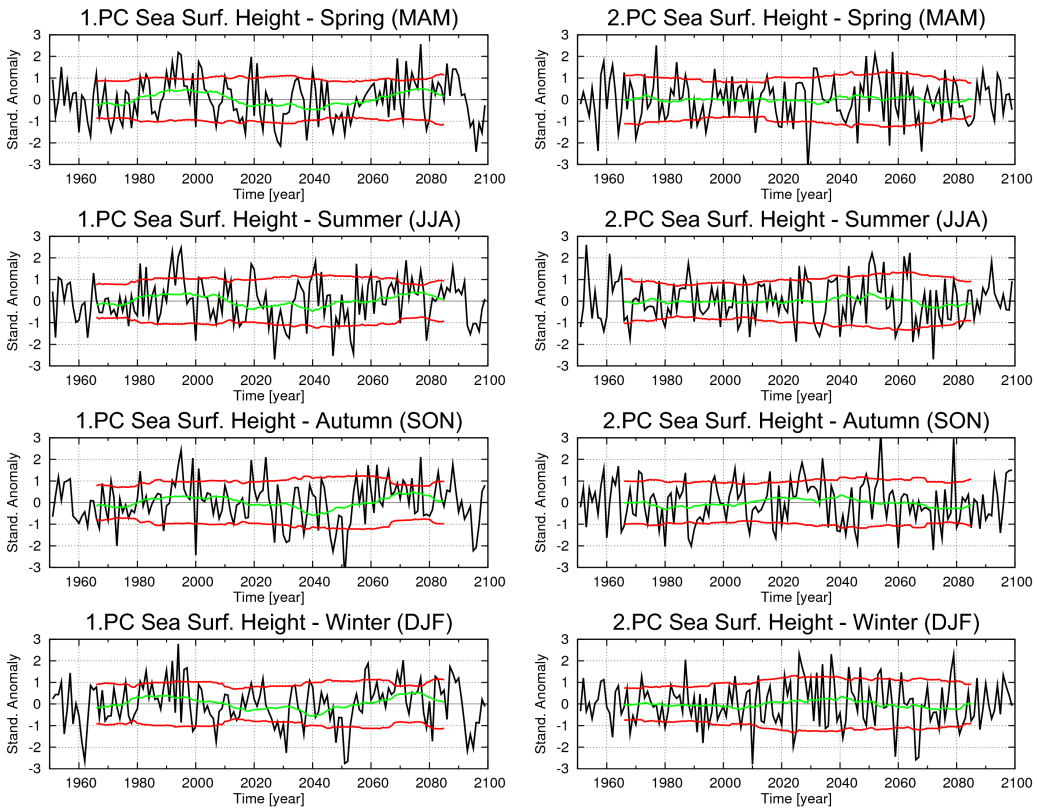

Figure 4.80: Black: First (left) and second (right) PCs of sea surface elevation. Green: 30-year running mean. Red: St.Dev. of 30-year running time slices.

tral densities at short periods), the water temperature spectra as being whitened (i.e. equal spectral densities at all periods), and both the salinity and SSH spectra as being reddened (i.e. higher spectral densities at long periods). Moreover, whereas prevalent 3- to 5-year periods can be identified for circulation anomalies, the diagrams hint at a leaning to 7- to 9-year periods for temperature anomalies and multi-decadal periods for salinity and SSH anomalies. However, direct comparison of PCs of an individual parameter among the four seasons did hardly yield any significant correlations, indicating a low seasonal memory of the considered quantities, retrospectively, and the lack of seasonal causal implications, prospectively. The low interseasonal correlations can be attributed to the strong influence of the atmosphere on the physical conditions in the North Sea. Flows in the atmosphere are about 100 times faster than flows in the ocean, bringing about the characteristic time scale of atmospheric phenomena to be in the order of days and weeks rather than months and seasons (Schlünzen and Krell, 2004). The climatological fluctuations in the extended PCs represented by the green curves are also reflected by the associated spectra, in particular by multi-decadal periods. Considering the red curves, the variabilities within the climatological time slices tend to fluctuate between 80 and 120% of the total variability with preferred periods of about 40 and 80 years, where the total variability is represented by the values ± 1 of the standardized PCs. As a general conclusion, though, according to the presented model results, the variabilities found by EOF analysis of the control period 1951-2000 do not undergo significant changes within the scenario period 2001-2099.

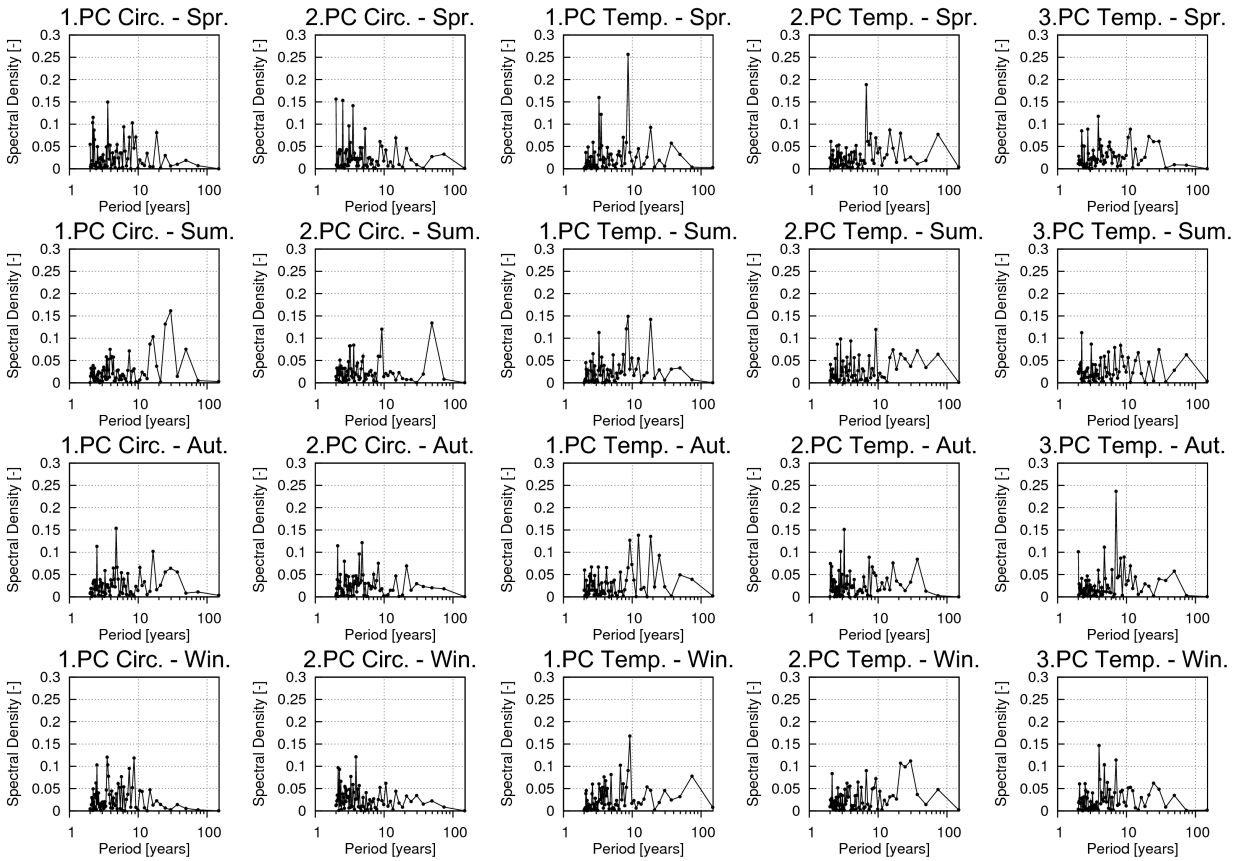

Figure 4.81: Spectral densities for the PCs shown in Fig. 4.76 to 4.80. See also Fig. 4.82.

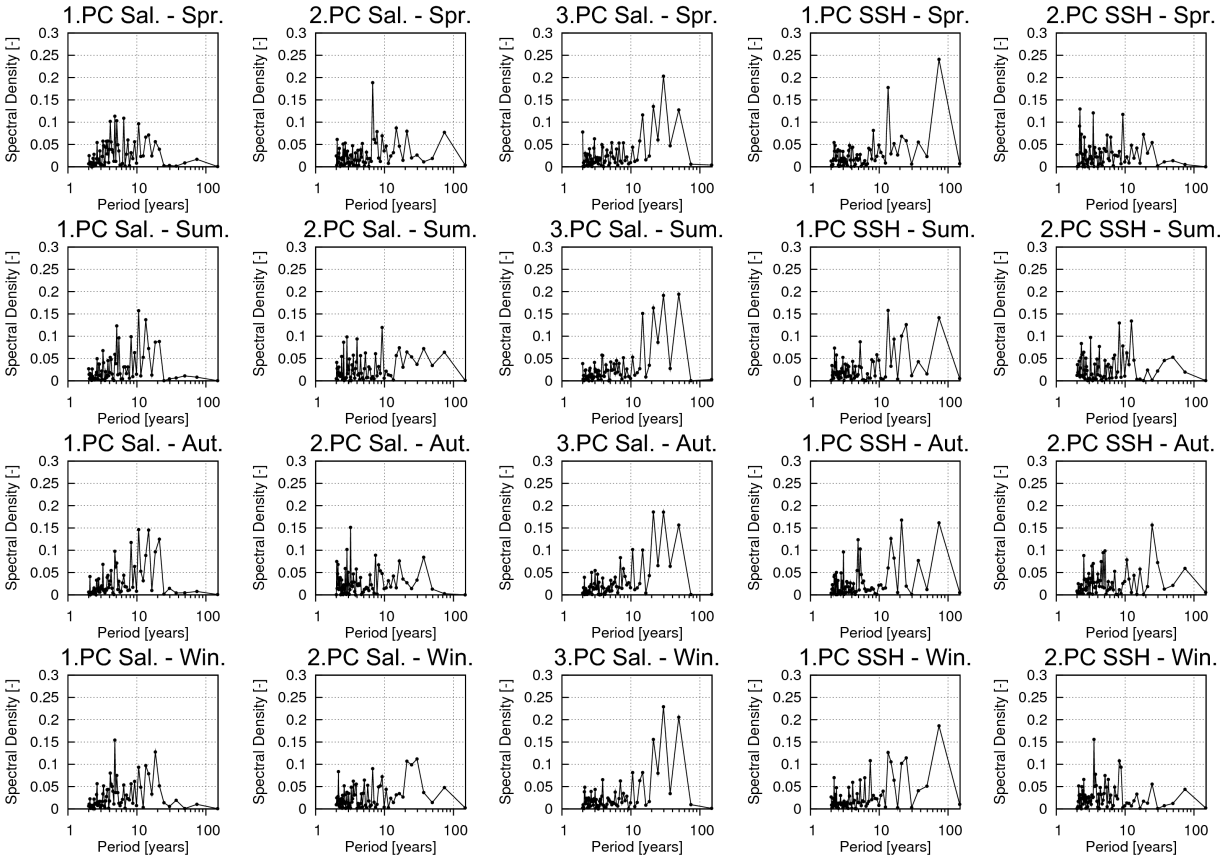

Figure 4.82: Spectral densities for the PCs shown in Fig. 4.76 to 4.80. See also Fig. 4.81.

Chapter 5

Summary and Conclusions

Theory and Methods As pointed out in the introduction (section 1.1), the operational objective of this study was to elaborate a solid model system to be used as a dynamical downscaling tool of potential global climate scenario runs. The evaluation of the involved model chain affirms the presented concept as a successful elaboration of a regionalization procedure for the North Sea (chapter 3). However, in order to reproduce reasonable hydrodynamic conditions in the North Sea for the control period with HAMSOM, optimizing modifications were applied at the open lateral boundaries and to the forcing data extracted from the two specific models MPIOM and REMO (section 2.2.3). The prescription of Baltic discharge into the North Sea at the eastern boundary of the HAMSOM domain and the incorporation of more reasonable SSH gradients at the northern boundaries were necessary to initiate the general long-term circulation as well as to account for appropriate salinity distributions in the eastern North Sea. The application of a bias correction provided the forcing data to reflect the same long-term statistics for a reference period as atmospheric reanalysis data and climatological ocean data. The straightforwardness of the chosen linear bias correction method especially accounts for maintaining the variability as well as the long-term trends of the original uncorrected data. To contribute to the controversial debate about the application of bias correction methods in climate research, some endorsing arguments are discussed in section 2.2.3, which finally concede added value to their application for predominantly pragmatic reasons.

Model Evaluation The evaluation of the presented model chain consists of comparisons of the free control run with a HAMSOM run driven with ERA40 reanalysis data, observational data of climatological water temperature and salinity distributions from Janssen et al. (1999), and literature research of volume transports, residence and flushing times, NAO correlations, surface heat and fresh water fluxes, and thermocline parameters. In general, the model results widely agree with the given references. The most pronounced deviation though is observed in the prevalent wind directions over the North Sea in particular in spring and winter, where the south-easterly wind component is overestimated in the meteorological forcing. Estimated from EOF analysis, these deviations introduce additional variability by about +13% to the general circulation of the North Sea in spring, relative to the ERA40 driven simulation, but reduce the variability by about -13% in winter (section 4.2.1). Nevertheless, the otherwise convincing model results qualify the developed model system as an appropriate and promising tool for performing a dynamical downscaling of the global future scenario run.

Model Results Apart from the operational objective, the scientific objective of this study was to provide a comprehensive examination and quantification of changes of hydrographic and hydrodynamic conditions in the North Sea for the 21st century. In the analysis of the model results of the downscaled scenario run particular attention shall be drawn on regional issues in order to provide a better understanding of potential climate change impacts. The analysis generally focuses on changes of the atmospheric forcing variables, the general circulation in the North Sea, heat fluxes and water temperature, thermocline parameters, fresh water fluxes and salinity, and changes of the sea surface elevation. Thereby, it comprehends trend analysis of time series of the various variables to address

change signals, and EOF analysis to address regional anomalies in the spatial distribution of the variables. The considered time scales are seasonal and annual means. For the definition of a robust and meaningful change signal a representative linear 100-year trend is constructed for any time series from the median parameters of a set of 30 running 100-year linear regression lines. Similarly, the upper and lower quartile of the parameters are used to provide an uncertainty range of the representative trends.

Atmosphere The 100-year trend analysis of the atmospheric forcing parameters suggests an increase of spatially averaged annual mean air temperature in the 21st century by about +2.11 °C with a distinctly stronger warming in winter (+2.31 °C) than in summer (+1.83 °C). The annual mean relative humidity increases by about +1.37 %-points. The increasing air temperature and relative humidity over the North Sea reflect the global IPCC projections of a generally warmer and moister climate. But also cloud cover and precipitation rates are increasing over the North Sea. In particular in summer the cloud cover significantly increases by about +2.88 %-points, while the strongest increase of precipitation by about +0.27 mm/d is observed in autumn. However, neither the mean near-surface wind speeds nor the duration of gale wind conditions undergo significant increase. Rather, the annual means show a slight decrease with seasonal maxima of just about -0.27 m/s and -1.92 h in winter, respectively. In autumn, however, the duration of gale wind conditions increases by about +8.19 h and the local maximum wind speeds increase by about +0.66 m/s. The combination of slightly lower mean wind speeds in spring, summer, and autumn but higher maximum wind speeds and more gale wind conditions in autumn induces a mean raising of the thermocline over the whole thermocline period but an increase of its maximum depth in the end of the period. The incorporation of wind directions in analyzing wind density functions and wind circulation patterns reveals the predominant winds in the North Sea region to remain the westerly winds. The most conspicuous change of the wind density though suggests a transition of easterly and south-easterly wind conditions in spring to even more westerly and north-westerly wind conditions. To a smaller degree, an increase of the relative frequency of westerlies is indicated for summer and autumn, too. The trend towards a higher frequency of westerly winds in the North Sea can be attributed to the intensification of the northern polar front, suggested by global climate simulations.

General Circulation For addressing changes in the general circulation represented by seasonal mean current velocity vectors, trend analyses were applied to depth-averaged current speeds and to volume transports through various lateral sections in the North Sea (section 4.1.2). On a seasonal scale, the increasing westerly and north-westerly wind density in spring gives rise to an enhanced general circulation in this season with a distinctly stronger northern inflow. As well confirmed by correlation distributions of the wind density function and the first PC of the general circulation (section 4.2.1), positive westerly and north-westerly wind anomalies come along with positive circulation anomalies. For the other seasons, however, the slightly decreasing mean wind speeds entail a slightly weaker general circulation, in particular in summer and winter. While more westerly winds are also indicated in summer and autumn, the respective reductions of wind speeds though indeed show higher confidence levels than the increasing westerly relative frequencies. Moreover,

when sea surface wind stresses are used in the calculation of wind density, instead of wind speeds, changes of wind speeds affect the wind density to a larger extent because of the quadratic proportionality between wind stress and wind speed, ascribing further relevance to the influence of changing wind speeds on the general circulation. The most significant seasonal 100-year changes of advective transports are the increasing northern inflow in spring by about +21% (+0.134 Sv), a decreasing inflow through the Dover Strait in summer by about -38% (-0.023 Sv), a weakening of the Skagerrak recirculation in autumn by about -12% (-0.113 Sv), and a reduction of the inflow through the Fair Isle Passage in winter by about -10% (-0.055 Sv), and an increase of Baltic discharge into the North Sea by about +18%. These seasonal changes dominate respective changes on the annual scale, too. The annual net increase of the northern inflow also slightly increases the Norwegian coastal outflow. As indicated by the stream function of depth-integrated volume transports, a substantial proportion of the northern inflow reverses into the Norwegian Coastal Current shortly after entering the northern North Sea. The reduction of the Fair Isle inflow causes a similar weakening of the Dooley Current but also a weakening of the south-eastward flow along the western side of the Norwegian Trench and accordingly, the recirculation in the Skagerrak. Because of the weaker Dooley Current, the northern inflow is guided south-eastward to a lesser extent, consequently enabling more water of North Atlantic origin to enter the central and southern North Sea. A westward intensification of northern inflow is also indicated by a strengthening of the East Shetland Current and increasing southward oriented current speeds in the central North Sea. The changes of depth-averaged current speeds in the entire northern North Sea as far as into the Skagerrak are statistical significant, indicated by confidence levels higher than 95%. An increase of northerly inflow in the 21st century as well as a reduction of the Skagerrak recirculation is also suggested from a similar model study by Ådlandsvik (2008).

EOF analysis of the seasonal mean velocity vectors (section 4.2.1) unveils the largest proportion of the total variability of the general circulation in the North Sea to be attached to the circulation along the Norwegian Trench. The strongest anomalies thereby occur in winter with a standard deviation of about ±8 cm/s of the mean current speeds, accounting for about 60% of the total variability. Because of comparatively low wind speeds, the general circulation in summer is subject to the weakest anomalies allowing for the formation of a rather stable circulation pattern. The second largest proportion of the total circulation variability, accounting for up to 26%, is associated with circulation anomalies in the southern North Sea and English Channel. Correlations of the corresponding PCs with the wind density functions clearly identify northwest-southeast oriented wind anomalies to coincide with circulation anomalies along the Norwegian Trench, and southwest-northeast oriented wind anomalies to coincide with circulation anomalies in the southern North Sea and English Channel. To quantify the connectivity between wind and circulation anomalies, these correlations are multiplied by the standard deviation of the wind density functions. Referred to as the effective wind variability, it accounts for both the degree of synchrony between wind and circulation anomalies, and the amplitude of the wind anomalies. Similarly, by multiplying the correlations of the advective volume transports through the open lateral boundaries of the model domain and the PCs of the circulation with the standard deviation

of the former, the effective inflow variability can be calculated. These two quantities single out the strength of influence of the wind and inflow anomalies, respectively, on the specific circulation anomalies represented by the EOF patterns. Further analysis of the PCs for the 21st century does not indicate a significant change of the respective amplitudes of the circulation anomalies. Moreover, frequency analysis of the PCs showed the circulation anomalies in the North Sea on a seasonal scale not to occur at a preferred period. However, the tendency is indicated of the frequency spectra being blued with stronger circulation anomalies prevalently to occur at short periods of about 3 to 5 years.

Sea Water Temperature and Surface Heat Fluxes According to the model results of the present study, the annual mean volume-averaged water temperature in the North Sea increases in the 21st century by about +1.73 °C with uncertainty ranging from +1.67 to +1.86 °C, estimated from median regression analysis (see section 4.1). The temperature increase gives rise to an increased total heat content of about +22% at the end of the 21st century. Thereby, the stronger warming of air temperature in winter than in summer is similarly reflected by the change of water temperature. While the SST increases in summer by about +1.54 °C, it increases in winter by about +1.95 °C, averaging to an annual mean SST increase of about +1.78 °C with uncertainty ranging from +1.73 to +1.91 °C. A similar model study of the impact of the A1B scenario on the Northwest European Shelf was investigated by Gröger et al. (2012). Results of their study, performed with a higher resolution version of MPIOM, though suggest the annually averaged SST in the North Sea to increase by nearly +2 °C in the 21st century. Yet two other dynamical downscaling studies for the North Sea were realized by Ådlandsvik (2008) and Holt et al. (2010). In the former study the A1B scenario simulated with the Bergen Climate Model (BCM) was downscaled for the period 2072-2097 using the Regional Ocean Model System (ROMS), and compared with the period 1972-1997 of the control run in a slice experiment. According to that study, the annual mean volume-averaged water temperature in the North Sea increases by about +1.4 °C, while the SST increases by about +1.7 °C. Statistical significance is ascribed to the proposed changes, since the standard deviation intervals of the two time slices do not overlap. The distinctly stronger warming of mean SST than of mean volume-averaged temperature results from the maximum warming to occur in spring and summer rather than in the present study to occur in winter. In Holt et al. (2010) the A1B scenario run of a global coupled oceanâ€“atmosphere model from the Met Office Hadley Centre (HadCM3 PPE) was downscaled by the Proudman Oceanographic Laboratory Coastal Ocean Modelling System (POLCOMS). Similar to Ådlandsvik (2008), the future period 2070-2098 is compared with conditions typical of 1961-1990. The temperature increase in the 21st century is quantified to 2-3 °C with a stronger warming trend in summer than in winter, too. From the resulting stronger vertical temperature drop across the thermocline, both studies may indicate an intesification of thermal stratification, in contrast to the results of the present work. Model biases of SST in their studies range from -0.5 to +0.7 °C, while an evaluation of the forcing data is not provided and a bias correction thus not applied. Because of nonlinear relations of long wave and latent surface heat fluxes to air and water temperatures, however, the projected temperature trends are biased as well. Moreover, in physical oceanography stratification is crucial for vertical energy transfer and buoyancy

effects such as the propagation of internal waves. Therefore, it is the *maximum* vertical temperature gradient of the water column which should be referred to as the thermal stratification´s intensity, rather than the temperature drop from the sea surface to the bottom.

The spatial distribution of SST change in winter is strongly influenced by the local bathymetry. Because of the effect of differential heating, the shallow southern and eastern North Sea undergoes maximum warming up to +2.8 °C with a similar spatial distribution of air temperature change. In summer, however, the warming of the sea surface is much more uniformly distributed, since the heat uptake from the atmosphere is widely confined to the surface layers of the stratified water column. The 30-year running trends of volume-averaged water temperature unveil an asymptotic progression of the 21st century warming with a maximum temperature increase around the year 2030 of about +0.03 °C/y to be followed by a steady though fluctuating decrease of warming intensity.

In decomposing the total surface heat flux for the two semi-annual periods spring/summer and autumn/winter, the former period is characterized by a positive net surface heat transfer from the atmosphere into the North Sea, whereas the latter period is characterized by a negative net surface heat transfer from the North Sea to the atmosphere. Considering the individual surface heat flux components, the continuously weaker cooling in the cold seasons turns out to be the main driver of the total warming of the North Sea in the 21st century. Significantly increasing mean cloud cover in spring and summer up to about +2.9 %-points causes a decrease of ingoing short wave radiation by about -5.5 W/m², entailing less net heat input at the sea surface by about -1.4 W/m². Since the warming trend of the atmosphere in winter is stronger than the warming trend of the North Sea in summer, the water temperature drop from summer to winter becomes smaller from year to year so that the SST in winter gets closer to the air temperature and hence, the air-sea temperature difference converges. The consequently decreasing sensible heat flux in autumn and winter by about -6.8 W/m² entails less net heat loss by about -8.3 W/m². These numbers indicate that the warming trend in winter is finally that strong that the North Sea undergoes significant warming in summer, too, even though the net surface heat flux in spring and summer is decreasing. In this conclusion changes of advective heat fluxes through the lateral open boundaries are negligible, since the temperature changes of the inflowing water masses are similar to the mean temperature change of the North Sea, and also the changes of their volume transports are comparatively small. The influence of advective heat fluxes on temperature changes in the North Sea is therefore expected to remain less than 20% for the 21st century, as estimated from both heat content analysis in section 4.1.3 and EOF analysis in section 4.2.2.

EOF analysis of depth-averaged water temperature well distinguishes such temperature variabilities induced by variabilities of surface heat fluxes from those induced by variabilities of advective heat fluxes. As mentioned above, the influence of the surface heat fluxes on the water temperature of the North Sea is estimated from respective explained variances to amount to about 80%. While the magnitude of surface heat flux-induced temperature

variabilities is also controlled by differential heating, the corresponding EOF patterns are dominated by a north-south gradient with high variability amplitudes in the southern and eastern North Sea up to about ±1 °C. Advective anomalies of the inflow via the English Channel induce respective temperature anomalies in the southern North Sea and particularly in the Southern Bight of up to about ±0.5 °C, accounting for up to 9% of the total temperature variance. Indicated by significant negative correlations between inflow anomalies at the Dover Strait and the western side of the Norwegian Trench, the temperature anomalies in the southern North Sea are accompanied by temperature anomalies of inversed sign along the Norwegian Trench of up to ±0.3 °C. Independent of the southern inflow anomalies, respective anomalies of the north-western inflows via the Fair Isle Passage and East Shetland Current account for up to 4% of the total variance with temperature anomalies up to about ±0.2 °C along the British coast. In summer and autumn, however, yet another variability pattern is identified. In these seasons a weak but negative correlation holds between air temperature and wind speed to come along with contrarian buoyancy productions in the water column, respectively. For the specific magnitudes of the involved air temperature and wind speed anomalies, however, the resulting wind-induced shear production has a stronger impact on buoyancy production than a change of the thermal forcing through the sea surface (Pohlmann, 1996b). Thus, anomalies of the depth of the thermocline are thereby determined by respective anomalies of the wind speed. The corresponding EOF patterns for summer and autumn account for such weather conditions that give rise to a wind-induced change of depth-averaged water temperature in the thermocline region (up to ±0.2 °C) but a surface heat flux-induced temperature change of inversed sign in the vertically mixed regions (up to ±0.4 °C). Similar to the EOF analysis of the general circulation, seasonal anomaly patterns of the water temperature in the North Sea do not undergo a significant change in the 21st century. The standard deviation of the anomaly amplitudes vary between 80 and 120% and the corresponding frequency spectra show a tendency of being whitened with a preference to 7- to 9-year periods.

Thermocline The spatial coverage of the thermocline is mainly determined by the local bathymetry and the tidal amplitude and therefore not subject to significant change. Time series analysis of the mean and maximum depth of the thermocline, however, well reflect the slight changes of seasonal mean and maximum wind speeds. The mean depth of the thermocline is decreasing by about -0.2 m, i.e. the thermocline is raising, because of the decreasing mean wind speeds in spring, summer, and autumn. The maximum depth, on the contrary, is increasing by about +2.4 m because of higher maximum wind speeds and more gale wind conditions in autumn. A deepening of the warm surface layer in late summer is also suggested by Ådlandsvik (2008), though not quantified explicitly. Both the mean and maximum intensity of the thermocline are decreasing, induced by the stronger warming trend in winter than in summer. Since the temperature of the deeper waters in summer is determined by the water temperature of the preceding winter, the temperature difference between warm surface waters and underlying cold waters is decreasing, too, because of the aforementioned major warming in winter.

Salinity Seasonal distributions of salinity changes in the 21st century largely reflect the distinct salinity drop of all inflowing water masses from the North Atlantic by about -0.38 psu in combination with minor changes of associated volume transports. The atmospheric forcing is also marked by an intensifying hydrological cycle which leads to enhanced moisture transports from the tropics to high latitudes, entailing a considerable freshening of the Atlantic Ocean north of about 40°N (Gröger et al., 2012). The largest salinity drop of about -0.9 psu is thereby observed at the southern inflow through the English Channel. In the eastern North Sea more low-saline waters enter the Skagerrak caused by increasing Baltic discharge of about +780 m^3/s, where the induced salinity drop is supposed to be underestimated, since in the model run the salinity of Baltic discharge is fixed at monthly climatologies. Changes of surface fresh water fluxes in the North Sea indicate lower evaporation rates in summer because of lower wind speeds and higher relative humidity, and higher precipitation rates in winter to yield an increase of the positive total surface fresh water flux into the North Sea by about +61%. An increasing downward fresh water flux in the 21st century is also expected for the Baltic Sea and its catchment area, causing a significant freshening of the Baltic discharge (Schrum, 2001; Meier, 2006; Bárdossy and Pegram, 2011). In the absence of a unified North Sea/Baltic Sea model, e.g. as presented in Schrum (2001) or Schrum et al. (2003), Baltic discharge in Ådlandsvik (2008) and Holt et al. (2010) is prescribed with climatological salinity, too. The climatological treatment of the Baltic´s salinity clearly reduces the predictability of the involved model systems. However, the constraint is unlikely to significantly affect the results in the open North Sea but rather certainly has a sgnificant impact along the Norwegian coast. Nonetheless, the hydrological model used in section 2.6 to calculate the projected Baltic discharge suggests the changes in Baltic river runoff under the A1B scenario to be significantly smaller in magnitude than the variability of the North Sea exchange with the Baltic, in consistency with results given in Holt et al. (2010).

Moreover, the hydrological model used in Holt et al. (2010) suggests the annual mean increase of North Sea river runoff under the A1B scenario to be one order of magnitude smaller than the increase of total surface fresh water flux. For the present study this ratio approximately corresponds to an increase of river runoff by just about 2% in the 21st century. The climatological monthly river runoffs used in the present study (section 2.3) are therefore regarded to be a minor shortcoming.

Favorable conditions for enhanced ice coverage in shallow coastal North Sea regions due to the decreasing salinity indeed compete with unfavorable conditions to come along with the increasing winter temperatures. However, final local implications of these two parameters with respect to ice coverage cannot directly be concluded from the present study. Riverine fresh water supply is treated climatologically constant and the Wadden areas along the Continental coast, as being primarily affected by intermittent ice cover, are excluded from the model domain, since the model implementation does not allow for ocean grid cells to fall dry. According to the present results, the total volume-averaged salinity in the North Sea decreases by about -0.59 psu with a minimum salinity of about 33.5 psu in the 2070s. The most pronounced salinity drop, however, is recognized in the Skagerrak

region. From the south, more low-saline waters are conveyed into the Skagerrak because of the increasing Baltic discharge and from the west, less saline North Sea waters enter the Skagerrak because of the weaker recirculation rates (see section 4.1.2).

In general, the salinity decrease in the North Sea is stronger at the sea surface than in deeper layers because of increasing surface fresh water supply and Baltic discharge. These trends, however, tend to intensify the stratification in terms of increasing vertical density gradients and would even become stronger when increasing river runoff and decreasing salinity of the Baltic Sea were incorporated, as done in Gröger et al. (2012). Combining their projected change of the vertical salinity gradient of about +0.1 psu from the sea surface to the bottom with the change of the vertical temperature gradient of about -0.5 °C taken from the present work nonetheless yields a slight weakening of the vertical density gradient, in consistency with the decreasing intensity of the thermocline discussed in section 4.1.4.

EOF analyses of depth-averaged salinity single out the variability of Baltic discharge to be responsible for the largest fraction of salinity anomalies in the North Sea. Maximum standard deviations of about ±1 psu in the Kattegat entail strong salinity anomalies in the Skagerrak and along the Norwegian coast, accounting for up to 66% of the total salinity variance. Negatively correlated anomalies of the total surface fresh water flux of up to ±1 mm/d in the same regions further intensify the salinity anomalies. The second and third salinity EOFs reflect the strong influence of the English Channel water on the salinity of the southern North Sea. Thereby, they allow a clear differentiation between salinity anomalies of the English Channel flow and anomalies of the strength of its volume transport. Salinity anomalies of the otherwise regular southern inflow influence the baroclinic component of the general circulation in the southern North Sea, providing for spatially rather homogeneous salinity deviations. The strength of the English Channel flow, on the contrary, directly contributes to the barotropic component of the general circulation, enabling under mere transport anomalies of the southern inflow the steady Continental fresh water supply to induce pronounced salinity anomalies of the Rhine and Elbe river plumes. For the A1B scenario the anomaly patterns for salinity do not show significant changes. Nevertheless, the frequency spectra of the PCs show a tendency of being reddened with a leaning to multi-decadal periods.

Sea Surface Height In consistency to the other parameters discussed so far, the analysis of SSH is also based on seasonal means. Extreme value analysis for crucial coastal flooding events related to global sea level rise or changing wind conditions, however, is inappropriate on seasonal scales. Effective high-water shore protection rather requires temporal high resolution for SSH data of about one hour or less and model runs with more tidal constituents than M_2 incorporated in order to account for the spring-neap tidal cycle. Moreover, wind waves should not be ignored since the significant wave height in the North Sea for a return period of 50 years amounts to about 10 to 12 m with maximum wave heights up to 23 m (Richwien and Lesny, 2004). Such effects are usually take into account by surge models. For an ensemble study of extreme storm surge related water levels in the North Sea under the A1B scenario, see e.g. Sterl et al. (2009). The seasonal changes

and dynamics of SSH considered in the present study thus comprise the uniformly imposed global mean sea level rise, local thermo- and halo-steric effects, the wind-induced south-eastern surge, and geostrophic pressure gradients linked to the general circulation.

Apart from the global mean sea level rise of about +46 cm in the 21st century, decreasing flow speeds along the Norwegian Trench because of the weaker general circulation in summer, autumn, and winter induce weaker horizontal SSH gradients perpendicular to the flow direction. In spring, however, the increase of westerly wind conditions gives rise to an enhanced general circulation and increased flow speeds along the Norwegian Trench, which consequently induce stronger horizontal SSH gradients in this season. Furthermore, the increase of westerly wind conditions entails a maximum total SSH increase up to about +58 cm to occur in the southern and eastern North Sea because of more frequent wind surges. A similarly pronounced SSH rise in the eastern North Sea is observed in winter, which can be attributed to the thermo- and halo-steric effects. They are induced, respectively, by the strongest seasonal temperature increase, recorded in the eastern North Sea in winter, and by the strongest increase of fresh Baltic discharge, entailing a substantial decrease of salinity in the Kattegat and Skagerrak regions.

EOF analysis of seasonal mean SSH reveals the most characteristic seasonal SSH variabilities in the North Sea to be driven by large scale anomalies of atmospheric pressure fields and wind conditions over the North Atlantic. Accounting for up to 89% of the total SSH variance, wind-induced surges in the south-eastern North Sea and respective anomalies of the general circulation result in maximum standard deviations of SSH anomalies of up to ±7 cm in the German Bight. Indicated by the second EOF patterns and their much lower explained variances of up to 9%, SSH anomalies in the North Sea as a response to regional wind anomalies are of minor importance. Nevertheless, correlations of the wind density functions and the second PCs of SSH again reflect the sensitivity of circulation anomalies and related SSH anomalies to north-westerly and south-easterly wind anomalies. Similar to salinity anomalies, the frequency spectra of the PCs of SSH are generally reddened with a tendency to multi-decadal periods. Significant changes in the anomaly patterns are again not recorded in the scenario period.

Ocean and Climate Modeling For a better interpretation of the presented model results, some reviewing words about general problems in ocean and climate modeling shall be remarked. Assumptions, approximations, and simplifications in numerical models are necessary to make the model run in the first place, to keep the model run stable, and at last to comply with the evaluation requirements by creating physically meaningful *and* reasonable results. The assumptions, approximations, and simplifications, together with systematic discretization and iteration errors finally culminate in model errors in a wide sense, which lead to deviations of the model results from reality (Ferziger and Perić, 2002). Typical sources of such methodological errors in numerical climate and ocean models are: Spatial discretisation of the geographic domain, spatial and temporal discretisation of the conservation equations, application of turbulance closure schemes, iterative solution of the algebraic equation system, determination of integral quantities via numerical integra-

tion, Boussinesq approximation, hydrostatic approximation, treatment of the fluid flow as incompressible, assumption of the fluid´s specific heat capacity as constant, underrelaxation, numerical diffusion, salinity restoring, empirical assumptions of unknown physical parameters, and so forth. One can put it provocatively, the number of assumptions in a model is equal to the number of lines in its code. However, these methodological errors can in principal be reduced by model improvements such as higher grid resolutions or more accurate implementation techniques. The problem of limited predictability though will always remain, since the most restrictive difficulty in providing reliable predictions for the weather, the climate, and the ocean is the chaotic behavior of the considered dynamical systems. Chaotic behavior can be deterministically described by the Lorenz equations (Strogatz, 2000), as indeed implemented in weather forecast models. However, since the accuracy of knowing a physical state of reality is always limited, in the very end owing to quantum uncertainties, the Lorenz equation´s high sensitivity to initial conditions inevitably leads to model results that significantly differ from reality after just a view time steps of simulation. Chaotic processes are therefore characterized as being fully deterministic but necessarily unpredictable anyhow. The predictability of a dynamical system is thereby quantified by the Lyapunov time, indicating the characteristic time scale on which the system is chaotic. Since the Lyapunov time for the weather system is in the order of days, a projected forecast for the 21st century seems rather inaccessible. Nevertheless, chaotic processes usually allow to predict the statistical pattern of future events in a definite way, permitting e.g. long-term trends of otherwise chaotic systems to still evolve. Chaotic fluctuations in the atmosphere, for instance, tend to cancel out on time-scales larger or equal to 30 years, advocating the conception of climate and accordingly, climate change. Moreover, chaotic systems may also tend to organize themselves into critical, unstable states which display maximum degree of sensitivity to small disturbances (Barrow, 2003). Remarkably, this state of affairs *increases* the predictability, since it allows an overall balance of a complex chaotic system to persist.

Outlook Accounting for the difficulties of ocean and climate forecasting, model ensemble studies are often invoked in order to utilize future projections in providing uncertainty ranges for the projected variables. Further scientifically valuable work tying up to the presented study would therefore be a detailed comparison of results from other models and other scenarios. Moreover, sensitivity studies of various forcing parameters would yield useful information for estimating the model uncertainties but would also provide another possibility to identify the main drivers for potential climate changes and their implications for the ocean. In this context the presented study has to be understood as an examination of regional effects of one particular potential climate change scenario on the North Sea.

Acknowledgment

This dissertation would not have been possible without the guidance and help of several individuals who in one way or another contributed their valuable assistance in the preparation and completion of this study. In particular, I would like to thank Thomas Pohlmann, Bernhard Mayer, Jian Su, Johannes Pätsch, Kieran O'Driscoll, and Xinping Chen.

As this work contributed to the EU/BMBF-funded MarinERA project *ECODRIVE*, my gratitude is also expressed to the coordinater Jürgen Alheit and all participants for frequent critical but constructive remarks. Thanks to the Max Planck Institute for Meteorology for providing the relevant MPIOM and REMO model results. Supercomputing resources and data storage capacities have been provided by the DKRZ (Deutsches Klimarechenzentrum, Hamburg).

Note

The technical description of the introduced model system and its evaluation, explicated in chapter 2 and 3, respectively, are also reported in Mathis et al. (2013). Model results of the A1B scenario run, analyzed in chapter 4, are also presented in Mathis and Pohlmann (2013). In these two manuscripts, all content related to the present dissertation emerged from my own work and is therefore my personal contribution.

Bibliography

Ådlandsvik, B., 2008. *Marine downscaling of a future climate scenario for the North Sea*. Tellus 60A (3), 451–458.

Ådlandsvik, B., Bentsen, M., 2007. *Downscaling a twentieth century global climate simulation to the North Sea*. Ocean Dynamics 57 (4-5), 453–466.

Akaike, H., 1973. *Information Theory and an Extension of the Maximum Likelihood Principle*. In: Petrov, B. N., Csàki, F. (Eds.), 2nd International Symposium on Information Theory. Akademia Kiadó, Budapest, pp. 267–281.

Andersson, A., Fennig, K., Klepp, C., Bakan, S., Grassl, H., , Schulz, J., 2010. *The Hamburg Ocean Atmosphere Parameters and Fluxes from Satellite Data - HOAPS-3*. Earth Syst. Sci. Data 2, 215–234.

Asselin, R., 1972. *Frequency filter for time integrations*. Monthly Weather Review 100, 487–490.

Backhaus, J. O., 1985. *A three-dimensional model for the simulation of shelf sea dynamics*. Dt. Hydrogr. Z. 38, 165–187.

Backhaus, J. O., 1990. *On the atmospherically induced variability of the circulation of the Northwest European Shelf Sea and related phenomena - a model experiment*. Modeling Marine Systems 1, 93–134, Davies, A. M. (Ed.), Boca Raton, Florida, CRC Press.

Backhaus, J. O., Pohlmann, T., Hainbucher, D., 1986. *Regional Aspects of the Circulation on the North European Shelf*. ICES CM 1986 (C:38), 17 pp.

Bader, D. C., Covey, C., Gutowski Jr., W. J., Held, I. M., Kunkel, K. E., Miller, R. L., Tokmakian, R. T., Zhang, M. H., 2008. *Climate Models: An Assessment of Strengths and Limitations*. A Report by the U.S. Climate Change Science Program and the Subcommittee on Global Change Research. Department of Energy, Office of Biological and Environmental Research, Washington D.C., USA, 124 pp.

Banner, F. T., Collins, B., Massie, K. S., 1979. *The North-West European Shelf Seas: Physical and chemical oceanography, and physical resources*. Elsevier Oceanography Series. Elsevier Scientific Publishing Company, 338 pp.

Bárdossy, A., Pegram, G., 2011. *Downscaling precipitation using regional climate models and circulation patterns toward hydrology*. Water Resources Researc 47, W04505, 18 pp.

Barrow, J. D., 2003. *The Constants of Nature*. Vintage, London, 352 pp.

Becker, G. A., 1981. *Beiträge zur Hydrographie und Wärmebilanz der Nordsee*. Dt. Hydrogr. Z. 34 (5), 167–262.

Becker, G. A., Frohse, A., Damm, P., 1997. *The northwest european shelf temperature and salinity variability*. Dt. Hydrogr. Z. 49 (2-3), 135–151.

Becker, G. A., Pauly, M., 1996. *Sea surface temperature changes in the North Sea and their causes*. ICES Journal of Marine Science 53, 887–898.

Blaas, M., Kerkhoven, D., de Swart, H. E., 2001. *Large-scale circulation and flushing characteristics of the North Sea under various climate forcings*. Climate Research 18, 47–54.

Boyer, T., Levitus, S., Garcia, H., Locarnini, R. A., Stephens, C., Antonov, J., 2005. *Objective analyses of annual, seasonal, and monthly temperature and salinity for the world ocean on a 0.25° grid*. International Journal of Climatology 25 (7), 931–945.

Bryden, H. L., 1973. *New polynomials for thermal expansion, adiabatic temperature gradient and potential temperature of seawater*. Deep-Sea Res. 20, 401–408.

Chapman, S., Lindzen, R. S., 1970. *Atmospheric Tides*. D. Reidel, Dordrecht, 200 pp.

Chen, X., Liu, C., O'Driscoll, K., Su, J., Mayer, B., Pohlmann, T., 2012. *On the nudging terms at open boundaries in regional ocean models*. Ocean Modelling (in press).

Christensen, J., Boberg, F., Christensen, O., Lucas-Picher, P., 2008. *On the need for bias correction of regional climate change projections of temperature and precipitation*. Geophys. Res. Lett. 35, L20709, 6 pp.

Climate, 2006. *Special section: Climate models at the Max Planck Institute for Meteorology (MPI-M)*. Journal of Climate 19 (16), 218 pp.

Colebrook, J. M., Taylor, A. H., 1979. *Year-to-year changes in sea-surface temperature, North Atlantic and North Sea, 1948 to 1974*. Deep Sea Research Part A. Oceanographic Research Papers 26 (7), 825–850.

Dai, A., Wang, J., 1999. *Diurnal and semidiurnal tides in global surface pressure fields*. J. Atmos. Sci. 56, 3874–3891.

Damm, P. E., 1997. *Die saisonale Salzgehalts- und Frischwasserverteilung in der Nordsee und ihre Bilanzierung*. Berichte aus dem ZMK, Reihe B, Ozeanographie 28, 259 pp, Hamburg, Inst. für Meereskunde.

Damm, P. E., Hinzpeter, H., Luthardt, H., Terzenbach, U., 1994. *Seasonal and Interannual Variability in the Atmosphere and in the Sea*. In: Sündermann, J. (Ed.), Circulation and Contaminant Fluxes in the North Sea. Springer, Berlin, pp. 11–55.

Delhez, E. J. M., Damm, P., de Goede, E., de Kok, J. M., Dumas, F., Gerritsen, H., Jones, J. E., Ozer, J., Pohlmann, T., Rasch, P. S., Skogen, M., Proctor, R., 2004. *Variability of shelf-seas hydrodynamic models: lessons from the NOMADS2 project*. J. Mar. Syst. 45, 39–53.

Déqué, M., Jones, R. G., Wild, M., Giorgi, F., Christensen, J. H., Hassell, D. C., Vidale, P. L., Rockel, B., Jacob, D., Kjellström, E., de Castro, M., Kucharski, F., van den Hurk, B., 2005. *Global high resolution versus Limited Area Model climate change projections over Europe: quantifying confidence level from PRUDENCE results*. Clim. Dyn. 25, 653–670.

Dippner, J. W., 1997. *SST Anomalies in the North Sea in Relation to the North Atlantic Oscillation and the Influence on the Theoretical Spawning Time of Fish*. Dt. Hydrogr. Z. 49 (2/3), 267–275.

Dooley, H. D., Furnes, G. K., 1981. *Influence of the wind field on the transport of the northern North Sea*. In: Sætre, R., Mork, M. (Eds.), The Norwegian Coastal Current. Univ. of Bergen, Bergen, Norway, pp. 57–71.

Dyke, P., 2007. *Modelling Coastal and Offshore Processes*. Imperial College Press, London, 412 pp.

Ehret, U., Zehe, E., Wulfmeyer, V., Warrach-Sagi, K., Liebert, J., 2012. *HESS Opinions ¨Should we apply bias correction to global and regional climate model data?¨*. Hydrol. Earth Syst. Sci. 16, 3391–3404.

Eisma, D., Kalf, J., 1987. *Dispersal, concentration and deposition of suspended matter in the North Sea*. J. Geological Society of London 144, 161–178.

Etling, D., 2008. *Theoretische Meteorologie: Eine Einführung (German Edition)*. Springer-Verlag, 3rd Edition, 388 pp.

Feistel, R., 1993. *Equilibrium thermodynamics of seawater revisted*. Prog. Oceanog. 31, 101–179.

Ferziger, J. H., Perić, M., 2002. *Computational Methods for Fluid Dynamics*. Springer-Verlag, Berlin Heidelberg, 3rd Edition, 423 pp.

Feser, F., Rockel, B., von Storch, H., Winterfeldt, J., Zahn, M., 2011. *Regional climate models add value to global model data. A review and selected examples*. Bull. Am. Meteorol. Soc. 92 (9), 1181–1192.

Fofonoff, N. P., 1977. *Computation of potential temperature of seawater for an arbitrary reference pressure*. Deep-Sea Res. 24, 489–491.

Fouquart, Y., Bonnel, B., 1980. *Computations of solar heating of the earth´s atmosphere: A new parameterization*. Beitr. Phys. Atmos. 53, 35–62.

Furnes, G. K., 1980. *Wind effects in the North Sea*. Journal of Physical Oceanography 10, 978–984.

Furnes, G. K., Saelen, O. H., 1977. *Currents and hydrography in the Norwegian Coastal Current off Utsira during JONSDAP-76*. Report 2/77, 16 pp, Univ. of Bergen, Norway.

Genz, H., 2004. *Wie Naturgesetze Wirklichkeit schaffen. Über Physik und Realität*. Rowohlt Tb, 448 pp.

Gill, A. E., 1982. *Atmosphere-Ocean Dynamics*. Academic Press, International Geophysics Series 30, 662 pp.

Griffiths, R. W., Linden, P. F., 1981. *The stability of buoyancy-driven coastal currents*. Dyn. Atmos. Oceans 5, 281–306.

Gröger, M., Maier-Reimer, E., Mikolajewicz, U., Moll, A., Sein, D., 2012. *NW European shelf under climate warming: implications for open ocean - shelf exchange, primary production, and carbon absorption*. Biogeosciences Discussions 9 (11), 16625–16662.

Haerter, J. O., Hagemann, S., Moseley, C., Piani, C., 2011. *Climate model bias correction and the role of timescales*. Hydrol. Earth Syst. Sci. 15, 1065–1079.

Hagemann, S., Chen, C., Haerter, J. O., Heinke, J., Gerten, D., Piani, C., 2011. *Impact of a Statistical Bias Correction on the Projected Hydrological Changes Obtained from Three GCMs and Two Hydrology Models*. J. Hydrometeor 12, 556–578.

Hagemann, S., Dümenil, L., 1998a. *A parametrization of the lateral waterflow for the global scale*. Climate Dynamics 14 (1), 17–31.

Hagemann, S., Dümenil, L., 1998b. *Documentation for the Hydrological Discharge Model*. Technical Report No. 17, 42 pp, Max-Planck-Institute for Meteorology, Germany.

Harold, J. M., Bigg, G. R., Turner, J., 1999. *Mesocyclone activity over the Northeast Atlantic. Part 2: An investigation of causal mechanisms*. Int. J. Climatol. 19 (12), 1283–1299.

Hibler, W. D., 1979. *A dynamic thermodynamic sea ice model*. J. Phys. Oceanogr. 9, 815–846.

Hjøllo, S. S., Skogen, M. D., Svendsen, E., 2009. *Exploring currents and heat within the North Sea using a numerical model*. J. Marine Systems 78 (1), 180–192.

Holt, J., Wakelin, S., Lowe, J., Tinker, J., 2010. *The potential impacts of climate change on the hydrography of the northwest European continental shelf*. Progress in Oceanography 86, 361–379.

Hurrell, J. W., 1995. *Decadal trends in the North Atlantic Oscillation regional temperatures and precipitation*. Science 269, 676–679.

Hurrell, J. W., Deser, C., 2009. *North Atlantic climate variability: The role of the North Atlantic Oscillation*. Journal of Marine Systems 78, 28–41.

Hurrell, J. W., van Loon, H., 1997. *Decadal variations in climate associated with the North Atlantic Oscillation*. Climatic Change 36 (3), 301–326.

ICES, 1983. *Flushing times of the North Sea*. ICES, Copenhagen, Co-operative research report 123, 159 pp.

Jacob, D., 2001. *A note to the simulation of the annual and inter-annual variability of the water budget over the Baltic Sea drainage basin*. Meteorology and Atmospheric Physics 77, 61–73.

Jacob, D., den Hurk, B. J. J. M. V., Andræ, U., Elgered, G., Fortelius, C., Graham, L. P., Jackson, S. D., Karstens, U., Köpken, C., Lindau, R., Podzun, R., Rockel, B., Rubel, F., Sass, B. H., Smith, R. N. B., Yang, X., 2001. *A comprehensive model inter-comparison study investigating the water budget during the BALTEX-PIDCAP period*. Meteorology and Atmospheric Physics 77, 19–43.

Jacob, D., Podzun, R., 1997. *Sensitivity studies with the regional climate model REMO*. Meteorology and Atmospheric Physics 63, 119–129.

Janssen, F., Schrum, C., Backhaus, J. O., 1999. *A Climatological Data Set of Temperature and Salinity for the Baltic Sea and the North Sea*. Dt. Hydrogr. Z. 51 (9), 5–245.

Jones, J. E., 2002. *Coastal and shelf-sea modelling in the European context*. Oceanography and marine biology 40, 37–141.

Jungclaus, J. H., Botzet, M., Haak, H., Keenlyside, N., Luo, J. J., Latif, M., Marotzke, J., Mikolajewicz, U., Roeckner, E., 2006a. *Ocean circulation and tropical variability in the coupled model ECHAM5/MPI-OM*. Journal of Climate 19, 3952–3972.

Jungclaus, J. H., Haak, H., Esch, M., Roeckner, E., Marotzke, J., 2006b. *Will Greenland melting halt the thermohaline circulation?* Geophys. Res. Lett. 33, L17708, 5 pp.

Kalnay, E., Kanamitsu, M., Kistler, R., Collins, W., Deaven, D., Gandin, L., Iredell, M., Saha, S., White, G., Woollen, J., Zhu, Y., Celliah, M., Ebisuzaki, W., Higgins, W., Janowiak, J., Mo, K. C., Ropelewski, C., Wang, J., Leetmaa, A., Reynolds, R., Jenne, R., Joseph, D., 1996. *The NCEP/NCAR 40-year reanalysis project*. Bulletin of the American Meteorological Society 77, 437–471.

Katzfey, J. J., McGregor, J. L., Nguyen, K. C., Thatcher, M., 2009. *Dynamical downscaling techniques: Impacts on regional climate change signals*. Proceedings, World IMACS/MODSIM Congress, Cairns, 6 pp.

Klein, H., Lange, W., Mittelstaedt, E., 1994. *Tidal and residual currents in the northern North Sea: Observations*. Deutsche Hydrografische Zeitschrift 46 (1), 5–27.

Krause, G., Budeus, G., Gerdes, D., Schaumann, K., Hesse, K., 1986. *Frontal systems in the German Bight and their physical and biological effects*. In: Nihoul, J. C. J. (Ed.), Marine interfaces ecohydrodynamics: proceedings of the 17th International Liège Colloquium on Ocean Hydrodynamics. Elsevier Science Publishers (Elsevier Oceanography Series 42), Amsterdam, pp. 119–140.

Larsén, X. G., Mann, J., 2009. *Extreme winds from the NCEP/NCAR reanalysis data*. Wind Energy 12 (6), 556–573.

Lenderink, G., Buishand, A., van Deursen, W., 2007. *Estimates of future discharges of the river Rhine using two scenario methodologies: direct versus delta approach*. Hydrol. Earth Syst. Sci. 11 (3), 1145–1159.

Lenhart, H. J., Pohlmann, T., 1997. *The ICES-boxes approach in relation to results of a North Sea circulation model*. Tellus 49 A (1), 139–160.

Lenhart, H. J., Pohlmann, T., 2004. *North Sea hydrodynamic modelling: a review*. Senckenberg Marit 34, 53–88.

Li, H., Sheffield, J., Wood, E. F., 2010. *Bias correction of monthly precipitation and temperature fields from Intergovernmental Panel on Climate Change AR4 models using equidistant quantile matching*. J. Geophys. Res. 115, D10101, 20 pp.

Lin, S. J., Rood, R. B., 1996. *Multidimensional flux form semi-Lagrangian transport*. Mon. Wea. Rev. 124, 2046–2068.

Loewe, P., Koslowski, G., 1998. *The Western Baltic sea ice season in terms of a mass-related severity index 1879-1992. (II). Spectral characteristics and associations with the NAO, QBO, and solar cycle*. Tellus 50A (2), 219–241.

Lorenz, P., Jacob, D., 2005. *Influence of regional scale information on the global circulation: A two-way nesting climate simulation*. Geophys. Res. Lett. 32, L18706, 4 pp.

Luyten, P. J., Jones, J. E., Proctor, R., 2003. *A Numerical Study of the Long- and Short-Term Temperature Variability and Thermal Circulation in the North Sea*. Journal of Physical Oceanography 33 (1), 37–56.

Maier-Reimer, E., 1979. *Some effects of the Atlantic circulation and of river discharges on the residual circulation of the North Sea*. Dt. Hydrogr. Z. 32 (3), 126–130.

Majewski, D., 1991. *The Europa-Modell (EM) of the Deutscher Wetterdienst*. ECMWF Seminar on numerical methods in atmospheric models 2, 147–191.

Maraun, D., 2012. *Nonstationarities of regional climate model biases in European seasonal mean temperature and precipitation sums*. Geophys. Res. Lett. 39, L06706, 5 pp.

Marsland, S. J., Haak, H., Jungclaus, J. H., Latif, M., Roeske, F., 2003. *The Max-Planck-Institute global ocean/sea ice model with orthogonal curvilinear coordinates*. Ocean Modelling 5, 91–127.

Mathis, M., Mayer, B., Pohlmann, T., 2013. *An Uncoupled Dynamical Downscaling for the North Sea: Method and Evaluation*. Ocean Modelling (submitted).

Mathis, M., Pohlmann, T., 2013. *Projected Forecast of Hydrodynamic Conditions in the North Sea for the 21st Century*. Climate Dynamics (submitted).

Meier, H. E. M., 2006. *Baltic Sea climate in the late twenty-first century: a dynamical downscaling approach using two global models and two emission scenarios*. Clim. Dyn. 27, 39–68.

Mellor, G. L., Yamada, T., 1974. *A hierarchy of turbulence closure models for planetary boundary layers*. J. Atmos. Sci. 31, 1791–1806.

Melsom, A., Lien, V. S., Budgell, W. P., 2009. *Using the Regional Ocean Modeling System (ROMS) to improve the ocean circulation from a GCM 20th century simulation*. Ocean Dynamics 59 (6), 969–981.

Meyer, E. M. I., Pohlmann, T., Weisse, R., 2011. *Thermodynamic variability and change in the North Sea (1948-2007) derived from a multidecadal hindcast*. Journal of Marine Systems 86 (3-4), 35–44.

Michaelsen, K., Krell, U., Reinhardt, V., Grassl, H., Kaufeld, L., 1998. *Climate of the North Sea*. Einzelveröffentlichung 118, DWD/Zentr. Meeres- und Klimaforsch., Hamburg, Germany, 277 pp.

Mlawer, E. J., Taubman, S. J., Brown, P. D., Iacono, M. J., Clough, S. A., 1997. *Radiative transfer for inhomogeneous atmospheres: RRTM, a validated correlated-k model for the longwave*. J. Geophys. Res. 102 (D14), 16,663–16,682.

Morcrette, J.-J., Clough, S. A., Mlawer, E. J., Iacono, M. J., 1998. *Impact of a validated radiative transfer scheme, RRTM, on the ECMWF model climate and 10-day forecasts*. ECMWF Reading, Technical Memorandum 252, 47 pp.

Mork, M., 1981. *Circulation phenomena and frontal dynamics of the Norwegian Current*. Phil. Trans. R. Soc. Lond. A 302, 635–647.

Mudelsee, M., Chirila, D., Deutschländer, T., Döring, C., Haerter, J., Hagemann, S., Hoffmann, H., Jacob, D., Krahe, P., Lohmann, G., Moseley, C., Nilson, E., Panferov, O., Rath, T., Tinz, B., 2010. *Climate Model Bias Correction und die Deutsche Anpassungsstrategie*. Mitteilungen Deutsche Meteorologische Gesellschaft 03/2010, 2–7.

Nakicenovic, N., Swart, R. (Eds.), 2000. *Special Report on Emissions Scenarios: A Special Report of Working Group III of the Intergovernmental Panel on Climate Change*. Cambridge University Press, Cambridge, U.K., 599 pp.

Nilson, E., Carambia, M., Krahe, P., Rachimow, C., Beersma, J., 2010. *Bias-Korrekturmodelle im Vergleich: Eine Bewertung im Kontext der hydrologischen Klimafolgenforschung*. Forum für Hydrologie und Wasserbewirtschaftung, 8 pp.

Nordeng, T. E., 1994. *Extended versions of the convective parameterization scheme at ECMWF and their impact on the mean and transient activity of the model in the tropics*. ECMWF Reading, Technical Memorandum 206, 41 pp.

O'Driscoll, K., Mayer, B., Ilyina, T., Pohlmann, T., 2012. *Modelling the cycling of persistent organic pollutants (POPs) in the North Sea system: fluxes, loading, seasonality, trends*. Journal of Marine Systems (in press), 14 pp.

Oreskes, N., Shrader-Frechette, K., Belitz, K., 1994. *Verification, validation, and confirmation of numerical models in the earth sciences*. Science 263, 641–646.

Orlanski, I., 1976. *A simple boundary condition for unbounded hyperbolic flows*. Journal of Physical Oceanography 12, 251–269.

OSPAR, 2000. *Quality Status Report 2000: Region II Greater North Sea*. OSPAR Commission 136, London, 25 pp.

Otto, L., 1976. *Problems in the application of reservoir theory to the North Sea*. ICES CM 1976/C 18, 17 pp.

Otto, L., Zimmerman, J. T. F., Furnes, G. K., Mork, M., Sætre, R., Becker, G., 1990. *Review of the physical oceanography of the North Sea*. Netherlands J Sea Res 26 (2-4), 161–238.

Pickard, G. L., Emery, W. J., 1990. *Descriptive Physical Oceanography: An Introduction*. Butterworth-Heinemann, Oxford, 5th Edition, 336 pp.

Pielke, R. A. S., Wilby, R. L., 2012. *Regional climate downscaling: What´s the point?* Eos Trans AGU 93 (5), 52–53.

Pingree, R., 2005. *North Atlantic and North Sea Climate Change: curl up, shut down, NAO and Ocean Colour*. J. Mar. Biol. Ass. U.K. 85 (06), 1301–1315.

Pingree, R. D., 1978. *Cyclonic eddies and cross-frontal mixing*. J. Mar. Biol. Ass. U.K. 58, 955–963.

Pingree, R. D., Griffith, D. K., 1980. *Currents driven by a steady uniform wind stress on the shelf seas around the British Isles*. Oceanologica Acta 3, 227–236.

Pohlmann, T., 1991. *Untersuchung hydro- und thermodynamischer Prozesse in der Nordsee mit einem dreidimensionalen numerischen Modell*. Berichte des Zentrums fur Meeres- und Klimaforschung 23, 1–116.

Pohlmann, T., 1996a. *Calculating the annual cycle of the vertical eddy viscosity in the North Sea with a three-dimensional baroclinic shelf sea circulation model*. Continental Shelf Research 16 (2), 147–161.

Pohlmann, T., 1996b. *Calculating the development of the thermal vertical stratification in the North Sea with a three-dimensional baroclinic circulation model*. Continental Shelf Research 16 (2), 163–194.

Pohlmann, T., 1996c. *Predicting the thermocline in a circulation model of the North Sea - Part 1: model description, calibration and verification*. Continental Shelf Research 16 (2), 131–146.

Pohlmann, T., 2006. *A meso-scale model of the central and southern North Sea: Consequences of an improved resolution*. Continental Shelf Research 26 (19), 2367–2385.

Prandle, D., 1984. *A modelling study of the mixing of 137Cs in the seas of the European continental shelf* . Philos. Trans. R. Soc. Lond. A 310, 407–436.

Richwien, W., Lesny, K., 2004. *Windfarmen in der Nordsee*. Ingenieurwissenschaft - Essener Unikate 23, Universität Duisburg-Essen, Wissenschaftsverlag, Science Support Centre, 60–69.

Rodhe, J., 1996. *On the dynamics of the large-scale circulation of the Skagerrak*. J. Sea Res. 35, 9–21.

Rodhe, J., 1998. *The Baltic and North Seas: A process-oriented review of physical oceanography*. In: Robinson, A. R., Brink, K. H. (Eds.), The Sea. Vol. 11. John Wiley & Sons, pp. 699–732.

Roeckner, E., Arpe, K., Bengtsson, L., Brinkop, S., Dümenil, L., Esch, M., Kirk, E., Lunkeit, F., Ponater, M., Rockel, B., Sausen, R., Schlese, U., Schubert, S., Windelband, M., 1992. *Simulation of the present-day climate with the ECHAM model: impact of model physics and resolution*. MPI-M Report No. 93, 112 pp, Max-Planck-Institute for Meteorology, Germany.

Roeckner, E., Arpe, K., Bengtsson, L., Christoph, M., Claussen, M., Dümenil, L., Esch, M., Giorgetta, M., Schlese, U., Schulzweida, U., 1996. *The atmospheric general circulation model ECHAM-4: Model description and simulation of present-day climate*. MPI-M Report No. 218, 90 pp, Max-Planck-Institute for Meteorology, Germany.

Roeckner, E., Bäuml, G., Bonaventura, L., Brokopf, R., Esch, M., Giorgetta, M., Hagemann, S., Kirchner, I., Kornblueh, L., Manzini, E., Rhodin, A., Schlese, U., Schulzweida, U., Tompkins, A., 2003. *The atmospheric general circulation model ECHAM 5*. MPI-M Report No. 349, 140 pp, Max-Planck-Institute for Meteorology, Germany.

Roeckner, E., Brokopf, R., Esch, M., Giorgetta, M., Hagemann, S., Kornblueh, L., Manzini, E., Schlese, U., Schulzweida, U., 2006. *Sensitivity of simulated climate to horizontal and vertical resolution in the ECHAM5 atmosphere model*. Journal of Climate 19, 3771–3791, Spec. Issue.

Rogers, J. C., 1984. *The association between the North Atlantic oscillation and the Southern oscillation in the Northern Hemisphere*. Mon. Wea. Rev. 112, 1999–2015.

Rojas, R., Feyen, L., Dosio, A., Bavera, D., 2011. *Improving pan-European hydrological simulation of extreme events through statistical bias correction of RCM-driven climate simulations*. Hydrol. Earth Syst. Sci. 15, 2599–2620.

Schlünzen, K. H., Krell, U., 2004. *Atmospheric parameters for the North Sea: a review*. Marine Biodiversity 34 (1/2), 1–52.

Schmidli, J., Frei, C., Vidale, P. L., 2006. *Downscaling from GCM precipitation: A benchmark for dynamical and statistical downscaling*. Int. J. Climatol. 26, 679–689.

Schrödinger, E., 1962. *Was ist ein Naturgesetz? Beiträge zum naturwissenschaftlichen Weltbild*. Oldenbourg Wissenschaftsverlag, 6th Edition (2008), 147 pp.

Schrum, C., 2001. *Regionalization of climate change for the North Sea and the Baltic Sea*. Climate Research 18, 31–37.

Schrum, C., Harms, I., Hatten, K., 2005. *Modelling Air-sea exchange in the Barents Sea By using a coupled regional ice-ocean model*. Meteorologische Zeitschrift 14 (6), 1–3.

Schrum, C., Hübner, U., Jacob, D., Podzun, R., 2003. *A coupled atmosphere/ice/ocean model for the North Sea and the Baltic Sea*. Clim. Dyn. 21, 131–151.

Schrum, C., Siegismund, F., 2002. *Modellkonfiguration des Nordsee/Ostseemodells: 40-Jahres NCEP Integration*. Berichte aus dem Zentrum für Meeres- und Klimaforschung, Ozeanographie 44, 178 pp.

Schwarz, G., 1978. *Estimating the dimension of a model*. Annals of Statistics 6, 461–464.

Scorer, R. S., 1997. *Dynamics of Meteorology and Climate*. J. Wiley & Sons, Chichester, 2nd Edition, 686 pp.

Siegismund, F., Schrum, C., 2001. *Decadal changes in the wind forcing over the North Sea*. Climate Research 18, 39–45.

Simmons, A. J., Burridge, D. M., 1981. *An energy and angular-momentum conserving vertical finite-difference scheme and hybrid vertical coordinate*. Monthly Weather Review 109, 758–766.

Simpson, J. H., 1997. *Physical processes in the ROFI regime*. J. Mar. Syst. 12 (1), 3–15.

Simpson, J. H., Hunter, J. R., 1974. *Fronts in the Irish Sea*. Nature 250, 404–406.

Simpson, J. H., Pingree, R. D., 1978. *Shallow sea fronts produced by tidal stirring*. In: Bowman, M. J., Esaias, W. E. (Eds.), Oceanic fronts in coastal processes. Springer, New York, pp. 29–42.

Slangen, A. B. A., Katsman, C. A., van de Wal, R. S. W., Vermeersen, L. L. A., Riva, R. E. M., 2012. *Towards regional projections of twenty-first century sea-level change based on IPCC SRES scenarios*. Climate Dynamics 38, 1191–1209.

Smith, J. A., Damm, P. E., Skogen, M. D., Flather, R. A., Pätsch, J., 1996. *An investigation into the variability of circulation and transport on the north-west european shelf using three hydrodynamic models*. Ocean Dynamics 48 (3-4), 325–348.

Solomon, S., Qin, D., Manning, M., Chen, Z., Marquis, M., Averyt, K. B., Tignor, M., Miller, H. L. (Eds.), 2007. *Contribution of Working Group I to the Fourth Assessment Report of the Intergovernmental Panel on Climate Change*. Cambridge University Press, Cambridge, U.K., and New York, USA, 996 pp.

Steele, J. H., Thorpe, S. A., Turekian, K. K. (Eds.), 2009. *North Sea Circulation. Encyclopedia of Ocean Sciences*. Vol. 4. Academic Press, London, 2nd Edition, 73–81.

Sterl, A., van den Brink, H., de Vries, H., Haarsma, R., van Meijgaard, E., 2009. *An ensemble study of extreme storm surge related water levels in the North Sea in a changing climate*. Ocean Science 5, 369–378.

Strogatz, S. H., 2000. *Nonlinear Dynamics and Chaos: Applications to Physics, Biology, Chemistry, and Engineering*, 512 pp.

Sündermann, J., Becker, G., Damm, P., van den Eynde, D., Laane, R., van Leussen, W., Pohlmann, T., van Raaphorst, W., Radach, G., Schultz, H., Visser, M., 1996. *Decadal variability on the Northwest European shelf*. Dt. Hydrogr. Z. 48 (3/4), 365–400.

Svendsen, E., Berntsen, J., Skogen, M., Ådlandsvik, B., Martinsen, E., 1996. *Model simulation of the Skagerrak circulation and hydrography during Skagex*. J. Marine Systems 8, 219–236.

Taylor, G. I., 1922. *Tidal Oscillations in Gulfs and Rectangular Basins*. Proc. London Math. Soc. s2-20 (1), 148–181.

Tiedtke, M., 1989. *A comprehensive mass flux scheme for cumulus parameterization in large scale models*. Mon. Wea. Rev. 117, 1779–1800.

Tompkins, A., 2002. *A prognostic parameterization for the subgrid-scale variability of water vapor and clouds in large-scale models and its use to diagnose cloud cover*. J. Atmos. Sci. 59, 1917–1942.

Turrell, W. R., 1992. *New hypotheses concerning the circulation of the northern North Sea and its relation to North Sea fish stock recruitment*. ICES Journal of Marine Science 49, 107–123.

Uppala, S. M., Kållberg, P. W., Simmons, A. J., Andrae, U., da Costa Bechtold, V., Fiorino, M., Gibson, J. K., Haseler, J., Hernandez, A., Kelly, G. A., Li, X., Onogi, K., Saarinen, S., Sokka, N., Allan, R. P., Andersson, E., Arpe, K., Balmaseda, M. A., Beljaars, A. C. M., van de Berg, L., Bidlot, J., Bormann, N., Caires, S., Chevallier, F., Dethof, A., Dragosavac, M., Fisher, M., Fuentes, M., Hagemann, S., Hólm, E., Hoskins, B. J., Isaksen, L., Janssen, P. A. E. M., Jenne, R., McNally, A. P., Mahfouf, J.-F., Morcrette, J.-J., Rayner, N. A., Saunders, R. W., Simon, P., Sterl, A., Trenberth, K. E., Untch, A., Vasiljevic, D., Viterbo, P., Woollen, J., 2005. *The ERA-40 re-analysis*. Quart. J. R. Meteorol. Soc. 131, 2961–3012.

van Aken, H. M., van Heijst, G. J. F., Maas, L. R. M., 1987. *Observation of fronts in the North Sea*. J. Mar. Res. 45, 579–600.

van Heijst, G. J. F., 1986. *On the dynamics of a tidal mixing front*. In: Nihoul, J. C. J. (Ed.), Marine Interfaces Ecohydrodynamics. Elsevier, Amsterdam, pp. 165–194.

Vincent, P., Provost, C. L., 1988. *Semidiurnal tides in the northeast Atlantic from a finite element numerical model*. J. Geophys. Res. 93 (C1), 543–555.

Visbeck, M., Cullen, H., Krahmann, G., Naik, N., 1998. *An ocean model's response to North Atlantic Oscillation-like wind forcing*. Geophys. Res. Lett. 25 (24), 4521–4524.

von Storch, H., Zwiers, F. W., 1999. *Statistical Analysis in Climate Research*. Cambridge University Press, 494 pp.

Vyazilova, N. A., 2012. *Cyclone activity and circulation oscillations in the North Atlantic*. Russian Meteorology and Hydrology 37 (7), 431–437.

Wilks, D., 2005. *Statistical Methods in the Atmospheric Sciences*. Vol. 100. Academic Press, 2nd Edition, 648 pp.

Wiltshire, K. H., Kraberg, A., Bartsch, I., Boersma, M., Franke, H.-D., Freund, J., Gebühr, C., Gerdts, G., Stockmann, K., Wichels, A., 2010. *Helgoland Roads, North Sea: 45 Years of Change*. Estuaries and Coasts 33 (2), 295–310.

Winterfeldt, J., Weisse, R., 2009. *Assessment of value added for surface marine wind obtained from two Regional Climate Models*. Monthly Weather Review 137, 2955–2965.

Winther, N. G., Johannessen, J. A., 2006. *North Sea circulation: Atlantic inflow and its destination*. J. Geophys. Res. 111, C12018, 12 pp.

WMO, 2009. *WWRP 2009-1: Recommendations for the Verification and Intercomparison of QPFs and PQPFs from Operational NWP Models*. World Meteorological Organization, WMO/TD 1485.

Wüst, G., 1935. *The Stratosphere of the Atlantic Ocean*. Emery, W. J. (Ed.), 1978, Amerind, New Delhi, 112 pp.

Zeh, H. D., 2010. *The Physical Basis of The Direction of Time*. Springer-Verlag, Berlin Heidelberg, 5th Edition, 224 pp.